



**Silesian  
University  
of Technology**



**UNIVERSITY OF  
LATVIA**

**Silesian University of Technology**

**Faculty of Chemistry**

**Department of Inorganic Chemistry, Analytical Chemistry and Electrochemistry**

**University of Latvia**

**Faculty of Medicine and Life Sciences**

## **PhD THESIS**

***Modification of titanium and its alloys' surfaces in phosphate and carbonate-based  
suspensions with use of plasma electrolytic oxidation***

*Modyfikacja powierzchni tytanu i jego stopów metodą plazmowego utleniania  
elektrochemicznego w zawiesinach fosforanów i węglanów*

*Titāna un tā sakausējumu virsmas modificēšana fosfātu un karbonātu bāzes suspensijās,  
izmantojot plazmas elektrolītisko oksidēšanu*

**MSc Vladlens Grebnevs**

Discipline: Chemical Sciences

Doctoral school

Supervisors

Professor Wojciech Simka

Professor Arturs Viksna

**GLIWICE 2025**



**“The important thing in science is not so much to obtain new facts as to discover new ways of thinking about them.”**

— William Bragg

**“The only principle that does not inhibit progress is: anything goes.”**

— Paul Feyerabend

**“No force on earth can stop an idea whose time has come.”**

— Victor Hugo





I would like to express my deepest gratitude to my supervisors,  
Prof. Wojciech Simka and Prof. Arturs Viksna,  
for their continuous guidance, support, and encouragement of my initiatives and ideas  
throughout this doctoral research. Their insightful feedback and expertise in PEO, analytical  
chemistry, and biomaterials have been invaluable to the success of this work.

I am sincerely thankful to my colleagues and friends at the  
Silesian University of Technology and the University of Latvia  
for their constructive discussions, technical advice, and collaborative spirit that helped shape  
the direction of my research. I am particularly grateful to the members of the Electrochemistry  
Group for their support with experimental setups and data analysis.

I also wish to acknowledge the support of researchers from the  
University of Silesia in Katowice,  
AGH University of Science and Technology in Kraków,  
Jan Kochanowski University in Kielce,  
Adam Mickiewicz University in Poznań,  
and Institute of Atomic Physics and Spectroscopy, University of Latvia  
for their productive collaboration in the characterization of PEO coatings.

Finally, I am profoundly grateful to my family  
for their unconditional support, patience, and belief in me throughout this journey.  
Their unwavering encouragement has been my foundation during both the challenging and  
rewarding moments of my PhD.



## TABLE OF CONTENTS

LIST OF SYMBOLS AND MARKINGS .....	9
ABSTRACT .....	10
STRESZCZENIE .....	12
ANOTĂCIJA.....	14
1. INTRODUCTION .....	16
1.1. General background and relevance of the study.....	16
1.2. Biomedical implants .....	18
1.2.1. General concepts.....	18
1.2.2. Metals as a basis for materials for implants .....	19
1.2.3. Development of coatings .....	20
1.2.4. Calcium carbonate as an additive .....	21
1.2.5. Calcium carbonate coating approaches .....	22
1.3. Plasma electrolytic oxidation .....	24
1.3.1. Basic considerations .....	24
1.3.2. Recent developments, challenges and perspectives of the PEO method.....	26
1.3.3. Basic principles of PEO coating formation .....	27
1.3.4. Limitations of PEO method .....	28
1.3.5. Chemical modification of PEO coatings and bath additives .....	29
1.3.6. Factors influencing properties of PEO coatings .....	30
1.4. Carbonates in PEO .....	32
1.4.1. Current state-of-the-art .....	32
1.4.2. Potential pathways for CC and HA incorporation .....	34
1.4.3. Phenomena in CC-phosphate systems.....	36
1.4.4. Factors affecting the choice of CC synthesis method.....	37
1.4.5. Potential challenges in fabrication of CC-HA coatings.....	38
1.5. Calcium carbonate synthesis methods .....	39
1.5.1. Wet precipitation.....	39
1.5.2. Carbonation .....	40
1.5.3. Biomimetic and biomineralization synthesis.....	41
1.5.4. Microemulsion synthesis .....	41
1.5.5. Other synthesis methods.....	42
1.5.6. Comparison of synthesis methods .....	43
1.6. PEO-associated characterization methods.....	44
1.6.1. Structure of coatings .....	44
1.6.2. Coating chemical composition .....	46
1.6.3. Evaluation of biological properties.....	47
1.6.4. Other functional properties.....	48
1.6.5. Characterization of baths .....	49
2. AIM OF RESEARCH .....	51
3. MATERIALS AND METHODS .....	52
3.1. Preparation of PEO baths .....	52
3.2. Particles used in PEO .....	53
3.2.1. Phosphate particle synthesis .....	53
3.2.2. Carbonate particle synthesis .....	53

3.3.	Characterization of PEO baths .....	54
3.3.1.	Chemical analysis .....	55
3.3.2.	Other bath characteristics .....	56
3.4.	Preparation of PEO coatings .....	56
3.5.	Characterization of PEO coatings .....	58
3.5.1.	Coating structure and elemental composition .....	58
3.5.2.	Phase composition and elemental bonding .....	59
3.5.3.	Biological evaluation of coatings.....	60
3.5.4.	Other functional characteristics .....	61
4.	RESULTS AND DISCUSSION.....	63
4.1.	Part I – Preliminary experiments .....	63
4.1.1.	Phosphate electrolyte concentration, effect of pH and conductivity.....	64
4.1.2.	Carbonate electrolyte concentration.....	66
4.1.3.	The use of commercial particles and particle size issue .....	70
4.2.	Part II – Particle crystallinity effect .....	72
4.2.1.	Suspension characterization .....	74
4.2.2.	Surface morphology and porosity .....	77
4.2.3.	Roughness and wettability .....	79
4.2.4.	Coating thickness .....	82
4.2.5.	Elemental composition in a cross-section.....	84
4.2.6.	Raman spectroscopy analysis.....	88
4.2.7.	Bioactivity tests.....	89
4.3.	Part III – Fabrication and characterization of CC-HA coatings.....	92
4.3.1.	Basic interrelations.....	92
4.3.2.	Preparation and characterization of PEO baths.....	97
4.3.3.	Characterization of the PEO process .....	104
4.3.4.	Coating surface characteristics.....	105
4.3.5.	Coating cross-section .....	109
4.3.6.	Raman spectroscopy analysis.....	111
4.3.7.	Coating growth mechanism .....	114
4.3.8.	XRD analysis .....	122
4.3.9.	XPS analysis .....	124
4.3.10.	Ion release tests and surface wettability.....	126
4.3.11.	Corrosion resistance tests.....	128
4.3.12.	Surface scratch tests .....	132
4.3.13.	Assessment of biocompatibility and antibacterial performance .....	135
4.3.14.	Surface zeta potential measurements .....	137
5.	SUMMARY AND OUTLOOK.....	141
6.	LITERATURE .....	143
7.	DISSEMINATION OF RESULTS.....	176

## LIST OF SYMBOLS AND MARKINGS

AC – alternating current

ACP – amorphous tricalcium phosphate (also used as “amorphous TCP” or “a-TCP”)

BGP –  $\beta$ -glycerophosphate

CA – calcium acetate

CaP – calcium phosphate

CC – calcium carbonate

CC-HA – calcium carbonate and hydroxyapatite (in the context of suspensions and solids that contain both these phases, as well as coatings prepared in those containing electrolytes)

CO<sub>3</sub>-HA – carbonate-substituted hydroxyapatite

DC – direct current

DLS – Dynamic Light Scattering

EDX – Energy-Dispersive X-ray Spectroscopy

EIS – Electrochemical Impedance Spectroscopy

FTIR – Fourier-Transform Infrared Spectroscopy

HA – hydroxyapatite

ICP-OES - Inductively coupled plasma optical emission spectroscopy

PBS – Phosphate Buffered Saline

PDP – Potentiodynamic polarization

PEO – Plasma electrolytic oxidation

SBF – simulated body fluid

SEM – Scanning Electron Microscopy

TAV, Ti6Al4V – titanium-aluminium-vanadium alloy (weight fractions: Al - 6%, V – 4 %, Ti – balance)

TCP – tricalcium phosphate

TEM – Transmission Electron Microscopy

V<sub>lim</sub> – limiting voltage

XPS – X-Ray Photoelectron Spectroscopy

XRD – X-Ray Diffraction

b-, c-, a- – prefixes used in Section 4.2 to denote “blank,” “crystalline,” and “amorphous” particles, their respective baths, and PEO coatings

G,  $\sigma$  – electrical conductivity ( $\text{mS}\cdot\text{cm}^{-1}$ )

Ra – average roughness ( $\mu\text{m}$ )

Rz – maximum height of the profile, calculated as the difference between the highest peak and the lowest valley ( $\mu\text{m}$ )

v – vibration mode

$\gamma$  – mass concentration ( $\text{g}\cdot\text{L}^{-1}$ )

$\zeta$  – zeta potential (mV)

$\omega$  – mass fraction (%)

## ABSTRACT

The development of implant coatings with enhanced surface chemical properties for bone and dental defect treatment is a central challenge in biomaterials science. Combining calcium carbonate (CC) and hydroxyapatite (HA) integrates the high bioresorbability and calcium ion release of CC with the structural stability and bone-like chemistry of HA, enhancing bioactivity and promoting osteointegration along a biomimetic pathway. This doctoral dissertation presents a comprehensive investigation of the anodization-derived plasma electrolytic oxidation (PEO) process for the fabrication of implant coatings, considering it as one of the most promising surface modification techniques due to the high mechanical performance of the resulting layers and the limited influence of thermal effects, yet still insufficiently explored in the context of carbonate additives. The aim of this work was to develop PEO coatings on titanium implants incorporating CC and HA, overcoming the existing challenges associated with their incorporation, and ultimately obtaining bioactive, corrosion-resistant, and functionally robust layers with a well-defined phase composition. A further objective was to clarify particle-incorporation mechanisms in PEO, with particular emphasis on the role of particle crystallinity.

A literature overview covered fundamentals of biomedical implants; the roles, properties, and synthesis of CC; coating methods and characterization; and PEO principles, capabilities, and limitations. This review enabled the identification of the most suitable strategy for creating working PEO bath, which was based on the synthesis of CC particles via carbonation followed by their partial reaction with a dibasic phosphate electrolyte. The experimental work was divided into three stages: (1) Preliminary experiments aimed at establishing relationships between PEO parameters in phosphate-carbonate baths and resulting coating properties, focusing on morphology and elemental composition; (2) The influence of particle crystallinity—addressed here as an independent factor not previously examined—was evaluated with respect to coating phase composition, bioactivity, thickness and internal structure, wettability, and surface roughness; (3) Final optimization procedures were carried out, leading to the fabrication of the optimized CC–HA coatings including a detailed description of their fabrication protocol, as well as comprehensive physicochemical, biological and other functional characterization, and elucidation of the coating formation mechanism.

Key analytical methods for coating characterization included SEM for surface and cross-sectional morphology; EDX, XPS, XRD, and Raman spectroscopy for composition and phase analysis; and SBF tests, cell culture assays, and antibacterial tests for biological performance. Coating functional assessments comprised water contact angle (determination of wettability), immersion-based ion release, streaming potential (surface charge), scratch testing (adhesion strength), and corrosion studies using EIS and potentiodynamic polarization (PDP). Electrolyte bath characterization included pH and conductivity measurements, chromatographic monitoring of dissolved phosphate and carbonate contents, electron microscopy for particle size and morphology, elemental analysis and FTIR for particle chemistry, and XRD for particle crystallinity.

Results obtained within experiments in stage (1) showed that electrolyte concentration and conductivity directly correlate with coating pore size, with consistent trends across pH values. pH exerted a secondary yet notable effect on pore shape and surface elemental composition. Importantly, soluble carbonate salts did not yield incorporation of phases other than anatase; at higher concentrations they suppressed micro-discharges, reduced pore size, and rendered PEO inoperative above ~90–95%. Stage (2) demonstrated that suspended particle crystallinity markedly affects coating bioactivity—especially the kinetics of HA-like layer formation—as well as surface topography (pore shape, size distribution uniformity, total porosity, and pore density). Amorphous particles resulted in higher calcium content in outer layers, plausibly due to rougher particle surfaces enhancing retention within the porous oxide. Stage (3) confirmed that the literature-derived electrolyte-preparation strategy, combined with optimization of component concentrations, ratios, and process voltage, enables simultaneous

incorporation of CC and HA. Monitoring of bath preparation indicated that reaction of CC nanoparticles with phosphate ions produces 1–2  $\mu\text{m}$  CC–HA agglomerates that are optimal for PEO treatment. The resulting coatings displayed typical PEO morphology,  $\sim 25$   $\mu\text{m}$  thickness, moderate porosity, and elevated Ca and P contents. Raman spectroscopy identified CC, HA, anatase, and amorphous  $\text{TiO}_2$ ; XRD additionally detected rutile, perovskite, and brushite. Incorporation of CC–HA particles improved corrosion resistance and adhesion; the coatings were highly biocompatible, bacteriostatic, hydrophilic, moderately negatively charged, and released calcium ions continuously for one month in PBS.

Overall, the PEO method—and specifically the proposed electrolyte-preparation route—demonstrates the capacity for concurrent CC and HA incorporation and efficiently yields coatings that satisfy criteria relevant to *in vivo* use. To the best of current knowledge, this study constitutes the first successful direct incorporation of a carbonate phase as solid particles into a PEO coating and the first application of a carbonation-based particle synthesis tailored to PEO. The carbonation approach offers a neutral, ready-to-use suspension free of conductive impurities, avoiding purification or redispersion steps, which are common in suspension-assisted PEO. From a practical perspective, the developed coatings show promise for the fabrication of implants with enhanced osteointegration and improved long-term durability. Furthermore, the obtained results lay the groundwork for further optimization of carbonate-based systems for biomedical and broader applications. Future work should refine electrolyte composition, evaluate performance under clinically relevant conditions, deepen insight into carbonate behavior during PEO, and design alternative particle systems for standalone or combined CC incorporation.

## STRESZCZENIE

Rozwój powłok na implanty tytanowe o ulepszonych właściwościach chemicznych powierzchni, przeznaczonych do leczenia ubytków kostnych i stomatologicznych, stanowi centralne znaczne wyzwanie w nauce o biomateriałach. Połączenie węglanu wapnia (WW) i hydroksyapatytu (HA) łączy wysoką bioresorbowalność i zdolność uwalniania jonów wapnia, charakterystyczną dla WW, ze stabilnością strukturalną i o składzie chemicznym podobnym do kości, właściwym dla HA, co zwiększa bioaktywność i sprzyja osteointegracji wzdłuż biomimetycznej ścieżki. Niniejsza rozprawa doktorska przedstawia kompleksowe badania procesu anodowania w technologii plazmowego utleniania elektrolitycznego (PEO) do wytwarzania powłok na bioimplantach, uznawanego za jedną z najbardziej obiecujących technik modyfikacji powierzchni ze względu na wysokie parametry mechaniczne otrzymywanych warstw oraz ograniczony wpływ efektów cieplnych, a jednak wciąż niewystarczająco poznanego w kontekście dodatków węglanowych. Celem pracy było opracowanie powłok PEO na implantach tytanowych zawierających WW i HA, przezwyciężenie istniejących trudności związanych z ich wprowadzeniem oraz uzyskanie ostatecznie bioaktywnych, odpornych na korozję i funkcjonalnie wytrzymałych warstw o dobrze określonym składzie fazowym. Dodatkowym celem było wyjaśnienie mechanizmów wbudowywania cząstek w procesie PEO, ze szczególnym uwzględnieniem roli krystaliczności cząstek.

Przeprowadzono obszerne studium literaturowe obejmujące podstawy implantów biomedycznych; rolę, właściwości i syntezę WW; metody nanoszenia powłok i ich charakterystykę; a także zasady, możliwości i ograniczenia technologii PEO. Analiza ta umożliwiła zidentyfikowanie najbardziej odpowiedniej strategii tworzenia roboczej kąpieli PEO, opartej na syntezie cząstek WW metodą karbonatyzacji, a następnie ich częściowej reakcji z elektrolitem fosforanowym dwuzasadowym. Prace eksperymentalne podzielono na trzy etapy. (1) Eksperymenty wstępne, których celem było ustalenie zależności między parametrami PEO w kąpielach fosforanowo-węglanowych a właściwościami otrzymywanych powłok, ze szczególnym uwzględnieniem morfologii i składu pierwiastkowego. (2) Wpływ krystaliczności cząstek — analizowany tu jako niezależny czynnik, wcześniej niebadany — oceniano pod kątem składu fazowego, bioaktywności, grubości i struktury wewnętrznej powłok, zwilżalności oraz chropowatości powierzchni. (3) Przeprowadzono końcowe procedury optymalizacyjne, prowadzące do wytworzenia zoptymalizowanych powłok WW–HA, obejmujące szczegółowy opis ich protokołu wytwarzania, kompleksową charakterystykę fizykochemiczną, biologiczną i innych właściwości funkcjonalnych, a także wyjaśnienie mechanizmu formowania powłok.

Kluczowe metody analityczne obejmowały: SEM do analizy morfologii powierzchni i przekrojów; EDX, XPS, XRD oraz spektroskopię Ramana do analizy składu i faz; a także testy w SBF, hodowle komórkowe i testy antybakteryjne do oceny właściwości biologicznych. Oceny funkcjonalne obejmowały pomiar kąta zwilżania wodą (zwilżalność), badanie uwalniania jonów w warunkach immersji, pomiar potencjału przepływu (ładunek powierzchniowy), testy zarysowania (przyczepność) oraz badania korozyjne z wykorzystaniem EIS spektroskopii impedancyjnej i polaryzacji potencjodynamicznej. Charakterystyka elektrolitu obejmowała pomiar pH i przewodnictwa, chromatograficzne monitorowanie zawartości rozpuszczonych fosforanów i węglanów, mikroskopię elektronową do analizy wielkości i morfologii cząstek, analizę elementarną i FTIR do badania chemii składu chemicznego cząstek oraz XRD do określania ich składu fazowego i krystaliczności cząstek.

Etap (1) wykazał, że stężenie i przewodnictwo elektrolitu są bezpośrednio skorelowane z rozmiarem porów powłoki, przy czym obserwowane trendy były spójne w całym zakresie wartości pH. pH wywierało wtórny, lecz istotny wpływ na kształt porów i skład pierwiastkowy powierzchni. Istotne jest, że rozpuszczalne sole węglanowe nie powodowały powstawania faz innych niż anataz; przy wyższych stężeniach tłumiły mikrowyładowania, zmniejszały rozmiar porów i uniemożliwiały prowadzenie procesu PEO przy zawartości węglanu powyżej 90–95%.



Etap (2) wykazał, że krystaliczność zawieszonych cząstek znacząco wpływa na bioaktywność powłoki — szczególnie na kinetykę tworzenia warstwy podobnej do hydroksyapatytu — a także na topografię powierzchni (kształt porów, jednorodność rozkładu ich rozmiarów, całkowitą porowatość i gęstość porów). Cząstki amorficzne skutkowały wyższą zawartością wapnia w warstwach zewnętrznych, prawdopodobnie z powodu większej chropowatości ich powierzchni, co sprzyjało retencji w porowatym tlenku. Etap (3) potwierdził, że opracowana na podstawie literatury strategia przygotowania elektrolitu, w połączeniu z optymalizacją stężeń i proporcji składników oraz napięcia procesu, umożliwia jednocześnie wbudowywanie WW i HA. Monitorowanie przygotowania kąpeli wykazało, że reakcja nanocząstek WW z fosforanami prowadzi do powstawania aglomeratów WW–HA o wielkości 1–2  $\mu\text{m}$ , optymalnych do obróbki metodą PEO. Otrzymane powłoki wykazywały typową morfologię PEO, grubość około 25  $\mu\text{m}$ , umiarkowaną porowatość oraz podwyższoną zawartość Ca i P. Spektroskopia Ramana zidentyfikowała WW, HA, anataz i amorficzny  $\text{TiO}_2$ ; XRD dodatkowo wykryło rutyl, perowskit i brushyt. Wbudowanie cząstek WW–HA poprawiło odporność korozyjną i przyczepność; powłoki były wysoce biokompatybilne, bakteriostatyczne, hydrofilowe, o umiarkowanie ujemnym ładunku powierzchniowym, i uwalniały jony wapnia w sposób ciągły przez jeden miesiąc w PBS.

Ogólnie rzecz biorąc, metoda PEO — a w szczególności zaproponowana procedura przygotowania kąpeli — wykazuje zdolność do jednoczesnego wbudowywania WW i HA oraz skutecznie pozwala otrzymywać powłoki spełniające kryteria istotne dla zastosowań *in vivo*. Niniejsze badanie stanowi pierwsze udane bezpośrednie wbudowanie fazy węglanowej w postaci cząstek stałych do powłoki PEO oraz pierwsze zastosowanie syntezy cząstek metodą karbonatyzacji, dostosowanej do technologii PEO. Podejście to zapewnia neutralną, gotową do użycia zawiesinę wolną od przewodzących zanieczyszczeń, eliminując konieczność etapów oczyszczania lub redyspergowania, powszechnych w PEO wspomagany przez zawiesinę PEO wspomagany przez zawiesinę. Z praktycznego punktu widzenia opracowane powłoki rokują dobrze pod kątem wytwarzania implantów o zwiększonej osteointegracji i poprawionej długoterminowej trwałości. Ponadto uzyskane wyniki stanowią podstawę do dalszej optymalizacji systemów opartych na węglanach dla zastosowań biomedycznych i szerszych. Przyszłe prace powinny obejmować udoskonalenie składu elektrolitu, ocenę właściwości w warunkach istotnych klinicznie, pogłębienie wiedzy na temat zachowania węglanów podczas PEO oraz opracowanie alternatywnych systemów cząstek do samodzielnego lub łączonego wbudowywania WW.

## ANOTĀCIJA

Implantu pārklājumu ar uzlabotām virsmas ķīmiskajām īpašībām izstrāde kaulu un zobu defektu ārstēšanai ir centrālais izaicinājums biomateriālu zinātnē. Kalcija karbonāta (KK) un hidroksiapatīta (HA) kombinēšana apvieno KK augsto bioresorbējamību un kalcija jonu izdalīšanos ar HA strukturālo stabilitāti un kaulam līdzīgo ķīmiju, tādējādi uzlabojot bioaktivitāti un veicinot osteointegrāciju biomimētiskā ceļā. Šī doktora disertācija piedāvā visaptverošu anodizācijas iegūtā plazmas elektrolītiskās oksidācijas (PEO) procesa izpēti implantu bioaktīvo pārklājumu izgatavošanai, aplūkojot to kā vienu no daudzsološākajām virsmas modificēšanas metodēm, pateicoties augstajai mehāniskajai veiktspējai un ierobežotajai termisko efektu ietekmei, tomēr joprojām nepietiekami izpētītu karbonāta piedevu kontekstā. Šī darba mērķis bija izstrādāt uz titāna implantiem PEO pārklājumus, kas satur KK un HA, pārvarot pastāvošos izaicinājumus to iekļaušanā, un galu galā iegūt bioaktīvas, korozijizturīgas un funkcionāli stabilas kārtas ar skaidri definētu fāžu sastāvu. Papildu mērķis bija izskaidrot daļiņu iekļaušanās mehānismus PEO procesā, īpašu uzmanību pievēršot daļiņu kristāliskuma lomai.

Literatūras apskats ietvēra biomedicīnisko implantu pamatus; KK lomu, īpašības un sintēzi; pārklājumu metodes un raksturošanas pieejas; kā arī PEO principus, iespējas un ierobežojumus. Šis pārskats ļāva identificēt piemērotāko stratēģiju PEO elektrolīta sastāva izveidei, kuras pamatā bija KK daļiņu sintēze ar karbonizācijas metodi, kam sekoja to daļēja reakcija ar dibāzisko fosfāta elektrolītu. Eksperimentālais darbs tika sadalīts trīs posmos: (1) Sākotnējie eksperimenti bija vērsti uz attiecību noteikšanu starp PEO parametriem fosfātu–karbonātu vannās un iegūto pārklājumu īpašībām, galvenokārt koncentrējoties uz morfoloģiju un elementu sastāvu. (2) Daļiņu kristāliskuma ietekmes izvērtēšana, šeit aplūkota kā neatkarīgs faktors, kas līdz šim nav pētīts. Tika vērtēta tā ietekme uz pārklājuma fāžu sastāvu, bioaktivitāti, biezumu un iekšējo struktūru, mitrināmību un virsmas raupjumu. (3) Galīgā optimizācija, kas nodrošināja optimizētu KK–HA pārklājumu iegūšanu. Šajā posmā tika detalizēti aprakstīta to izgatavošanas metodika, veikta visaptveroša fizikāli ķīmiskā, bioloģiskā un funkcionālā raksturošana, kā arī pārklājumu veidošanās mehānisma izskaidrošana.

Galvenās analītiskās metodes pārklājumu raksturošanai ietvēra SEM virsmas un šķērsgriezuma morfoloģijai; EDX, XPS, XRD un Ramana spektroskopiju sastāva un fāžu analīzei; kā arī SBF testus, šūnu kultūras testus un antibakteriālos testus bioloģiskās veiktspējas izvērtēšanai. Funkcionālā raksturošana ietvēra ūdens kontakta leņķa noteikšanu (mitrināmība), jonu izdalīšanās mērījumus imersijas ceļā, plūsmas potenciālu (virsmas lādiņš), skrāpējuma testus (adhezijas stiprība) un korozijas pētījumus, izmantojot EIS un potenciostatiskās polarizācijas metodes. Elektrolīta vannas raksturošanā tika veikti pH un vadītspējas mērījumi, hromatogrāfiska fosfātu un karbonātu koncentrācijas kontrole, daļiņu izmēra un morfoloģijas analīze ar elektronu mikroskopiju, elementu analīze un FTIR spektroskopija daļiņu ķīmijai, kā arī XRD daļiņu kristāliskumam.

Rezultāti no 1. posma eksperimentiem parādīja, ka elektrolīta koncentrācija un vadītspēja tieši korelē ar pārklājuma poru izmēru, ar konsekventām tendencēm dažādos pH līmeņos. pH ietekme bija sekundāra, bet joprojām nozīmīga, īpaši poru formā un virsmas elementu sastāvā. Būtiski, ka šķīstošie karbonātu sāļi neradīja citas fāzes kā vien anatāze; pie augstākām koncentrācijām tie nomāca mikroizlādes, samazināja poru izmēru un padarīja PEO procesu nefunkcionālu, ja karbonātu saturs pārsniedza ~90–95%. 2. posmā tika pierādīts, ka suspendēto daļiņu kristāliskums būtiski ietekmē pārklājuma bioaktivitāti, īpaši HA tipa kārtas veidošanās kinētiku, kā arī virsmas topogrāfiju (poru formu, izmēru sadalījuma vienmērību, kopējo porainību un poru blīvumu). Amorfās daļiņas radīja augstāku kalcija saturu ārējos slāņos, iespējams, pateicoties raupjākām daļiņu virsmām, kas veicināja to aizturi porainajā oksīda struktūrā. 3. posms apstiprināja, ka no literatūras izrietošā elektrolīta sagatavošanas stratēģija, apvienojumā ar komponentu koncentrāciju, proporciju un procesa sprieguma optimizāciju, nodrošina KK un HA vienlaicīgu iekļaušanu. Vannas sagatavošanas novērojumi

parādīja, ka KK nanopartikulu reakcija ar fosfātiem veido 1–2  $\mu\text{m}$  lielus KK–HA aglomerātus, kas ir optimāli PEO procesam. Iegūtajiem pārklājumiem bija tipiska PEO morfoloģija, apmēram 25  $\mu\text{m}$  biezums, mērena porainība un paaugstināts Ca un P saturs. Ramana spektroskopija identificēja KK, HA, anatāzi un amorfo  $\text{TiO}_2$ ; XRD papildus noteica rutilu, perovskītu un brushītu. KK–HA daļiņu iekļaušana uzlaboja korozijas izturību un adhezijas īpašības. Pārklājumi bija ļoti bioloģiski saderīgi, bakteriostatiski, hidrofilī, ar mēreni negatīvu virsmas lādiņu, un tie nepārtraukti izdalīja kalcija jonus vienu mēnesi PBS šķīdumā.

Kopumā PEO metode – un jo īpaši piedāvātā elektrolīta sagatavošanas pieeja – demonstrē spēju vienlaicīgi iekļaut KK un HA, efektīvi radot pārklājumus, kas atbilst prasībām *in vivo* lietošanai. Šis pētījums ir pirmais, kas veiksmīgi parādījis karbonāta fāzes tiešu iekļaušanu PEO pārklājumā cietu daļiņu veidā, kā arī pirmais, kurā pielietota karbonizācijas metode PEO vajadzībām piemērotu daļiņu sintēzei. Karbonizācijas pieeja piedāvā neitrālu, gatavu suspensiju bez vadītspējīgiem piemaisījumiem, novēršot nepieciešamību pēc attīrīšanas vai atjaunošanas soļiem, kas ir bieži sastopami PEO procesā ar suspensijas pievienošanu. Praktiskā ziņā izstrādātie pārklājumi ir daudzsoļi implantu izgatavošanai ar uzlabotu osteointegrāciju un ilgtermiņa izturību. Turklāt iegūtie rezultāti veido pamatu turpmākai karbonāta bāzes sistēmu optimizācijai biomedicīnā un plašākās pielietojuma jomās. Nākotnes darbos būtu jāpilnveido elektrolīta sastāvs, jāvērtē pārklājumu darbība klīniski atbilstošos apstākļos, jādziļina izpratne par karbonātu uzvedību PEO procesā un jāizstrādā alternatīvas daļiņu sistēmas gan KK iekļaušanai atsevišķi, gan kombinācijā.

## 1. INTRODUCTION

### 1.1. General background and relevance of the study

Modern society is facing a range of global challenges that have a direct impact on public health. Among the most pressing factors are environmental degradation, population aging, sedentary lifestyles, unbalanced nutrition, and the growing prevalence of chronic diseases. These and related conditions contribute to a progressive increase in musculoskeletal disorders, including osteoporosis, osteoarthritis, osteomyelitis, as well as dental and maxillofacial pathologies such as periodontitis, bone tissue resorption, and traumatic injuries. According to the World Health Organization, more than 20% of individuals over the age of 50 experience compromised bone integrity and reduced bone strength, often requiring prolonged and costly treatment. Fractures remain particularly widespread, resulting both from mechanical trauma and age-related decreases in bone density. Furthermore, the incidence of joint surface degradation and other skeletal impairments is steadily increasing, driven not only by aging but also by lifestyle factors, occupational stress, and genetic predisposition [1], [2], [3].

The consequences of these pathologies extend far beyond the medical domain. They place a substantial burden on healthcare systems and significantly increase economic costs due to the need for surgical interventions, prolonged rehabilitation, and the use of advanced, high-cost pharmaceuticals and medical technologies. The rising incidence of such conditions underscores the urgent need for the development of novel, more effective solutions capable of restoring or replacing damaged bone tissue, thereby improving quality of life [4], [5], [6].

One of the most promising approaches in this field is the use of implants—temporary or permanent structures designed to replace or support damaged bone or dental tissue. While certain biomaterials can stimulate tissue regeneration, fully functional artificial bones and joints have yet to be developed. Implants, however, offer solutions to a broad range of clinical challenges, from fracture stabilization to the reconstruction of entire anatomical structures. Alternative methods, such as autologous transplantation, are often limited by the scarcity of donor material, potential immune rejection, and secondary complications. Consequently, implants remain a cornerstone of modern reconstructive surgery [7], [8], [9].

The use of implants has a long history, tracing back to ancient civilizations. Archaeological findings indicate that dental implants were employed in Ancient Egypt and Mesoamerican cultures. During the Middle Ages, concepts of restoring lost teeth or bone remained largely theoretical. However, with the advancement of medicine and surgery in the 19th and 20th centuries, implantology emerged as a distinct scientific discipline. By the late 20th century, the first truly functional implants made of metals, polymers, and ceramics were introduced, marking a significant milestone in the field [10], [11], [12].

A modern implant is a highly engineered device designed to meet a complex set of mechanical, chemical, and biological requirements, and the most reliable configuration typically consists of a metallic core—commonly titanium—coated with a thin ceramic layer. This design combines exceptional mechanical strength and load-bearing capacity with surface biocompatibility and bioactivity. The latter is particularly critical, as the implant surface directly interfaces with living tissues, determining the success of osteointegration and the long-term stability of the implant. Titanium and its alloys, particularly Ti-6Al-4V, have become the gold standard in implant manufacturing due to their unique combination of properties: low toxicity, excellent corrosion resistance, a strength-to-weight ratio comparable to that of natural bone, resistance to fatigue loading, and favorable machinability [13], [14], [15].

From a chemical perspective, the development of implant technologies can be broadly categorized into four generations. The “zero” generation comprised purely mechanical structures without any coating, occasionally featuring surface texture modifications to improve fixation. The first generation introduced hydroxyapatite ( $\text{Ca}_{10}(\text{PO}_4)_6(\text{OH})_2$ , HA)-based coatings, the primary mineral component of bone tissue, which enhanced implant adhesion and promoted bone formation. However, these coatings were largely inert and exhibited limited bioactivity.

The second generation advanced by incorporating bioactive and biodegradable additives, including polymers, bioglass, and ions such as magnesium, strontium, and zinc. The third generation has been focused on achieving biomimetic properties—both chemically and structurally resembling natural bone—while actively initiating and supporting the natural processes of tissue regeneration and remodeling [16], [17], [18].

Currently, calcium phosphate (CaP) compounds—such as HA, tricalcium phosphate (TCP), and amorphous calcium phosphate (ACP)—are widely employed as implant coatings. However, these materials often lack sufficient bioactivity, exhibit slow dissolution rates, and consequently do not always promote efficient bone regeneration. This has directed research interest toward alternative or composite coating systems. One particularly promising approach involves combining calcium carbonate ( $\text{CaCO}_3$ , CC) with HA. CC is a naturally occurring, biocompatible, and biodegradable material that demonstrates high bioactivity due to its significantly greater solubility—approximately ten times higher than that of HA. This property enables CC to gradually dissolve in biological fluids, generating a calcium-enriched microenvironment favorable for osteogenesis. Meanwhile, the remaining HA forms a stable coating matrix, preventing degradation from progressing to the metallic substrate. CC can be sourced from both biotic materials (e.g., mollusk shells) and abiotic origins, is easily synthesized under laboratory conditions, produces no toxic degradation products (breaking down into  $\text{CO}_2$  and  $\text{Ca}^{2+}$ ), and holds strong potential as a functional component in advanced implant coatings [19], [20], [21], [22].

Nevertheless, the fabrication of implants with carbonate-based coatings faces several technical challenges. Commonly employed techniques—such as plasma spraying, sol-gel processing, magnetron sputtering, and chemical deposition—either lead to thermal decomposition of CC, fail to achieve sufficient adhesion to the substrate, or compromise phase stability. These limitations stem primarily from the low thermal stability of CC (decomposition temperature  $\sim 750^\circ\text{C}$ ), its susceptibility to dissolution in acidic environments (e.g., during etching), limited solubility in neutral and alkaline conditions, and poor stability under electric fields. As a result, no standardized method has yet been established for producing carbonate coatings that fully meet the stringent requirements of medical implant applications [23], [24], [25].

Against this backdrop, plasma electrolytic oxidation (PEO) has emerged as a particularly promising surface modification technology for metallic implants. PEO is based on the formation of oxide coatings through high-voltage micro-arc discharges occurring in an electrolyte. When the applied voltage reaches a critical threshold, microscopic plasma discharges are generated on the metal surface, causing localized melting followed by the growth of an oxide layer that frequently incorporates electrolyte-derived species. PEO offers several key advantages: strong adhesion of the coating to the substrate, the ability to create a microporous structure, excellent corrosion and mechanical resistance, and tunable chemical composition through tailored electrolyte formulations. Unlike other coating techniques, the localized and transient thermal effects inherent to PEO provide the potential to incorporate thermally less phases—such as CC—without causing their complete decomposition [26], [27].

Despite its potential, PEO technology remains under active development, and optimizing its use for producing functional coatings with tailored chemical compositions is one of the field's key research directions. Chemical modification of PEO coatings is typically achieved either by introducing dissolved compounds into the electrolyte or by employing suspensions of solid particles. Most published studies have focused on phosphate-, silicate-, or alkaline-based electrolytic baths, whereas carbonate-based systems remain largely unexplored. To date, there have been no documented reports of deliberately achieving successful incorporation of a CC phase into PEO coatings on titanium substrates. Attempts to introduce carbonates directly into the electrolyte have proven ineffective and inherently limited, as under PEO conditions these compounds either undergo electrochemical decomposition at the anode, thermally decompose during discharge events, decompose due to local pH changes, or exhibit poor solubility in the presence of calcium ions [19], [28], [29].

In this context, the most promising approach involves introducing CC particles into the electrolyte as a dispersed suspension. This method enables the direct incorporation of the pre-formed carbonate phase into the oxide layer under the combined influence of electric field and the localized thermal energy generated by micro-discharges. Despite its considerable potential, suspension-assisted PEO as a surface functionalization strategy requires comprehensive optimization. Critical factors include controlling particle size, morphology, and surface charge; ensuring stable dispersion while preventing aggregation; overcoming challenges associated with achieving a sufficiently negative zeta potential; and addressing the limited commercial availability of particles with the desired properties. Additionally, fine-tuning the electrical parameters, hydrodynamic conditions, and process temperature is essential to achieve reproducible and high-quality coatings. Furthermore, the strategy must be designed to ensure the simultaneous incorporation of HA alongside CC, achieving a relatively homogeneous distribution of both phases within the coating in optimal proportions [30], [31], [32].

Thus, the relevance of this study lies in the need for a systematic, stepwise scientific approach to developing CC-HA PEO coatings for biomedical applications. Achieving this goal first requires a comprehensive investigation of PEO processes in electrolytes containing phosphate and carbonate suspensions and solutions. A detailed understanding of how electrolyte composition, the properties of the added phases, and processing parameters influence the morphology, phase composition, and structure of the resulting coatings will establish the foundation for designing next-generation composite biocompatible coatings that simultaneously exhibit bioactivity, bioresorbability, and long-term stability.

## **1.2. Biomedical implants**

### **1.2.1. General concepts**

Implants are medical devices designed to be implanted into the body, with the main purpose of replacing lost or damaged areas of solid calcified tissue, such as bone or teeth. Bone and teeth, the primary solid calcified tissues, are specialized biological structures composed of mineralized matrices—mainly CaP in bone and HA-enriched dentin and enamel in teeth. These tissues can become damaged or lost due to trauma, degenerative diseases (e.g., osteoporosis or periodontitis), infections, congenital defects, or surgical removal of diseased tissue. Implants aim to restore the anatomical shape and function of the affected area while meeting the requirements of biocompatibility, safety, and mechanical reliability throughout its entire service life. Modern implants are classified according to several criteria. First, based on the type of tissue they replace, they are divided into bone, dental, and cartilage implants, which also determines their overall shape and structural design to match the anatomical requirements of the target tissue. Separately, implants can also be categorized by their medical purpose or anatomical location as orthopedic (for bones and joints), maxillofacial (for facial skeletal structures), or dental (for teeth and supporting tissues). Second, depending on the base material, implants can be metallic, ceramic, polymeric, or composite. Another important criterion is the presence and type of surface coating. Coatings may be bioinert, bioactive, or resorbable, depending on their interaction with surrounding tissues. Additionally, implants differ by their service life: temporary (e.g., osteosynthesis systems, guided bone regeneration devices, or resorbable structures) and permanent (e.g., dental implants, joint prostheses, and spinal implants). Implant integration into the body occurs through osteointegration, a biological process in which surrounding bone tissue gradually grows and bonds with the implant surface. This strong mechanical and biological connection is promoted by the implant's material properties and surface characteristics, which enhance cell adhesion, proliferation, and mineralization. Successful osteointegration ensures long-term stability, proper load transfer, and full functional recovery of the damaged skeletal or dental structure [33], [34], [35], [36], [37].

### 1.2.2. Metals as a basis for materials for implants

Metals and their alloys form the basis of the vast majority of implants due to their combination of high strength, corrosion resistance, fatigue resistance, and relative ease of processing. The most widely used metals include titanium and its alloys (particularly Ti-6Al-4V), stainless steel (316L), cobalt-chromium alloys, tantalum, niobium, and magnesium. Among these materials, titanium is the most versatile and clinically preferred option. Its advantages include excellent corrosion resistance due to the formation of a passive TiO<sub>2</sub> film, non-toxicity and good biocompatibility, low density ( $\approx 4.5 \text{ g/cm}^3$ ) close to that of bone, relatively high strength, and a modulus of elasticity that reduces the “stress shielding” effect. Additionally, titanium is relatively affordable and widely available [38], [39].

One of the most commonly used materials for implant fabrication is the titanium alloy Ti-6Al-4V (TAV), which contains approximately 6% aluminum and 4% vanadium. This ( $\alpha+\beta$ )-titanium alloy offers high strength, good corrosion resistance, and relative ease of machining. Compared to commercially pure titanium, TAV provides a higher strength-to-weight ratio, making it suitable for small or load-bearing implants, greater resistance to plastic deformation, and stability in physiological environments due to the formation of a dense passive TiO<sub>2</sub> film. However, there are limitations: the release of Al<sup>3+</sup> and V<sup>5+</sup> ions in biological conditions raises concerns about neurotoxicity and inflammatory reactions. As a result, alternative vanadium-free alloys, such as Ti-6Al-7Nb, Ti-13Nb-13Zr, and  $\beta$ -titanium alloys, have been developed with improved biological inertness. Despite these developments, TAV remains the “gold standard” in orthopedics and dentistry because of its optimal balance of strength, cost-effectiveness, and manufacturability, particularly when combined with bioactive coatings that compensate for its inherent bioinertness [33], [40].

The use of stainless steel in implants is limited by potential ion release (Cr, Ni), while cobalt-chromium alloys, though superior for high-load applications, exhibit limited osteointegration. In recent years, magnesium alloys have attracted significant interest due to their biodegradability and density similar to bone. However, magnesium corrodes excessively fast in physiological conditions, producing hydrogen gas and increasing pH, which can hinder tissue healing. Tantalum and niobium implants, especially in porous forms such as trabecular metal, are also of great interest. Porous tantalum provides excellent osteointegration, high corrosion resistance, and chemical inertness, but its high cost, density, and processing challenges restrict its widespread use, confining it mainly to specialized orthopedic applications such as hip joint endoprostheses and spinal cages [41], [42], [43].

In addition to metallic implants, polymeric substrates are sometimes used, particularly in low-load applications, for temporary use, or for guided tissue regeneration. The most common biopolymers include polyesters such as polylactide (PLA), polyglycolide (PGA), and their copolymers (PLGA); polyurethanes and poly( $\epsilon$ -caprolactone) (PCL); and bioinert polymers such as high-density polyethylene (PE-HD), polyetheretherketone (PEEK), and polytetrafluoroethylene (PTFE). Polymer-based substrates offer several advantages: the ability to biodegrade, which is particularly important for temporary implants; flexibility and low density similar to soft tissues and bone; high processability and moldability, including compatibility with 3D printing and casting; and minimal risk of corrosion. However, they also have serious limitations for creating load-bearing or long-term implants, including low strength and stiffness that limit their ability to effectively transmit mechanical loads; limited osteointegration, as most polymers are bioinert and do not provide strong bone bonding; susceptibility to deformation, degradation, and swelling in physiological conditions; and potential local acidification and inflammation due to degradation products (e.g., lactic acid) [44], [45], [46].

In practice, polymers are mainly used as temporary scaffolds for bone tissue regeneration, in endodontics and maxillofacial surgery (e.g., resorbable membranes), and as part of hybrid composites where a strong metallic core is supplemented by a polymer layer or matrix. Compared to metallic substrates, polymers cannot match metals in terms of mechanical

stability, durability, and corrosion resistance. Metals, particularly titanium and its alloys, provide high strength with minimal volume, reliable fixation within bone tissue, and the ability to carry bioactive coatings that enhance biological performance. Therefore, in most clinically significant scenarios, particularly for load-bearing, long-term implants, metallic substrates (especially titanium and Ti-6Al-4V) remain the preferred choice, while polymers serve primarily as auxiliary or temporary solutions [33], [47].

### 1.2.3. Development of coatings

Despite their undeniable advantages—such as high mechanical strength, corrosion resistance, and technological reliability—metallic implants are inherently biologically inert and typically fail to fully interact with surrounding living tissues. Early generations of implants were often made of bare metals and were successfully used in orthopedics and dentistry (e.g., hip stems, dental screws, fixation plates). However, their functional performance was limited and primarily served as passive structural supports without actively promoting bone bonding or tissue regeneration. As the understanding of biomaterials advanced, it became evident that simply placing a metallic object in the body was insufficient for long-term success and functional integration. This realization led to the emergence of the surface coating concept. From an engineering perspective, this is the most rational approach: the metallic core provides strength and load-bearing capacity, while the outer surface layer is designed to enhance biological functionality and biocompatibility, actively interacting with surrounding tissues and promoting the healing of hard tissue. Another driving factor for coating development is that even highly stable materials, such as titanium and its alloys, may experience localized corrosion during long-term implantation. This effect is particularly pronounced in inflammatory environments characterized by low pH, chloride ions, proteins, and other aggressive species. Alloys such as Ti-6Al-4V can release metallic ions (e.g.,  $\text{Al}^{3+}$  and  $\text{V}^{5+}$ ), which may have toxic effects, trigger inflammatory or allergic reactions, and contribute to elastic modulus mismatch with bone tissue [11], [48], [49].

Today, coatings have become an integral component of implant design, and their range of functionalities continues to expand. Beyond basic biocompatibility and corrosion protection, coatings can regulate ionic exchange with surrounding tissues, provide antibacterial protection, serve as carriers for drug delivery, and control the resorption rate of biodegradable implants. Moreover, ongoing research is targeting new, previously unattainable properties and configurations of implant coatings, reflecting both advances in materials science and an evolving understanding of bone biology [50], [51]. The evolution of implant coatings has progressed through distinct stages, showing a clear trend toward biomimicry—designing implant surfaces that increasingly resemble the natural mineral composition and functionality of bone tissue. This development can be broadly divided into four generations. The first generation of passive bioinert coatings (1970s–1980s) aimed to ensure basic biocompatibility and corrosion resistance. Made of stable oxides such as  $\text{TiO}_2$ ,  $\text{Al}_2\text{O}_3$ , and  $\text{ZrO}_2$ , these coatings provided mechanical fixation but lacked biological activity, often leading to fibrous tissue encapsulation instead of bone bonding. The second generation (1980s–1990s) introduced osteoconductive coatings such as HA, TCP, and bioactive glasses. These materials partially mimicked bone's inorganic phase, forming chemical bonds with the bone matrix and improving osteoconduction and implant stability. The third generation (2000s) enhanced biological response through ionically modified coatings. Ion-substituted HAs ( $\text{Mg}^{2+}$ ,  $\text{Sr}^{2+}$ ,  $\text{Zn}^{2+}$ ) and nanostructured CaP composites closely matched natural apatite, stimulating osteogenesis, angiogenesis, and cellular differentiation while strengthening chemical integration with bone. The fourth generation (2010s–present) focuses on multifunctional, adaptive “smart” coatings. Examples include hybrid CC/HA composites, peptide-functionalized surfaces, and stimuli-responsive layers capable of delivering therapeutic agents or ions. Combining biomimetic composition, osteoinduction, antibacterial protection, and controlled biodegradation, these coatings represent a step toward fully integrated, regenerative implant systems [16], [17].



Improvements in implant performance are pursued through various approaches. Some of these involve modifications of surface physical properties, such as optimizing surface topography and roughness to enhance mechanical interlocking with bone tissue. At the same time, coatings are increasingly endowed with stimuli-responsive functionalities, including piezoelectric, light-responsive, and pH-responsive systems that dynamically adapt to the surrounding biological environment [52]. Nevertheless, the primary research focus remains on tailoring surface chemistry—specifically, through the synthesis of new bioactive additives and the exploration of novel technological approaches for their incorporation into coating systems, while ensuring proper overall performance of the resulting layers under real-world conditions. Notable examples include diamond-like carbon (DLC), silicon carbide, and fullerene-based coatings [53], [54]. Polymer-based layers, such as polyetheretherketone (PEEK), are employed to improve stability, wear resistance, and biomechanical performance. Additionally, peptide-based coatings—for example, those containing RGD (arginine–glycine–aspartic acid) peptides—have been developed to promote cell adhesion and bone formation by facilitating integrin binding [55], [56]. Among the wide array of promising additives and functional phases, CC has emerged as a particularly attractive candidate due to its natural role in bone mineralization, high bioactivity, and bioresorbability [57]. However, most of these novel compounds are designed to serve a single specific function and cannot independently provide full multifunctionality. Therefore, they are typically incorporated into coatings in combination with one or more additional components. As auxiliary additives, materials characteristic of previous coating generations are still frequently employed—for instance, bone-like inorganic phases such as HA and other CaP derivatives, silicon-containing compounds, and bioactive glasses, owing to their proven reliability. Consequently, many studies are also directed toward developing strategies for the simultaneous integration of multiple components, ensuring their uniform distribution within the coating, and achieving an optimal volumetric and molar ratio of these phases [22], [58], [20].

#### 1.2.4. Calcium carbonate as an additive

Building upon advancements in coating technologies, over the past decade CC has emerged as a particularly promising functional component in biomedical coatings, offering a range of unique advantages not shared by other currently investigated additives. To identify the key aspects of CC's distinctiveness, it is first necessary to consider its fundamental properties. CC is a naturally occurring, abundant mineral that exists in several crystalline polymorphs—calcite, aragonite, and vaterite—each with its own characteristic solubility and stability. Chemically, CC is relatively stable under physiological conditions, but it dissolves more readily in acidic environments, releasing calcium and carbonate ions. However, compared with CaP-based minerals typically used for coatings, even the least soluble polymorph, calcite, exhibits a solubility approximately an order of magnitude higher. This property enables CC to release calcium ions *in vivo* in a relatively dynamic and sustained manner, imparting bioactive characteristics, resorbability, and controlled biodegradation. Ultimately, these features make CC a particularly promising candidate for temporary bioactive coatings that gradually dissolve and are replaced by natural bone tissue [57], [59].

In long-term applications, CC is likewise advantageous, as its rapid ion release promotes early-stage bone cell adhesion and proliferation, thereby initiating and supporting mineralization. It is particularly useful as an additive to coatings based on biologically inert materials. This also applies to HA—especially in its highly crystalline form—for which numerous practical observations indicate that its sole presence on a surface can hinder the formation of chemical bonds with bone tissue, impair implant fixation, and ultimately reduce service life. In such cases, the inclusion of CC can promote osteointegration while ensuring that bone–metal contact is preceded by the complete resorption of the coating. In other words, the implant surface should undergo full, controlled resorption while maintaining a stable, three-dimensional HA-based matrix that supports ingrowth and the formation of dense, calcified

tissue [20], [60], [61]. The high potential of CC in bone regeneration is further supported by both cell culture and *in vivo* studies [62], [63], [64]. Additionally, the weak alkalinity of CC imparts buffering capacity, allowing its dissolution products to neutralize acidic microenvironments that frequently arise around implants due to inflammation. This localized pH regulation plays a critical role in mitigating inflammatory responses and establishing conditions favorable for tissue healing and osteointegration [65], [66].

In addition to the above, it should be noted that in living organisms CC plays both vital structural and metabolic roles. It is a principal biomineral in marine shells, corals, and exoskeletons, and contributes to the early stages of mineralization in vertebrate bones and teeth. Within the human bone matrix, released carbonate ions can naturally substitute for phosphate or hydroxyl groups in HA, thereby enhancing bone remodeling and metabolic activity. The resorbable nature of CC also allows it to participate more actively in bone turnover compared with HA. Furthermore, in the presence of phosphates, CC can be readily converted into HA or B-type carbonate HA via a dissolution–precipitation mechanism, making it a precursor in the formation of bone mineral phases. Once in the body, the conversion of CC is primarily mediated by osteoclasts and carbonic anhydrase, and it is not accompanied by the formation of any toxic by-products [22], [67], [68], [69], [70].

Further confirming the potential of CC for implant coatings, it should be noted that in the broader field of biomaterials, CC has also been successfully employed in the form of ceramics, gels, cements, and composite particles, as well as in scaffolds and drug-delivery systems. In all these cases, the incorporation of CC is consistent with the concept of “fourth-generation” biomaterials—those possessing biomimetic properties and capable of engaging the body’s natural tissue regeneration mechanisms. Furthermore, CC-based composites are under investigation as contrast agents for medical imaging. This breadth of application can be attributed to the availability of CC in diverse forms, including nanostructured, porous, functionalized, and composite particles. Beyond the field of biomaterials, CC-based coatings also hold considerable potential. Possible applications include environmental engineering, such as water treatment, filtration systems, and sorption processes, owing to CC’s known ability to neutralize acidic pollutants and adsorb phosphates, heavy metals, and acidic gases. Functionalized CC surfaces also show promise as co-catalysts in organic synthesis, pollutant degradation, and hydrogen production. Moreover, the incorporation of carbonate into coatings may enhance the corrosion resistance of underlying metals, as demonstrated in several studies, and in some respects offers a safer alternative to traditional corrosion inhibitors [71], [72], [73], [74], [75].

Overall, while CC demonstrates a broad range of beneficial properties and versatile applications across biomedical and non-biomedical fields, the focus of this study remains specifically on implant coatings. Given the need for long-term mechanical stability alongside early-stage bioactivity, the use of CC as a sole coating component is not considered practical. Instead, a combined approach should be adopted by incorporating CC into a more stable matrix. In this regard, the most promising solution appears to be its combination with HA, as it provides a stable, bioactive framework that complements the beneficial resorbability of CC, while also being the most abundant CaP mineral [20], [76], [77].

#### **1.2.5. Calcium carbonate coating approaches**

At first glance, the fabrication of CC-based coatings—either as standalone layers or in combination with HA—may appear to be a straightforward task, seemingly implementable using principles similar to those applied for earlier generations of coatings composed solely of CaPs. In reality, however, several factors must be considered in an integrated manner. These include the general requirements for implant coatings, the principles underlying classical methods for their fabrication, and the potential limitations arising from the intrinsic properties of both CC and the coating technologies themselves.

When addressing the choice of a coating fabrication method for biomedical applications from a general standpoint—irrespective of its composition or intended function—it must be guided by a set of fundamental requirements. While the final coatings are expected to provide essential characteristics, such as biocompatibility and bioactivity, ensured by the incorporated additives, the chosen deposition technology should not introduce any unwanted chemical contaminants. Such impurities—arising either from the intrinsic principles of the technique or from by-products generated during processing—may diminish or even counteract the intended beneficial effects of the bioactive additives. Moreover, the prepared coatings must demonstrate functional integrity and mechanical stability, forming a strong bond with the substrate that can be maintained under physiological conditions, for example, by withstanding surgical handling and *in vivo* mechanical stresses without delamination or cracking. Depending on the clinical application, coatings should be either long-lasting for permanent implants or resorbable for temporary devices designed to support bone regeneration. An effective coating must also act as a robust barrier against corrosion and wear, thereby reducing harmful ion release and mitigating inflammatory reactions. Additionally, the surface topography and porosity of the coating should be optimized to enhance mechanical interlocking with bone tissue, facilitate nutrient diffusion, and support vascularization. When incorporating bioactive additives, such as CC, these must be firmly integrated into the coating matrix to prevent uncontrolled leaching or structural weakening. Finally, the selected coating deposition method must be fully compatible with the implant's material and geometry, allowing for uniform, defect-free coverage without introducing residual stresses or altering the substrate's inherent properties [51], [78], [79].

Common methods for implant surface modification are generally categorized into hydroprocessing and pyroprocessing techniques. Hydroprocessing methods operate in aqueous or solution-based environments at relatively low temperatures, enabling the deposition of bioactive coatings under mild conditions. Examples include sol-gel processing, electrophoretic deposition, dip-coating, and brush-coating. Pyroprocessing techniques, by contrast, involve high-temperature or vacuum-based physical and chemical processes such as thermal spraying, chemical vapor deposition (CVD), physical vapor deposition (PVD), laser cladding, and ion implantation. The primary distinction between these approaches lies in the energy input and the resulting coating characteristics: hydroprocessing typically produces porous, hydrated layers that enhance biological interactions, whereas pyroprocessing yields dense, mechanically robust films with superior wear resistance but often limited bioactivity [80], [81].

PVD is a vacuum-based process in which material is vaporized and condensed onto the implant surface, frequently assisted by plasma to improve adhesion. It provides precise control of thickness and composition, resulting in dense, wear-resistant, and high-purity layers. However, due to their limited thickness, PVD coatings may not ensure long-term corrosion protection. Additionally, achieving uniform deposition on complex geometries is challenging, and the method involves high equipment costs. CVD utilizes chemical reactions of gaseous precursors near the substrate to form solid coatings. Depending on the process, activation may be thermal or plasma-based. This method produces conformal, uniform coatings with excellent adhesion and controlled stoichiometry. It is commonly applied to deposit bioinert and bioactive layers, such as titanium nitride or diamond-like carbon, enhancing wear resistance and hemocompatibility. Nonetheless, the high temperatures required can alter the substrate microstructure or induce residual stresses, while some precursors pose handling and safety challenges [82], [83].

The sol-gel technique is a wet-chemical process where a colloidal suspension is applied to the implant surface and subsequently dried and heat-treated to form a ceramic layer. It is cost-effective, suitable for complex geometries, and enables homogeneous incorporation of bioactive compounds like HA, promoting osteointegration. However, sol-gel coatings often have limited adhesion and mechanical strength, leading to cracking or delamination under physiological loading. Thermal spraying methods, including plasma spraying and high-velocity oxy-fuel spraying, deposit molten or semi-molten particles onto the implant, forming thick,

rough coatings widely used for HA deposition. Their drawbacks include potential microstructural inhomogeneities, residual stresses from rapid solidification, relatively low adhesion strength, and possible dissolution or degradation of the coating in physiological environments [84].

Other techniques have been explored for specialized applications. Electrophoretic deposition enables controlled ceramic particle deposition under an electric field, offering a simple and cost-effective approach for coating complex shapes. Laser cladding and ion implantation allow localized surface modifications with tailored chemical and mechanical properties. Dip-coating and brush-coating are occasionally used for experimental bioactive layers but lack reproducibility and mechanical stability for large-scale applications. These less common methods typically serve as complementary or experimental strategies when mainstream techniques do not fully meet clinical requirements [84], [85], [86], [87].

From the perspective of developing CC-containing coatings with properties favorable for bone implants, the aforementioned methods may present notable limitations, arising both from the specific physical principles underlying these processes and from the intrinsic properties of CC itself. First, if a hydroprocessing procedure is carried out in acidic environments, carbonate ions are prone to rapid conversion into  $\text{CO}_2$  and loss from the solution. In neutral and alkaline conditions, the simultaneous presence of soluble carbonate sources with calcium and phosphorus ions can lead to precipitation, thereby destabilizing the medium. Although hydroprocessing techniques such as sol-gel synthesis and electrophoretic deposition are, in principle, capable of introducing carbonate phases, in practice they often yield coatings with insufficient adhesion and mechanical durability under physiological conditions. In the case of pyroprocessing, which can produce denser and more wear-resistant layers, the main limitation is the relatively low decomposition temperature of CC, approximately  $750^\circ\text{C}$  [88]. Indeed, methods such as PVD, CVD, and thermal spraying operate at temperatures that either decompose carbonates or hinder their incorporation. For the same reason, using pyroprocessing to improve the adhesion strength of CC-containing coatings prepared via hydroprocessing can also result in CC decomposition [78]. Among pyroprocessing techniques, pulsed laser deposition is a notable exception, as it offers operational flexibility and has demonstrated the ability to adjust substrate temperatures to levels suitable for CC deposition. Nevertheless, it remains a line-of-sight method, which poses challenges for coating complex-shaped surfaces [89]. Overall, only a subset of the reviewed techniques can successfully enrich implant surfaces with carbonates, and none consistently produces adherent, durable coatings on three-dimensional substrates that meet the requirements for next-generation implants, namely the combination of bioactivity, corrosion resistance, and mechanical stability. Accordingly, an alternative and more reliable approach is required to achieve stable CC-HA composite coatings.

### **1.3. Plasma electrolytic oxidation**

#### **1.3.1. Basic considerations**

Plasma electrolytic oxidation (PEO), also known as micro-arc oxidation (MAO), has evolved over several decades as a surface engineering technique designed to enhance the properties of metals such as aluminum, titanium, magnesium, zirconium, tantalum, and their alloys. The origins of PEO trace back to conventional anodizing processes developed in the early 20th century, with patents for anodic oxidation on aluminum emerging as early as 1923 in Germany and 1927 in the United Kingdom. In the mid-20th century, researchers observed that increasing the anodizing voltage beyond the dielectric breakdown of the oxide layer led to the appearance of micro-discharges on the surface. Early scientific reports in the 1960s and 1970s (notably by Markov and colleagues in the former USSR) described these plasma-assisted processes and their ability to produce thicker, more crystalline oxide layers compared to traditional anodizing. The term “micro-arc oxidation” was introduced in Russian literature

during the 1980s, while “plasma electrolytic oxidation” gained broader use in the 1990s as the process gained international recognition. Over time, advancements in power supply technology (transitioning from simple DC sources to pulsed and bipolar systems), electrolyte formulation, and mechanistic understanding transformed PEO from a niche laboratory phenomenon into a robust industrial surface engineering method [90], [91], [92].

A typical PEO setup consists of three main components: a power supply, an electrolytic bath (sometimes called “electrolyte bath”, simply “bath” or “electrolyte”), and electrodes (anode and cathode). The workpiece, usually a metal, serves as the anode and is immersed in an aqueous electrolyte contained within a corrosion-resistant tank. A separate counter electrode is commonly used as the cathode, often made of stainless steel but other conductive and corrosion-resistant materials can also be employed. The electrolyte composition depends on the desired coating properties and often contains alkaline solutions with silicate, phosphate, or aluminate additives, with optional incorporation of bioactive ions or nanoparticles. The power supply is a key element, capable of delivering high voltages (typically 200–600 V) and various current waveforms (DC, pulsed DC, or bipolar AC). This enables the controlled initiation and maintenance of micro-discharges on the anode surface once the dielectric breakdown voltage of the oxide layer is exceeded. Cooling and stirring systems are often integrated into the bath to maintain uniform temperature and electrolyte homogeneity during treatment. Additional diagnostic tools such as oscilloscopes, optical emission spectrometers, and acoustic sensors can be coupled to the system for monitoring plasma activity [26], [93], [94], [95].

The applications of PEO span multiple high-performance fields where durable, functional oxide coatings are required. In aerospace and automotive industries, PEO is applied to aluminum and magnesium components to significantly improve wear resistance (hardness exceeding 1500 HV for some alumina-rich coatings) and corrosion protection, enabling the use of lightweight alloys in aggressive environments. In biomedical engineering, PEO has become particularly important for titanium and magnesium-based implants, enhancing bioactivity and promoting osteointegration. Beyond biomedical and structural applications, PEO is employed in electronics for dielectric films with breakdown voltages over 2000 V, in energy technologies for photoelectrochemical electrodes and catalytic supports, and in marine engineering for enhanced corrosion resistance of ship and offshore structures in saline environments [93], [96], [97].

The positive properties of PEO coatings arise from the unique high-energy plasma-assisted oxidation mechanism, which produces coatings with high hardness (up to 2000 HV in some systems), excellent metallurgical adhesion to the substrate, and superior wear and corrosion resistance compared to traditional anodic films. The process typically yields a multi-layered structure comprising a dense inner barrier layer ( $<1\ \mu\text{m}$ ) and a porous outer layer (up to 100–150  $\mu\text{m}$ ), allowing post-treatment sealing or impregnation with functional agents. The localized high temperatures (up to 10,000 K in discharge channels) and rapid quenching favor the formation of crystalline phases such as  $\alpha\text{-Al}_2\text{O}_3$  (corundum) on aluminum alloys,  $\text{TiO}_2$  (rutile and anatase) on titanium, and  $\text{MgAl}_2\text{O}_4$  (magnesium aluminate spinel) on magnesium alloys. Another advantage is the ability to incorporate alloying elements or functional species (Ca, P, Si, Sr, Ag) directly into the oxide matrix during growth, enabling multifunctional coatings without additional deposition steps.

Compared to other implant coating methods such as PVD, CVD, sol–gel processing, and thermal spraying, PEO avoids high-vacuum environments or line-of-sight limitations typical for PVD/CVD. It generates mechanically robust, crystalline oxide layers in a single step without requiring post-deposition heat treatment. The inherently porous and relatively thick coatings produced by PEO are particularly beneficial for bone tissue integration. Furthermore, the short-lived and localized nature of plasma micro-discharges allows the incorporation of thermally sensitive phases—such as CC—that would typically decompose under conventional high-temperature techniques. From a general standpoint, PEO offers several advantages over other coating techniques. The process is environmentally friendly, typically conducted in

aqueous electrolytes without toxic solvents, and yields coatings with strong metallurgical bonding and chemical stability under extreme conditions (high temperatures, saline environments, acidic or alkaline media). In a sense, this method can be regarded as a combination of pyro- and hydroprocessing. However, PEO also presents challenges, including relatively high energy consumption (up to 1–3 kWh/m<sup>2</sup>), limited applicability to non-valve metals (Section 1.3.4), and difficulties in achieving uniform coatings on complex geometries due to uneven current distribution. Achieving desired properties requires careful optimization of processing parameters, including electrolyte composition, applied current density, voltage, pulse frequency, and treatment duration [93], [98], [99], [100].

### 1.3.2. Recent developments, challenges and perspectives of the PEO method

Biomedical coatings represent one of the most active and impactful areas of PEO-related research, driven in part by the need for long-lasting, biocompatible, and multifunctional implant surfaces. Significant efforts aim to develop coatings that simultaneously promote osteointegration, control degradation rates, and provide antibacterial activity. This is achieved through ion doping (Ca, Zn, Sr, Ag), incorporation of bioactive nanoparticles such as HA or bioglass, and hybrid PEO-hydrothermal or sol-gel post-treatments creating composite bio-ceramic layers. Recent studies have demonstrated that Ca- and P-enriched PEO coatings on titanium implants enhance osteoblast adhesion and bone mineralization, achieving up to 50% faster bone-implant integration compared to untreated surfaces. Silver-doped coatings have shown strong antibacterial effects against *Staphylococcus aureus* and *Escherichia coli*, while maintaining cytocompatibility with osteogenic cells. For magnesium-based biodegradable implants, PEO processing combined with strontium or zinc ion incorporation has been reported to improve corrosion resistance more than 10× compared to bare magnesium alloys while simultaneously stimulating new bone tissue formation. Multifunctional coatings containing HA nanoparticles have also been developed to accelerate bone healing and provide long-term protection against implant-associated infections. When fabricated on titanium substrates, PEO coatings inherently incorporate TiO<sub>2</sub>, typically in the rutile and anatase polymorphic forms. The occurrence of these phases is not considered detrimental; on the contrary, they are well-documented to possess favorable biocompatibility [101], [102], [103], [104], [105].

Outside biomedical applications, research is advancing toward low-energy and high-throughput processing. Development of optimized pulse regimes and advanced power supply designs—particularly pulsed bipolar modes—has been shown to improve energy efficiency and refine coating morphology. Hybrid electrolytes containing suspended nanoparticles are emerging as a strategy to enhance microstructure, hardness, and multifunctionality of PEO coatings. In addition, novel molten salt PEO processes have enabled treatment of refractory metals (Nb, Mo, Ta) at elevated temperatures without water-based electrolytes. Gas-assisted PEO, where reactive gases such as CO<sub>2</sub> or NH<sub>3</sub> are introduced into the discharge zone, is opening new pathways for carbonated or nitrogen-doped oxide coatings with catalytic and photocatalytic properties. Functional PEO coatings are also being explored for advanced energy and industrial applications, including lithium-ion batteries, supercapacitors, solid oxide fuel cells, self-lubricating surfaces, and anti-icing layers for aerospace components. To further extend coating durability and versatility, combined post-treatment approaches are being developed. Beyond conventional hydrothermal sealing and sol-gel deposition, emerging techniques such as laser glazing have demonstrated improved densification, sealing of porosity, and enhancement of wear and corrosion resistance [90], [106], [107], [108], [109].

The technological evolution of the PEO process has advanced markedly in recent years. The chemical versatility of PEO-based surface modification has continuously broadened, driven by the development of novel electrolyte systems capable of introducing previously unconsidered functional ions and compounds into the oxide layer. Notably, carbonate-based electrolytes have only relatively recently emerged in the scientific literature. To date, there has been no compelling evidence of the direct incorporation of carbonate phases within PEO

coatings, let alone systematic exploration of carbonate-containing PEO systems for biomedical applications. In particular, the concept of 'PEO in particle suspension' has emerged as a distinct research direction, not only as a strategy for the *in situ* formation of composite coatings with a modified phase composition of the surface but also as an approach for tailoring additional functionalities. In this process, external particles are deliberately introduced into the electrolyte with the intention of being incorporated into the growing oxide layer. Beyond the incorporation of increasingly innovative and previously unutilized particles—including oxides, borides, nitrides, carbon nanotubes, and even bio-derived materials—ongoing studies aim to elucidate the underlying mechanisms governing the formation of particle-containing PEO coatings. At present, there remains no comprehensive understanding of how various particle characteristics, including size, morphology, surface charge, and concentration, influence the coating's microstructure and, ultimately, its functional performance [30], [110], [111].

A deeper understanding of how process parameters influence coating properties across diverse electrolytic systems has become a general focus of recent studies. Electrolyte characteristics—including chemical composition, concentration, pH, temperature, and viscosity—still require systematic investigation and modeling to fully elucidate their roles in plasma discharge behavior and oxide layer development. Likewise, key PEO processing parameters such as current mode, applied voltage, current density, oxidation time, and substrate type are being comprehensively examined to optimize coating performance. Considering these variables simultaneously is enabling the establishment of predictive frameworks for tailoring coating architecture and functionalities. Importantly, such systematic studies are expected to reveal fundamental interrelations governing PEO coating formation and facilitate the development of coatings with previously unattainable phase compositions, including carbonate-containing layers, either as standalone phases or in combination with other oxides [27], [106], [112], [113].

In parallel with these methodological advances, PEO has been successfully applied to an expanding range of metallic substrates. Beyond the traditional valve metals (the term explained in Section 1.3.4), recent studies have demonstrated coating formation on various new alloys and refractory metals, enabling comparative analyses of coating growth behavior, microstructure evolution, and property development across different alloy chemistries. This substrate diversification is not only broadening the technological applicability of PEO but also deepening the fundamental understanding of plasma-assisted oxidation mechanisms. Furthermore, the integration of real-time diagnostics (e.g., optical emission spectroscopy, acoustic monitoring) and advanced computational tools such as machine learning-based parameter optimization is facilitating the transition toward digitally assisted, adaptive PEO processes. Collectively, these innovations are solidifying PEO as a next-generation surface engineering technology with rapidly expanding capabilities in biomedical, industrial, and energy-related applications [106], [114], [115], [116].

### **1.3.3. Basic principles of PEO coating formation**

The formation of PEO coatings is a complex, multi-stage process that combines electrochemical, thermal, and plasma-chemical phenomena. Initially, the process evolves from conventional anodizing, during which a thin, compact oxide film – often only a few nanometers thick – develops on the metal substrate. As the applied voltage increases, a critical breakdown threshold is reached, triggering localized dielectric breakdown of the oxide film and the onset of transient micro-discharges (sparks). These discharges, typically lasting microseconds, momentarily pierce the insulating oxide layer, establishing temporary conductive pathways that directly connect the metal substrate to the electrolyte. Within these highly localized plasma channels, temperatures can reach up to ~10,000 K, causing localized melting and even vaporization of the substrate material. Despite these breakdown events, a compact barrier layer remains intact at the metal/oxide interface, ensuring strong adhesion and corrosion resistance of the growing coating. Within the discharge sites, oxygen species – generated both

electrochemically and thermally – react with molten substrate material, forming titanium dioxide, which rapidly solidifies upon cooling. Repeated cycles of localized breakdown, temporary metal–electrolyte connection, melting, oxidation, and re-solidification lead to a gradual buildup of an oxide layer several micrometers thick, characterized by a network of interconnected discharge channels and surface pores that act as signatures of the PEO process [28], [93], [117].

As the oxide layer grows, its increasing thickness and resistance necessitate progressively higher voltages to sustain the process. This evolution results in the appearance of larger but less frequent micro-discharges, which can either form at previously inactive surface regions or reoccur at earlier discharge sites, deepening existing pores. Coating growth proceeds via two complementary mechanisms: inward growth, driven by electrochemical oxidation of the metal at the barrier layer, and outward growth, resulting from the ejection of molten oxide onto the surface during plasma events. The outward growth mechanism is responsible for the characteristic crater-like surface morphology and, in cases of insufficient cooling, the formation of sealed internal pores within the coating. Additionally, gas evolution, primarily oxygen generation at the anode, contributes to internal porosity through entrapment of gas bubbles within solidifying oxide. The final pore structure, including the balance between open surface porosity and internal voids, is strongly influenced by processing parameters such as voltage, current mode, frequency, and treatment duration, which collectively control the energy and distribution of micro-discharges [93], [118], [119].

The PEO process also facilitates chemical incorporation from the electrolyte into the growing oxide layer. Under the influence of strong electrophoretic forces generated by electric field, negatively charged anions, such as phosphates or silicates, migrate toward the anode and accumulate near active discharge sites. These species can be incorporated into the coating either by being captured in molten oxide at discharge locations or by penetrating through transient plasma channels into deeper regions of the coating. Once captured, anions can react with titanium or titanium oxide to form complex compounds, such as amorphous titanium phosphates or crosslinked Ti-P-O networks, or precipitate as insoluble salts. Plasma-assisted reactions, high temperatures, and localized rapid cooling contribute to the amorphous or nanocrystalline nature of these phases. Unlike anions, cations are generally repelled from the anode; however, limited incorporation can occur through mechanisms such as capillary-driven transport into discharge channels. Ultimately, the interplay between electrochemical oxidation, plasma discharges, thermal effects, and ionic transport governs the microstructure and composition of PEO coatings, producing strongly adherent oxide layers with a characteristic porous morphology and the ability to integrate electrolyte-derived chemical species into their structure [30], [90], [120], [121].

In addition to ionic incorporation, PEO coatings can integrate suspended solid particles from the electrolyte, enabling composite layer formation. Negatively charged particles, driven by electrophoretic forces, migrate toward the anode similarly to anions and may become entrapped within molten oxide generated during micro-discharges. Depending on their size, morphology, and surface charge, particles can penetrate discharge channels, adhere to the surface, or undergo partial decomposition and reaction with the substrate or oxide matrix under plasma conditions. These interactions can lead to inert physical entrapment, reactive incorporation with phase transformations, or partial bonding to the oxide network. Particle incorporation often enhances coating thickness, modifies porosity, and introduces new phases or functionalities, significantly influencing the final structure and properties of PEO layers [32], [120], [122], [123].

#### **1.3.4. Limitations of PEO method**

The applicability of PEO is inherently limited to a specific group of metals known as valve metals. These metals naturally form stable, adherent, and electrically insulating oxide films in electrolytic environments. Under high applied voltages, the oxide undergoes dielectric



breakdown, initiating localized plasma discharges essential for the formation of thick, crystalline, ceramic-like coatings characteristic of PEO. The term “valve” originates from the behavior of these metals in early rectifying circuits, where the oxide layer acted as a one-way electrical barrier, much like a valve, permitting current to pass preferentially in one direction while blocking it in the opposite direction [124].

Typical valve metals include aluminum (Al), titanium (Ti), zirconium (Zr), tantalum (Ta), niobium (Nb), and magnesium (Mg). These metals share a common property of forming strong, self-passivating oxide films (e.g.,  $\text{TiO}_2$  on Ti,  $\text{Al}_2\text{O}_3$  on Al) that are chemically stable and strongly adherent to the underlying metal substrate. Alloys rich in these elements, such as Ti–6Al–4V or Mg–Al alloys, can also be treated because their surface behavior is dominated by the valve metal component. Non-valve metals, such as steels or copper, do not naturally form stable dielectric oxides under anodic conditions. Therefore, PEO can only be performed on these materials after special pre-treatments or the application of intermediate coatings that provide a suitable oxide-forming surface [124], [125].

A further limitation is the difficulty of achieving uniform coatings on components with highly complex geometries. Although PEO is not a line-of-sight technique and can, in principle, coat intricate shapes, homogeneous layer formation depends on uniform electrolyte access and electric field distribution. Components with deep recesses, narrow channels, sharp edges, or shielded regions can experience non-uniform plasma activity, leading to variations in coating thickness and composition. High-surface-area features—often produced via subtractive manufacturing techniques such as laser micromachining—can distort the electrical response, necessitating careful optimization of process parameters or specialized bath and circulation designs to avoid localized over-oxidation or insufficient coating in hard-to-reach regions [126], [127], [128].

PEO also exhibits intrinsic process limitations that restrict its broader use. The method requires high voltages, typically exceeding 200 V, resulting in considerable energy consumption and limited cost-effectiveness for large-scale applications. The stochastic nature of micro-arc discharges complicates precise control of coating properties, leading to heterogeneity in thickness, porosity, and composition. The ceramic-like oxide layers, while hard and wear-resistant, are brittle and susceptible to cracking under mechanical or thermal stresses. Coating growth is inherently self-limiting; excessive voltage or prolonged treatment causes unstable discharges and potential coating breakdown. At small bath volumes and high specific anode surface areas, the process consumes electrolyte constituents over time and, in some cases, can generate environmentally hazardous byproducts that require careful monitoring and waste treatment. Additionally, PEO coatings typically have a rough and porous surface morphology, advantageous for biomedical osteointegration but unsuitable for applications demanding smooth surfaces without post-processing. Finally, localized high temperatures during discharge events can induce thermal stresses or microstructural changes in the substrate, particularly in thin or low-melting-point metals such as magnesium alloys, potentially compromising structural integrity [93], [117], [129], [130].

### **1.3.5. Chemical modification of PEO coatings and bath additives**

Beyond its fundamental ability to form adherent and wear-resistant oxide layers, PEO offers a unique opportunity to chemically modify the coating through the introduction of reactive species either in the electrolyte or via alternative, less conventional approaches. Such chemical modifications can be achieved by incorporating particles or soluble additives into the electrolyte, as well as through emerging methods that utilize molten salt electrolytes or reactive gaseous environments.

When additives are introduced as dissolved ions or soluble precursors, they are transported into the growing oxide layer primarily through electrochemical and electrophoretic processes. This approach has been widely exploited to incorporate bioactive elements such as  $\text{Ca}^{2+}$ ,  $\text{PO}_4^{3-}$ ,  $\text{Sr}^{2+}$ ,  $\text{Zn}^{2+}$ , and  $\text{Mg}^{2+}$ , as well as corrosion inhibitors like fluoride and silicate

species. For instance, PEO coatings on titanium enriched with Ca and P can achieve Ca/P ratios close to stoichiometric HA (1.6–1.7), enhancing bone cell adhesion and mineralization. Similarly, silicon-containing electrolytes produce Si-doped TiO<sub>2</sub> coatings that exhibit improved osteoblast activity and up to 50% higher corrosion resistance compared to undoped layers. The advantage of using solutions lies in their homogeneous ion distribution and relatively straightforward concentration control, allowing for uniform incorporation throughout the oxide matrix. However, the incorporation efficiency is inherently limited due to plasma-driven decomposition reactions, which can lead to incomplete or non-stoichiometric embedding of the desired species, as well as to competitive reactions forming undesired phases (e.g., CaF<sub>2</sub> or amorphous phosphate) [131], [132].

Alternatively, suspended solid particles—such as HA, bioglass, or antibacterial nanoparticles (e.g., Ag, Cu, ZnO)—can be dispersed in the electrolyte and physically entrained into the discharge channels during coating formation. Particle-assisted PEO offers the possibility to incorporate species that are otherwise insoluble or chemically unstable in aqueous solutions, thus expanding the compositional range of achievable coatings. The particle size, zeta potential, and concentration strongly influence the incorporation mechanism, with smaller, well-dispersed particles exhibiting higher embedding efficiency. Nonetheless, in the microscale particle incorporation is often spatially heterogeneous, leading to localized agglomerates and less predictable chemical gradients within the oxide. Moreover, stable suspension of solid particles requires tailored electrolyte formulations, surfactants or pH adjustments, ultrasonic treatment and mixing conditions to avoid sedimentation and ensure reproducible results during prolonged treatment times [133], [134], [135].

In addition to these reactive species, various auxiliary additives are occasionally employed in PEO electrolytes to improve processing stability, coating quality, or specific functional properties. Surfactants and dispersants are often added to stabilize particle suspensions and promote uniform distribution during particle-assisted PEO. Complexing agents, such as EDTA or citrate salts, can be used to control metal ion activity, preventing premature precipitation and enabling more efficient incorporation into the oxide layer. Organic solvents and viscosity modifiers may also be introduced to adjust electrolyte conductivity and discharge behavior, leading to finer coating microstructures and reduced surface defects. Furthermore, additives like phosphates or silicates, although not always intended as primary dopants, play a role in discharge stabilization and act as network formers in the developing oxide, thereby indirectly influencing coating composition and morphology [113].

Beyond classical aqueous approaches, emerging strategies have expanded the chemical modification capabilities of PEO. The use of molten salt electrolytes allows processing at elevated temperatures and improves the incorporation of species with limited solubility in water, leading to coatings with unique morphologies and compositions. Another recent development is the introduction of gases, such as carbon dioxide, into the discharge environment, which can promote the formation of carbonate-containing or carbon-enriched oxide layers directly during processing. These methods offer additional flexibility for tailoring surface chemistry without relying solely on dissolved additives [136], [137].

### **1.3.6. Factors influencing properties of PEO coatings**

PEO coatings possess a range of properties that collectively determine their performance. Among these, thickness, surface morphology, and porosity are most frequently assessed due to their strong influence on coating functionality and their utility in elucidating process mechanisms. These characteristics, in turn, link the physical structure to chemical, biological, mechanical, and corrosion performance. Understanding the influence of process parameters on these primary features provides a basis for interpreting PEO coating formation principles and tailoring coatings to specific functional requirements. In biomedical applications, such requirements commonly include enhanced bioactivity, strong adhesion, and long-term corrosion resistance. In practice, the ultimate properties of PEO coatings result from the

complex interplay of operational variables, including electrical regime, applied voltage, current density, pulse waveform, frequency, electrolyte conductivity, temperature, and treatment duration [90], [102].

Electrical parameters are among the most influential factors controlling the PEO process. Micro-arc discharges, which facilitate high-temperature reactions and oxide growth, initiate when the applied voltage surpasses the dielectric breakdown threshold of the growing oxide film. Increasing the voltage elevates discharge energy, leading to thicker coatings with larger pores and higher surface roughness. While such features can enhance biological anchoring, excessive voltages may cause unstable sparking, microcrack formation, and coating brittleness. Voltage also strongly impacts the chemical composition of PEO coatings. High-energy discharges promote the decomposition of electrolyte-derived species, such as  $\text{Ca}^{2+}$ ,  $\text{PO}_4^{3-}$ , and  $\text{SiO}_3^{2-}$ , enhancing their incorporation into the oxide layer and improving bioactive element uptake. However, at very high voltages, selective evaporation or phase segregation can occur, altering the Ca/P ratio and favoring high-temperature crystalline phases such as rutile  $\text{TiO}_2$  or calcium titanates over HA [94], [135], [138].

Current density similarly affects both the physical and chemical characteristics of the coating. Elevated current densities accelerate oxide growth and increase surface roughness but may reduce coating uniformity and compactness, compromising corrosion resistance. Chemically, higher current densities enhance the flux of ionic species into discharge channels, promoting their incorporation into the oxide. However, localized overheating can decompose certain functional species or lead to chemical inhomogeneity. Achieving an optimal balance between voltage and current density is therefore critical for producing coatings with the desired thickness, porosity, chemical homogeneity, and mechanical integrity [104], [129], [139], [140], [141].

The mode of current delivery—whether direct current (DC), alternating current (AC), or pulsed direct current—also significantly influences plasma behavior and coating evolution. Pulsed current, particularly when employing asymmetric bipolar pulses, provides intermittent cooling periods that mitigate thermal stresses, resulting in denser and less cracked coatings with superior corrosion resistance. Pulse frequency and duty cycle further modulate discharge dynamics. High frequencies generate numerous low-energy discharges that produce smoother surfaces, finer porosity, and more uniform elemental incorporation. Short-lived sparks help preserve functional species, such as carbonates and phosphates, improving chemical homogeneity. In contrast, low frequencies create fewer but more energetic micro-arcs capable of thermally decomposing electrolyte species, leading to phase transformations such as phosphate to pyrophosphate conversion and chemically nonuniform dopant distribution. The ratio of anodic-to-cathodic pulses also affects coating chemistry, as cathodic pulses enhance electrophoretic transport and reduction of cations such as  $\text{Ca}^{2+}$  and  $\text{Mg}^{2+}$ , improving their incorporation into the oxide layer and influencing the final Ca/P stoichiometry, a key parameter for bioactive coatings [94], [129], [142].

Electrolyte conductivity dictates the current flow and breakdown voltage necessary for discharge initiation. Moderate conductivity provides stable plasma activity and uniform coating development, while high conductivity accelerates growth but can trigger unstable discharges, leading to excessive roughness and lower compactness. Low conductivity delays discharge initiation, producing thinner coatings with limited protective properties. The electrolyte composition determines the elemental and phase constitution of the coating. Soluble salt electrolytes, such as those containing calcium, phosphate, or silicate salts, readily dissociate and incorporate into the oxide via plasma-assisted reactions, forming chemically doped coatings with enhanced bioactivity, corrosion resistance, and HA-forming potential. Particle-containing electrolytes, such as those with HA, CC, or  $\text{TiO}_2$  particles, enable physical entrapment or chemical bonding of particles into the oxide layer, resulting in composite coatings with increased thickness, higher roughness, improved wear resistance, and additional functionalities such as antibacterial properties. The efficiency of particle incorporation depends

on plasma–particle interactions; higher voltages and longer treatment times improve particle embedding but can also coarsen the surface and reduce chemical uniformity [117], [133], [143], [144].

Electrolyte and substrate temperatures influence reaction kinetics, coating phase composition, and adhesion. Elevated temperatures lower the breakdown voltage and accelerate oxide growth but can enlarge pores and induce thermal stresses that weaken adhesion. Thermal effects also drive phase transformations, such as anatase-to-rutile transition and CaP crystallization, modifying chemical stability and corrosion resistance. Effective temperature management, often through external cooling, is essential for producing dense, chemically homogeneous, and strongly adherent coatings. Processing time governs coating thickness, porosity, surface evolution, and chemical enrichment. Extended treatment durations typically produce thicker, more protective coatings with greater incorporation of electrolyte-derived species. However, excessive exposure to micro-discharges can cause pore coarsening, microcrack formation, and thermal decomposition of functional groups, ultimately impairing corrosion protection and bioactivity. Optimizing treatment duration is therefore crucial to achieve a balance between chemical composition, bioactivity, and mechanical stability, while preventing the formation of overly porous or chemically degraded surfaces that may promote bacterial colonization [112], [143], [145], [146].

## **1.4. Carbonates in PEO**

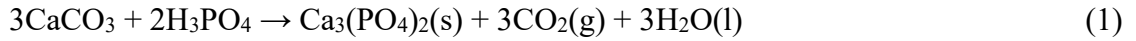
### **1.4.1. Current state-of-the-art**

Compared to other compounds, carbonates are rarely reported as intentional additives in PEO baths [30], [90], [93], [102], [147], [148], [149]. Most studies focus on improving corrosion resistance or wear behavior using carbon-based nanomaterials such as graphene, graphite, or carbon nanotubes rather than carbonate salts or particles [150]. A systematic review of the literature reveals that carbonate-containing phases are only sporadically observed in PEO coatings and often form as incidental byproducts during oxidation of reactive substrates like magnesium [151]. For titanium and its alloys, which are widely used in biomedical implants, deliberate carbonate incorporation remains largely unexplored. Existing reviews on bioactive PEO coatings emphasize calcium–phosphate chemistry, describing carbonate inclusion only briefly and without mechanistic clarity [104], [139]. No dedicated review has examined carbonate additives or their controlled use in PEO for biomedical surface functionalization.

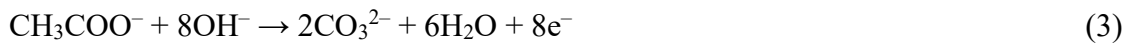
Studies on non-titanium substrates provide indirect insights into carbonate chemistry during PEO. Magnesium-based alloys are the most investigated systems, where soluble carbonate salts such as  $\text{Na}_2\text{CO}_3$  are added to improve electrolyte conductivity or modify surface porosity. These additions can lead to limited incorporation of magnesium carbonate ( $\text{MgCO}_3$ ) or lithium carbonate ( $\text{Li}_2\text{CO}_3$ ), which can enhance corrosion resistance and microhardness. However, carbonate formation is usually secondary to dominant MgO or phosphate phases and often results from plasma-driven reactions between dissolved  $\text{CO}_2$  species and the substrate rather than intentional deposition [151] [152]. In some cases,  $\text{CO}_2$  gas bubbling during PEO accelerates coating growth and promotes  $\text{MgCO}_3$  formation [137]. For aluminum, beryllium, and copper substrates, carbonate-containing phases do not form due to thermal instability or competing reactions, though carbonate salts can influence plasma discharge behavior and coating uniformity [153], [154], [155], [156].

On titanium-based substrates, direct use of soluble carbonate electrolytes similarly fails to incorporate carbonates into PEO coatings. Experiments with sodium carbonate alone or combined with silicates produce typical porous  $\text{TiO}_2$  layers composed of anatase and rutile, with no carbonate phases detected. The role of carbonate ions in these systems is limited to providing bath conductivity and modulating plasma intensity. Even at high voltages or with complex bath compositions, carbonate incorporation does not occur, and titanium’s chemical

inertness prevents reaction pathways analogous to those seen on magnesium [157] [158] [159] [160] [161] [162]. Attempts to add solid CC particles to phosphoric acid-based electrolytes also proved ineffective, as particles decomposed or dissolved (Eq. 1), yielding coatings containing only CaP phases [163] [164]. In another study, addition of  $\text{Ag}_2\text{CO}_3$  powder into the PEO bath also resulted in its dissolution via complexation with ammonia, precluding the formation of carbonate phases in the coatings [165]. Direct addition of solid particles to an alkaline PEO bath on titanium did not initiate discharges, and the process remained in the anodization stage, yielding only titanium oxide layers [166]. The only partially successful approach involved silicon-coated CC nanoparticles, which altered surface morphology of PEO coatings and ensured calcium ion release during subsequent coating immersion tests, suggesting limited entrapment in the oxide layer but without detectable carbonate phase formation [167].



Indirect generation of carbonate phases during PEO has been observed using soluble precursors like CA and BGP. At sufficiently high voltages ( $>450$  V), the thermal decomposition of CA (Eq. 2) or the electrochemical conversion of acetate ions (Eq. 3), coupled with the capture of calcium ions, enables the *in situ* formation and incorporation of CC (Eq. 4). However, this process is highly sensitive to treatment time and voltage: prolonged oxidation densifies the oxide layer, sealing pores and reducing coating adhesion, while insufficient voltage suppresses carbonate precipitation. Coatings often stratify, with carbonate phases enriched near the surface [168] [169] [170]. Similar behavior occurs with modified electrolyte compositions or titanium alloys containing niobium, zirconium, or tantalum, where altered discharge characteristics affect carbonate stability [171], [172]. Conversely, at lower voltages or in mildly acidic phosphate electrolytes, carbonate phases are absent, and coatings remain amorphous or phosphate-dominated [173] [174] [175]. These findings confirm that carbonate formation in soluble baths is nontrivial and lacks the controllability needed for robust biomedical coating strategies.



Additionally, several studies have reported findings indirectly related to carbonate incorporation. In one instance, a titanium surface was treated in an electrolyte containing barium acetate and NaOH, which resulted in the formation of a  $\text{BaCO}_3$  phase within a coating approximately  $3\ \mu\text{m}$  thick. No dielectric breakdown or micro-discharges occurred during the process, indicating that it did not qualify as PEO, and the surface lacked the characteristic microporous morphology of such coatings. The  $\text{BaCO}_3$  phase was attributed to the migration of barium and carbonate ions under an applied ionic current [176]. In another case, PEO was employed as a preparatory step for carbonate deposition: a porous oxide layer was first generated on titanium in an alkaline phosphate-based electrolyte, followed by ultrasonic sealing in a  $\text{NaHCO}_3$  and  $\text{Ca}(\text{NO}_3)_2$  solution, which introduced  $\text{MgCO}_3$  and CC phases into the coating [177].

Taking the above into account, deliberate incorporation of carbonate phases into PEO coatings faces considerable challenges, particularly when phosphate-based electrolytes are employed. Although suspension-based PEO, where insoluble particles are electrophoretically incorporated into the growing oxide layer, has successfully been used for HA, zirconia, silica, and other bioactive ceramics—often enhancing coating thickness and compositional control [31], [111], [133], [178]—no confirmed study has demonstrated stable entrapment of CC particles on titanium substrates. The main potential obstacles include carbonate decomposition under high plasma temperatures, dissolution in acidic environments with conversion to  $\text{CO}_2$ , and difficulties in controlling particle size and dispersion. In alkaline phosphate electrolytes,

simultaneous presence of  $\text{Ca}^{2+}$ ,  $\text{PO}_4^{3-}$ , and  $\text{CO}_3^{2-}$  ions promotes non-stoichiometric precipitation of carbonate and phosphate phases in solution, decreasing bath conductivity and destabilizing plasma discharges [19]. When acetate–phosphate baths are used, carbonate can form *in situ*; however, this occurs only within a narrow process window that balances phase precipitation with maintenance of coating porosity. Furthermore, carbonate phases are intrinsically less thermally stable than HA or titanium oxide, making them particularly susceptible to spark-induced decomposition during coating growth [88].

Nevertheless, particle-based approaches can be considered a more promising pathway for incorporating CC, including in combination with HA. This stems from the fact that solid particles are inherently less prone to plasma-induced thermal decomposition than dissolved carbonate species, as their physical volume provides localized regions shielded from the highest temperatures. Achieving this, however, requires solving several tactical challenges: selecting an appropriate synthesis route for CC particles with controlled size and morphology, optimizing electrical parameters to promote stable particle capture, and ensuring the co-presence of CC and HA within the suspension and final coating without undesirable phase transformations.

#### 1.4.2. Potential pathways for CC and HA incorporation

Based on earlier discussion (Section 1.2.4), it is fair to state that achieving stable and reproducible biphasic CC-HA coatings remains challenging primarily due to the inherent physicochemical limitations of the carbonate phase. This is evidenced by the fact that, unlike CC, the incorporation of HA in PEO coatings is relatively well understood, with multiple approaches having been experimentally validated. HA can be introduced directly as suspended particles in the electrolyte, which are electrophoretically driven toward the anodic surface and embedded into the growing oxide layer, or indirectly generated *in situ* via high-temperature reactions of dissolved calcium and phosphate species during plasma discharge. In both cases, phosphate-containing electrolytes play a central role, serving not only as phosphorus sources but also as conductive media necessary to sustain the PEO process. Therefore, a critical aspect of developing a viable PEO process lies in identifying suitable bath configurations that enable the simultaneous activation and incorporation of both CC and HA while maintaining coating integrity and stability. Consequently, selecting an appropriate HA source is closely linked to the choice of conducting electrolyte, as it must ensure sufficient bath conductivity while enabling effective HA incorporation.

Given the poor solubility of CC and its susceptibility to thermal decomposition [88], introducing carbonates into PEO coatings is significantly more complex. Maintaining carbonate stability requires a basic environment, as carbonate and bicarbonate ions readily transform into carbon dioxide under acidic conditions. From this perspective, three primary bath configurations can be envisioned for simultaneous CC and HA incorporation. The first option involves using only soluble phosphorus-containing electrolytes, where carbonate and calcium ions are dissolved and react near the anode to precipitate CC and HA phases. While this is the simplest approach in terms of bath composition, it faces substantial limitations: in basic solutions, calcium and phosphate salts can precipitate prematurely in the bulk electrolyte, lowering conductivity and disrupting discharge activity, whereas in alkaline regimes compatible with carbonates, the formation of HA during plasma discharges may be incomplete without additional calcium sources. Moreover, the high temperatures within micro-arc channels may lead to carbonate decomposition, resulting in limited incorporation efficiency.

The second approach is based on introducing both dissolved phosphate salts and suspended HA particles into the PEO electrolyte, which also contains CC particles. This two-phase suspension method offers a higher probability of achieving a coating with the desired CC/HA phase composition. Phosphate ions from the soluble electrolyte can penetrate the porous oxide layer more uniformly than solid particles, enabling widespread phosphorus incorporation and facilitating HA formation. Simultaneously, HA particles can be physically embedded within the coating, complementing *in situ* precipitation. However, this method introduces technical

challenges, including the need to synthesize HA particles of suitable size to match those of CC and to prevent heterocoagulation between the two types of particles [179]. Successful incorporation depends heavily on the physicochemical properties of the suspension, particle size distribution, and the electrophoretic mobility of each component under the applied electric field [110], [180], [181].

The third possible configuration involves using non-phosphorus-based electrolytes supplemented with HA alongside CC particles. While this theoretically simplifies the electrolyte chemistry, its practical feasibility is limited. Common non-phosphoric electrolytes such as silicates, fluorides, and alkali hydroxides may irreversibly react with CC, leading to co-precipitation of undesired phases like calcium silicate or calcium fluoride [182], [183]. Additionally, alkali hydroxides readily absorb carbon dioxide from the surrounding air, causing fluctuations in bath conductivity and instability during oxidation [184]. Organic bases are unsuitable due to their low decomposition temperatures, which risk introducing contaminants into the coating [113]. These factors make non-phosphorus electrolytes incompatible with carbonate-containing suspensions for bioactive PEO coatings.

Among phosphorus-based electrolytes, mono-, di-, and tribasic phosphates of alkali metals are commonly used [185] [31] [186]. Expanded options include tetrasodium pyrophosphate, sodium hexametaphosphate, calcium hypophosphite, and sodium tripolyphosphate [187] [188] [189] [190]. However, not all are appropriate for carbonate retention. For instance, sodium dihydrogen phosphate creates a mildly acidic environment that readily dissolves carbonates, while hexametaphosphate, having nearly neutral pH, offers insufficient carbonate stability. Calcium hypophosphite decomposes above 300 °C, releasing phosphine gas, which presents safety hazards [191]. Sodium phosphate, although widely used, is strongly alkaline ( $\text{pH} \approx 12$ ) and requires extensive post-treatment to remove residual alkali from the microporous structure—an operation that risks damaging coatings and dissolving incorporated carbonates. Similarly, pyrophosphate and tripolyphosphate electrolytes ( $\text{pH} \approx 10$ ) also necessitate post-treatment [19]. Of all these candidates, disodium hydrogen phosphate ( $\text{Na}_2\text{HPO}_4$ ) presents the most favorable characteristics: its mildly basic pH ( $\sim 9$ ) provides stability for both CC and HA, and its phosphate ions act as precursors for *in situ* HA formation. Thus,  $\text{Na}_2\text{HPO}_4$  emerges as the optimal choice for an electrolyte that balances conductivity, phase stability, and bioactive ion delivery.

To complement the electrolyte, obtaining a suspension that reliably contains both CC and HA phases is crucial. Three approaches can be envisioned. The first involves separate synthesis of CC and HA particles followed by their co-suspension. While straightforward, this method requires two distinct synthesis processes and careful post-filtration to achieve compatible particle sizes, which increases preparation time and complexity. The second approach is co-precipitation synthesis, wherein both phases form simultaneously in a controlled reaction medium [192]. Although this route is more efficient and can ensure better particle homogeneity, achieving precise control over the final CC/HA ratio can be challenging due to competing nucleation and growth kinetics of the two phases. A third set of strategies includes post-synthesis particle modification methods such as etching, grafting, or immersion into a reactive environment. Etching typically involves partially dissolving CC particles in an acidic or chelating medium followed by re-precipitation of HA on the exposed surfaces, whereas grafting refers to depositing a secondary phase—such as HA—onto pre-formed CC particles via surface functionalization or chemical bonding. Both approaches can theoretically yield core-shell CC/HA structures with well-defined interfaces; however, they require multiple processing steps, specialized reagents, and careful control of reaction conditions to avoid full carbonate dissolution. Moreover, these techniques often exhibit limited scalability and reproducibility, making them less suitable for preparing large volumes of uniform suspension for PEO baths [193] [194].

Immersion into a reactive environment can be considered the most practical and controllable method for producing CC-HA composite particles, both within this third set of

strategies and the broader approach involving non-phosphorus-based electrolytes supplemented with HA particles alongside CC. It relies on the dissolution–precipitation mechanism, where pre-synthesized CC particles are partially converted into HA through reaction with a phosphate solution, particularly  $\text{Na}_2\text{HPO}_4$ . This transformation is thermodynamically driven by the lower solubility of HA and its altered surface charge compared to CC, leading to the spontaneous formation of biphasic particles in which CC cores are coated with or intergrown with HA domains. Experimental findings demonstrate that the extent of transformation and the CC/HA ratio can be finely tuned by adjusting phosphate concentration, pH, temperature, and reaction time. This approach is operationally simpler than co-suspension or other post-modification techniques, avoids the need for multiple synthesis routes or complex particle handling, and produces stable, homogeneously distributed CC-HA composites ideally suited for suspension-based PEO applications [195], [196], [197]. The principles of CC and phosphate interactions are described more in detail in Section 1.4.3.

In addition to the main functional components of PEO electrolytes, various supplementary additives have been explored to improve bath properties and modify plasma behavior during coating growth. Organic solvents (e.g., alcohols, ketones, glycerol) and surfactants are sometimes introduced to alter electrolyte viscosity, suppress gas bubble formation, or enhance particle dispersion in suspension-based baths. Ammonia and other volatile bases have been tested to control pH and ionic conductivity dynamically. Certain additives also act as plasma modifiers, stabilizing discharge activity and promoting more uniform coating growth. However, despite these potential benefits, their use in biomedical applications is limited due to several drawbacks. Many organic compounds and surfactants are not biocompatible, can thermally decompose in plasma to produce undesirable byproducts, or contaminate the resulting oxide layer. Strong bases, while improving conductivity, may react with carbonate species or destabilize suspensions, leading to inhomogeneous coatings. Moreover, additives that significantly alter the chemical environment of the bath may complicate reproducibility and scale-up. For these reasons, development of bioactive CC-HA-containing coatings via PEO typically prioritizes simpler, water-based electrolytes with minimal auxiliary compounds, focusing instead on optimizing bath composition and particle design to achieve stable, clean, and reproducible incorporation of functional phases [180], [198], [199].

### 1.4.3. Phenomena in CC-phosphate systems

The interaction between CC particles and phosphate electrolytes within PEO baths is governed by interconnected dissolution, precipitation, chemisorption, and phase transformation processes. The central factor driving these reactions is the marked solubility difference between CC and HA, with HA being roughly ten times less soluble [200], [201]. When CC particles are introduced into a phosphate-rich electrolyte, partial dissolution occurs, releasing  $\text{Ca}^{2+}$  and  $\text{CO}_3^{2-}$  ions. In the presence of hydrogen phosphate ions ( $\text{HPO}_4^{2-}$ ), these ions undergo thermodynamically favorable precipitation, forming HA. As a result, CC gradually transforms into HA while generating additional carbonate ions in solution. This dissolution–precipitation mechanism is considered the primary pathway for CC-to-HA conversion [202], [203].

The process is highly sensitive to pH and electrolyte composition. In mildly basic conditions ( $\sim\text{pH } 9$ ), typical of disodium hydrogen phosphate ( $\text{Na}_2\text{HPO}_4$ ) baths, HA nucleation is promoted [204]. Local consumption of hydroxide ions can transiently reduce pH near reacting surfaces. Interestingly, studies report slight alkalization of the electrolyte due to proton capture by dissolved carbonate species, forming bicarbonate ions. During early stages, HA predominates; however, as carbonate concentration increases, B-type carbonate-substituted hydroxyapatite ( $\text{CO}_3\text{-HA}$ ) can form. Solid-state transformation of preformed HA to  $\text{CO}_3\text{-HA}$  is also possible. The solubility of  $\text{CO}_3\text{-HA}$  lies between stoichiometric HA and CC, allowing progressive carbonate substitution within the apatite lattice [68], [202], [205].



Beyond dissolution–precipitation, irreversible chemisorption of phosphate ions on CC particle surfaces is another critical mechanism. Adsorption of calcium–phosphate ion pairs or direct phosphate–carbonate ion exchange leads to the formation of a thin HA layer on carbonate particles. This chemisorption, energetically favorable ( $\Delta G \approx -40$  kJ/mol), modifies particle surface charge and electrokinetic properties, yielding biphasic particles without separate HA crystal formation. Chemisorption is most efficient in mildly alkaline electrolytes (pH 8–9.5), making  $\text{Na}_2\text{HPO}_4$  particularly suitable for stabilizing carbonate while promoting HA nucleation [206], [207], [208] [209].

Reaction kinetics and phase composition depend on particle size, phosphate concentration, CC-to-phosphate ratio, temperature, stirring, and carbonate polymorph. Low phosphate concentrations or near-neutral pH result in slow reactions, requiring up to two weeks for noticeable transformation without agitation. Stirring or the addition of amino acids significantly accelerates kinetics. Varying the phosphate-to-carbonate ratio tunes the final composition: partial conversion produces CC/HA mixtures, while phosphate excess favors complete transformation to HA. Morphological analyses show two main transformation pathways: topotactic reactions, where precursor carbonate shape is largely retained, and agglomeration-driven pathways forming petal-like or irregular HA clusters under high phosphate conditions. The crystallinity of HA is controlled by reaction environment. At room temperature and moderate alkalinity, low-crystallinity HA forms, indicated by weak diffraction peaks around  $31^\circ$  (2 $\theta$ ). Hydrothermal treatment (120–180 °C) markedly enhances crystallinity. Surface observations of partially transformed particles reveal smoothed edges, increased roughness, and localized HA inclusions, confirming that chemisorption and dissolution–precipitation act simultaneously [196], [197], [204], [206], [210], [211].

Overall, phosphate electrolytes—particularly  $\text{Na}_2\text{HPO}_4$ —offer an effective medium for converting carbonate into HA or generating biphasic CC/HA suspensions. These composite particles typically feature uniform phase distribution and surface properties favorable for electrophoretic migration and entrapment during PEO coating growth. Designing an optimal bath therefore requires balancing carbonate stability with controlled HA formation kinetics, emphasizing precise tuning of pH, ion ratios, and reaction conditions during CC synthesis and suspension preparation. This understanding underpins strategies for achieving reproducible bioactive PEO coatings enriched with both carbonate and HA phases.

#### **1.4.4. Factors affecting the choice of CC synthesis method**

Selecting a suitable synthesis method for incorporating CC into PEO coatings requires consideration of particle size, morphology, and suspension behavior. PEO-generated oxide layers are characterized by nano-, submicron-, and micron-sized pores formed through plasma-driven melting, resolidification, and oxygen evolution. The most frequent pore diameter is typically 1–2  $\mu\text{m}$ , similar to the average surface roughness of PEO coatings. CC particles within this size range are expected to optimally adhere to or infiltrate the porous oxide structure, becoming trapped by plasma discharges during coating growth [186], [189], [212].

A strictly narrow size distribution is not essential due to surface heterogeneity; however, particles significantly larger than 2–3  $\mu\text{m}$  show poor interaction with the oxide surface and are less likely to incorporate. For instance, micrometer-sized  $\text{Al}_2\text{O}_3$  particles (>30  $\mu\text{m}$ ) were shown to remain largely suspended during PEO processing [213], whereas smaller 1–4  $\mu\text{m}$  particles successfully embedded into the coating [214]. Conversely, nanoparticles, with high surface area and mobility, are rapidly incorporated but may decompose under plasma heating [215]. To preserve CC integrity, the proportion of particles below 0.5–1  $\mu\text{m}$  should therefore be limited.

Particle shape and polymorphic form also critically influence behavior in PEO. CC exists in three anhydrous polymorphs: calcite (thermodynamically stable, rhombohedral/cubic), vaterite (metastable, spherical), and aragonite (metastable, needle-like). Hydrated forms and amorphous CC are metastable and highly soluble, rendering them unsuitable for PEO. Among the crystalline forms, calcite is preferred due to its thermal stability and resistance to

decomposition. Vaterite and aragonite gradually transform into calcite in aqueous solutions, destabilizing suspensions and altering particle size over time. Furthermore, elongated aragonite particles may lead to poor collision efficiency and mechanical incompatibility with tissues if exposed on implant surfaces. Non-equiaxed morphologies, including branched, toroidal, hollow, or porous particles, can enhance electrokinetic interactions with the oxide surface owing to their increased surface area and charge. Such anisotropic shapes can be synthesized using biomolecules or by inducing microgradients during crystallization [216] [217] [218] [219], [220].

CC synthesis methods are diverse, encompassing wet precipitation, biomimetic and biomineralization routes, carbonation, microemulsions, polymerization, solid-state reactions, electrochemical methods, and spray drying. Wet precipitation remains the most widely applied due to simplicity, requiring only aqueous mixing of calcium and carbonate sources. Across synthesis strategies, product characteristics can be tuned by adjusting reagent type and concentration, feed ratios, reaction medium, additives, agitation intensity, temperature, and pH. Established trends include: particle size increasing with reaction time and temperature; high supersaturation and organic additives favoring metastable vaterite and aragonite; and dilute solutions promoting stable calcite formation [59], [216], [221], [222].

Despite extensive research on CC synthesis, PEO studies rarely focus on tailoring particles specifically for electrolyte suspensions. Many reports lack detailed descriptions of particle origin, synthesis protocols, or characterization, often relying on commercial powders [223], [224], [225], [226]. Suspension preparation is usually limited to simple stirring, ultrasonic dispersion, bubbling, or surfactant addition [223], [224], [226]. This scarcity of systematic data hampers rational selection of synthesis methods for PEO applications. A critical evaluation of CC synthesis approaches, particularly regarding particle size control, polymorphic stability, and ease of implementation, is therefore essential for optimizing CC-HA coating fabrication.

#### **1.4.5. Potential challenges in fabrication of CC-HA coatings**

Following Section 1.4.2, the most viable strategy for preparing a working PEO bath consists of simultaneously using CC and HA particles. This section outlines anticipated challenges and provides practical guidelines for implementing PEO coatings in such a bath, while also addressing general issues commonly encountered during PEO in particle suspensions. From a particle engineering standpoint, the efficiency of their incorporation into PEO coatings is strongly influenced by particle size, where the optimal value can be attributed to the characteristic pore dimensions in the forming oxide layer, typically around 1–2  $\mu\text{m}$  [186], [189], [212]. Achieving an optimal particle size distribution is therefore essential. In cases where a synthesis method inherently produces particles outside the desired size range, post-synthesis treatments can be employed to tailor particle characteristics. Size reduction can be performed via high-energy ball milling or prolonged ultrasonic dispersion to break down agglomerates. Additionally, surface modification strategies, such as coating particle surfaces with thin layers of biocompatible agents (e.g., phosphates or silanes), can prevent re-agglomeration and enhance wetting behavior in aqueous electrolytes [227], [228], [229].

Equally important for effective particle incorporation during PEO is the preparation and maintenance of a stable particle suspension. It is similarly crucial to account for dilution effects and maintain vigorous stirring to prevent particle sedimentation. The order of component addition may play a critical role in avoiding agglomeration caused by weakened electrostatic repulsion; therefore, the lower-conductivity solution (phosphate electrolyte) should be introduced into the CC suspension [230]. When utilizing various CC synthesis methods, particle purification steps—such as filtration, drying, and resuspension—may be necessary, which can promote agglomeration and increase the hydrodynamic particle size. In this case, mechanical dispersion techniques, particularly ultrasonic treatment, are also useful for breaking down these agglomerates, though they can be time-consuming [231]. Continuous mixing is similarly crucial

to maintain homogeneity and ensure reproducible particle dosing during PEO coating formation [224]. In general, suspension stability is governed by factors such as zeta potential and electrophoretic mobility, which determine the extent of electrostatic repulsion between particles and their transport efficiency toward the anode [180], [181], [226], [232], [233]. Long-term stability can be enhanced through careful pH adjustment or, less preferably and only in exceptional cases, the addition of benign dispersants [234], [235].

The next challenge concerns the interaction between phosphate ions and CC particles, which can modify particle size, shape, crystallinity, and the bath's physicochemical properties. As discussed before (Section 1.4.3), two main mechanisms are possible: (i) CC dissolution followed by HA precipitation and (ii) chemisorption of phosphates onto CC surfaces. Excessive dissolution could result in a coating dominated by HA with insufficient CC content, while complete chemisorption would form a uniform HA shell, potentially shielding CC particles from releasing  $\text{Ca}^{2+}$  ions, their primary bioactive function. Factors such as particle concentration, CC-to-phosphate ratio, and the specific surface area of CC (dictated by size, porosity, and surface structuring) strongly influence these processes. A balanced carbonate-to-phosphate ratio of approximately 1:1 is recommended as a starting point to achieve the desired composite structure in the coating.

Bath conductivity must be controlled to achieve optimal sparking behavior during PEO. If conductivity is too low, sparking may not initiate, while excessively high conductivity can lead to intense discharges, resulting in overly thick and cracked coatings. Because CC-phosphate reactions may cause gradual conductivity changes, additional adjustments to the electrolyte composition may be needed. Released carbonate ions are not expected to significantly hinder coating formation and may even enhance particle incorporation by modifying discharge characteristics and improving particle migration toward the anode [236], [166], [174].

Process electrical parameters—such as voltage, current density, pulse duty cycle, and frequency—directly determine plasma temperature and spark behavior. Since CC decomposes under high heat, it is crucial to promote partial thermal reactivity: plasma must enable bonding between CC/HA particles and titanium dioxide without complete decomposition. Pulsed current operation is preferable to DC, as it generates milder sparking and reduces thermal damage, leading to thicker, more uniform coatings with fewer cracks. Optimization of pulse characteristics should aim for the lowest frequency that still achieves the desired coating properties while maintaining practical power supply requirements [237], [238], [155]. Bath temperature reduction can further increase coating thickness and growth rate but must be balanced against rising conductivity and reduced solubility of electrolyte components, which may cause unwanted precipitation [239], [112], [240], [241].

## **1.5. Calcium carbonate synthesis methods**

### **1.5.1. Wet precipitation**

The wet precipitation method is the most established and commonly used approach for synthesizing particles suitable for PEO applications. It involves preparing separate aqueous solutions containing calcium (e.g.,  $\text{CaCl}_2$ ) and carbonate ions (e.g.,  $\text{Na}_2\text{CO}_3$ ), followed by mixing to induce precipitation of CC. The resulting particles are then filtered, washed, and dried. Variations include instantaneous or gradual mixing of solutions, as well as simultaneous addition to a reaction vessel. Mechanical stirring is typically used to facilitate mixing [242], [59], [243], [244].

The standard process often yields particles larger than 2  $\mu\text{m}$  due to rapid aggregation and agglomeration. This is attributed to high ionic strength in the reaction medium, which reduces the Debye length of electrostatic double layers around forming particles, weakening their repulsive forces and leading to fusion into larger structures. Increasing reagent

concentrations exacerbates this effect, producing particles up to 10  $\mu\text{m}$  in size. Conversely, diluting the reactants significantly can reduce particle size to submicron levels, though at the cost of lower productivity and increased resource use during filtration. Particle size distribution heterogeneity is another limitation. During mixing, conductivity gradients lead to varying particle sizes; larger crystals form early, while smaller ones appear later as local supersaturation and ionic strength evolve during mixing. Such size disparity increases collision probability and further agglomeration. Strategies to mitigate this include using excess reagent, adding a supporting electrolyte to adjust ionic strength (and, where appropriate, a common-ion to moderate supersaturation), or simultaneously adding solutions to narrow size distribution [59], [245], [246].

Additives can be introduced to influence nucleation and growth kinetics. Organic and inorganic salts, surfactants, polymers, alcohols, and amino acids can modify medium properties, adsorb on particle surfaces, and guide polymorphic form and shape. Some additives enable particle size reduction to  $\sim 400\text{--}500$  nm. Physical agitation methods, such as ultrasound and microwave irradiation, further decrease particle size by disrupting crystal organization and promoting rapid cooling during cavitation events. Ultrasound can produce particles as small as 0.5  $\mu\text{m}$ , and, when combined with dispersants and advanced drying methods (centrifugation, lyophilization), nanoparticles of 50–200 nm can be obtained [59], [216], [221], [222].

Despite these advancements, wet precipitation remains challenging for producing uniformly submicron CC particles at scale. Agglomeration during filtration and drying remains an issue, often requiring post-processing steps like ultrasonic dispersion before suspension in PEO baths. Nonetheless, its simplicity, accessibility, and flexibility make wet precipitation the predominant method for synthesizing CC particles intended for bioactive PEO coatings.

### 1.5.2. Carbonation

The carbonation approach is one of the most widely applied methods for synthesizing CC particles for PEO baths. Unlike wet precipitation, carbonation involves a solid–liquid–gas reaction system where calcium hydroxide ( $\text{Ca}(\text{OH})_2$ ) reacts with carbon dioxide ( $\text{CO}_2$ ) dissolved in water. The process begins with the dissociation of  $\text{Ca}(\text{OH})_2$  into calcium and hydroxide ions. Concurrently,  $\text{CO}_2$  dissolves and hydrolyzes to bicarbonate ( $\text{HCO}_3^-$ ) and carbonate ( $\text{CO}_3^{2-}$ ) ions, which then react with calcium ions to precipitate CC. This reaction can be considered a neutralization process that consumes hydroxide and produces water as a by-product [247].

Classical carbonation uses simple, non-toxic reagents and requires relatively straightforward equipment—mechanical stirring, a gas supply, and basic temperature control—making it an environmentally friendly synthesis route. It offers a wide range of tunable particle sizes, from a few hundred nanometers to tens of micrometers, by adjusting parameters such as  $\text{CO}_2$  concentration, flow rate,  $\text{Ca}(\text{OH})_2$  content, temperature, and stirring speed. Reactor design also plays a role; systems like bubble columns, packed beds, and microchannel reactors enhance gas–liquid contact and mass transfer, increasing nucleation rates and allowing finer control of particle size and morphology [247], [248].

The process proceeds through a short-lived amorphous CC phase that subsequently crystallizes, predominantly into calcite under standard conditions. Particle morphology can be further tuned by modifying supersaturation levels: high supersaturation favors rapid nucleation and smaller particles, while low supersaturation promotes crystal growth, yielding larger particles. However, excessive  $\text{CO}_2$  or prolonged reaction can acidify the medium and dissolve already-formed carbonate. Careful pH monitoring and timely reaction termination are thus critical for maintaining product integrity. Additives such as surfactants and ammonia are sometimes employed to stabilize pH, prevent bubble coalescence, and achieve nanoscale particles, though standard carbonation typically produces uniform submicron powders without requiring such modifications [222], [249], [250], [251], [252]. Importantly, carbonation generates no ionic or solid by-products, leaving only CC and dissolved  $\text{CO}_2$  in the reaction

medium, which eliminates the need for downstream purification. Because of its scalability, environmental benefits, and ability to yield phase-pure, size-controlled CC particles, carbonation is considered an effective and practical method for preparing precursors used in bioactive PEO coatings.

### **1.5.3. Biomimetic and biomineralization synthesis**

Biomimetic precipitation and biomineralization are two related approaches inspired by natural processes of CC formation. Biomimetic precipitation involves introducing biologically derived or bioinspired additives—such as amino acids, polysaccharides, peptides, proteins, or extracellular polymeric substances (EPS)—into a conventional precipitation or carbonation reaction. These additives influence nucleation and crystal growth by selectively adsorbing on specific crystal planes or altering local supersaturation. This can produce morphologies and polymorph distributions that mimic those found in biological systems. Particle sizes as low as 0.5  $\mu\text{m}$  have been reported under optimized conditions; however, the process often suffers from co-precipitation of organic residues, slow reaction kinetics compared to abiotic precipitation, and poor scalability. Large biomolecules such as DNA or albumin typically promote anisotropic growth, leading to irregularly shaped particles that may not meet size and uniformity requirements for stable PEO suspensions [253], [254], [255].

Biomineralization, in contrast, uses living microorganisms to mediate mineral formation through their metabolic activity. Three mechanisms are recognized: biologically controlled mineralization (e.g., shell or bone formation by specialized cells), biologically influenced mineralization (where CC nucleates on cell-associated EPS layers), and biologically induced mineralization (precipitation in the extracellular medium influenced by microbial metabolites). Bacteria can locally increase pH and carbonate concentration, providing nucleation sites for CC. Initial nuclei on bacterial surfaces are typically around 100 nm; however, crystals rapidly grow in multiple directions, resulting in particles exceeding 2  $\mu\text{m}$ , often reaching tens of micrometers when bacterial aggregation occurs. This size range is incompatible with the microstructural requirements of PEO coatings, which favor particles below  $\sim 2 \mu\text{m}$  for effective incorporation [256], [257].

Biomineralization further introduces challenges in terms of product purity and reproducibility. Embedded biomolecules and bacterial remnants may decompose during the high-temperature PEO process, contaminating the coating. The method also lacks predictable control over CC polymorphs (calcite, aragonite, vaterite) and exhibits slow kinetics, with nucleation and growth occurring over hours to days. Producing PEO-compatible particles would require stringent control of bacterial surface charge, metabolic activity, and enzyme kinetics (e.g., urease), as well as additional steps to separate and sterilize the final product [258].

Despite these limitations, both biomimetic and biomineralization routes highlight pathways by which biological molecules and microorganisms can influence mineral morphology. Currently, neither approach provides a straightforward or scalable solution for synthesizing CC or HA particles suitable for PEO coatings. Biomimetic precipitation may offer limited particle size reduction and shape tuning, whereas biomineralization remains hindered by large particle dimensions, variability, and purification challenges. Further research would be needed to adapt these bioinspired methods for producing finely controlled, clean, and thermally stable particles compatible with PEO processes.

### **1.5.4. Microemulsion synthesis**

Microemulsion synthesis represents an advanced and versatile method for generating CC and HA particles tailored for PEO processes. This approach involves the formation of thermodynamically stable microemulsions—typically water-in-oil systems—stabilized by surfactant molecules that spontaneously self-assemble into micelles at a critical concentration. These micelles, with diameters ranging from 5 to 100 nm, act as confined “nano-reactors,” enabling controlled nucleation and growth of inorganic particles without significant

agglomeration. Under specific conditions, primary micelles can coalesce into larger swollen reverse micelles / bicontinuous microemulsions enabling larger (still stable) droplet sizes, providing scalability in particle size synthesis [259].

In practice, two separate microemulsion solutions are prepared: one containing a calcium salt and the other a carbonate precursor. Upon mixing, ion exchange occurs within micellar cores through intermicellar collisions and a fusion–fission mechanism. The dynamic surfactant layer temporarily desorbs, allowing the contents of neighboring micelles to merge and react before re-encapsulation. This mechanism produces solid particles trapped within micellar cores, while excess counterions remain in solution. The final product is isolated through centrifugation, solvent washing, or self-evaporation of the oil phase, ensuring removal of surfactant residues that could otherwise compromise biocompatibility [259], [260].

One of the strengths of microemulsion synthesis is its tunability. Particle sizes can be adjusted from a few tens of nanometers to several micrometers by modifying surfactant type and concentration, the ratio of oil to water, and the presence of co-surfactants or co-solvents. For instance, increasing surfactant concentration or employing shorter hydrophobic tails reduces micelle diameter, yielding finer particles, while introducing co-solvents can enlarge the micellar core, favoring submicron or micron-sized particles. Published studies have reported CC nanoparticles of <100 nm, submicron particles around 0.5  $\mu\text{m}$ , and larger structures exceeding 10  $\mu\text{m}$ , demonstrating the method's broad range of control. Additionally, advanced microemulsion designs—such as bicontinuous emulsions or those generating  $\text{CO}_2$  *bubbles in situ*—allow further tailoring of particle morphology, porosity, and polymorphic composition [261].

From a PEO perspective, microemulsion-synthesized particles offer several advantages. The technique enables the preparation of nearly monodisperse, spherical or ellipsoidal particles with controlled surface characteristics, facilitating stable suspension in PEO electrolytes. Furthermore, due to the confinement effect of micelles, heterogeneous nucleation is minimized, resulting in high-purity phases without co-precipitated organic residues. These features are particularly relevant when producing bioactive CC or HA additives aimed at improving coating biofunctionality, corrosion resistance, and drug delivery capabilities.

However, challenges remain in translating microemulsion-synthesized particles to practical PEO applications. Post-synthesis purification is resource-intensive, often requiring multiple centrifugation and washing steps to remove surfactants and residual oil phases. Additionally, particle aggregation can occur during drying, necessitating ultrasonic dispersion before suspension preparation. Despite these limitations, microemulsion synthesis stands out as a flexible and scalable method for engineering particle size and morphology to meet the stringent requirements of bioactive PEO coatings [259].

### 1.5.5. Other synthesis methods

Several alternative methods for synthesizing CC exist beyond conventional wet precipitation, though they remain rarely used in laboratories or industry due to specialized equipment needs, scalability issues, and difficulties in controlling product properties. These techniques—solid-state synthesis, electrochemical synthesis, spray drying, and polymerization-based synthesis—may still offer potential for producing particles suitable for suspension-assisted PEO coatings.

Solid-state synthesis relies on thermal decomposition of organic calcium salts (e.g., oleate, stearate), where self-released  $\text{CO}_2$  forms CC. Heating powdered salts above 400  $^{\circ}\text{C}$  produces highly crystalline calcite ( $\sim 100$  nm), with particle growth promoted by higher temperatures and precursor melting. Above 750  $^{\circ}\text{C}$ , CC converts to CaO. Variations include aerosol pyrolysis, where CA solution is nebulized, dried, and pyrolyzed at  $\sim 500$   $^{\circ}\text{C}$ , yielding spherical particles averaging 2  $\mu\text{m}$  (500 nm–several  $\mu\text{m}$ ). Finer sprays reduce size. Flame spraying of calcium 2-ethylhexanoate, using methane–oxygen combustion, generates particles as small as 20 nm with adjustable crystallinity and shape [262], [263], [264].

Electrochemical synthesis uses a three-compartment cell containing  $\text{CaCl}_2$  and  $\text{NaHCO}_3$  solutions. Hydroxide ions rapidly convert bicarbonates to carbonates near the cathode, leading to nucleation and growth of CC. Typically, this process forms whiskers or flake-like aragonite crystals  $>10\text{ }\mu\text{m}$ . Adjusting reagent concentration, voltage, and duration can promote calcite precipitation and achieve particle sizes down to  $1\text{ }\mu\text{m}$ , though these usually appear as by-products. Pre-electrolysis at higher voltages increases nucleation density and decreases size. The method is simple but detaching particles from electrodes without altering their properties remains challenging [265], [266].

Spray drying transforms CC suspensions into powders by atomizing droplets and drying them in a heated gas stream ( $100\text{--}200\text{ }^\circ\text{C}$ ). Often used as a post-treatment after precipitation or milling, fully automated systems integrating reagent mixing and drying can serve as standalone synthesis routes similar to aerosol pyrolysis. Agglomeration during droplet drying can increase particle size from  $1\text{ }\mu\text{m}$  to  $>50\text{ }\mu\text{m}$ . Using diluted suspensions and fluidized bed reactors with inert particles (glass beads, sand) minimizes agglomeration and maintains particle sizes around  $1\text{--}2\text{ }\mu\text{m}$ . Spray-dried HA powders have been used in PEO coatings, suggesting suitability for CC [267], [268], [269].

Polymerization-based synthesis, reported only once, uses triethylamine (TEA) in ethanol to stabilize  $(\text{CaCO}_3)_n$  oligomers through hydrogen bonding. Bubbling  $\text{CO}_2$  into a  $\text{CaCl}_2$ –TEA solution produces oligomers ( $n = 3\text{--}11$ ), which aggregate into amorphous CC upon solvent evaporation and convert to calcite when heated to  $320\text{ }^\circ\text{C}$ . This method forms CC monoliths rather than discrete micro/nanoparticles, though polymerization inhibitors or aqueous dilution could enable size control [270].

#### 1.5.6. Comparison of synthesis methods

The comparative analysis of CC synthesis techniques (summarized in Table 1) highlights substantial differences in precursor states, method configurations, achievable particle sizes, and suitability for integration into PEO baths. While a variety of synthetic routes have been reported—including wet precipitation, carbonation, biomimetic mineralization, microemulsion processing, polymerization, electrochemical synthesis, and several solid-state approaches—only a subset aligns with the strict particle size and purity requirements of the target PEO process.

Electrochemical methods and biomineralization frequently yield particles exceeding  $2\text{ }\mu\text{m}$ , rendering them unsuitable for this application. Electrochemical synthesis further suffers from the tendency to generate metastable aragonite, while polymerization lacks robust experimental foundations for producing well-defined CC powders. Excluding these approaches, the remaining methods can be assessed based on synthesis simplicity, controllability of particle size, and achievable product purity. Among liquid-phase techniques, wet precipitation, carbonation, biomimetic synthesis, and microemulsion methods offer considerable flexibility because reaction variables—concentration, molar ratio, mixing dynamics, temperature, and pH—can be tuned to influence nucleation and growth. Spray drying, spray pyrolysis, and flame spraying can similarly control droplet size in aerosolized systems, whereas molten salt decomposition offers fewer adjustable parameters and limited literature for guidance. Moreover, submicron particles produced by this latter approach are smaller than optimal for the PEO process.

A common challenge across these methods lies in post-processing. When CC particles are generated as suspensions, their recovery typically involves filtration, washing, and thermal drying—steps that promote particle agglomeration through solvent-induced recrystallization. Techniques such as lyophilization mitigate this effect but cannot fully prevent aggregation. Centrifugation, dialysis, and microemulsion purification introduce further mechanical stresses or contamination risks. Solid-state and spray-drying techniques, while producing dry powders, still require additional purification to remove residual salts and prevent electrostatic

agglomeration during storage. Ultimately, all these methods demand prolonged ultrasonic dispersion to restore particle size before PEO application.

**Table 1.** Summary of CC synthesis methods

Method	Calcium and/or carbonate source	Configuration	Specified examples	Characteristic particle sizes ( $\mu\text{m}$ )	Reference
Wet precipitation	$\text{Ca}^{2+}$ (aq) $\text{CO}_3^{2-}$ (aq)	standard	-	$2 \leq$	[243]
		additive engineering	surfactants, alcohols	$0.5 \leq$	[271]
		physical agitation	ultrasound, microwaves		[272]
Biomimetic		with simple biomolecules	amino acids, polysaccharides	$1 \leq$	[273]
		with macromolecules	peptides, proteins		[274]
		standard	-	$0.1\text{-}10$	[275]
Carbonation	$\text{Ca}(\text{OH})_2$ (s)	additive engineering	surfactants, alcohols, salts		[250]
	$\text{CO}_2$ (g)	physical agitation	ultrasound, microwaves	$\sim 0.05\text{-}10$	[276]
	$\text{Ca}^{2+}$ (aq)	non-gaseous $\text{CO}_2$ addition	dry ice, supercritical $\text{CO}_2$		[277]
	$\text{CO}_3^{2-}$ (aq)	use of advanced reactors	packed-bed, bubble column		[278]
		denitrifying bacteria			[279]
Biom mineralization	$\text{Ca}^{2+}$ (aq)	biologically influenced	sulfate-reducing bacteria	$2 \leq$	[280]
	other (optional)		anaerobic bacteria		[281]
		biologically induced	<i>Synechococcus</i> at pH~9		[282]
Microemulsion	$\text{Ca}^{2+}$ (aq)	Winsor II/IV type	surfactants, polar phase,	$0.01\text{-}10$	[283]
	$\text{CO}_3^{2-}$ (aq)	Winsor III type	non-polar (oil) phase		[284]
Polymerization	$\text{Ca}^{2+}$ (aq)	ionic oligomer crosslinking based on H-bonding	triethylamine (binder)	n/a*	[270]
	$\text{CO}_3^{2-}$ (aq)				
Solid state	Carboxylate salts of calcium	molten salt decomposition	Ca oleate, Ca stearate	0.1	[262]
		spray pyrolysis	CA acetate aerosol	0.5	[263]
		flame spray	salt aerosol in $\text{O}_2/\text{CH}_4$ flame	0.02	[264]
Electrochemical	$\text{Ca}^{2+}$ (aq)	cathodic reduction	from solution containing	$>10$	[265]
	$\text{CO}_3^{2-}$ (aq)		$\text{CaCl}_2$ and $\text{NaHCO}_3$		
Spray drying	Suspended	standard	-	$n/a^{**}$	[267]
	CC particles	fluidized bed reactor	fluidized bed of glass spheres		[269]

\* method is designed to produce CC monoliths

\*\* depends on conditions of nucleation and crystal growth

Carbonation stands out as a distinct approach due to its reaction pathway involving calcium hydroxide and carbon dioxide. It inherently avoids by-product formation and, at stoichiometric equilibrium, produces suspensions containing negligible concentrations of dissolved ions, resulting in near-zero conductivity [250]. Importantly, this method generates CC directly as a stable aqueous suspension, eliminating the need for filtration, drying, and resuspension steps that otherwise enlarge particle size. Reaction parameters—including  $\text{CO}_2$  flow rate, gas distribution, and reagent concentration—enable synthesis across a broad size range, meeting PEO requirements without introducing non-biocompatible additives. Given its simplicity, purity, tunability, and ability to bypass agglomeration-prone post-processing, carbonation is identified as the most suitable synthesis route for producing CC particles intended for incorporation into composite CC/HA layers via PEO.

## 1.6. PEO-associated characterization methods

### 1.6.1. Structure of coatings

The structural characteristics of PEO coatings, including thickness, internal architecture, surface morphology, surface roughness, and porosity, are critical parameters that determine their mechanical integrity, corrosion protection, biological performance, and other functional characteristics [90], [150]. A variety of analytical and imaging techniques are employed to evaluate these features, providing complementary information about coating growth and microstructural organization.

The thickness of PEO coatings is a fundamental property influencing protective performance and mechanical behavior. Cross-sectional SEM is commonly used for direct thickness measurements: the coating is embedded, polished, and imaged, with secondary electrons emitted under electron beam irradiation revealing the coating–substrate interface. SEM typically provides a spatial resolution of 1–10 nm, allowing precise visualization of layer



boundaries. Cross-sections are typically prepared by mounting the coated sample in epoxy resin, followed by grinding and polishing to expose a flat cross-sectional surface suitable for high-resolution imaging. Optical microscopy, operating with visible light, offers lower magnification and resolution, typically  $\sim 0.5\text{--}1\text{ }\mu\text{m}$ , but remains suitable for thicker coatings or routine checks. Non-destructive methods include eddy current probes and magnetic induction (only for ferromagnets) gauges, which measure thickness based on the interaction of a magnetic field with the conductive substrate beneath the dielectric coating. These devices typically have a measurement resolution of  $0.1\text{--}1\text{ }\mu\text{m}$ , depending on coating thickness and instrument calibration. In addition to overall thickness, cross-sectional SEM can reveal key internal structural features such as discharge channels and inner pores, essential for understanding coating formation mechanisms and functional properties [118], [285].

The surface morphology of PEO coatings typically exhibits a porous, roughened structure formed by localized plasma discharges. SEM is the primary technique for visualizing surface topography, producing high-resolution images of pores, microcracks, and incorporated particles by detecting secondary and backscattered electrons emitted from the surface. SEM typically operates in the magnification range of  $10\times$  to  $100,000\times$ , allowing both low-magnification overviews and detailed imaging of fine surface features. Three-dimensional optical profilometry and confocal laser scanning microscopy rely on optical triangulation or confocal optics to generate topographic maps of the coating surface, making them well-suited for analyzing larger areas with vertical resolution below  $1\text{ nm}$  and lateral resolution of hundreds of nanometers. At the nanoscale, Atomic Force Microscopy (AFM) uses a sharp scanning tip to detect surface height variations with vertical resolution of  $0.1\text{--}0.2\text{ nm}$  and lateral resolution down to  $\sim 10\text{ nm}$ , enabling detailed imaging of nano-textured regions [111], [286].

Surface roughness, while related to topography, refers specifically to the quantitative measurement of surface irregularities that can influence wettability, cell adhesion, and mechanical interlocking with tissues or secondary coatings. Roughness is commonly quantified using contact or optical profilometry, which calculates parameters such as arithmetic ( $R_a$ ), root mean square ( $R_q$ ), and peak-to-valley ( $R_z$ ) roughness from measured surface profiles. A contact profilometer operates on the principle of a stylus mechanically tracing the surface while a displacement sensor records its vertical movement, converting it into a surface height profile. Contact profilometers typically offer a vertical resolution of  $\sim 10\text{--}20\text{ nm}$  and lateral resolution of  $\sim 1\text{ }\mu\text{m}$ , whereas optical profilometers achieve sub-nanometer vertical resolution and hundreds of nanometers lateral resolution, allowing rapid, non-destructive mapping of larger areas. AFM provides complementary nanoscale roughness characterization, particularly useful for differentiating micro- and nano-textured regions. Additionally, SEM-based 3D reconstruction techniques, using stereoscopic imaging or photogrammetry algorithms, enable quantitative roughness mapping with sub-micron depth resolution. These methods are often combined to correlate roughness parameters with morphological features observed in SEM or confocal laser scanning microscopy images [287], [288].

Porosity is another key structural parameter affecting the functional properties of PEO coatings, including corrosion resistance and bioactivity. It can be estimated through image analysis of SEM micrographs, where binary thresholding and pore detection algorithms quantify porosity percentage and pore size distribution. Mercury intrusion porosimetry measures the volume of mercury forced into pores under increasing pressure and is capable of detecting pores in the approximate size range of  $3\text{ nm}$  to  $100\text{ }\mu\text{m}$ , making it suitable for both micro- and mesoporous structures. Gas adsorption techniques such as Brunauer–Emmett–Teller (BET) analysis determine surface area and porosity by measuring the adsorption of inert gases at cryogenic temperatures and are particularly sensitive to pores in the range between  $2$  and  $50\text{ nm}$ . However, BET is not commonly applied to PEO coatings due to their predominantly macroporous structure. Non-destructive three-dimensional characterization can be achieved using X-ray computed microtomography (micro-CT), which reconstructs the coating's internal pore network based on X-ray attenuation differences, typically resolving pores larger than  $\sim 0.5\text{--}$

1  $\mu\text{m}$ , allowing for detailed analysis of pore connectivity and distribution. Additionally, electrochemical impedance spectroscopy (EIS) can indirectly assess coating compactness and defect density by evaluating how electrolyte penetrates the coating through frequency-dependent impedance responses [118], [288], [289].

### 1.6.2. Coating chemical composition

Accurate chemical characterization of PEO coatings is crucial for understanding their composition, structure, and functional properties. Since PEO coatings typically consist of complex structures with crystalline and amorphous oxides and possible incorporation of electrolyte-derived species like ions and particulate matter, a combination of surface-sensitive and bulk analytical techniques is employed to fully characterize their elemental and phase composition. Below is a summary of the most commonly used techniques, including their principles and detectable elements or phases.

**X-ray-Based Analytical Techniques.** Several X-ray-based techniques are widely used for the chemical and structural characterization of PEO coatings. Energy-Dispersive X-ray Spectroscopy (EDX), typically coupled with SEM, enables rapid qualitative and semi-quantitative elemental analysis. When an electron beam interacts with the coating, it generates characteristic X-rays that are detected and assigned to specific elements. EDX can map elemental distribution across the surface or cross-sections of the coating, identifying incorporated electrolyte-derived species such as calcium, phosphorus, and carbon. However, it is less sensitive to light elements and provides limited accuracy for trace components. X-ray Photoelectron Spectroscopy (XPS) is a surface-sensitive technique that measures the kinetic energy of electrons emitted from the coating when irradiated with X-rays. It provides detailed information on the chemical states of elements within the top few nanometers of the surface. For PEO coatings, XPS is particularly valuable for identifying oxidation states of titanium (e.g.,  $\text{Ti}^{4+}$  in  $\text{TiO}_2$ ) and detecting carbonate, phosphate, or hydroxyl species derived from the electrolyte. Depth profiling via ion sputtering can further reveal compositional changes within near-surface layers, though sputtering may induce artifacts. Complementary to EDX and XPS, XRD is employed to determine the crystalline phases present in the PEO layer. By measuring the diffraction of X-rays from the coating's crystal planes, XRD identifies phases such as anatase, rutile, HA, or CC. This method provides insight into crystallinity, phase transformations, and stress states induced during the PEO process. However, its sensitivity decreases for thin coatings or amorphous components, which may not produce well-defined diffraction peaks [290], [291].

**Vibrational Spectroscopy.** Vibrational spectroscopic techniques provide molecular-level information on functional groups and crystalline phases within PEO coatings. Fourier-Transform Infrared Spectroscopy (FTIR) detects absorption of infrared light due to vibrational modes of chemical bonds. It is particularly effective for identifying carbonate ( $\text{CO}_3^{2-}$ ), phosphate ( $\text{PO}_4^{3-}$ ), and hydroxyl ( $\text{OH}^-$ ) groups incorporated from the electrolyte, complementing elemental analysis methods. Raman Spectroscopy, based on inelastic scattering of monochromatic light, offers similar but complementary information to FTIR. Raman spectra can distinguish crystalline oxide phases such as anatase and rutile and detect carbonate ions in the coating matrix. Due to its high spatial resolution, Raman spectroscopy is often used for localized surface analysis and mapping of phase distribution across the coating. Combined, FTIR and Raman spectroscopy provide comprehensive identification of molecular species and structural features that cannot be resolved by X-ray techniques alone [138], [292].

**Depth Profiling Techniques.** Understanding the through-thickness chemical distribution is crucial for evaluating coating performance. Glow Discharge Optical Emission Spectroscopy (GDOES) is particularly useful for depth profiling, as it progressively sputters the coating with a low-pressure plasma while monitoring the emitted optical spectra of elements. This allows rapid, quantitative determination of elemental concentration profiles from the outer porous layer down to the substrate, including detection of light elements like carbon,

nitrogen, and oxygen. GDOES provides high depth resolution and is suitable for multilayered PEO structures. Additionally, cross-sectional analytical techniques are commonly employed to investigate the internal composition and layering of the coating. Cross-sections prepared by mechanical polishing or ion milling can be analyzed via SEM-EDX for elemental mapping or examined with other high-resolution methods such as EPMA or Raman line scans. These analyses reveal gradients in composition, the thickness of barrier layers, and interfacial chemistry between the coating and substrate [143], [293].

### 1.6.3. Evaluation of biological properties

The biological performance of PEO coatings is of primary importance for implant applications, as it determines how effectively the modified surface integrates with surrounding tissues and resists microbial colonization. *In vitro* cell culture assays are commonly used to assess cytocompatibility, where relevant cell types (e.g., osteoblasts, fibroblasts, mesenchymal stem cells) are cultured on coated samples. Parameters such as cell adhesion, proliferation, and differentiation are analyzed using optical or fluorescence microscopy, colorimetric viability assays (MTT, Alamar Blue), or biochemical markers of osteogenic activity (e.g., alkaline phosphatase activity, mineralized matrix formation). Advanced techniques such as confocal laser scanning microscopy, quantitative PCR, and flow cytometry may also be employed to study cell morphology, gene expression, and signaling pathways influenced by the coating's chemistry and surface topography. Long-term culture studies under dynamic flow conditions can further mimic the physiological environment and provide deeper insight into coating performance *in vivo* [294], [295].

Antibacterial activity is another critical factor for preventing post-implant infections. Coated surfaces are typically exposed to bacterial strains (e.g., *Staphylococcus aureus*, *Escherichia coli*), followed by quantification of bacterial adhesion, biofilm formation, or colony-forming units (CFU) after incubation. In addition to conventional microbiological counting methods, advanced techniques such as live/dead fluorescence staining, confocal biofilm imaging, and quantitative real-time PCR are used to visualize bacterial viability and assess antimicrobial efficiency more accurately. Evaluating antibacterial properties is particularly important when PEO coatings incorporate therapeutic agents or metallic ions (e.g., silver, copper) intended to inhibit bacterial growth [296], [297].

Bioactivity is frequently evaluated using simulated body fluid (SBF) immersion tests, which assess the coating's ability to nucleate and grow HA-like phases that mimic natural bone mineral. SBF is an aqueous solution containing ion concentrations similar to human blood plasma, including  $\text{Na}^+$ ,  $\text{K}^+$ ,  $\text{Mg}^{2+}$ ,  $\text{Ca}^{2+}$ ,  $\text{Cl}^-$ ,  $\text{HCO}_3^-$ ,  $\text{HPO}_4^{2-}$ , and  $\text{SO}_4^{2-}$ , and tests are typically conducted at physiological temperature (37 °C) to replicate *in vivo* conditions. After immersion, samples are analyzed by SEM for morphological observation, XRD for crystalline phase identification, and FTIR for chemical composition, providing information on the coating's bone-bonding potential. The kinetics of apatite layer formation are also monitored over different immersion periods to evaluate the coating's long-term bioactive behavior. Complementary *in vitro* assays, such as protein adsorption studies, can further elucidate how bioactive surfaces interact with biological molecules that mediate cell attachment and osteointegration [298], [299].

Furthermore, ion release studies, performed using ICP-OES or ICP-MS, quantify the leaching of therapeutic ions (e.g.,  $\text{Ca}^{2+}$ ,  $\text{Mg}^{2+}$ ,  $\text{Ag}^+$ ,  $\text{Zn}^{2+}$ ), as well as metallic ions originating from the substrate itself, such as  $\text{Ti}^{4+}$ , into surrounding media over time. These measurements are critical for evaluating long-term coating stability and assessing potential biological effects such as antibacterial activity, osteogenesis promotion, or cytotoxicity due to excessive ion concentrations. Time-resolved ion release profiling can also be correlated with antibacterial and bioactivity tests to establish functional relationships between coating chemistry and biological outcomes. In addition to these *in vitro* assays, more advanced evaluations such as hemocompatibility testing, protein adsorption analysis, and *in vivo* animal implantation studies

are often conducted to validate biological safety and performance, ensuring that PEO coatings meet the stringent requirements for clinical biomedical applications [189], [300].

#### 1.6.4. Other functional properties

Beyond their physical and chemical characteristics, PEO coatings must be evaluated for their functional performance, which determines their suitability for specific applications such as biomedical implants, corrosion protection, and advanced functional materials. A variety of electrochemical, mechanical, surface, and biological tests are employed to assess these properties.

The corrosion resistance of PEO coatings is commonly evaluated by EIS and PDP, both of which provide electrochemical insights into coating performance in corrosive environments. In EIS, a small AC potential is applied over a broad frequency range while monitoring the resulting current response. The impedance is typically plotted as Nyquist or Bode diagrams and interpreted using equivalent electrical circuit models to estimate coating properties such as barrier resistance, pore resistance, and charge transfer kinetics at the coating–substrate interface. This method is highly sensitive to coating degradation, detecting early-stage failures and defect formation long before visible corrosion occurs. PDP involves sweeping the electrode potential in the anodic and cathodic directions and recording the resulting current response to generate Tafel plots. From these curves, corrosion potential ( $E_{\text{corr}}$ ), corrosion current density ( $i_{\text{corr}}$ ), and passivation behavior can be determined, providing quantitative data on corrosion rate and protection efficiency. While both techniques are complementary, EIS is generally considered more accurate for evaluating intact coatings, as it is non-destructive and can detect subtle changes in coating resistance and porosity over time. PDP, although widely used and straightforward, involves driving the system into non-equilibrium conditions, which may locally damage the coating or alter its electrochemical behavior. For this reason, EIS is often preferred for long-term corrosion monitoring, whereas PDP provides valuable confirmation of corrosion kinetics and the overall protective effectiveness of the coating [301], [302].

The surface charge of PEO coatings, expressed as zeta potential, plays a crucial role in determining their interactions with surrounding proteins, ions, and cells once implanted or exposed to aqueous environments. This property reflects the electrostatic potential at the shear plane of the solid–liquid interface and is a key factor governing protein adsorption, initial bacterial adhesion, and subsequent cellular responses such as proliferation and differentiation. In the context of PEO, zeta potential is particularly important because the process often incorporates electrolyte-derived ions (e.g.,  $\text{Ca}^{2+}$ ,  $\text{PO}_4^{3-}$ ,  $\text{CO}_3^{2-}$ ) and creates a heterogeneous, porous oxide surface that can significantly influence surface charge. Measurements of zeta potential are typically performed using electrokinetic analyzers, which detect streaming potential or streaming current as an electrolyte flows tangentially across the coated surface. The resulting data are used to calculate zeta potential values, which can change with pH, ionic strength, and surface composition. This information provides insights into the electrochemical nature of PEO-modified surfaces and is particularly valuable for predicting biointerface behavior and tuning surface properties for improved biocompatibility [303], [304].

Wettability is another essential surface property of PEO coatings, strongly affecting their biological performance and corrosion resistance. The oxide layer formed during PEO typically exhibits a rough, porous topography, which, together with surface chemistry (e.g., hydroxylation, presence of incorporated ions), determines its hydrophilic or hydrophobic character. Wettability is commonly assessed through static water contact angle measurements, where a controlled droplet of water is placed on the coating surface and imaged to determine the angle formed at the liquid–solid interface. Hydrophilic surfaces (low contact angle) generally promote protein adsorption in favorable conformations, enhance cell adhesion and spreading, and improve integration with biological tissues. Conversely, hydrophobic surfaces (high contact angle) may reduce bacterial colonization or be tailored for applications requiring reduced fluid interaction. The PEO process parameters (voltage, electrolyte composition,

treatment time) can significantly alter surface chemistry and topography, thus modulating wettability [305], [306].

The mechanical integrity of PEO coatings is critical for ensuring long-term durability under physiological or industrial conditions, where coatings are often exposed to cyclic loading, friction, and potential delamination forces. Among various mechanical tests, scratch testing is widely used to evaluate coating adhesion and cohesive strength. In this method, a diamond stylus is drawn across the coating under a progressively increasing normal load while continuously monitoring penetration depth, friction force, and acoustic emissions. The critical load ( $L_c$ ) at which coating delamination, cracking, or spallation occurs is recorded, providing a direct measure of adhesion to the substrate. Post-test SEM analysis of the scratch track is often performed to characterize the failure mode and determine whether damage is adhesive (coating–substrate interface) or cohesive (within the coating itself). Other mechanical tests complement scratch testing to provide a more comprehensive understanding of coating performance. Nanoindentation measures hardness and elastic modulus by pressing a sharp indenter (typically Berkovich geometry) into the coating and recording the resulting load-displacement curve, offering nanometer-scale resolution of mechanical properties. This technique is particularly useful for characterizing the heterogeneous, multilayered structure of PEO coatings. Micro-abrasion wear testing, on the other hand, evaluates wear resistance by exposing the coated surface to rotating abrasive particles in a liquid medium, simulating mechanical degradation in service environments. Additional tests such as micro-tensile adhesion testing, impact testing, or tribological pin-on-disk measurements can also be employed for specific applications, enabling a thorough assessment of the coating’s mechanical robustness and long-term reliability [23], [307].

PEO coatings are also developed for non-biomedical applications, where additional functional properties may be relevant. For instance, coatings designed for photocatalytic activity are characterized using UV-Vis spectroscopy or photodegradation tests of organic dyes under UV or visible light. Photoluminescence measurements assess optical properties for applications in sensing or light emission. In specialized high-technology applications, such as superconductors or advanced electronics, properties like electrical conductivity, superconducting transition temperature, or magnetic behavior may be characterized using four-point probe measurements, SQUID magnetometry, or resistivity testing. These methods demonstrate the versatility of PEO coatings across diverse engineering and scientific fields [93], [308], [309], [310].

#### **1.6.5. Characterization of baths**

The properties of the electrolyte bath play a critical role in PEO, as they determine discharge behavior, coating growth kinetics, and the incorporation of species into the oxide layer. Proper characterization of the bath is therefore essential for understanding and controlling the coating process. Since PEO baths often consist of a complex mixture of dissolved ions and suspended particles, their characterization can be divided into three categories: particle properties, electrolyte composition, and bulk suspension properties.

The size and distribution of suspended particles are typically measured using Dynamic Light Scattering (DLS), where fluctuations in scattered light intensity caused by Brownian motion are analyzed to determine hydrodynamic diameter. Particle size directly affects mass transport and incorporation efficiency into the growing oxide layer, influencing coating morphology and thickness distribution. The electrostatic surface charge of particles, expressed as zeta potential, is obtained via electrophoretic mobility measurements and provides insight into colloidal stability: high absolute zeta potential values (typically  $>30$  mV) indicate good dispersion, whereas low values suggest aggregation. Particle charge also governs their electrophoretic movement toward the anode during PEO, impacting their deposition efficiency. Complementary analytical techniques such as SEM, TEM, and EDX can be used to examine particle morphology, size distribution, and chemical composition, while XRD can confirm

phase purity and detect any transformations that may occur during suspension preparation or PEO processing. The chemical composition of particles can also be analyzed in detail using techniques such as ICP-OES/ICP-MS when elemental or surface chemistry information is required. All these techniques can be employed not only for initial characterization but also to trace possible changes in particle properties during suspension preparation or throughout the PEO treatment [30], [110], [311].

The dissolved ionic species in the electrolyte define the electrochemical environment necessary for oxide formation and plasma discharge generation. Major cations and anions such as sodium, potassium, calcium, phosphate, and silicate are typically quantified using ICP-OES, while specific anions, for example, carbonates, can be analyzed by ion chromatography or spectrophotometric methods. In formulations containing organic additives, UV-Vis spectroscopy or TOC analysis can be used for detection. The chemical composition of the liquid phase can also be characterized in more detail using ICP-MS for trace element detection. Similar to suspended particles, the composition of the liquid phase is not always static: reactions during bath preparation (e.g., acid-base neutralization, precipitation of salts) or during PEO (e.g., hydrolysis, dissolution of anodic layer material into the bath) may alter both ionic concentrations and speciation. Continuous monitoring and periodic re-analysis of the electrolyte chemistry are therefore necessary to ensure stable bath conditions and consistent coating properties [312], [313].

In addition to the properties of individual components, bulk suspension characteristics such as pH, electrical conductivity, and viscosity play crucial roles in process stability. pH affects oxide growth kinetics and the incorporation of electrolyte species into the coating, while conductivity governs current flow and plasma discharge behavior. These parameters are routinely measured with calibrated probes to ensure reproducibility. Suspension stability is equally important, as particle settling or aggregation can lead to inhomogeneous coatings; in addition to zeta potential measurements, stability can be evaluated visually, via turbidimetry, or through sedimentation tests, and in some cases complemented by particle size monitoring over time to detect agglomeration. In more concentrated suspensions, viscosity measurements further describe particle–particle and particle–electrolyte interactions. Comprehensive characterization of these bath properties, including monitoring changes during bath preparation and PEO operation, is essential for maintaining stable processing conditions and achieving coatings with tailored composition and functional performance [32], [314].

## **2. AIM OF RESEARCH**

The aim of this dissertation is to develop plasma electrolytic oxidation (PEO) coatings on titanium implants containing calcium carbonate (CC) and hydroxyapatite (HA), overcoming current challenges in carbonate phase incorporation and achieving bioactive, corrosion-resistant, and functional layers with controlled phase composition. The research also aims to broaden the fundamental understanding of particle incorporation mechanisms in PEO coatings and to evaluate the versatility of the developed coating strategy across different implant materials.

To achieve this aim, the following objectives are set:

1. Conduct preliminary investigations of carbonate-based electrolytes (including both soluble salts and suspended particles) using established approaches to bath formulation, and determine their influence on coating morphology and composition.
2. Examine the effect of particle crystallinity on PEO coating characteristics using HA as a model system, addressing this aspect of particle incorporation that has not previously been studied in PEO processes.
3. Develop and optimize processing strategies to fabricate CC–HA composite coatings on titanium and carry out comprehensive structural, chemical, biological, and functional characterization.

### **Hypotheses:**

- Traditional approaches to preparing PEO electrolytes have limited applicability for the incorporation of carbonate phases.
- Particles provide a viable route for introducing carbonate phases into PEO coatings, and particle crystallinity is a critical characteristic—alongside size, shape, and chemical composition—that determines the resulting coating properties.
- Particle synthesis via carbonation route offers a suitable and practical strategy for preparing CC-based PEO suspensions.
- The interaction of CC particles with phosphate-based electrolytes is an effective method for the co-deposition of HA in the PEO bath.
- The incorporation of CC and HA phases will positively influence the functional properties of PEO coatings, particularly enhancing their biological performance.

### 3. MATERIALS AND METHODS

#### 3.1. Preparation of PEO baths

The working baths used in this study consisted of either aqueous solutions (electrolytes) or particle-containing suspensions. Unless otherwise specified, their standard volume and preparation temperature were 200 mL and 20–25 °C (ambient conditions). Prepared solution- and particle-based baths were stored at room temperature, hermetically sealed, without exposure to CO<sub>2</sub> or air, and for no longer than 1 month. Before use in the PEO coating process, all baths were cooled to the operational temperature of 10 °C. Suspensions additionally underwent ultrasonic treatment and mechanical stirring at 300 rpm to ensure homogeneity. To minimize contamination risks, a single bath was used to prepare no more than 20–30 coating replicates. For solution-based PEO experiments, bath preparation was a straightforward process involving dissolving one or more salts at room temperature to reach the desired concentration. For single-component baths, concentrations typically ranged between 20 and 50 mM. Depending on the specific experimental requirements, the following salts or their combinations were used: KH<sub>2</sub>PO<sub>4</sub>, NaH<sub>2</sub>PO<sub>4</sub>, Na<sub>2</sub>HPO<sub>4</sub>, Na<sub>3</sub>PO<sub>4</sub>, NaHCO<sub>3</sub>, and Na<sub>2</sub>CO<sub>3</sub>. To facilitate preparation, stock solutions of these salts were maintained at concentrations of approximately 0.1–0.2 M.

For particle-based baths, the standard preparation procedure involved dispersing a pre-weighed particle powder, manually pre-ground in a mortar, into 100 mL of deionized water. The powder was added gradually in small portions (0.5–1 g) with a weighing accuracy of ±0.01 g while simultaneously applying ultrasonic treatment and mechanical stirring at 300 rpm, which continued throughout the preparation process. Fifteen minutes after the final powder addition, the required amount of salt was introduced to serve as the base electrolyte, and the suspension volume was adjusted to 200 mL with deionized water. As a final step, the resulting suspension was kept under the same ultrasonic and mechanical treatment for 2 hours to ensure complete dispersion. This method was applied to both commercial particles (Section 3.2) and synthetic TCP powders used for crystallinity studies (Section 3.2.1). In the case of preparing a suspension from CC particles synthesized via carbonation (Section 3.2.2), the procedure was more complex due to ongoing physicochemical interactions between CC and phosphates (Section 1.4.3). To account for all relevant details, a description is provided below, including the standard parameters used in the final version of the CC–HA bath and applied in the preparation of the final CC–HA coating configuration for their comprehensive characterization:

Initially, 120 mL of deionized water and 1.64 g of dibasic sodium phosphate dihydrate (Na<sub>2</sub>HPO<sub>4</sub>·2H<sub>2</sub>O, Fluka, 99.8%) were introduced into a 250 mL jacketed thermostatic beaker. The mixture was stirred magnetically at 300 rpm while being cooled to a stable temperature of 10 °C using a circulating cryostat with a water–ethylene glycol coolant. Once Na<sub>2</sub>HPO<sub>4</sub>·2H<sub>2</sub>O was fully dissolved, a phosphate solution with a concentration of 76.7 mM was obtained. Subsequently, 80 mL of the pre-cooled (10 °C) homogenized CC stock suspension (Section 3.2.2) was swiftly added, resulting in a 200 mL suspension containing 46 mM Na<sub>2</sub>HPO<sub>4</sub> and 64 mM CC. Immediately upon mixing, physicochemical interactions between CC and phosphate ions commenced, involving simultaneous dissolution–precipitation and chemisorption reactions (Section 1.4.3). Prior to use, the suspension underwent a maturation stage and was treated as a “CC–HA precursor bath.” To ensure complete maturation and reproducible properties, the freshly prepared precursor bath was magnetically stirred at 300 rpm for 48 hours in a closed, thermostated 250 mL vessel maintained at 10 °C. This duration was experimentally determined to be sufficient for achieving physicochemical equilibrium. During maturation, pH and conductivity were continuously monitored. The temperature was deliberately kept identical to that used during the subsequent PEO treatment. After maturation, the resulting suspension—referred to hereafter as the “CC–HA bath”—was ready for use in preparing a series of PEO coatings. When stored for later use or reused for another coating series, additional stirring was applied, either prolonged during storage or restarted immediately before initiating a new PEO



process. A schematic representation of the preparation procedure and the key physicochemical transformations is provided in Figure 1. If necessary, modifications to this procedure were introduced, for example, when studying the effect of a particular parameter.

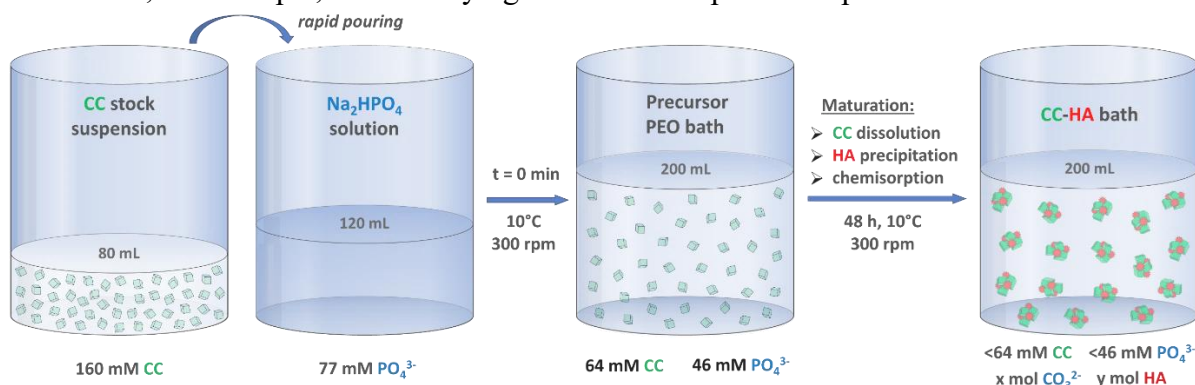


**Figure 1.** Schematic drawing showing the CC-HA bath preparation stages.

### 3.2. Particles used in PEO

For preliminary experiments in the preparation of CC- and HA-containing PEO coatings, commercial CC ( $\leq 50 \mu\text{m}$  particle size, 98% purity, Sigma Aldrich, USA) and commercial spray-dried crystalline stoichiometric HA particles ( $2.5 \mu\text{m}$ , Fludinova SA, Portugal) were used. The same HA particles were also employed in the part of the study dedicated to investigating the effect of particle crystallinity on the properties of PEO coatings (Section 4.2) and were further characterized by surface morphology analysis, hydrodynamic diameter determination, elemental composition analysis, etc. (see Section 3.3). The remaining particles (TCP and CC) were purposefully synthesized with tailored characteristics, with the synthesis procedures described below.

#### 3.2.1. Phosphate particle synthesis

Amorphous TCP was prepared using a conventional wet-precipitation approach with modifications to established protocols [315], [316] to tailor the particle characteristics. The precipitation reaction was initiated by rapidly (within 2–3 seconds) adding a 0.106 M solution of  $(\text{NH}_4)_2\text{HPO}_4$  ( $\geq 99\%$ , Sigma-Aldrich) into a 0.167 M aqueous solution of  $\text{Ca}(\text{NO}_3)_2 \cdot 4\text{H}_2\text{O}$  ( $\geq 99\%$ , Merck, Germany) containing sufficient  $\text{NH}_3(\text{aq})$  (Chempur, Poland) to adjust the pH to 10.0. A slight molar excess of calcium ions (5%) was employed to ensure complete conversion and maximize product yield. The mixture was stirred vigorously with a magnetic stirrer for 5 minutes, after which the resulting suspension was vacuum-filtered through a Büchner funnel (18.5 cm diameter) lined with filter paper (retention 2–4  $\mu\text{m}$ , Grade F2044, CHMLAB, Spain). The precipitate was sequentially washed: six times with 200 mL portions of 0.125%  $\text{NH}_3(\text{aq})$ , followed by rinsing with 125 mL of deionized water, and finally with 125 mL of 96% ethanol. All chemicals and washing solvents were of analytical-grade purity. The washed material was dried in air at  $80^\circ\text{C}$  for 12 hours, then manually ground in an agate mortar and stored in a desiccator under ambient conditions.

#### 3.2.2. Carbonate particle synthesis

The typical carbonation synthesis process, depicted in Figure 2, was carried out under thermostatically controlled conditions at an ambient temperature of  $18.0 \pm 0.5^\circ\text{C}$ . A three-neck round-bottom flask (15 cm diameter) with a central ground glass joint (29/32) and two side joints (14/23) was vertically mounted and filled with 1 L of deionized water (conductivity:  $0.055 \mu\text{S} \cdot \text{cm}^{-1}$ ). A PTFE-coated stainless-steel stirring rod of centrifugal type, equipped with two foldable blades (mixing part diameter: 80 mm), was introduced through the central neck and coupled to a mechanical stirrer. The stirrer was positioned approximately 3 cm above the

flask bottom and operated at a constant speed of 600 rpm, which was maintained throughout the entire synthesis. A combined electrode for simultaneous pH and conductivity measurements, integrated with a temperature sensor, was placed through one of the side necks to continuously record solution parameters during the reaction. Subsequently, 12.00 g of  $\text{Ca}(\text{OH})_2$  powder (Thermo Scientific, 99.8% purity) was accurately introduced into the stirred water via a glass joint funnel through the remaining side neck. For  $\text{CO}_2$  delivery, a 5 mL glass pipette was inserted into the suspension through the same neck and connected to a gas-feeding setup comprising a  $\text{CO}_2$  cylinder, pressure regulator, and calibrated rotameter (operating range:  $5\text{--}30\text{ L}\cdot\text{h}^{-1}$ ). After the suspension reached a stable pH of approximately 13.0, carbonation was initiated by bubbling high-purity  $\text{CO}_2$  gas (Air Liquide Polska, Cracow, Poland; 100% volume fraction) at a constant flow rate of  $15\text{ L}\cdot\text{h}^{-1}$ . The reaction was continued until the pH decreased to a neutral level of  $7.0 \pm 0.1$ . Following completion, the mixture was left to rest for 2 h to ensure full equilibration of the system. The final product was a CC suspension with a concentration of  $16\text{ g}\cdot\text{L}^{-1}$  (160 mM), referred to as the “CC stock suspension” in subsequent descriptions.

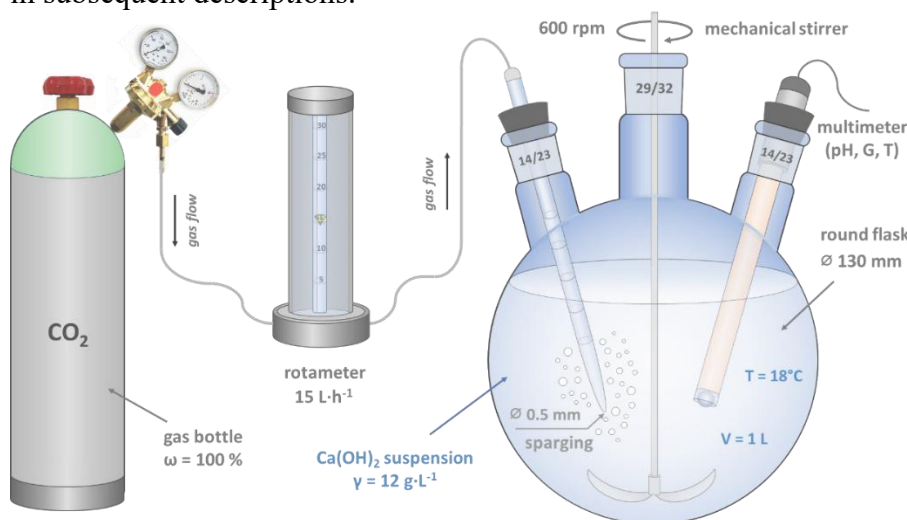


**Figure 2.** Schematic illustration of the CC stock suspension synthesis process using the carbonation method.

### 3.3. Characterization of PEO baths

For characterization purposes, individual baths were prepared following the procedures described in Section 3.1. The properties assessed can be broadly categorized as follows: (i) characteristics of the suspension as a whole system (conductivity, pH, zeta potential, and distribution of particle size expressed in their hydrodynamic diameter), (ii) properties of the liquid phase (concentrations of calcium, phosphate, and carbonate ions), and (iii) properties of the suspended particles (morphology, crystal size, hydrodynamic diameter, elemental and phase composition, crystallinity, and functional groups). For baths containing only a liquid phase, characterization was limited to pH and conductivity measurements. The chemical composition of the electrolytes and particles was analyzed based on the anticipated constituents. Importantly, for non-reactive systems—which include all PEO baths except those containing CC–phosphate suspensions—particle characterization was performed *ex situ*, i.e., using the pristine powders prior to dispersion. Similarly, the chemical composition of the liquid phase was not reanalyzed when it was already well-defined. Although the CC suspension synthesized via carbonation was also non-reactive, particle analysis in this case required their extraction through filtration followed by drying.

The CC–HA bath, in contrast, exhibits dynamic equilibrium due to reactions between CC and phosphate ions (Section 1.4.3). Consequently, time-resolved characterization was

necessary, with the mixing point defined as the starting reference. In practice, this involved periodic sampling of the CC–HA bath over the entire maturation cycle, with sampling frequency adjusted according to the parameter under investigation. Measurements of pH and conductivity for this bath were performed continuously, without physical sampling, with data recorded every 5 minutes. During the sampling procedure, the bath temperature and stirring rate were maintained at 10 °C and 300 rpm, respectively, matching the conditions employed in the PEO process. This setup enabled simultaneous analysis of both suspended particles and the liquid phase. Specifically, 5 mL aliquots of the well-stirred suspension were collected using an automatic pipette and transferred into Eppendorf Safe-Lock microtubes. Samples were centrifuged at 10,000 rpm for 5 minutes, after which the supernatant was separated into another 5 mL microtube for subsequent phosphate and carbonate quantification. The precipitate underwent three washing steps with deionized water, was air-dried at 80 °C for 24 hours, and was later analyzed to determine the mass fractions of phosphate and carbonate incorporated into the particles. In parallel, an additional sampling protocol was employed to characterize the suspension properties, as detailed in Section 3.3.2. TEM, FTIR, and XRD analyses of CC-HA particles were performed only once, with a single sampling conducted at the very end of the maturation process. Due to the larger amount of sample required for XRD, the sampling procedure in this case involved passing 50 mL of the stirred suspension through F2044-grade quantitative filter paper (CHMLAB Group, Barcelona, Spain) under vacuum filtration conditions. The precipitate was then repeatedly washed with deionized water, air-dried at 80 °C for 24 hours, and ground in a mortar to break down macro-agglomerates. The resulting powder was divided into three corresponding portions and used for the analyses.

### 3.3.1. Chemical analysis

For quantification of calcium and phosphorus mass fractions in the particles, 20 mg of the powder was accurately weighed ( $\pm 0.01$  mg) and dissolved in 100 mL of 1% HNO<sub>3</sub> solution using a glass volumetric flask. The measurements were carried out on a Varian 710-ES inductively coupled plasma optical emission spectrometer (ICP-OES) equipped with a glass SeaSpray nebulizer and a double-pass glass cyclonic spray chamber. Calcium and phosphorus concentrations were determined via the calibration curve method, with matrix effects simulated by adding an appropriate amount of HNO<sub>3</sub>. Calibration standards were prepared by diluting stock solutions of Ca (1000 mg·L<sup>-1</sup>, Thermo Scientific, Belgium) and P (1000 mg·L<sup>-1</sup>, Certipur, Merck, Darmstadt) to final concentrations of 0–100 mg·L<sup>-1</sup> for Ca and 0–50 mg·L<sup>-1</sup> for P. A linear calibration model with a correlation coefficient exceeding 0.9990 was applied. For determining carbonate mass fractions in the suspended particles, 5 mg of the powder was precisely weighed ( $\pm 0.01$  mg) and placed into tin capsules (h = 8 mm, d = 5 mm; Elemental Microanalysis Ltd, Okehampton, UK). Total carbon content was analyzed using a Continuous Flow Horizon 2 IRMS (Nu Instruments Ltd, Wrexham, UK) coupled with a EuroEA3024 elemental analyzer (Eurovector, Pavia, Italy), and the obtained carbon values were subsequently converted to carbonate mass fractions.

The concentrations of dissolved carbonates and phosphates in the supernatants were quantified via ion chromatography using a Dionex Integriion high-pressure IC system (Thermo Fisher, MS, USA). The system was equipped with a Dionex IonPac™ AS18-4μm (4 × 150 mm) analytical column, a Dionex EGC III KOH potassium hydroxide eluent generator, and a Dionex AS-AP autosampler. Ultrapure deionized water (resistivity >18 MΩ·cm) was produced using a Millipore Milli-Q™ system (Billerica, MA, USA). A laboratory-validated method for the simultaneous analysis of seven anions (fluoride, chloride, nitrate, nitrite, sulfate, and phosphate) was employed to determine the target analytes. For phosphate quantification, seven-point calibration curves (0.05–0.5 mg·L<sup>-1</sup>) were prepared by diluting a 1000 mg·L<sup>-1</sup> phosphate anion standard for ion chromatography (Hach Lange GmbH, Düsseldorf, Germany), achieving correlation coefficients ( $R^2$ ) > 0.9990. Supernatant samples were diluted 1000-fold prior to analysis. Carbonate ions typically appear in the chromatographic background before sulfate. A

modified method, based on a Thermo Scientific protocol [317] developed for volcanic gas analysis in caustic solutions, was adapted for carbonate quantification in aqueous samples. Carbonate calibration standards (0, 5, 10, 20, 50, 100, and 250 mg·L<sup>-1</sup>) were prepared from analytical-grade sodium bicarbonate (Merck, Darmstadt, Germany), with  $R^2 > 0.9990$ ; blank water samples were used for zero-level calibration. Supernatants for carbonate analysis were diluted 1:10 in chromatographic vials with deionized water. Each sample, including controls, was analyzed in triplicate. Chromatographic runs were performed in isocratic mode at 30°C with the following operating conditions: eluent flow rate 1 mL·min<sup>-1</sup>, loop volume 250 µL, injection volume 25 µL, and suppressor current 124 mA. The overall method uncertainties (U) were estimated at 16% for PO<sub>4</sub><sup>3-</sup> and 10% for CO<sub>3</sub><sup>2-</sup>. The limits of quantification (LOQ) were determined as 0.2 mg·L<sup>-1</sup> for phosphate and 15 mg·L<sup>-1</sup> for carbonate. Final quantification results were recalculated and expressed in millimolar (mM) units.

### 3.3.2. Other bath characteristics

To measure suspension conductivity and pH, a CX-601 multifunction device (Elmetron, Zabrze, Poland) was used. Zeta potential and particle size measurements were conducted at room temperature using a Zetasizer Nano ZS analyzer (Malvern Panalytical, UK) equipped with a 633 nm He-Ne laser. For statistical reliability, three replicate measurements were performed for each sample. Sampling procedure for particle size analysis involved taking 50-200 µL of the suspension depending on its concentration and type of particles, transferring the measured portion into a plastic tube, adding deionized water to a total volume of 10 mL, and subjecting the resulting suspension to ultrasound treatment for 5 minutes. Immediately after sonication, 1 mL of the suspension was transferred into a polystyrene cuvette and used for measurements. Zeta potential measurements were performed in a U-shaped cuvette (DTS1070, Malvern Panalytical, UK) using the same sample preparation procedure. Particle size measurement results were reported as average hydrodynamic diameters.

A JEOL ARM 200FS TEM was employed to examine the surface morphology and particle size. In some cases, a Jeol JSM-7800 PRIME SEM was used for particle analysis, operating at a 15 keV accelerating voltage and 5 mA beam current. The powders were mounted onto a ~1 × 1 cm<sup>2</sup> section of conductive adhesive carbon tape (Agar Scientific, United Kingdom). The diametral cross-sectional area of the particles was manually measured from the acquired SEM images using ImageJ software, assuming a spherical particle geometry. Based on these measurements, distribution curves were plotted, representing the total diametral cross-sectional area of the particles as a function of the individual diametral cross-sectional area values. XRD was conducted to trace changes in the crystallinity and phase composition of the suspended particles. XRD patterns were recorded at ambient temperature using a Bruker D8 Discover diffractometer with Cu Kα1 radiation (wavelength 1.54180 Å), equipped with a LynxEye position-sensitive detector. The tube voltage and current were set to 40 kV and 40 mA, respectively. The divergence slit was adjusted to 0.6 mm, and the antiscatter slit was set to 8.0 mm. Diffraction patterns were recorded from 20° to 70° on the 2θ scale. FTIR spectra were acquired using a Perkin Elmer Frontier instrument using ATR accessory to detect the kind of functional groups. The spectra were recorded in the wavenumber range of 4000-400 cm<sup>-1</sup> with a resolution of 4 cm<sup>-1</sup>, based on 64 scans. For data presentation, the regions 600-1400 cm<sup>-1</sup> and 2400-4000 cm<sup>-1</sup> were used.

### 3.4. Preparation of PEO coatings

The PEO coatings were prepared following a standardized protocol, with specific adjustments introduced as required to meet the objectives of individual experiments. A 200 mL portion of the freshly formulated electrolyte was introduced into a thermostated, double-walled cylindrical glass reactor (total capacity: 250 mL; inner diameter: 6 cm). The bath temperature was stabilized at 10 °C via a recirculating cryostat circulating a water–ethylene glycol mixture

through the reactor jacket. To suppress sedimentation of suspended particles and ensure efficient heat dissipation from the anode, continuous magnetic stirring was applied at a fixed rate of 300 rpm and maintained throughout the entire coating series. The cathode consisted of a stainless-steel hollow cylinder (5 cm diameter, 5 cm height) featuring a lateral cut-out and a welded rod for secure positioning within the stirred electrolyte (Figure 3a). Metallic discs (thickness: 0.40 mm; diameter: 1.00 cm) served as the anode substrates. Only one circular face of each disc was exposed to oxidation, defining a working surface area of 0.785 cm<sup>2</sup>. Prior to processing, the substrates were sequentially polished using SiC abrasive papers up to 1000 grit, ultrasonically cleaned in a surfactant solution, and rinsed with deionized water. The materials investigated included commercially pure titanium (Iwet, Grabówka, Poland) and Ti6Al4V alloy (Iwet, Grabówka, Poland). Samples were fixed in a custom-designed holder (Figure 3b) to ensure consistent positioning during coating deposition.

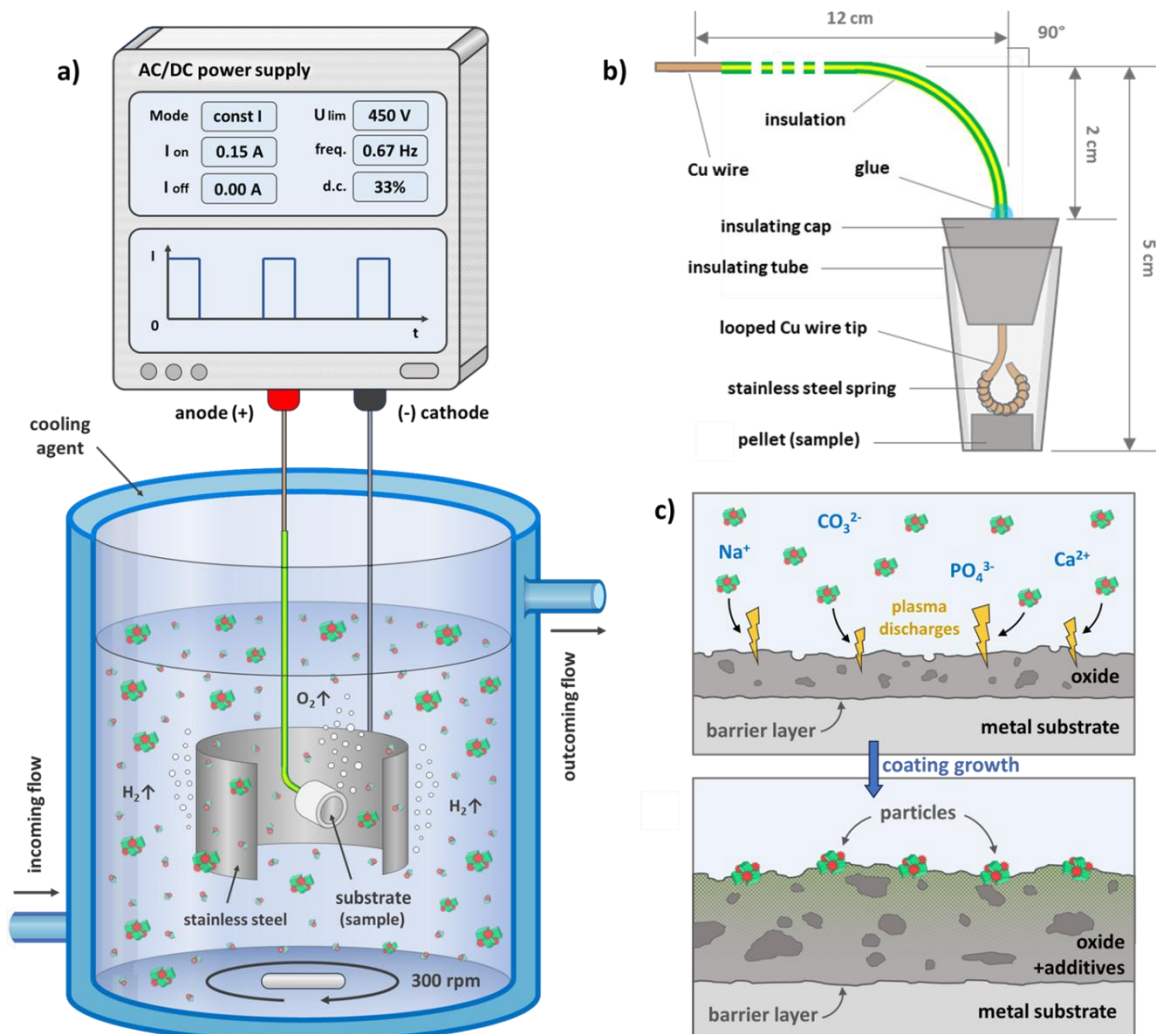


**Figure 3.** (a) Experimental setup employed for PEO coating preparation; (b) schematic illustration of the custom-fabricated anode holder; (c) conceptual depiction of the general mechanism of PEO coating growth in particle-containing suspensions.

The sample holder used during PEO coating deposition was fabricated from a 2 mm-thick, insulated copper wire bent at a 90° angle (Figure 3b). The wire was threaded sequentially through a truncated cone-shaped insulating cap and an elastic tube, the inner diameter of which matched that of the cylindrical substrate, ensuring a tight press-fit contact with the titanium disc. This design prevented electrolyte ingress onto the lateral surface of the specimen. The metallic discs were manually inserted into the elastic tube so that the active surface was positioned equidistantly from the tube's edge and immersed to a depth of approximately 1 mm.

This configuration allowed the anodic working face to remain vertically oriented, thereby reducing oxygen bubble adhesion and accumulation during the oxidation process. All exposed parts of the holder were fabricated from insulating materials. Furthermore, the interface between the copper wire insulation and the conical cap was sealed with adhesive to eliminate moisture penetration. To enhance electrical conductivity, the terminal end of the copper wire was bent into a hook and passed through a stainless-steel spring. The spatial arrangement and dimensions of the electrodes were optimized to achieve uniform coating conditions: the cylindrical stainless-steel cathode was positioned concentrically with the reactor vessel, while the anodic working surface was fully immersed inside the hollow cathode, facing the lateral cut-out and extending slightly beyond the virtual continuation of the cathode wall (Figure 3a). This geometry was specifically designed to promote more homogeneous current distribution and accelerated mass transport across the anodic surface.

The PEO treatments were performed using a PWR400H DC power supply (Kikusui, Japan) operated in galvanostatic mode under remote control via Wavy 5.01 software. A voltage limit, varied between 300 and 500 V depending on the experimental conditions, was imposed during each run. To investigate the influence of electrolyte composition on the electrical response during PEO, transient voltage and current profiles were recorded at 0.5 s intervals. The resulting data, averaged over three independent replicates, were plotted as voltage–time and current–time curves. From these plots, the time required to reach the preset voltage limit was extracted and compared across different bath compositions using an independent two-sample t-test (OriginPro 2024b), with a statistical significance threshold of  $p < 0.05$ . The oxidation program consisted of 400 consecutive cycles of 1.5 s each, corresponding to a total treatment time of 10 min. If not specified otherwise, the process was stopped when the current values dropped to no more than 10% of the initially set value. For experiments with alternative treatment durations, the number of cycles was proportionally adjusted. Each cycle comprised two stages: a 0.15 A current pulse applied for 0.5 s, followed by a 1.0 s interval with no current applied. Step transitions were employed between successive cycles and stages, thereby generating a pulsed current with a square waveform, a frequency of 0.67 Hz, and a duty cycle of 33%. Once the process voltage reached the predefined limit, the operation automatically switched to potentiostatic mode, maintaining the limiting voltage for the remainder of the treatment. Following completion of the PEO process, the coated sample was carefully removed from the custom holder (Figure 3b), rinsed thoroughly with deionized water, and dried at 110 °C for 24 h to eliminate residual moisture from its porous structure. The holder itself was dried under an air stream before preparing the next coating replicate. The overall mechanism of PEO coating formation in particle-containing suspensions is schematically depicted in Figure 3c.

### 3.5. Characterization of PEO coatings

#### 3.5.1. Coating structure and elemental composition

Surface and cross-sectional characterization of the PEO coatings was carried out using a Phenom Pro-X SEM (Thermo Fisher Scientific) operated at an accelerating voltage of 15 kV and equipped with an EDX detector. The analysis encompassed surface morphology, open porosity, roughness parameters, and elemental composition. Surface morphology was evaluated at multiple magnifications to examine coating uniformity and to identify characteristic structural features. Quantitative analysis of open porosity was performed using ImageJ software based on SEM micrographs acquired at 1000× magnification from ten randomly selected surface regions for each coating type. Three-dimensional surface topography reconstructions were additionally captured at magnifications tailored to optimally visualize the distinct surface features of each coating. Surface roughness was assessed at five independent locations per coating, and the results were reported as the arithmetic mean values of  $R_a$  (average roughness) and  $R_z$  (vertical peak-to-valley height difference). Complementary roughness measurements



were performed using a contact profilometer (Mitutoyo SJ-301, resolution: 0.01  $\mu\text{m}$ , measurement length: 5 mm), and the results were compared with SEM-derived roughness values. Elemental analysis was conducted via EDX using spot, area, and mapping modes. For cross-sectional evaluation, coated samples were mounted in VersoCit-2 resin (Struers, Copenhagen, Denmark), cured, and then ground with SiC abrasive papers up to 1000 grit. Final polishing was achieved using a 3  $\mu\text{m}$  diamond suspension. The polished cross-sections were sputter-coated with gold for 180 s under an ionized argon atmosphere (Sputter Coater 108auto, Cressington, Watford, UK) to mitigate surface charging during SEM examination. Cross-sectional imaging provided information on coating thickness, internal structural features, and elemental gradients from the outer surface toward the substrate. The latter was quantified through EDX line-scan measurements performed at ten vertically aligned positions, and the results were averaged to generate elemental distribution profiles. Statistical comparisons of elemental composition—derived from EDX area analyses at distinct surface regions—were carried out using a two-tailed unpaired Student's t-test with a significance level of  $p < 0.05$ . Mean values and corresponding standard errors were reported for each coating. An identical statistical approach was used to evaluate differences in overall surface porosity between the investigated coatings. All statistical analyses were performed in OriginPro software (version 2024b).

### 3.5.2. Phase composition and elemental bonding

Raman spectroscopy was performed using a WITec alpha 300R confocal Raman microscope (CRM) equipped with an air-cooled solid-state laser ( $\lambda = 532 \text{ nm}$ ) and a CCD detector. The excitation beam was delivered through a polarization-maintaining single-mode optical fiber with a core diameter of 50  $\mu\text{m}$  and focused onto the sample surface via a long-working-distance Olympus MPLAN objective lens (100 $\times$ /0.90 NA), ensuring an optimal balance between lateral and depth resolution [318]. The lateral resolution (LR) was estimated using the Rayleigh criterion ( $\text{LR} = 0.61\lambda/\text{NA}$ ), yielding a value of 0.36  $\mu\text{m}$ . The depth resolution (DR), defined as the minimum resolvable separation along the Z-axis, was calculated according to  $\text{DR} = \lambda/\text{NA}^2$ , resulting in 0.65  $\mu\text{m}$  at the focal plane. Due to refractive index effects and laser scattering in materials with  $n \approx 1.5$ , the effective depth resolution was further adjusted based on Everall's correction model [319], [320], giving values of 1.85  $\mu\text{m}$ , 3.70  $\mu\text{m}$ , and 5.55  $\mu\text{m}$  for focal depths of 1, 2, and 3  $\mu\text{m}$ , respectively. The Raman-scattered light was collected through a 50  $\mu\text{m}$  multi-mode fiber and analyzed by a monochromator calibrated against a neon lamp emission spectrum. Beam alignment was verified using the characteristic Raman peak of silicon at 520.7  $\text{cm}^{-1}$ . Individual spectra were acquired over the 120–4000  $\text{cm}^{-1}$  range with a spectral resolution of 3  $\text{cm}^{-1}$ , using a laser power of 20 mW.

Surface Raman mapping was performed for CC-HA coatings over a 70  $\mu\text{m} \times 70 \mu\text{m}$  area with a spatial resolution of 210  $\times$  210 pixels (44,100 spectra in total). The integration time was set to 80 ms per spectrum, with a sample positioning accuracy of  $\pm 0.2 \mu\text{m}$ . The acquired spectra, including both individual spectra and those extracted from imaging datasets, were post-processed using a third-degree auto-polynomial baseline correction and automatic cosmic ray removal, implemented by comparing each CCD intensity value at each wavenumber to adjacent pixel values [318]. Chemical images were generated by applying a sum filter that integrated signal intensities within predefined Raman shift regions: 450–550  $\text{cm}^{-1}$  for  $\text{B}_{1g}$  modes of  $\text{TiO}_2$ , 900–1000  $\text{cm}^{-1}$  for the  $\nu_1(\text{PO}_4^{3-})$  band, and 1070–1110  $\text{cm}^{-1}$  for the  $\nu_1(\text{CO}_3^{2-})$  band. This approach enabled the preliminary identification of chemical and structural heterogeneity within the analyzed coatings prior to detailed spectral evaluation. The final chemical analysis was performed on normalized spectra using WITec Project Five Plus software.

XRD measurements were performed at ambient temperature using a D8 Discover diffractometer (Bruker) equipped with a LynxEye position-sensitive detector and operated with  $\text{CuK}\alpha$  radiation ( $\lambda = 1.54180 \text{ \AA}$ ). The X-ray tube was set to 40 kV and 40 mA. A 0.6 mm divergence slit and an 8.0 mm antiscatter slit were used. Diffraction patterns were collected

over the  $2\theta$  range of  $3^{\circ}$ – $70^{\circ}$  with a step size of  $0.02^{\circ}$  and a counting time of 30 s per step. Phase identification was carried out using the ICDD PDF-2 database (Release 2021).

XPS analyses were conducted with a PREVAC EA15 hemispherical electron energy analyzer, equipped with a 2D multi-channel plate detector and an Al-K $\alpha$  X-ray source (PREVAC dual anode XR-40B, photon energy 1486.6 eV). The base pressure during measurements was maintained at  $5.5 \times 10^{-8}$  Pa. Survey spectra were acquired with a pass energy of 200 eV and a step size of 0.9 eV, while high-resolution spectra were recorded at 100 eV pass energy with a 0.05 eV step size. Binding energy calibration was performed using the adventitious carbon C–C peak at 284.8 eV. Spectral fitting was carried out in CASA XPS software using built-in algorithms. High-resolution peaks were modeled with a mixed Gaussian–Lorentzian function (70% Gaussian, 30% Lorentzian), and background subtraction was performed using the Shirley method.

### 3.5.3. Biological evaluation of coatings

To evaluate the in vitro bioactivity of the coatings, immersion tests were conducted in simulated body fluid (SBF) prepared according to a previously reported composition [321]. For each substrate and electrolyte formulation, four coated samples were fabricated. The specimens were vertically immersed in 20 mL of SBF within polypropylene test tubes and incubated at  $37^{\circ}\text{C}$  in the dark. The solution was refreshed every three days to maintain ion concentration stability. Samples were retrieved after immersion periods of 7, 14, 21, and 28 days, rinsed, sonicated in deionized water to remove loosely attached deposits, and examined by SEM to assess surface mineralization.

Human dermal fibroblasts (D6P10) were used to assess cytocompatibility and cell adhesion properties of the coatings (Ethics committee for research in life sciences and medicine of the University of Latvia approval No. 71-35/17). Uncoated titanium discs of identical dimensions and origin to those described in Section 3.4, polished to 1000 grit, served as reference samples. Prior to testing, all specimens were sterilized by autoclaving and placed into 24-well plates containing DMEM/F-12 medium supplemented with 10% fetal bovine serum and incubated overnight. Cells were seeded onto the sample surfaces at a density of  $10^4$  cells/cm $^2$  in complete culture medium. Wells containing cells but no samples served as positive controls (tissue culture plate control), while wells with medium only acted as negative controls. Cell adhesion was quantified on day 1 and proliferation on days 3 and 7 using a resazurin-based colorimetric assay [322]. Each experimental condition was tested in triplicate. Following the final time point, samples were washed twice with PBS and fixed with 3.5% formaldehyde (Sigma-Aldrich) for 10 min. Permeabilization was performed with a solution of 1% bovine serum albumin (BSA) and 0.1% Triton X-100 in PBS. The actin cytoskeleton was stained with ActinRed 555 (Thermo Scientific, USA) and nuclei with Hoechst 33342 (Thermo Scientific, USA) at a 1:1000 dilution. Stained samples were analyzed using a Nikon Eclipse TI fluorescence microscope (Japan) with DAPI and TRITC channels.

The antibacterial performance of the coatings was investigated using *Escherichia coli* (ATCC 25922) and *Staphylococcus aureus* (ATCC 25923). Uncoated titanium discs of matching size and surface preparation served as references. Samples were sterilized by autoclaving at  $121^{\circ}\text{C}$  for 15 min and then immersed in 2 mL bacterial suspensions ( $10^5$  CFU/mL) in sterile 24-well plates. The plates were gently agitated at  $37^{\circ}\text{C}$  for either 2 or 6 h to allow bacterial adhesion. Non-adherent bacteria were removed by rinsing with phosphate buffer solution (pH 7.2). Adhered bacteria were detached by ultrasonication (120 W) for 5 min in an ultrasonic bath (Emmi-20HC, EMAG) followed by 1 min of vortex mixing (V-1 plus, Biosan) in 1 mL sterile saline solution. Aliquots of 10  $\mu\text{L}$  were plated on Mueller–Hinton agar, streaked for isolation, and incubated at  $37^{\circ}\text{C}$  for 24 h. Colony-forming units (CFUs) were subsequently counted. Three independent experiments were performed for each condition. Statistical analysis of CFU counts was conducted using one-way analysis of variance (ANOVA)



in Statistica® v.8 (SPSS Inc., Chicago, IL, USA), with  $p < 0.05$  considered statistically significant. Standard deviations were calculated for each dataset.

### 3.5.4. Other functional characteristics

Surface wettability of the coatings was evaluated via dynamic water contact angle measurements using a goniometer (DataPhysics OCA 15EC, Germany). A 0.2  $\mu\text{L}$  droplet of deionized water was deposited on each sample, which had been stored in a desiccator for 24 h prior to testing. The evolution of the contact angle over time was recorded, and final results were expressed as mean values calculated from three independently prepared coatings.

The release behavior of Ca and Ti ions from the coatings was investigated under both static and dynamic conditions. Coated titanium discs were vertically mounted at the bottom of 50 mL polypropylene tubes and stabilized with plastic clips. Subsequently, 50 mL of phosphate-buffered saline (PBS, pH 7.3) was added, and samples were incubated at 37 °C for 30 days. For the static release study, 4 mL aliquots were withdrawn at predetermined intervals. In the dynamic study, the entire PBS volume was replaced every three days. Calcium and titanium concentrations were quantified using inductively coupled plasma optical emission spectrometry (ICP-OES, Varian 710-ES) equipped with a glass SeaSpray nebulizer and a double-pass glass cyclonic spray chamber. Calibration standards were prepared in PBS matrix by serial dilutions of stock Ca and Ti solutions (1000  $\text{mg}\cdot\text{L}^{-1}$ , Thermo Scientific, Belgium; Certipur, Merck, Darmstadt, Germany). Calibration curves exhibited linearity with correlation coefficients  $> 0.9990$ . Prior to analysis, all samples were diluted and filtered through 0.22  $\mu\text{m}$  syringe filters. Reported values represent mean  $\pm$  standard deviation of three independent experiments conducted on separate CC-HA coatings.

The electrokinetic potential of coating surfaces was measured by streaming potential using an electrokinetic analyzer (SurPASS 3, Anton Paar, Austria). For each coating type, two replicate samples were prepared. A modified PEO process (Section 3.4) was employed using  $25 \times 10$  mm rectangular Ti sheets (thickness: 0.3 mm, purity:  $> 99.9\%$ , Iwet, Grabówka, Poland), polished to 1000 grit. A Ti rod (12 cm length) was welded to the short edge of each sheet and insulated with heat-shrink tubing, leaving a  $20 \times 10$  mm active area exposed on both sides. After PEO treatment, the insulated portion was removed, and the  $20 \times 10$  mm coated specimen was washed with distilled water and air-dried at 80 °C for 24 h. During measurement, samples were mounted in the adjustable gap cell using double-sided adhesive tape (Tesa, Germany), with a gap height of 110  $\mu\text{m}$ . Prior to testing, samples were rinsed twice with 0.01 M KCl solution (pH 5.8) to establish the cell constant. Streaming potential measurements were performed four times per sample across a pH range of 5.8–9.0, adjusted by incremental addition of 0.1 M NaOH.

The adhesion strength of CC-HA and Blank coatings was evaluated via scratch testing using a CSM open-platform tribometer following PN-EN ISO 20502:2016-05 guidelines. A Rockwell diamond indenter was drawn across the coating surface while the normal load was linearly increased from 0.03 N to 30 N. Acoustic emission, friction force, and friction coefficient were simultaneously monitored. The critical load ( $L_c$ ), defined as the minimum force causing coating detachment, was determined from these signals and microscopic inspection of the scratch tracks. Test parameters included a scratch length of 3 mm, a loading rate of  $10 \text{ N}\cdot\text{min}^{-1}$ , and a table speed of  $1 \text{ mm}\cdot\text{min}^{-1}$ .

Corrosion resistance was investigated electrochemically using a 250 mL thermostated flat corrosion cell (Bio-logic, France) operated at 37 °C. Disc-shaped coated samples served as working electrodes and were sealed against the electrolyte with a rubber O-ring (6 mm diameter). A platinum plate and a saturated calomel electrode (SCE) were used as counter and reference electrodes, respectively. Potentials were reported versus the normal hydrogen electrode (NHE), with SCE calibrated to +0.233 V vs. NHE under experimental conditions. PBS solution (pH 7.3) was used as the electrolyte, prepared by dissolving 8.00 g NaCl, 1.44 g  $\text{Na}_2\text{HPO}_4$ , 0.20 g KCl, and 0.24 g  $\text{KH}_2\text{PO}_4$  in 1 L deionized water. Electrochemical tests were

conducted with a potentiostat/galvanostat (PARSTAT4000A, Ametek, USA–UK) and VersaStudio software (v. 2.63.3). Prior to polarization, samples were immersed in PBS for 2 h to stabilize their open-circuit potential (EOC), which was continuously monitored. EIS was then performed at EOC with a 10 mV<sub>RMS</sub> sinusoidal perturbation over 100 kHz–0.01 Hz (10 points per decade; total acquisition time  $\approx$  4000 s). After a 300 s stabilization period, PDP scans were initiated from  $-0.25$  V vs. EOC to  $+2.0$  V vs. NHE at a scan rate of  $10 \text{ mV} \cdot \text{min}^{-1}$ . Following the forward scan, the potential was reversed by  $0.2$  V to assess hysteresis. EIS data were analyzed using ZSimpWin software (v. 3.60, Ametek, USA). Each experiment was repeated in triplicate, and results are reported as mean  $\pm$  standard deviation.

## 4. RESULTS AND DISCUSSION

In accordance with the aims and objectives of this dissertation, the experimental work was divided into three parts, each dedicated to a specific aspect of the overall study. Part 1 focuses on analyzing the influence of various variables on the course of the PEO process in carbonate- and phosphate-based electrolytes, positioning the results as preliminary data for further use in optimizing CC–HA coatings. Part 2 is devoted to a single parameter identified as the most relevant and least studied — the crystallinity of particles. Hydroxyapatite (HA) particles were synthesized and characterized, and PEO coatings were prepared and examined in terms of a broader set of characteristics, including bioactivity and phase composition using Raman spectroscopy. Finally, Part 3 describes the synthesis of CC–HA particles via a carbonation method, followed by their use in preparing the final version of the PEO electrolyte, after first determining the optimal component concentrations and process voltage. The resulting CC–HA coatings were characterized including a wide range of structural, physicochemical, biological, and other functional parameters. In addition, drawing on fundamental principles of the PEO process, a growth mechanism for CC–HA coatings was proposed, providing a detailed explanation of the possible causes behind all observed structural features.

### 4.1. Part I – Preliminary experiments

As outlined in the literature review in the Section 1.4.1, PEO baths containing carbonates—either alone or in combination with other additives—remain relatively underexplored. At the same time, many aspects related to the addition of solid particles to the PEO bath also require clarification, particularly those concerning CaP and biomineral phases. Consequently, achieving the ultimate goal—namely, the fabrication of CC–HA coatings with optimal properties—requires a series of preliminary, intermediate experiments aimed at assessing the influence of multiple variables on the outcome of the PEO process, conducted in both phosphate- and carbonate-based baths. Establishing these interrelationships is expected to provide a comprehensive practical understanding of the PEO process, to identify potential nuances associated with carbonate incorporation, and ultimately to serve as an empirical foundation for further optimization work, supplying the methodological tools for the incorporation of CC and HA phases into the PEO coating. At this stage, an in-depth comparative assessment of the influence of various PEO process parameters on the functional properties of the coatings is not envisaged; instead, the evaluation is limited to a few selected characteristics, deliberately chosen according to the specific parameter under investigation.

Two fundamental characteristics used to confirm the contribution of a given variable were surface morphology and elemental composition, both of which allow direct or indirect tracing of any changes, assessing their extent, and drawing conclusions about whether this factor should be taken into account in further work and whether it requires additional investigation. In the first case, SEM was employed, enabling direct evaluation of the external structure, including pore size and shape; in the second case, EDX spectroscopy was used to analyze a selected surface region. In most cases, this information was sufficient to establish simple facts—for example, whether particles were incorporated (which would be indicated, for instance, by the appearance of calcium or an increase in its content compared to a coating without particle addition). On the side of the PEO bath, the variables include the source of phosphates and carbonates, their form (particles or dissolved species), their mutual molar ratio and concentration, the presence of auxiliary additives, as well as pH and conductivity (in conjunction with other parameters). Separate parameters concern the chemical composition, the presence of any form of pre-treatment, the physical form, density, and microstructure of the substrate used, along with all derived properties such as mechanical characteristics, electrical and thermal conductivity—which also applies to the oxides formed during the PEO procedure. Finally, several additional parameters can be distinguished, including bath temperature, stirring rate (mass transfer), viscosity, and the duration of the PEO process.

The use of particles as a means of modifying the chemical composition of the bath can be considered a single variable; however, this measure is accompanied by a large number of associated parameters. These include the physical size and shape, density, degree of dispersion, concentration, and zeta potential. These characteristics, in turn, determine the hydrodynamic diameter (the actual size of the particles in the bath), their tendency toward thermal decomposition (larger particles being less prone), and their mobility under the influence of an electric field (smaller particles being more mobile). If the particles are synthetic, the set of synthesis-related parameters that affect the final size and shape should also be taken into account. Such parameters may include, for example, the rate of reagent mixing, their concentrations, and other factors depending on the synthesis method used. In practice, however, the use of commercially available particles is more common—provided they possess characteristics (primarily size) suitable for the PEO process—which eliminates the need for synthesis and leaves only the task of dispersing them (adding them to the bath) [19], [30].

The objective of the work in terms of the current Part I is not to assess every possible parameter, given their interdependence (for example, bath temperature determines conductivity, which in turn is closely related to electrolyte concentration), as well as the existence of certain studies reporting established trends, which may facilitate the prediction and interpretation of results [106], [113]. Therefore, in the present Section 4.1, only the most relevant and practical parameters are presented in sequence, within the context of the overall study aimed at producing PEO coatings containing CC and HA.

#### **4.1.1. Phosphate electrolyte concentration, effect of pH and conductivity**

Three parameters of the PEO bath—concentration, pH, and conductivity—were evaluated simultaneously in a comprehensive study using phosphate salts such as mono-, di-, and tribasic sodium phosphate, all three of which are widely used in PEO processes [19]. Depending on concentration, solutions of these salts exhibit pH values of approximately ~4.5–5.5, ~8.0–9.5, and ~11.5–12.5, respectively. Given that these ranges do not overlap, solutions of these salts can be used for an objective comparison of the pH effect at three distinct points corresponding to weakly acidic, weakly alkaline, and moderately alkaline pH levels. The use of more acidic solutions, for example phosphoric acid, is impractical, as it would lead to complete dissolution of CC and HA particles. In the case of monobasic phosphate salt, such a risk also exists, although to a lesser extent, and only partial dissolution of CC and HA is more likely to occur [110]. Conductivity and concentration in this series of experiments were evaluated in conjunction, as the two parameters exhibit an almost linear relationship (Figure 4). For this purpose, three series of solutions with different concentrations, corresponding to specific conductivity ranges, were prepared. In this case, the range selected was approximately ~2 to 8 mS·cm<sup>-1</sup>, based on observations during the PEO process (Figure 5). The final concentration ranges were thus determined empirically, based on actual changes in conductivity. The measurement results are shown in a single plot in Figure 4. It can be seen that tribasic sodium phosphate exhibits the highest specific conductivity, as indicated by the steepest slope of the curve. Consequently, a lower concentration of this compound is required to achieve the same level of conductivity compared to di- and, especially, monobasic phosphate salts. For example, to obtain a conductivity of ~6 mS·cm<sup>-1</sup>, only a 0.02 M solution of Na<sub>3</sub>PO<sub>4</sub> is required, whereas for NaH<sub>2</sub>PO<sub>4</sub>, a 0.12 M solution must be used. This difference can be explained by the larger number of ions in Na<sub>3</sub>PO<sub>4</sub> (four in total), the higher charge of the phosphate ion (-3), and its complete dissociation, in contrast to other salts involved in acid–base equilibria.

After preparing a series of coatings in these solutions and analyzing the changes in surface morphology as a function of concentration, a clear trend was observed in all cases: an increase in pore size, as well as a tendency toward the formation of more rounded pores with thickened pore walls at higher concentrations. This may indicate higher sparking temperatures and more intense melting and resolidification processes. For coatings prepared in mono- and dibasic solutions, differences in morphology were practically negligible, whereas in the case of

the tribasic salt, an additional feature in the form of elongated, non-uniform pores was observed. This may be related to the increased proportion of sodium in the tribasic electrolyte, which could have modified the discharge formation process (enhancing their temperature) [237].

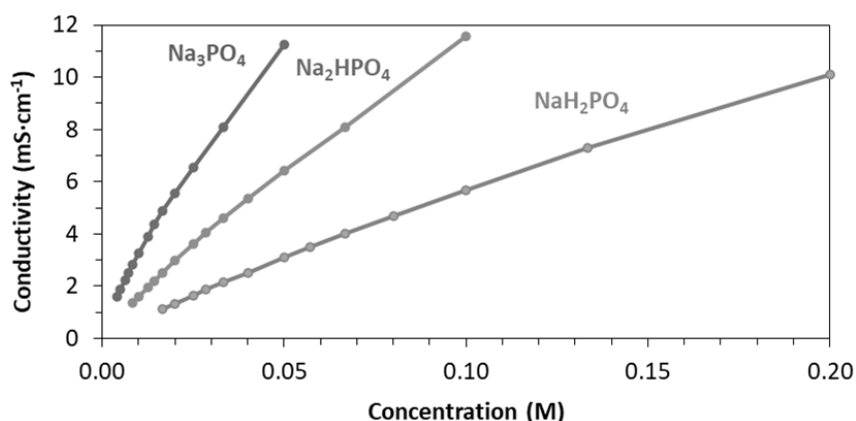


**Figure 4.** Dependence of electrical conductivity on concentration — comparison of solutions of three different electrolytes.

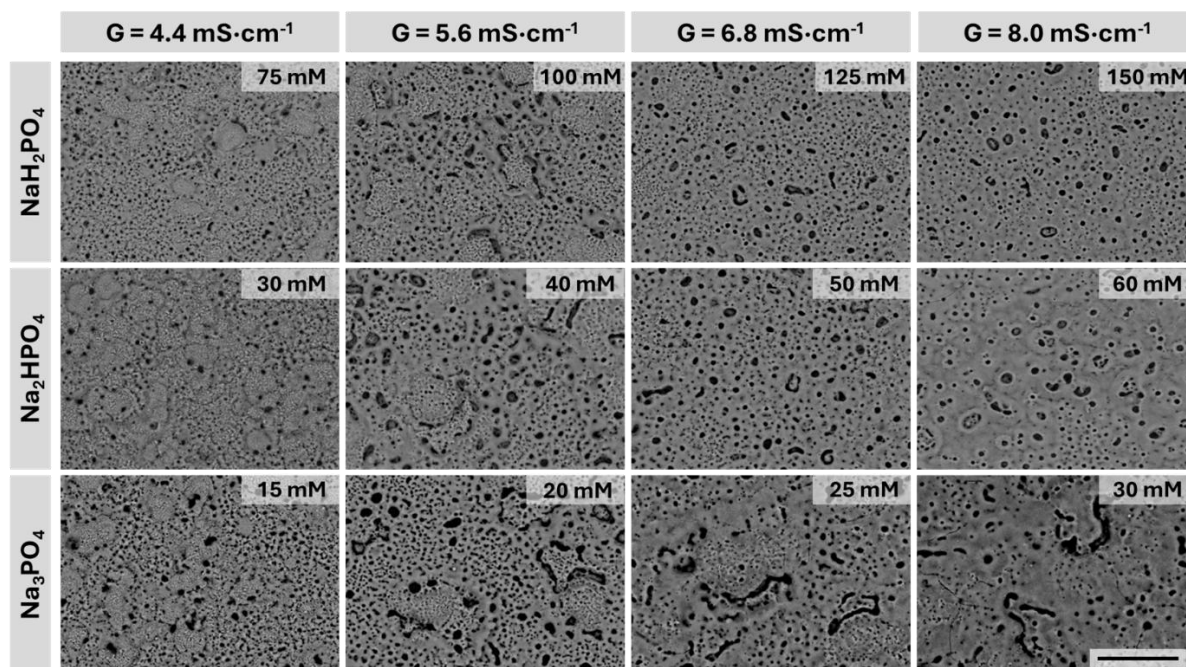


**Figure 5.** SEM images of PEO coating surfaces produced in equi-conductive mono-, di-, and tribasic phosphate electrolytes, with the corresponding concentrations indicated (scale bar: 30  $\mu\text{m}$ ).

For comparative analysis, three electrolytes with a constant conductivity of approximately  $5.6 \pm 0.1 \text{ mS}\cdot\text{cm}^{-1}$  were prepared for mono-, di-, and tribasic sodium phosphate salts, corresponding to concentrations of 100, 40, and 20 mM, respectively. PEO coatings were produced in these electrolytes and used for surface-area EDX analysis. As shown in Table 2, the Na content was highest for the coating produced in the tribasic electrolyte, with a clear tendency to decrease toward the monobasic solution. Although this trend was contrary to the actual concentration of  $\text{Na}^+$  ions in solution, it is likely that the extent of  $\text{Na}^+$  incorporation was determined by the relative ratio of ions in the bath, which was highest in the tribasic electrolyte. Phosphorus content, on the other hand, showed greater consistency among the three electrolytes, although a slight decrease was still observed toward the basic, less concentrated solutions. Accordingly, an inverse tendency was noted for Ti, which may be mutually linked to the phosphorus dynamics. It is likely that minor variations in the Ti fraction indirectly indicate differences in the thickness of the PEO layer, with thinner layers exhibiting higher Ti content. The oxygen fraction, in turn, remained within a constant range of 76–77%.

**Table 2.** Comparison of the elemental composition of PEO coatings produced in equi-conductive solutions of mono-, di-, and tribasic sodium phosphate.

Electrolyte bath	pH	G, mS·cm <sup>-1</sup>	Na <sup>+</sup> , mM	P (%)	Ti (%)	Na (%)	O (%)
100 mM NaH <sub>2</sub> PO <sub>4</sub>	4.72	5.57	100	6.67 ± 0.10	16.2 ± 0.3	0.08 ± 0.02	77.0 ± 0.8
40 mM Na <sub>2</sub> HPO <sub>4</sub>	9.23	5.63	80	6.31 ± 0.12	16.9 ± 0.3	0.19 ± 0.04	76.6 ± 0.6
20 mM Na <sub>3</sub> PO <sub>4</sub>	12.32	5.65	60	5.21 ± 0.09	18.2 ± 0.4	0.26 ± 0.04	76.4 ± 0.9

In summary, in all electrolytes the PEO layer was successfully formed, exhibiting distinct surface features—namely, alternating micro- and submicroporosity of varying sizes. Surface morphology and elemental composition of the coatings, when compared across electrolytes, were generally similar over the entire concentration range. Nevertheless, among the three, the tribasic phosphate electrolyte resulted in slightly more specific characteristics; however, these did not lead to dramatic changes that could significantly affect the properties of the produced surfaces, including their functional performance, and are expected to have only a minor impact on the subsequent fabrication of CC–HA coatings.

From a practical standpoint, however, the choice between mono-, di-, and tribasic electrolytes is important, and among the three, the dibasic form appears to be the optimal option. This is due to its ability to ensure the chemical stability of CC and HA phases, as well as the fact that it is not excessively alkaline, which would otherwise require thorough rinsing prior to use in *in vivo* tests. Considering the absence of dramatic changes during coating fabrication (Figure 5), the preference for the dibasic electrolyte can be justified. The final selection of Na<sub>2</sub>HPO<sub>4</sub> concentration is discussed later in Section 4.3.1, from the perspective of achieving the optimal particle size.

#### 4.1.2. Carbonate electrolyte concentration

The literature provides considerable evidence for the inability to incorporate a carbonate phase into PEO coatings produced on relatively inert materials such as Ti and its alloys from carbonate salt solutions, such as Na<sub>2</sub>CO<sub>3</sub> [19]. However, no information is available regarding the effect of carbonate electrolyte concentration on the morphology and elemental composition of the coatings, as well as the impact of altering the carbonate-to-other-soluble-component ratio in the bath. Given the strict focus of this study on carbonates, and considering that carbonate ions can be released into solution as a byproduct of CC interaction with phosphates (Section 1.4.3), a comparative evaluation of their influence will be highly valuable. Therefore, two series of equi-conductive baths ( $5.6 \pm 0.1$  mS·cm<sup>-1</sup>) were prepared based on Na<sub>2</sub>HPO<sub>4</sub> electrolyte with the addition of varying amounts of NaHCO<sub>3</sub> and Na<sub>2</sub>CO<sub>3</sub> in such a way that the carbonate and phosphate contents were mutually varied from 0 to 100%. This approach eliminates conductivity as a contributing factor to the final structure and elemental composition of the coating, by preventing it from influencing discharge intensity. The data for the prepared solutions are presented in Table 3.

The baths were numbered according to increasing carbonate content, where 1 corresponds to the lowest fraction at 12.5%, and 9 to the highest at 100%, when phosphate was absent. The letter designation indicates the carbonate source, with HC referring to sodium bicarbonate (NaHCO<sub>3</sub>) and C to sodium carbonate (Na<sub>2</sub>CO<sub>3</sub>). For comparison, data are also presented for a phosphate bath without carbonate additives, prepared analogously to that described in Section 4.1.1, which served as the reference system. Using the example of bath HC-1, the indicated carbonate percentage means that NaHCO<sub>3</sub> was added in an amount providing 12.5% carbonate ions relative to the total molar amount of carbonate and phosphate ions in the bath. Due to the adjustment of bath conductivity to approximately the same level within 1–2% and the relatively low specific conductivity of NaHCO<sub>3</sub> solutions compared with Na<sub>2</sub>HPO<sub>4</sub> and Na<sub>2</sub>CO<sub>3</sub>, the HC baths required a higher total salt content. This is most evident when comparing baths HC-4 and C-4, where, to compensate for conductivity, the phosphate concentration in the former was 30% higher. In addition, pH variations were observed as a result

of carbonate additive incorporation, owing to their differing  $pK_a$  values, which led to increased acidity at higher carbonate contents when  $\text{NaHCO}_3$  was used, and increased alkalinity when  $\text{Na}_2\text{CO}_3$  was added. As established earlier (Section 4.1.1), even a pH change of 3–4 units does not lead to significant changes in the coatings; therefore, differences of less than 1 unit (Table 3) can be regarded as negligible, not requiring additional compensatory measures (e.g.,  $\text{NaOH}$  addition to raise pH).

**Table 3.** Composition and pH of equi-conductive electrolyte baths with varying phosphate and carbonate ion content, prepared using  $\text{Na}_2\text{HPO}_4$ ,  $\text{NaHCO}_3$ , and  $\text{Na}_2\text{CO}_3$ .

Nr.	Carbonate source	$\text{PO}_4^{3-}$ , %	$\text{CO}_3^{2-}$ , %	$\text{PO}_4^{3-}$ , mM	$\text{CO}_3^{2-}$ , mM	pH	G, $\text{mS}\cdot\text{cm}^{-1}$
0	-	100	0	46.0	0	9.23	5.65
HC-1	$\text{NaHCO}_3$	87.5	12.5	42.4	6.4	9.16	5.71
HC-2		75.0	25.0	39.5	12.7	9.02	5.62
HC-3		62.5	37.5	35.2	20.9	8.89	5.67
HC-4		50.0	50.0	30.2	30.6	8.74	5.58
HC-5		37.5	62.5	24.7	41.1	8.68	5.70
HC-6		25.0	75.0	17.6	53.0	8.62	5.67
HC-7		12.5	87.5	9.5	65.1	8.57	5.61
HC-8		6.4	93.6	5.0	72.9	8.54	5.62
HC-9		0	100	0	78.4	8.51	5.59
C-1	$\text{Na}_2\text{CO}_3$	87.5	12.5	40.2	5.73	10.50	5.64
C-2		75.0	25.0	34.6	11.5	10.74	5.68
C-3		62.5	37.5	28.8	17.2	10.90	5.72
C-4		50.0	50.0	22.9	22.9	11.02	5.63
C-5		37.5	62.5	17.0	28.4	11.12	5.59
C-6		25.0	75.0	11.3	33.9	11.23	5.57
C-7		12.5	87.5	5.8	39.4	11.30	5.60
C-8		6.4	93.6	2.8	41.6	11.34	5.67
C-9		0	100	0	44.9	11.37	5.66

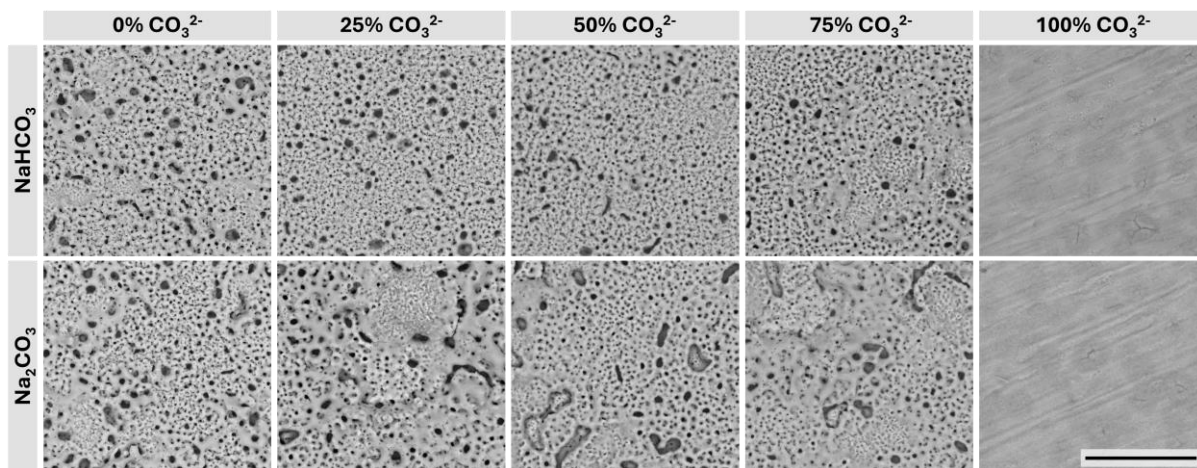


**Figure 6.** Surface morphology of coatings produced in  $\text{Na}_2\text{HPO}_4$  baths with varying carbonate ion content introduced via  $\text{NaHCO}_3$  and  $\text{Na}_2\text{CO}_3$  salts (scale bar: 30  $\mu\text{m}$ ).

Examining the surface morphology of the produced coatings (Figure 6) allows the conclusion that carbonate ions, under the given equi-conductive conditions, have a visually noticeable but not decisive effect on the PEO process. This holds true for both carbonate sources up to at least 75% of the total anion content. The general visual effect of increasing carbonate content in the bath can be interpreted as a slight decrease in pore size. With  $\text{NaHCO}_3$  addition, pore shape remained largely comparable even at high carbonate contents, whereas  $\text{Na}_2\text{CO}_3$  promoted the formation of non-uniform, elongated pores—an effect similar to that observed in  $\text{Na}_3\text{PO}_4$  baths (Section 4.1.1)—which may be attributed to higher pH levels. A distinctly different surface morphology was observed in the complete absence of phosphates: as seen, a

porous structure did not form in either case, with traces of sandpaper polishing on the anode surface still visible. These observations indicate that the transition from anodizing to the PEO process did not occur, and sparking was not initiated [323]. Considering the possible causes of this phenomenon, it is likely that carbonate ions may act as microarc energy absorbers, including through  $\text{CO}_3^{2-} \rightarrow \text{CO}_2$  decomposition upon heating in the discharge zone. Gas release within microdischarges could alter the local plasma phase, reduce channel temperature, and consequently “quench” sparks at an early stage of their formation [137].

**Table 4.** Results of surface region EDX analysis of coatings prepared in equi-conductive electrolyte baths containing different proportions of dibasic sodium phosphate and carbonate salts; each bath is numbered in accordance with Table 2.

Nr.	P (%)	C (%)	Ti (%)	Na (%)	O (%)
0	6.0	4.9	16.6	0.2	72.4
HC-1	5.9	4.4	16.9	0.2	72.6
HC-2	5.8	5.0	17.3	0.1	71.9
HC-3	5.7	4.5	17.7	0.2	72.1
HC-4	5.3	4.5	18.1	0.1	71.9
HC-5	5.0	4.6	18.7	0.1	71.6
HC-6	4.2	4.0	19.5	0.1	72.2
HC-7	3.1	4.0	20.9	0.0	72.0
HC-8	1.8	4.2	21.9	0.1	72.1
HC-9	0.2	3.3	23.6	0.0	72.9
C-1	5.8	4.3	16.8	0.2	72.9
C-2	5.7	4.8	16.9	0.2	72.4
C-3	5.5	4.7	17.2	0.2	72.5
C-4	5.1	4.1	17.9	0.2	72.8
C-5	4.5	4.3	18.5	0.1	72.6
C-6	3.6	4.3	19.8	0.1	72.3
C-7	2.4	4.3	21.3	0.0	71.9
C-8	1.5	4.1	22.5	0.0	71.9
C-9	0.2	3.8	23.8	0.0	72.3

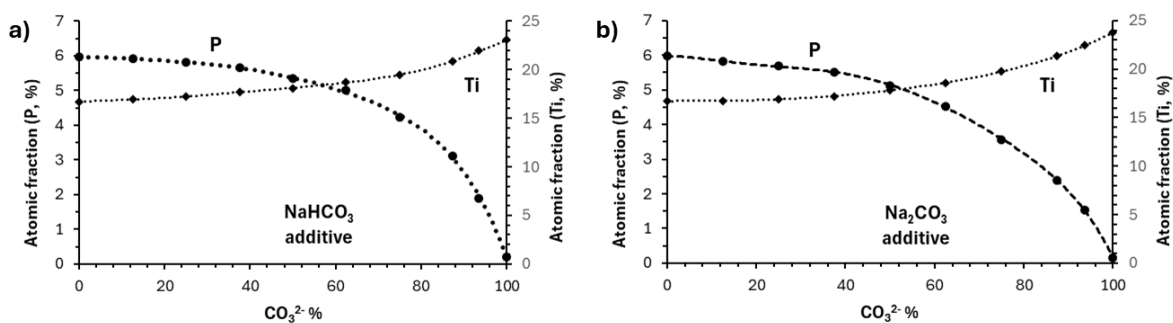
The results of elemental analysis confirm the successful formation of the PEO layer and the incorporation of phosphorus up to relatively high carbonate contents in the bath, corresponding to HC-8 and C-8 in Examining the surface morphology of the produced coatings (Figure 6) allows the conclusion that carbonate ions, under the given equi-conductive conditions, have a visually noticeable but not decisive effect on the PEO process. This holds true for both carbonate sources up to at least 75% of the total anion content. The general visual effect of increasing carbonate content in the bath can be interpreted as a slight decrease in pore size. With  $\text{NaHCO}_3$  addition, pore shape remained largely comparable even at high carbonate contents, whereas  $\text{Na}_2\text{CO}_3$  promoted the formation of non-uniform, elongated pores—an effect similar to that observed in  $\text{Na}_3\text{PO}_4$  baths (Section 4.1.1)—which may be attributed to higher pH levels. A distinctly different surface morphology was observed in the complete absence of phosphates: as seen, a porous structure did not form in either case, with traces of sandpaper polishing on the anode surface still visible. These observations indicate that the transition from anodizing to the PEO process did not occur, and sparking was not initiated [323]. Considering the possible causes of this phenomenon, it is likely that carbonate ions may act as microarc energy absorbers, including through  $\text{CO}_3^{2-} \rightarrow \text{CO}_2$  decomposition upon heating in the discharge zone. Gas release within microdischarges could alter the local plasma phase, reduce channel temperature, and consequently “quench” sparks at an early stage of their formation [137].

Table 4. Nevertheless, it should be noted that the atomic fraction of phosphorus, while remaining approximately constant within the range of 0–50%  $\text{CO}_3^{2-}$ , exhibited a slow downward trend, which became progressively more pronounced beyond this point. Titanium content, in contrast, demonstrated the opposite trend. The remaining elements showed no clear



tendencies, unlike P and Ti (Examining the surface morphology of the produced coatings (Figure 6) allows the conclusion that carbonate ions, under the given equi-conductive conditions, have a visually noticeable but not decisive effect on the PEO process. This holds true for both carbonate sources up to at least 75% of the total anion content. The general visual effect of increasing carbonate content in the bath can be interpreted as a slight decrease in pore size. With  $\text{NaHCO}_3$  addition, pore shape remained largely comparable even at high carbonate contents, whereas  $\text{Na}_2\text{CO}_3$  promoted the formation of non-uniform, elongated pores—an effect similar to that observed in  $\text{Na}_3\text{PO}_4$  baths (Section 4.1.1)—which may be attributed to higher pH levels. A distinctly different surface morphology was observed in the complete absence of phosphates: as seen, a porous structure did not form in either case, with traces of sandpaper polishing on the anode surface still visible. These observations indicate that the transition from anodizing to the PEO process did not occur, and sparking was not initiated [323]. Considering the possible causes of this phenomenon, it is likely that carbonate ions may act as microarc energy absorbers, including through  $\text{CO}_3^{2-} \rightarrow \text{CO}_2$  decomposition upon heating in the discharge zone. Gas release within microdischarges could alter the local plasma phase, reduce channel temperature, and consequently “quench” sparks at an early stage of their formation [137].

Table 4, Figure 7). These findings may also indicate that carbonates “quench” the plasma, leading to the formation of less porous and thinner PEO layers. It is worth noting that at identical carbonate percentages in the bath, the mass fraction of P was slightly lower for baths containing  $\text{Na}_2\text{CO}_3$ , with this effect being systematic and most pronounced at  $\text{CO}_3^{2-}$  contents of 50% and above. This observation is consistent with the lower overall phosphate concentrations in these baths compared to those containing  $\text{NaHCO}_3$  (Table 3), thereby reducing the likelihood of their incorporation simply due to lower abundance. Overall, it can be concluded that the presence of carbonates in the bath—whether intentionally added or released as a result of CC particle interaction with phosphates (Section 1.4.3)—is not a factor that significantly affects or limits the occurrence of the PEO process in phosphate electrolytes, as long as they are not present in overwhelming amounts. However, they can still leave specific signatures, particularly in the presence of particles. In this regard, it is necessary to fine-tune the interaction of CC with the PEO bath, in particular by selecting the molar ratio of components (Section 4.3.1) and, if necessary, adjusting the electrical parameters, e.g., by increasing the voltage to maintain discharge intensity at the same level.



**Figure 7.** Dynamics of changes in the atomic fractions of P and Ti in PEO coatings produced in  $\text{Na}_2\text{HPO}_4$  baths containing different amounts of carbonates introduced via two salts

For the coatings produced in two baths—HC-4 and C-4—containing equimolar amounts of carbonates and phosphates, XRD analysis was additionally performed to reveal possible differences in their phase composition. The absence of phases other than  $\text{TiO}_2$  in the coatings confirms the widely reported trend in the literature regarding the low potential of soluble carbonate salts to be incorporated into PEO coatings on relatively inert metals such as Ti, including leaving no detectable changes in XRD patterns (Figure 8). In addition, no effect was observed from changing the carbonate source, which was also accompanied by pH modification (Table 3). Furthermore, increasing the carbonate concentration in the bath had only a very weak

effect on the elemental composition of the coatings, as previously demonstrated by the EDX analysis (Examining the surface morphology of the produced coatings (Figure 6) allows the conclusion that carbonate ions, under the given equi-conductive conditions, have a visually noticeable but not decisive effect on the PEO process. This holds true for both carbonate sources up to at least 75% of the total anion content. The general visual effect of increasing carbonate content in the bath can be interpreted as a slight decrease in pore size. With  $\text{NaHCO}_3$  addition, pore shape remained largely comparable even at high carbonate contents, whereas  $\text{Na}_2\text{CO}_3$  promoted the formation of non-uniform, elongated pores—an effect similar to that observed in  $\text{Na}_3\text{PO}_4$  baths (Section 4.1.1)—which may be attributed to higher pH levels. A distinctly different surface morphology was observed in the complete absence of phosphates: as seen, a porous structure did not form in either case, with traces of sandpaper polishing on the anode surface still visible. These observations indicate that the transition from anodizing to the PEO process did not occur, and sparking was not initiated [323]. Considering the possible causes of this phenomenon, it is likely that carbonate ions may act as microarc energy absorbers, including through  $\text{CO}_3^{2-} \rightarrow \text{CO}_2$  decomposition upon heating in the discharge zone. Gas release within microdischarges could alter the local plasma phase, reduce channel temperature, and consequently “quench” sparks at an early stage of their formation [137]. Table 4).

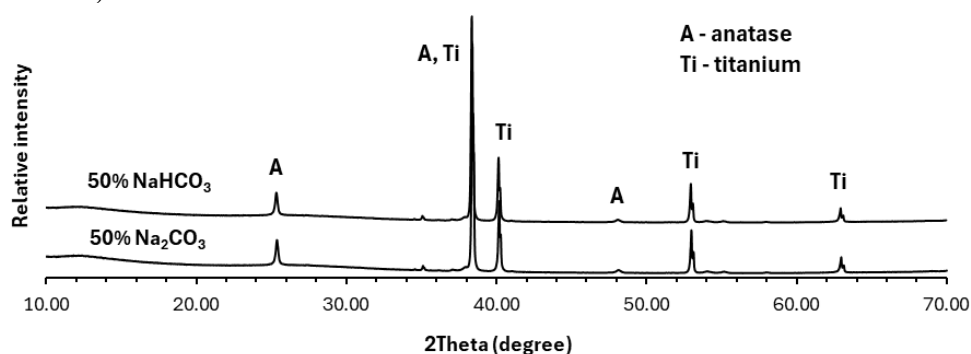


**Figure 8.** XRD patterns of PEO coatings prepared in baths with  $\text{NaHCO}_3$  and  $\text{Na}_2\text{CO}_3$  additions to achieve equimolar phosphate and carbonate amounts.

#### 4.1.3. The use of commercial particles and particle size issue

The PEO process imposes specific requirements on the properties of incorporated particles, with particle size being a key factor determining their successful integration into the coating and in sufficient quantities. CC particles are no exception, which raises the question of whether commercially available or laboratory-synthesized particles are more suitable for meeting these requirements. The use of commercially sourced particles is more frequently reported in PEO-related literature. This trend can be logically explained by the significant time investment associated with particle synthesis, the need for precise size control under laboratory conditions, and, in many cases, the lack of appropriate equipment or sufficient researcher expertise. Conversely, in-house particle synthesis may be preferable under certain circumstances, such as when commercial particles are prohibitively expensive, difficult to obtain (particularly in the case of rare compounds or bi-/multiphase particles), contain unacceptable impurities, exhibit insufficient purity, or are unavailable in the desired size or morphology.

In Section 1.4 of the literature review, it was established that the use of particles larger than approximately 2–3  $\mu\text{m}$  is generally ineffective due to spatial and other constraints. In the case of CC, an additional limitation arises at the lower end of the size range: particles as small as  $\sim 500$  nm may also be undesirable (Section 1.4) because of their relatively low thermal stability. The availability of commercial particles within the critical size range of  $\sim 500$  nm to 2–3  $\mu\text{m}$  is limited. In this interval, HA particles dominate the market (e.g., Fluodinova SA, Portugal), whereas CC particles offered by leading trusted suppliers, such as Sigma-Aldrich

(USA), are typically available only in much larger sizes, often several tens of micrometers. Moreover, CC particles within the desired size range are frequently surface-modified to impart hydrophobic properties (e.g., CACO3-108, Getnano, France), which is disadvantageous for their use in aqueous PEO electrolytes. In contrast, HA particles are designed specifically for biomedical research (Fluodinova SA, Portugal) and are well-suited for PEO applications due to their spherical morphology, which facilitates wetting and stable suspension in the electrolyte. However, CC particles with diameters of  $\sim 50\ \mu\text{m}$  or greater far exceed the upper size limit for effective incorporation, eliminating the possibility of their integration into the coating. These factors collectively highlight the necessity of exploring tailored synthesis strategies for producing CC particles with appropriate properties for use in the PEO process.

Nevertheless, a control experiment was necessary to verify the validity of this assumption and to determine whether any indirect influence of the particles on the surface properties could be observed — namely, whether there was any measurable particle participation in the process. The fundamental surface characteristics selected for evaluation included morphology and calcium atomic fraction (analyzed via SEM/EDX), surface roughness (contact profilometry), and wettability (water contact angle). The experimental parameters were as follows: a base electrolyte of 50 mM  $\text{Na}_2\text{HPO}_4$ , a limiting voltage of 450 V, a particle concentration of  $100\ \text{g}\cdot\text{L}^{-1}$ , and commercially pure titanium as the substrate. CC microparticles (Sigma-Aldrich, USA) were added in small portions and dispersed using prolonged ultrasonication for 24 hours. This approach was intended not only to minimize particle agglomeration but also to potentially accelerate the dissolution of CC followed by its recrystallization into smaller particles [324]. For comparison, a reference bath without particle addition was prepared under identical conditions. As supporting evidence, coatings were also fabricated using commercial HA microparticles (Fluodinova SA, Portugal) under the same processing parameters, except for a lower particle concentration of  $20\ \text{g}\cdot\text{L}^{-1}$ . The results of these experiments are presented in Figure 9.

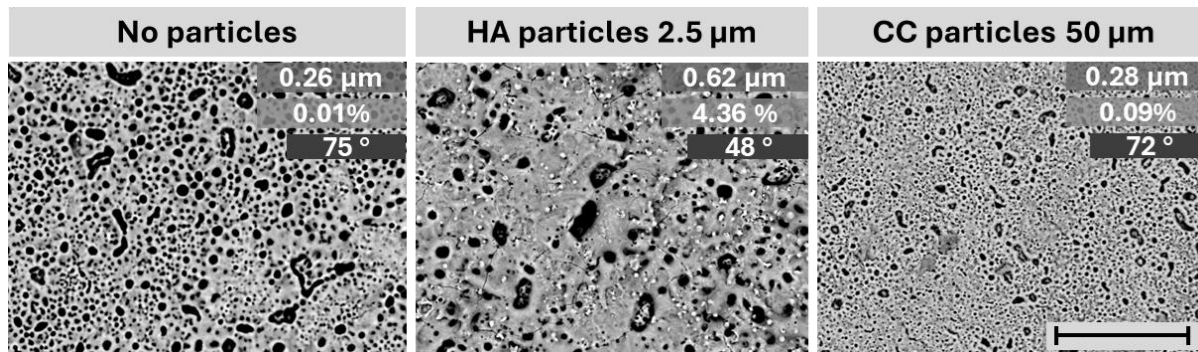


**Figure 9.** The effect of commercial particles on the surface morphology, average roughness ( $R_a$ ,  $\mu\text{m}$ ), wettability (contact angle,  $^\circ$ ), and calcium atomic fraction (%) of PEO coatings prepared in  $\text{Na}_2\text{HPO}_4$ -based electrolytes. From left to right: coating without particles, coating with HA particle addition, and coating with CC particle addition (scale bar: 50  $\mu\text{m}$ ).

Based on the results shown in Figure 9, a PEO layer was successfully formed in all three baths. However, as expected, HA particles exhibited a much more pronounced effect on the modification of the coating properties. The most critical parameter in this context is the calcium content, which directly indicates particle incorporation. For the HA-containing coating, the Ca atomic fraction reached 4.36%, clearly demonstrating a substantial contribution of HA particles to the coating growth. The second most significant indicator of particle incorporation is the appearance of particulate inclusions on the coating surface. However, this parameter is not always fully reliable. Under certain PEO processing conditions involving more intense discharges, the particles may partially melt and lose their original morphology during incorporation. This phenomenon was partially observed in subsequent experiments (Section 4.2, Figure 11), where the incorporated particles were less distinguishable from the surrounding

matrix. In parallel, changes in roughness and wettability provided additional indirect confirmation of particle involvement. The mechanisms underlying the influence of particles on these properties are discussed in detail in Section 4.2.3, in the context of evaluating the effect of CaP particle crystallinity on PEO coating characteristics.

In contrast, for CC-containing electrolytes, all analyzed properties of the PEO layer remained virtually unchanged. Only minor variations were observed in contact angle and surface roughness, while the Ca atomic fraction of 0.09% likely reflects limited CC dissolution followed by the incorporation of a small amount of calcium ions rather than intact CC particles. This value is insufficient even from the perspective of total calcium incorporation, let alone when considering calcium specifically in the form of CC or HA. Furthermore, surface morphology analysis did not reveal any visible CC particles within the coating. A slight reduction in overall porosity was observed compared to the particle-free reference sample. This effect is most likely attributable to a modest decrease in electrolyte conductivity caused by the relatively high CC concentration ( $100 \text{ g}\cdot\text{L}^{-1}$ ), where the particles acted as physical barriers to electrical current flow. Overall, these findings indicate that direct utilization of commercial CC particles with a typical size of  $\sim 50 \text{ }\mu\text{m}$  is ineffective, even when subjected to prolonged ultrasonication aimed at dispersion and partial size reduction, as well as purposeful selection of a higher particle concentration of  $100 \text{ g}\cdot\text{L}^{-1}$ . Consequently, tailored synthesis of CC particles undoubtedly emerges as a more promising strategy to obtain particles with properties suitable for PEO applications.

## 4.2. Part II – Particle crystallinity effect

As an introduction to Section 4.2, it is important to refer back to the literature review (Section 1.3.5) and reiterate earlier conclusions regarding the current understanding of the interrelationship between particle characteristics and PEO coating properties. To date, important initial steps have been taken to elucidate these interconnections. Among the most extensively studied particle parameters are chemical stability, melting point, and size [19], [30], [31], [213]; however, particular attention has recently been devoted to the latter. For example, it has been demonstrated that both micro- and nanosized particles can be readily incorporated into PEO coatings, albeit through different mechanisms depending on particle size [31], [213]. This difference has been shown to exert a pronounced influence on coating properties such as surface morphology, pore size, vertical distribution of the introduced elements, wettability, and bioactivity. Based on the available experimental evidence, it is advisable to select a particle size large enough to minimize rapid melting and extensive phase transformations of the incorporated compound, yet small enough to remain comparable to the pore (discharge) dimensions [19], [30].

It is evident that the range of particle characteristics influencing PEO coating properties extends far beyond the parameters discussed above, indicating the necessity for further systematic investigations to elucidate the role of each relevant factor, both independently and in combination. In the context of CaP particles, a comprehensive understanding of these interdependencies is particularly important for optimizing PEO-modified metallic implants. One critical parameter, largely unexplored in previous research yet highly relevant to implantology, is crystallinity. For bioactive coatings, crystallinity plays a decisive role in controlling both degradation kinetics and the rate of osteointegration, thereby directly affecting the functional performance of bone implants within the physiological environment [325], [326]. Evidence suggests the existence of an optimal crystallinity level, adherence to which yields the most favorable outcomes in implant fabrication [327]. Within specific artificial biological matrices, crystallinity can be readily tuned by adjusting the ratio of HA to amorphous TCP—two abundant and extensively studied bioactive compounds [328] that represent opposite extremes of structural order. More broadly, the concept of crystallinity holds significant

relevance for the development of coatings across a variety of applications, extending well beyond the biomedical field [329].

Given that the influence of particle addition on the progression of PEO processes in suspensions is often ambiguous and difficult to predict—and that, as demonstrated in previous studies, variations in particle type can cause substantial changes in the resulting oxide coatings[31], [32], [133], [213]—it is reasonable to hypothesize that crystallinity is no exception. In this context, the lower mass density and less well-defined morphology of amorphous particles may account for possible differences in their behavior. Furthermore, assumptions regarding the tendency of amorphous particles to undergo crystallization during PEO, and the consequent changes in coating properties arising from such transformations, can lead to contradictory interpretations. For these reasons, the preliminary experiments—including those described in Section 4.1—initially also incorporated an assessment of the effect of particle crystallinity on PEO coating characteristics. However, due to the multifaceted nature of this comparison and the large number of ambiguous findings, the investigation of this parameter was designated as a separate part of the study (Part II).

The primary aim of the present study was to describe, compare, and interpret changes in the physicochemical properties of oxide coatings induced by the incorporation of crystalline and amorphous CaP particles into the PEO electrolyte, to elucidate their interrelation with the bioactivity of the resulting coatings, and to assess the applicability of these findings with particular emphasis on implantology. In the experimental work, both commercially pure titanium and the titanium–aluminum–vanadium alloy (Ti6Al4V, TAV) were selected as substrates for coating deposition. In addition to their widespread use in biomedical applications, the key motivation for employing both materials was to evaluate the repeatability and reproducibility of the results—namely, the coating properties—when PEO processing is applied to substrates with differing elemental compositions.

As crystalline particles, a previously tested commercial spray-dried HA powder with an average particle size of 2.5  $\mu\text{m}$  was selected, as it had already demonstrated the ability to incorporate into the PEO layer and to modify its morphology. It should be noted, however, that the actual mean size of these commercial HA particles was an order of magnitude smaller—approximately 400 nm—as determined by SEM analysis (Section 4.2.1). Amorphous particles were synthesized separately in order to eliminate the influence of particle size by matching it as closely as possible to that of the crystalline HA. For this purpose, the classical wet precipitation method was employed, as unlike the neutralization reaction route [330], it favors the formation of more compact structures, somewhat resembling spray-dried spheres (Figure 10), though generally larger in size. This size increase can be attributed, in part, to filtration effects during the removal of ionic by-products of the exchange reaction, making subsequent thorough ultrasonic treatment necessary.

The investigation of particle crystallinity was carried out in parallel with the experiments described in Section 4.1, prior to the final determination of the optimal process parameters, such as PEO voltage and bath pH. Consequently, the conditions applied here do not correspond exactly to those ultimately selected for the fabrication of CC–HA coatings (Section 4.3). On the other hand, the present study focuses on particles as a general concept, and the use of carbonate particles with varying degrees of crystallinity could be regarded solely as a specific case—one that coincidentally aligns with the broader aim of this research part. In other words, employing carbonate particles was not a prerequisite for this experiment, and the coating preparation parameters were not required to be perfectly tailored to carbonate-based baths. It should be emphasized, however, that the choice of CaP–based particles was largely dictated by their more accessible, straightforward, and easily adjustable synthesis procedure [331] compared with other biominerals, including CC.

For clarity of presentation, in the current Section 4.2 the crystalline and amorphous particles are designated with the prefixes c- and a-, respectively. These prefixes also apply to

the corresponding baths and coatings produced. The blank bath and its resulting coatings are denoted by the prefix b-.

#### 4.2.1. Suspension characterization

Prior to initiating the experimental coating fabrication, the solid particles employed in the c-HAP and a-TCP electrolytes underwent thorough characterization using multiple analytical techniques. This evaluation highlighted both similarities and distinctions in their fundamental properties, which could potentially influence the PEO process. Nevertheless, this comparison alone was insufficient to guarantee complete objectivity in the investigation. Even when particles exhibit nearly identical chemical characteristics and solubility, they may still impact the electrolyte properties differently after suspension preparation, subsequently altering the PEO kinetics and mechanism, and ultimately modifying the coating features. To account for this, additional key parameters of the reaction medium—electrical conductivity, calcium ion concentration, and pH—were also measured [332], [333]. A summary of the particle characterization is provided in Figure 10. SEM imaging revealed clear distinctions in particle shape and surface morphology: crystalline HAP particles exhibited a well-defined, rounded geometry with smooth surfaces, whereas amorphous TCP particles displayed a less uniform, though approximately spherical, form. Additionally, the amorphous particles possessed a more developed surface area, reduced mass density, and a pronounced tendency to aggregate into complex structures, making it challenging to visually distinguish individual particle boundaries. These features are typical for amorphous particles synthesized via wet precipitation methods, as similarly reported in previous studies [334], [335], [336].

The particle size distribution curves represent the frequency of particles as a function of their diametral cross-sectional area in a two-dimensional space. Given the wide range of values observed for both crystalline and amorphous particles ( $0.05\text{--}10\ \mu\text{m}^2$ ), the x-axis is displayed on a logarithmic scale for improved visualization. Both distributions exhibited a single dominant peak corresponding to the most prevalent particle size ( $0.46\ \mu\text{m}^2$  for crystalline HAP and  $0.42\ \mu\text{m}^2$  for amorphous TCP), indicated by dotted lines and labeled as the median (M). Similarly, the mean cross-sectional areas ( $\bar{A}$ )—represented by dashed lines—were also closely aligned between the two types of particles ( $0.77\ \mu\text{m}^2$  for HAP and  $0.71\ \mu\text{m}^2$  for TCP). The primary distinction was in the full width at half maximum (FWHM) of the peaks, which was narrower for the amorphous sample ( $0.53\ \mu\text{m}^2$ ), suggesting a slightly more uniform particle size distribution. However, this difference is unlikely to significantly impact the PEO process, as both electrolytes contained a substantial proportion of particles spanning a similar size range. Consequently, particle size can be regarded as comparable, enabling a fair comparison of the PEO coatings produced in the respective electrolytes.

The negligible difference in particle sizes effectively minimized potential variations in factors such as melting behavior under the short-lived sparks generated during PEO (with localized temperatures reaching up to  $10,000\ \text{K}$ ) [337], particle penetration into the porous oxide layer [31], and the subsequent incorporation mechanism [338]. The mean particle size was comparable to the pore dimensions typically formed on Ti substrates under similar electrical conditions [339], [340], thereby increasing the likelihood of particle incorporation and producing noticeable modifications in the surface morphology of the resulting oxide coatings. Consistent with the observations of Lu et al. [30], who reported that particles ranging from  $0.1$  to  $10\ \mu\text{m}$  are most commonly introduced into electrolytes, recalculations based on the diametral cross-sectional areas of the approximately spherical particles revealed that  $\sim 95\%$  of both crystalline HAP and amorphous TCP particles in this study had diameters within the  $0.35\text{--}2.50\ \mu\text{m}$  range.

FTIR spectra of both particle powders exhibited all characteristic signals of an apatitic structure [341], notably the strong absorption bands around  $550\ \text{cm}^{-1}$  and  $1030\ \text{cm}^{-1}$ , corresponding to the  $\nu_4$  and  $\nu_3$  vibrational modes of the phosphate ion. Additional weaker signals detected in the  $860\text{--}880\ \text{cm}^{-1}$  and  $1350\text{--}1650\ \text{cm}^{-1}$  regions suggested the presence of

carbonates within the molecular structure of both CaPs. While the spectral peak positions were identical for the two samples, the amorphous TCP spectrum showed two major distinctions: (i) a significantly more intense, broad band near  $3000\text{ cm}^{-1}$ , attributed to OH groups, and (ii) a smoother appearance of the vibrational signals. The enhanced OH absorption primarily resulted from ethanol washing during amorphous TCP synthesis and the higher specific surface area of the particles, which increased water adsorption [342]. The signal smoothing reflected the lower crystallinity of amorphous TCP particles [343]. The degree of crystallinity was further validated via X-ray diffraction (XRD), where the patterns were consistent with crystalline and amorphous materials, respectively. For crystalline HAP, sharp diffraction peaks confirmed stoichiometric composition, whereas the amorphous TCP sample displayed a single broad peak near  $30^\circ$ , typical of non-crystalline CaP phases [335].

To further validate the previous findings, thermogravimetric analysis (TGA) was conducted over a temperature range from ambient conditions to  $1000^\circ\text{C}$ . The results revealed total mass losses of 6% for crystalline HAP and 9% for amorphous TCP. Interestingly, the derivative thermogravimetric (DTG) curves displayed atypical behavior within the  $100\text{--}400^\circ\text{C}$  range, which, as previously indicated by FTIR results, stemmed from the higher amount of adsorbed compounds in the synthesized amorphous TCP powder. Additionally, the DTG profile of amorphous TCP exhibited a distinct peak at  $650^\circ\text{C}$ , absent in the crystalline HAP sample. This feature was most likely linked to variations in carbonate incorporation modes within the apatite structure [344]. Concurrently, the sharp increase observed in the differential thermal analysis (DTA) curve of amorphous TCP at the same temperature was attributed to its crystallization process [345].

Electrolyte properties are summarized in Table 5. The detected calcium content in both c-HAP and a-TCP electrolytes originated from natural particle dissolution. The concentrations, measured in only a few  $\text{mg}\cdot\text{L}^{-1}$ , were too low to consider dissolved calcium as a competing source of this element for incorporation into the resulting oxide coatings. This ensured that particle incorporation could be assessed with minimal interference. Among the tested systems, the blank electrolyte exhibited the highest electrical conductivity, which can be logically attributed to the absence of suspended particles that would otherwise impede current flow [346]. The slightly lower conductivity observed in the a-TCP electrolyte was likely due to the larger specific surface area of its particles and the additional adsorption of phosphate ions from the solution, further reducing ion mobility. Despite this, the conductivities (G) of both c-HAP and a-TCP electrolytes remained comparable and, importantly, indicated that no significant particle agglomeration occurred within the prepared suspensions.

**Table 5.** Calcium ion concentration, electrical conductivity (G), and pH values of the prepared PEO electrolytes measured before and after pH adjustment.

Electrolyte	$\text{Ca}^{2+}$ , $\text{mg}\cdot\text{L}^{-1}$	G, $\text{mS}\cdot\text{cm}^{-1}$	pH before	pH after
Blank	not detected	$7.31 \pm 0.05$	$4.55 \pm 0.02$	$7.49 \pm 0.03$
c-HAP	$1.6 \pm 0.2$	$6.72 \pm 0.09$	$6.82 \pm 0.04$	$7.44 \pm 0.03$
a-TCP	$2.5 \pm 0.3$	$6.55 \pm 0.12$	$7.46 \pm 0.03$	not adjusted

It was observed that introducing particles into the electrolyte increased its pH by 2–3 units, mainly due to adsorbed carbonates on the particle surfaces. This effect was most pronounced for amorphous TCP, which resulted in the highest pH among the tested electrolytes. To equalize these differences and avoid complications related to electrolyte composition, the pH was adjusted using a  $0.1\text{ M K}_2\text{CO}_3$  solution. Following this adjustment, the pH variation between electrolytes was reduced to less than 0.05. Beyond pH standardization, this correction offered additional advantages: it established a neutral medium that minimized CaP solubility, slowed the crystallization rate of amorphous TCP [347], and imparted a slightly negative zeta potential to the suspension, given that the isoelectric point of HAP typically lies between 7.0 and 7.7 depending on the electrolyte composition [348], [349]. Under these conditions, rapid migration of suspended particles toward the anode during DC-mode PEO was prevented,

thereby avoiding the formation of a dense amorphous macro-layer of unreacted particles on the substrate surface.

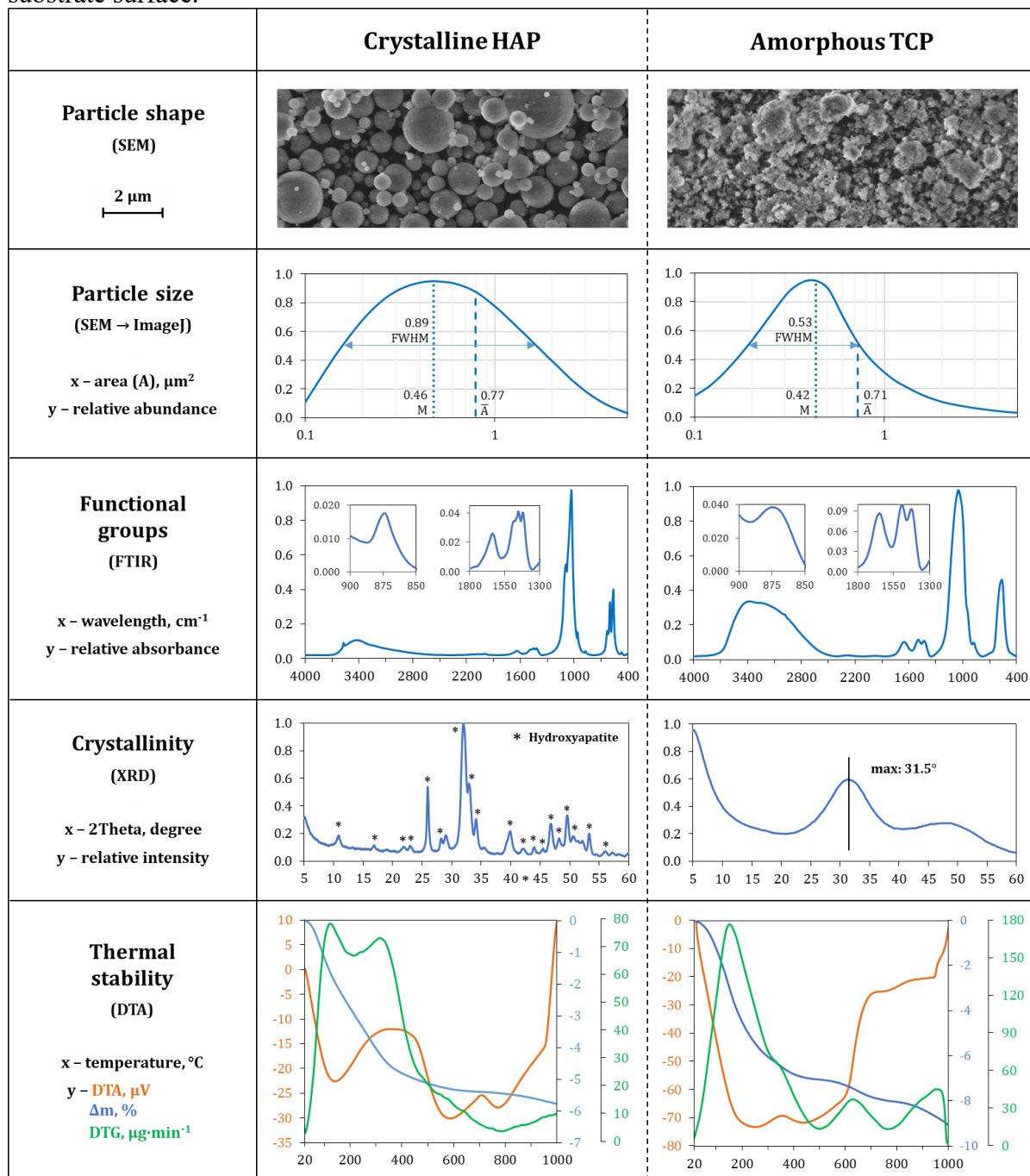


**Figure 10.** Comparison of the properties of crystalline HAP and amorphous TCP particles used for preparation of PEO electrolytes.

Based on the collected data, both CaP powders demonstrated characteristics consistent with their respective degrees of crystallinity, while exhibiting minimal differences in particle size and other key parameters. Additionally, their calcium and phosphorus contents were proportional and in line with the expected stoichiometry (Section 3.2.1). The close similarity in the solid mass fractions of calcium and phosphorus—differing by only about 4% and 6%, respectively—provides a solid foundation for objectively comparing coating properties with crystallinity as the primary variable. Literature reports suggest that more pronounced disparities in elemental composition could significantly affect coating characteristics, particularly bioactivity [185], [350]. Furthermore, suspensions prepared with these particles displayed



nearly identical electrical conductivity and calcium ion concentrations, with pH values subsequently adjusted to ensure comparability (Table 5).

#### 4.2.2. Surface morphology and porosity

To initiate the comparative analysis of coatings produced by PEO in blank, c-HAP, and a-TCP electrolytes, SEM was employed at various magnifications to examine surface morphology and derive initial insights into particle incorporation behavior. Low-magnification observations (50 $\times$ , 100 $\times$ , and 250 $\times$ ) consistently revealed that all coatings exhibited a uniform surface morphology across the entire sample area, with no localized anomalies. This uniformity justified selecting random locations for high-magnification imaging to obtain representative morphological data. Distinct differences in surface features became evident starting from 1000 $\times$  magnification. SEM micrographs captured at 2000 $\times$  (Figure 11, top rows) highlighted variations in microporosity and enabled pore size comparison, while higher magnification images (8000 $\times$ , bottom rows) revealed clear distinctions in pore geometry, ultramicroporosity, inter-pore connectivity, and particle incorporation within the oxide layer. In all cases, a porous oxide coating was formed, though the degree and nature of porosity varied among the samples.

Since visual inspection alone was insufficient to objectively distinguish differences in coating morphology, statistical analysis was applied to validate or challenge the preliminary observations and to better elucidate the effects of adding crystalline HAP and amorphous TCP particles to the PEO electrolyte. The pore areas of the coatings were quantified, and the resulting data were used to generate a plot (Figure 12) illustrating the relative contribution of pores of different sizes to the overall two-dimensional porosity. To enable direct comparison with particle dimensions, the x-axis range was set identical to that used in Figure 10 ('Particle size'), where crystalline HAP and amorphous TCP particles occupied 96% and 94% of the two-dimensional space within a diametral cross-sectional area range of 0.1–5  $\mu\text{m}^2$ . In addition to the distribution curves, Figure 12 also reports the total coating porosity, expressed as the percentage of the two-dimensional surface area covered by pores.

To clarify the concept behind this data representation, consider first the black dashed line corresponding to the b-Ti coating. For pores with an area of 0.8  $\mu\text{m}^2$ , multiplying the pore count by their respective area (0.8  $\mu\text{m}^2$ ) yields a nominal value of 0.4, which is shown on the plot as relative abundance. Performing the same calculation for pores with an area of 0.2  $\mu\text{m}^2$  results in a value of 0.8. This indicates that pores of 0.2  $\mu\text{m}^2$  contribute twice as much to the total porosity of this coating as pores of 0.8  $\mu\text{m}^2$ . When comparing coatings, this relationship further implies that, for example, upon adding crystalline HAP particles to the electrolyte, the total pore area of 1.0  $\mu\text{m}^2$  pores on the c-TAV coating becomes approximately 3.5 times greater than that observed on the b-TAV coating.

By analyzing the curve profiles in Figure 12, several conclusions can be drawn regarding coating porosity. First, the presence of a distinct peak maximum in each curve facilitated the identification of the most prevalent pore area, while the sharpness of the peak served as a direct indicator of coating uniformity and the absence of structural defects. Based on this parameter, the c-Ti and a-Ti coatings demonstrated the highest degree of homogeneity. Nevertheless, both the b-coatings and the c-TAV coating could also be classified as relatively uniform. In contrast, the elongated shape of the a-TAV curve suggested a less homogeneous structure, a finding that aligns with visual SEM observations (Figure 11). When comparing electrolytes, the smallest variation in porosity between Ti and TAV substrates occurred with the blank electrolyte: the b-TAV coating's curve appeared only slightly below that of b-Ti. In the other electrolytes, the differences were more pronounced—and in some cases substantial—indicating that particle addition significantly modified the coating morphology on different substrates. This conclusion also applies to c-coatings following pore size distribution analysis. Overall, the morphology analysis highlights several distinctive features for each coating type, summarized in Table 6.

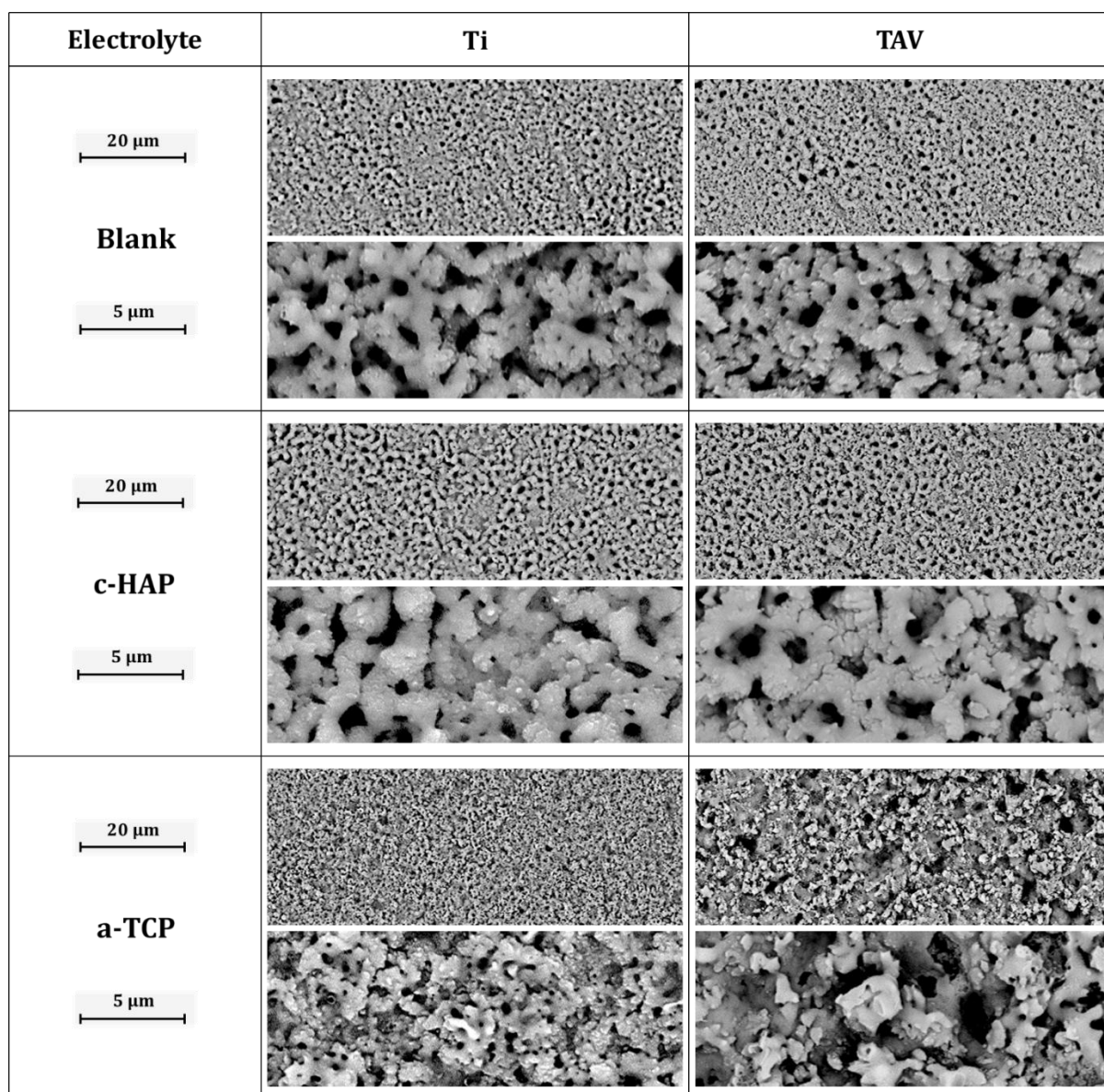


**Figure 11.** SEM micrographs of the coating surfaces obtained in different electrolytes, captured at lower (2000 $\times$ , top row) and higher (8000 $\times$ , bottom row) magnifications, illustrating variations in surface morphology, pore structure, and particle incorporation.

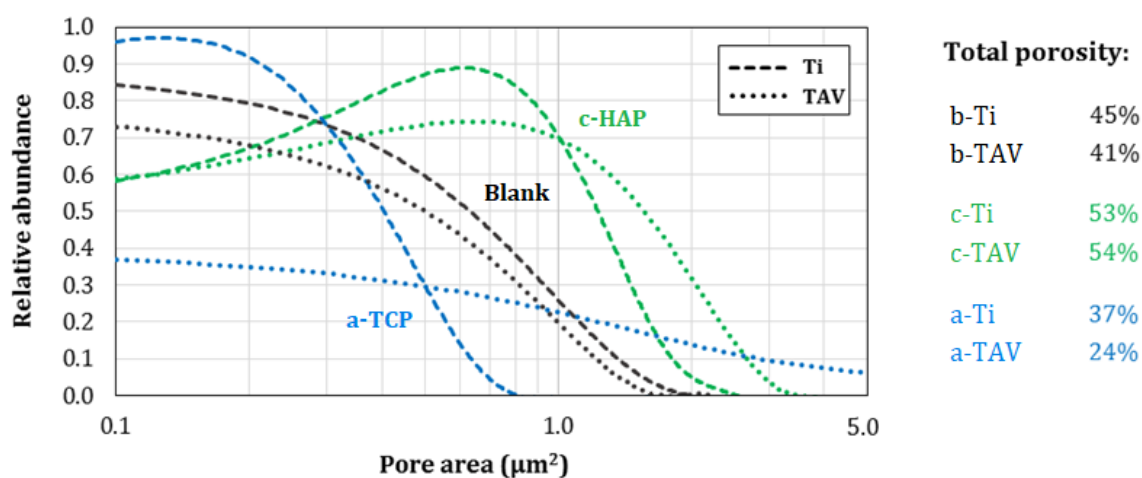


**Figure 12.** Distribution curves illustrating the contribution of pores of varying sizes to the overall two-dimensional porosity of oxide coatings formed on Ti and TAV substrates.

**Table 6.** Summary of coating surface porosity characteristics.

Characteristics	Ti coatings			TAV coatings		
	b-	c-	a-	b-	c-	a-
Definite pore shape	✓	partly	✗	✓	partly	✗
Uniformity in pore size	✗	partly	✓	✗	partly	✗
Dominance of ultramicropores	✓	✗	✓	✓	✗	✗
Pores larger than 1.0 $\mu\text{m}^2$ in area	partly	✓	✗	partly	✓	✓

The analysis of the distribution curves further supports the proposed hypothesis regarding particle incorporation patterns. Considering that particles with diametral cross-sectional areas up to at least 5.0  $\mu\text{m}^2$  were present in the electrolytes (Supplementary Data 1), and using the 0.3–1.0  $\mu\text{m}^2$  pore area range as a reference, it appears likely that, following the PEO process, amorphous TCP particles primarily accumulated on the coating surface, whereas crystalline HAP particles were predominantly incorporated into the middle layers of the oxide coatings. At the initial stage of PEO, smaller, spherical crystalline HAP particles could more easily penetrate the pores, leading to further lateral expansion and an overall increase in surface porosity. In contrast, amorphous TCP particles, with their higher surface development, were more prone to adhering to the outer surface of the coating, irrespective of particle size. These particles could partially melt and even seal larger pores. Nevertheless, larger crystalline HAP particles might still become incorporated during the later stages of the process, when sufficiently large pores had formed, providing the necessary physical space for their entrapment. This assumption is further supported by the presence of localized regions with reduced porosity ( $\sim 5 \times 5 \mu\text{m}$ ) observed on c-Ti and c-TAV coatings (Figure 11). To verify these hypotheses, EDX analysis was performed, with results presented and discussed in Section 4.2.3.

The literature offers no clear consensus on the relationship between particle addition to the PEO electrolyte and the resulting coating morphology and porosity, largely due to the diverse range of particles with varying properties employed across different studies. The influence of particles on coating characteristics appears to be highly system-specific, making detailed cross-study comparisons challenging. Nonetheless, qualitative changes relative to blank coatings are consistently observed, regardless of the specific PEO parameters or substrate used for oxide layer formation [292], [351], [352]. Our findings, particularly the evident presence of incorporated CaPs within pore connections, align with the observations of Seyfoori et al. [215], who introduced crystalline HAP nanoparticles into a PEO electrolyte to fabricate biphasic CaP-containing films on a magnesium alloy. In their study, the PEO-treated coatings displayed pore connections enriched with spherical inclusions measuring 70–100 nm. Conversely, when micro-sized CaP particles were added, a general reduction in coating porosity was reported, although the extent of this effect strongly depended on the applied electrical parameters and the pH of the electrolyte [31], [353].

#### 4.2.3. Roughness and wettability

The water contact angle (CA) measurements and surface roughness results of the coatings are summarized in Table 7. The reported CA, Ra, and Rz values represent averages calculated from sixteen measurements taken across four distinct regions of four coating replicates. Original images from the wettability tests are presented in Figure 13. Regarding the contact angle (CA), the measured values did not differ substantially enough to classify the coatings as distinctly hydrophobic or hydrophilic relative to one another. However, using a CA of 90° as the reference point for wettability—a widely accepted criterion [354]—the coatings can be described as slightly hydrophobic (b- and c-coatings) or slightly hydrophilic (a-coatings). This classification applied consistently to coatings on both substrates, as indicated by nearly identical CA values for coatings formed in the same electrolytes. The influence of particle incorporation on wettability was evident, particularly for the a-coatings, which exhibited a pronounced shift toward hydrophilicity, accompanied by an approximate 40% decrease in CA. The trends in surface roughness followed a similar pattern to CA changes:

while the increase in roughness for c-coatings was less than 20% compared to b-coatings, the roughness of a-coatings was 2–3 times higher. Furthermore, coatings on TAV substrates were more sensitive to particle addition, displaying more substantial and consistent increases in roughness than those formed on Ti.

**Table 7.** Average solid-liquid CA and roughness (Ra, Rz) values of oxide coatings prepared in different electrolytes.

Substrate	Electrolyte	CA, °	Ra, $\mu\text{m}$	Rz, $\mu\text{m}$
Ti	Blank	107.2	0.36	1.43
	c-HAP	97.8	0.42	1.69
	a-TCP	76.9	0.75	2.71
TAV	Blank	107.3	0.44	1.62
	c-HAP	98.5	0.59	2.19
	a-TCP	79.3	1.16	4.34

Binding the porosity data (Figure 12) along with roughness and CA measurements (Table 7), comparative plots were constructed (Figure 14) to visually assess correlations among these parameters as a function of substrate type and electrolyte composition. If one were to consider only the effect of roughness changes [355] while disregarding the influence of CaP particle incorporation [356], the Wenzel model [357] would predict that the observed increase in roughness along the blank  $\rightarrow$  c-HAP  $\rightarrow$  a-TCP sequence should decrease wettability, given that b-coatings initially exhibited slight hydrophobicity. In practice, however, the experimental results demonstrated a markedly different trend, contradicting this theoretical expectation. One might attribute the decrease in CA for c-coatings to their increased porosity relative to b-coatings [358], [359], yet this explanation does not hold for a-coatings, where wettability increased even more significantly despite lower porosity. These observations strongly suggest that particle incorporation occurred during coating formation. Similar reductions in CA—typically 30–50% compared to blank coatings—have been reported in other PEO studies following the incorporation of HA [352] and other hydrophilic particles [360], [361].

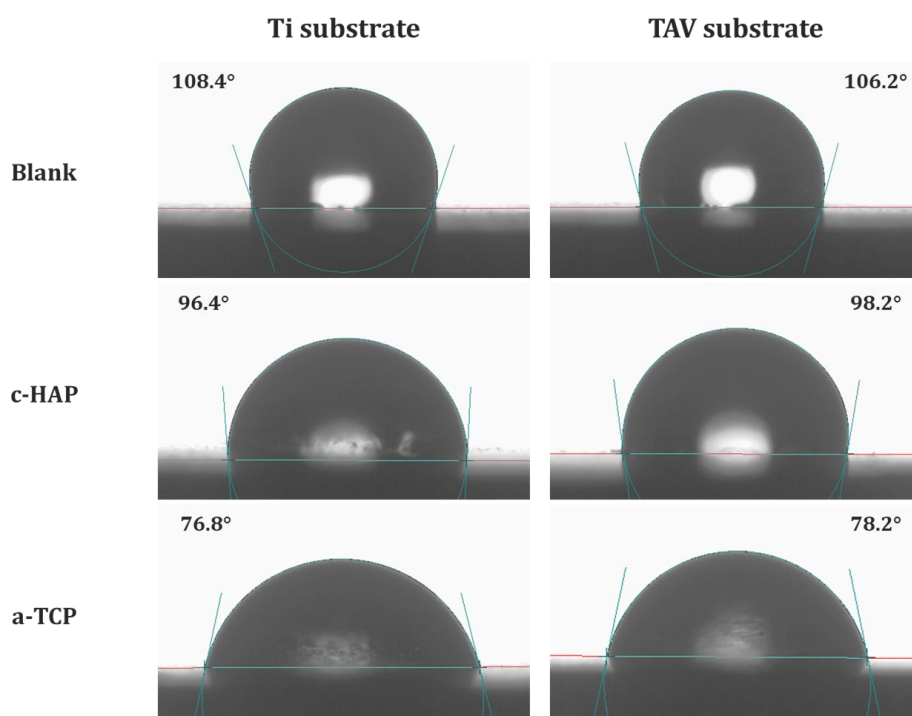


**Figure 13.** Original images from the contact angle (CA) measurements along with the corresponding CA values obtained during testing.

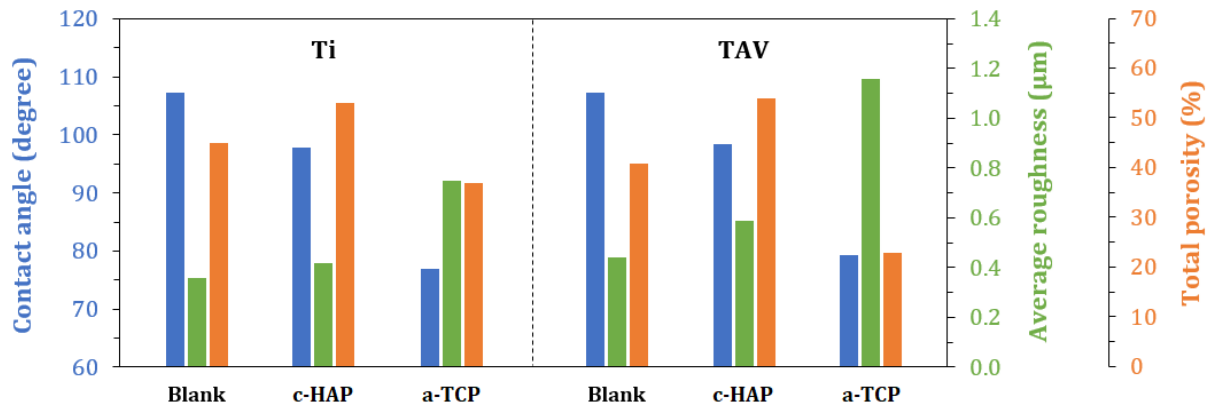


**Figure 14.** Summary plot illustrating the measured contact angles (CA), average surface roughness, and two-dimensional porosity values of the oxide coatings prepared on Ti and TAV substrates in different electrolytes.

Several observations further support the conclusion that the observed changes in CA were primarily driven by the presence of CaP phases, with surface roughness playing only a secondary role [362], [363]. Quantitatively, this is evidenced by the pronounced differences in roughness and porosity between b-Ti and b-TAV coatings, despite their identical CA values, even when accounting for the substrates' distinct chemical compositions. A similar pattern was observed for the a-coatings, which showed nearly identical wettability (CA difference of only 3°) despite substantial differences in roughness and porosity. Thus, while Figure 14 illustrates a clear correlation between CA and roughness for Ti and TAV coatings, these parameters can be considered independent in this context, both resulting from CaP phase incorporation rather than directly influencing each other. This behavior indirectly suggests a higher mass fraction of CaP phases in a-coatings compared to c-coatings. However, unlike SEM analysis, CA measurements alone cannot confirm whether these phases are present as solid particles. Moreover, the negligible differences in surface wettability between c-coatings and between a-coatings produced on Ti and TAV substrates indicate that particle incorporation mechanisms and CaP content in the surface layers are largely substrate-independent and primarily governed by particle properties.

Changes in the roughness of oxide coatings are known to be influenced by a combination of particle properties, including melting point, chemical composition, and size [30]. Previous studies have reported varying effects of particle incorporation, with coating roughness either increasing [215], decreasing [31], or remaining largely unchanged [364]. Considering that the crystalline HAP and amorphous TCP particles added to the electrolytes had diametral cross-sectional areas comparable to the typical pore sizes of oxide coatings formed on Ti substrates [340], and that CaPs generally undergo inert incorporation during PEO due to their relatively high melting points [30], it was anticipated that their interaction with the oxide layer would noticeably increase surface roughness. The most significant roughness enhancement was observed in a-coatings, where Ra values for coatings on Ti and TAV substrates were 108% and 164% higher, respectively, than those of the corresponding b-coatings. Similar findings, both in absolute and relative terms, were reported by Ma et al. [352], who incorporated HAP nanoparticles into PEO-derived bioactive coatings on Ti substrates under pulse current conditions. In that study, the roughness of the particle-free coating measured 0.49 μm, whereas the addition of nanoparticles produced a more than threefold increase, reaching 1.55 μm.

The substantially greater roughness observed for a-coatings provides further confirmation of the SEM-based findings that amorphous TCP particles preferentially adhere to the outer surface layers of the coating, unlike crystalline HAP particles. Crystalline HAP tended to partially fill surface pores, which could have theoretically resulted in a reduction in roughness compared to b-coatings. However, the observed increase in roughness was attributed to the



formation of thickened pore walls. Additionally, the higher roughness measured for the c-TAV coating compared to the c-Ti coating (0.59  $\mu\text{m}$  vs. 0.42  $\mu\text{m}$ ) aligns with the distribution trends seen in Figure 12, which indicated a larger average pore contribution for c-TAV. The even more pronounced roughness difference between the a-coatings (0.75  $\mu\text{m}$  for Ti and 1.16  $\mu\text{m}$  for TAV) also matches the SEM observations. Despite its lower overall surface porosity, the a-TAV coating exhibited increased roughness primarily due to the presence of periodically occurring large pores, which were larger than those found in the other coatings.

Summarizing the intermediate findings on the surface characteristics (morphology, porosity, roughness, and wettability), the following key conclusions can be drawn:

1. Particle incorporation: Both crystalline HAP and amorphous TCP particles were successfully incorporated into the coatings, as directly confirmed by SEM analysis and indirectly supported by CA and roughness data.
2. Homogeneity: All coatings deposited on Ti and TAV substrates exhibited homogeneity at both micro- and macro-scales.
3. Particle-specific effects: While both types of particles influenced all investigated parameters, amorphous TCP produced more pronounced changes compared to the Blank coatings.
4. Minimal wettability dependence on substrate: The chemical composition of the substrate had only a minor impact on coating wettability, suggesting a consistent degree of particle incorporation for both crystalline and amorphous particles.
5. Substrate effect on morphology: The substrate composition had a moderate influence on the morphology, porosity, and roughness of c-coatings, whereas this effect was significantly stronger for a-coatings.
6. Incorporation behavior: The observed differences in morphology between c- and a-coatings, along with the enhanced wettability and roughness of a-coatings, are most likely attributed to the surface characteristics of the amorphous TCP particles, which facilitated their more active incorporation into the surface layers.

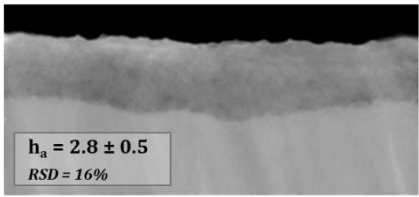
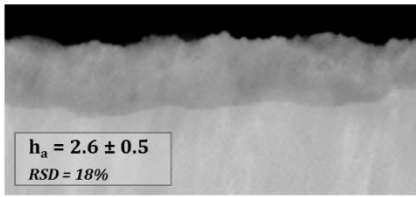
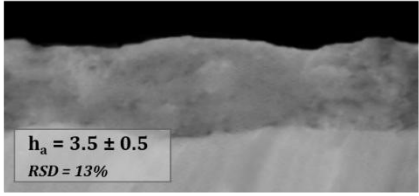
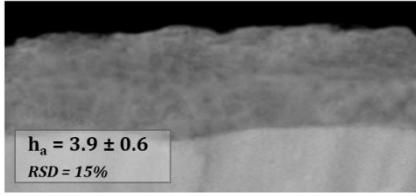
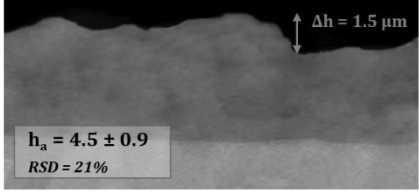
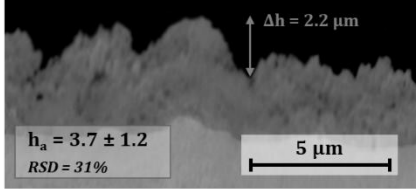
Further validation of conclusions (4) and (6) is presented in Sections 4.2.4 and 4.2.5. Moreover, since the use of amorphous TCP resulted in coatings with improved wettability, increased micro-roughness, and reduced total porosity, incorporating these particles into PEO electrolytes appears to be the more advantageous approach for enhancing the biological performance of the coatings. Such modifications are expected to promote cell adhesion, attachment, and proliferation more effectively, ultimately leading to superior osteointegration of implants [365], [366], [367].

#### 4.2.4. Coating thickness

Since crystalline HAP and amorphous TCP particles were shown to significantly influence the surface properties of the coatings, the study was extended to examine the internal structure of the oxide layers down to the barrier layer at the substrate interface. The aim was not only to verify the presence of the oxide layer but also to evaluate its uniformity, density, and thickness, as well as the effects of the electrolyte and substrate on these characteristics. Figure 15 presents cross-sectional images of the coatings along with average thickness values and error margins, enabling an assessment of thickness uniformity. The displayed areas primarily highlight the layer's density and structure rather than precise thickness measurements due to magnification limitations. The upper regions correspond to the resin used for sample mounting during cross-section preparation. Although some polishing-induced irregularities were observed during SEM examination, they were corrected; in Figure 15, the resin appears as a uniform black background.

In all samples, a distinct oxide layer was evident, clearly differentiated from the lighter region of the pure substrate. Visual inspection indicated that particle addition consistently increased layer thickness. As with surface properties, structural changes were more pronounced in the a-coatings, producing substrate-specific results. Quantitatively, c-coatings were 25–50%

thicker than b-coatings, whereas a-coatings showed thickness increases of approximately 60% on Ti and 40% on TAV substrates. However, the thickness difference between b- and c-coatings remained negligible, falling within the experimental error range.

Electrolyte	Ti	TAV
Blank		
c-HAP		
a-TCP		

**Figure 15.** SEM cross-sectional images of oxide coatings formed on Ti and TAV substrates, along with the calculated average oxide layer thickness ( $h_a$ ,  $\mu\text{m}$ ).

The oxide layer thickness uniformity for the blank coating showed an RSD of 16–18%. Incorporating crystalline HAP particles slightly improved homogeneity, lowering RSD by 3%, likely due to partial closure of surface pores. In contrast, a-coatings exhibited reduced uniformity, particularly on TAV substrates. This can be attributed to the stronger adherence of amorphous TCP particles, forming a denser calcium-phosphate layer. For a-TAV coatings, additional factors likely contributed to barrier layer curvature during PEO, possibly related to phase composition changes (discussed in Section 4.2.6). As a result, the RSD increased to 31%, reflecting uneven oxide layer boundaries. This deformation also explains the smaller average thickness of a-TAV compared to a-Ti. The observed local heterogeneity, responsible for increased roughness, indicates that no unwanted macro-sized particle clusters were deposited during coating formation. Supporting this, representative images in Figure 15 show that the local thickness difference (marked by yellow bullets) remained below the surface roughness ( $R_z$ ) values for both substrates (Table 7), being approximately twice smaller ( $\Delta h_{a\text{-Ti}} = 1.5 < R_{z\text{-Ti}} = 2.71$ ;  $\Delta h_{a\text{-TAV}} = 2.2 < R_{z\text{-TAV}} = 4.34$ ).

Accurate visual assessment of layer density was challenging because the cross-section preparation process partially smeared the oxide's porous structure. After applying corrections, however, it was possible to detect larger pores and internal macro-defects. A higher density of dark dots and spots indicated larger cavities, revealing that the densest layers were found in both b-coatings and the a-Ti coating. In contrast, c-Ti, c-TAV, and a-Ti coatings displayed increasing numbers of dotted dark regions in that order. For c-Ti and c-TAV, these features likely resulted from slight structural deformation caused by the incorporation of larger crystalline HAP particles. In a-Ti, the effect was further intensified by barrier layer deformation previously discussed. Since no particles were involved in b-coating formation and inhomogeneity factors were minimized, these coatings exhibited more uniform and systematically grown dense oxide layers.

The obtained results are consistent with literature reports indicating that, under a potentiostatic DC regime, oxide coating thickness typically does not exceed a few tens of

microns [93]. Specifically, CaP coatings produced under comparable conditions usually reach 2–10  $\mu\text{m}$  [31], [180], [199], [215], whereas alternating current processes incorporating HAP particles can achieve up to twice this value, reaching  $\sim 20 \mu\text{m}$  [368]. Beyond current type and electrical parameters, coating thickness also depends on processing time and electrolyte concentration [239], both of which generally increase layer growth. Although particle addition usually has minimal influence on thickness, significant thickening or thinning has occasionally been reported [369]. In this study, since oxidation conditions were identical, the observed thickness variations can be attributed solely to particle presence, their incorporation mechanism, and their interactions with the oxide layer, which are strongly linked to their differing physicochemical properties (Figure 10).

#### 4.2.5. Elemental composition in a cross-section

Previous sections discussed particle incorporation and its impact on oxide coating properties. However, conclusions regarding CaP phases were primarily inferred indirectly. Similarly, the hypothesis of increased CaP content in the outer regions of coatings with amorphous particle addition was not yet experimentally confirmed. To validate these assumptions, chemical analysis of cross-sections was conducted in four distinct regions of each coating, and the average elemental profiles were plotted as a function of relative coating depth (Figure 16). As an illustration of profile generation, Figure 19 shows four calcium concentration profiles measured in different regions of the c-TAV coating, along with the resulting averaged curve representing overall calcium distribution. Table 8 provides numerical data on calcium content across coating areas, offering detailed insight into the incorporation of phases originating from crystalline HAP and amorphous TCP particles. Representative point EDX spectra recorded at various coating depths for two coatings are presented in Figure 17.

The prepared cross-sectional samples contained both primary coating constituents formed during PEO and secondary components originating from the embedding resin and sputtered gold. Consequently, elemental profiles included Ca, P, Ti, K, O, C, Au, and, for TAV coatings, Al and V. For analysis, K, C, and Au were excluded due to their negligible relevance. Although potassium was present in the electrolyte as ions alongside phosphates, its incorporation into the coatings was minimal, not exceeding 0.2% (atomic ratio). For calculation purposes, the combined atomic fractions of the remaining elements, excluding oxygen, were normalized to 100%. Oxygen content was less informative because of its high abundance in metal oxides, the electrolyte, and suspension components; therefore, its line scan profiles are presented separately in Figure 18 as supporting evidence of oxide layer formation.

Analysis of all six coatings revealed no major differences between samples prepared in the same electrolyte on different substrates, except for the expected absence of Al and V in Ti substrates (Figure 17). For b-coatings, the elemental composition was virtually identical across substrates, while in c- and a-coatings, calcium mass fractions varied by only 1–2% throughout the measured depth (Table 8). The remaining elements exhibited comparable variation patterns (Figure 17), including oxygen distribution (Figure 18). These findings indicate a highly consistent particle incorporation behavior across the tested substrates and suggest a high likelihood of similar results for other titanium-based coatings.

To visualize elemental distribution and assess the impact of particle addition, the spectra (Figure 17, Figure 18) were divided into distinct regions. In the c-Ti and c-TAV coatings, region 0 represents the outermost layer adjacent to the surface, characterized by open porosity and a low solid fraction, resulting in reduced atomic percentages of all elements. Moving inward to region 1, the Ca content increased sharply, reaching levels comparable to Ti near the start of this layer. Region 1 contained both closed and partially open pores with limited environmental exposure and was particularly enriched in calcium, accompanied by a gradual rise in phosphorus. Region 2 showed slightly fewer pores, evidenced by a steady increase in substrate element fractions. Calcium decreased in this layer, while phosphorus initially exceeded



calcium, peaked around the middle, and declined towards the end. In region 3, residual calcium and phosphorus were still detectable but were rapidly displaced by substrate elements. The pronounced increase in Ti, Al, and V, along with a reduction in oxygen content (Figure 18), indicated pore closure, transition through a thin amorphous barrier layer, and eventual merging into region 4—the pure substrate. Based on the calcium profile of the c-TAV coating, most incorporated particles accumulated in region 1, though substantial amounts were also present in the outer region 0 when compared to substrate element concentrations.

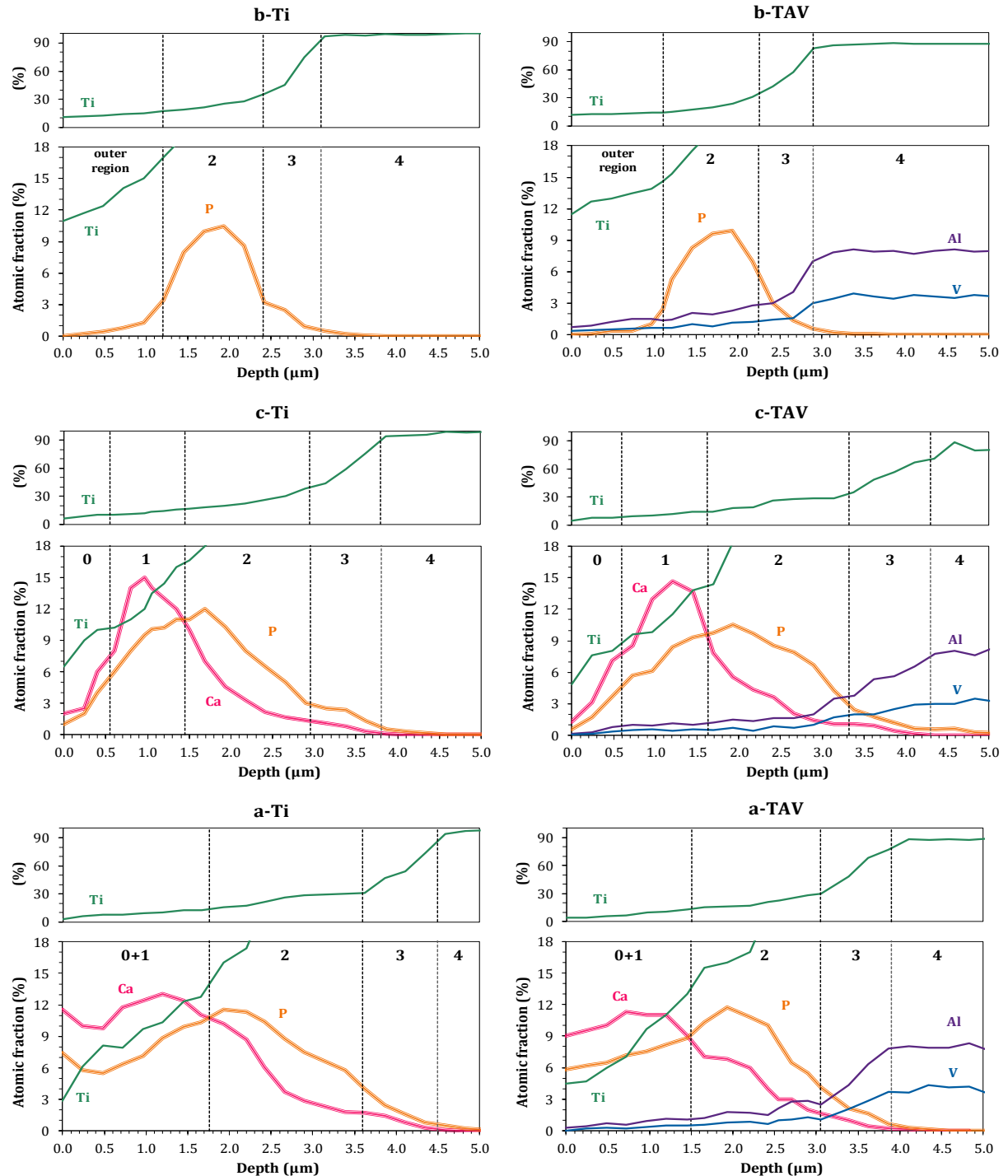


**Figure 16.** Cross-sectional elemental composition of oxide coatings formed on Ti and TAV substrates with crystalline HAP or amorphous TCP particle additions to the electrolyte. The upper panels show data for Ti on a full atomic ratio scale, while the lower panels display all detected elements on a narrower scale. Regions are defined as follows: 0 – outer layer with low calcium content; 1 – layer with elevated calcium content; 0+1 – combined outer region with increased calcium; 2 – layer enriched in phosphorus; 3 – zone with markedly reduced porosity; 4 – uncoated substrate.

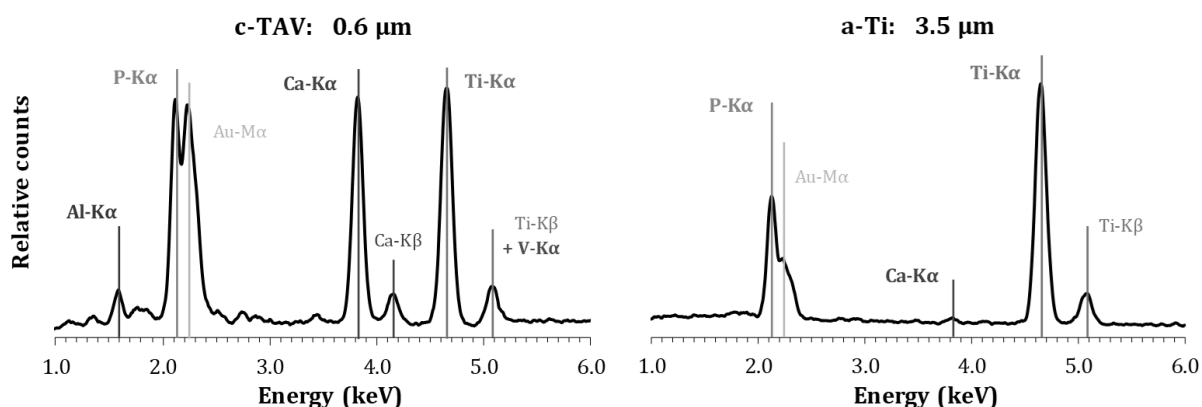


**Figure 17.** Representative spot EDX spectra recorded at various depths from the surface of c-TAV and a-Ti coatings.

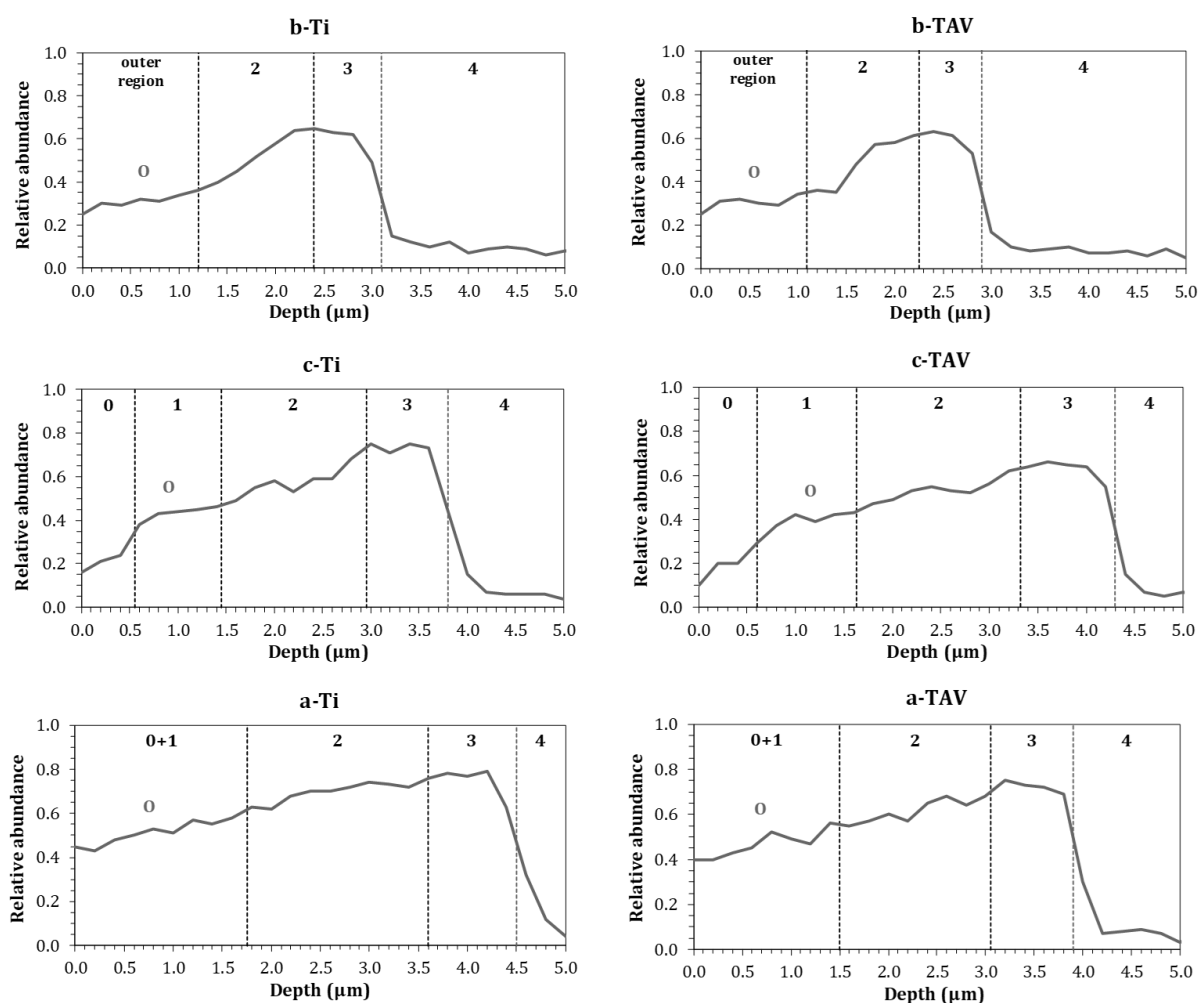


**Figure 18.** Relative oxygen abundance as a function of distance from the coating surface. Lines represent averaged measurements taken at four different coating locations. Regions are defined as follows: 0 – outer layer with low calcium content; 1 – layer with elevated calcium content; 0+1 – combined outer region with increased calcium; 2 – layer enriched in phosphorus; 3 – zone with sharply reduced porosity; 4 – uncoated substrate.

Similar behavior was observed for the a-Ti and a-TAV coatings, with one notable distinction—these coatings contained significantly more calcium, particularly in the outer layer, where its atomic fraction substantially exceeded that of Ti. As a result, layers 0 and 1 could not be clearly separated, unlike in the c-coatings, and are therefore combined as “0 + 1” in Figure 17. The remaining regions of the a-coatings showed only minor differences and were designated

using the same criteria as for the c-coatings. Although calcium levels in layers 2 and 3 of the a-coatings were still slightly higher (Table 8), the variation was modest (1–2%). Consequently, the use of amorphous particles enables the formation of oxide coatings with increased CaP content. Supporting this, oxygen elemental profiles (Figure 18) indicate a slightly higher relative oxygen abundance in the “0 + 1” regions, further evidencing greater CaP phase incorporation in the surface layers of a-coatings.

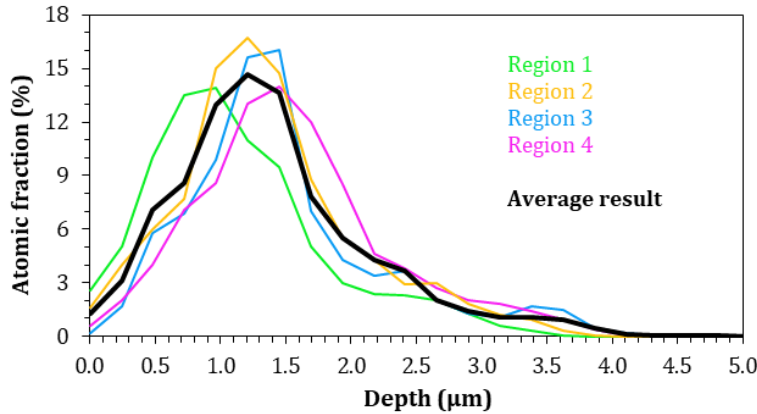


**Figure 19.** Example of calcium distribution repeatability as a function of distance from the c-TAV coating surface. Colored curves represent calcium content measured in four distinct regions of the coating, while the black curve shows the averaged calcium profile.

**Table 8.** Calcium atomic fraction at different depths of oxide coatings produced with particle addition, along with Ca/P ratios determined for their outer layers.

Electrolyte	Substrate	Atomic ratio (Ca), %				Ca/P in the upper layer*
		Layer 0	Layer 1	Layer 2	Layer 3	
c-HAP	Ti	5.2	12.8	4.3	0.8	1.64
	TAV	4.6	11.3	3.9	1.0	1.62
a-TCP	Ti	11.6*	11.6*	6.1	1.7	1.52
	TAV	10.2*	10.2*	5.4	1.5	1.53

\*upper layer includes layer 0 and layer 1

Phosphorus profiles also provide valuable insights into the oxide layer structure. In all coatings, the phosphorus concentration gradient was shifted toward deeper oxide regions. Since phosphorus originated from phosphate ions ( $\text{KH}_2\text{PO}_4$ ) in the electrolyte, its distribution suggests that negatively charged phosphate ions were highly mobile during PEO, enabling penetration into deeper porous structures while migrating toward the positive anode. Consequently, phosphorus remained abundant in region 2 of both c- and a-coatings, whereas CaP particles were physically hindered from reaching this depth. This makes phosphorus a reliable indirect indicator of pore presence in deeper layers.

In upper layers, phosphorus served as a marker distinguishing regions with open versus closed porosity. During post-treatment in an ultrasonic bath, phosphate species deposited on pore openings during PEO were washed away from open regions but remained in closed regions inaccessible to the washing solution. This effect is particularly evident in the b-coatings, where phosphorus is nearly absent from outer layers, and in the “0” and “0 + 1” regions of c- and a-coatings, where the Ca/P ratio closely matched that of the added CaP particles (Table 8). From this, it can be inferred that closed pores frequently appear beginning in the mid-section of region 1, coinciding with the peak calcium atomic fraction.

Comparable calcium distribution profiles for c- and a-coatings with respect to depth have been reported in the literature. For instance, Lee et al. [199] observed maximum calcium concentrations in the upper layers of their coatings; however, the Ca peak was less pronounced due to the smaller average particle size (50–100 nm), which facilitated deeper entrapment at similar incorporation levels. Similarly, Yeung et al. [31] used crystalline HAP particles

(Fludinova, Portugal) and produced coatings where calcium was predominantly surface-localized with reduced content in the middle layers. This difference may stem from multiple factors, including a lower particle concentration ( $20 \text{ g}\cdot\text{L}^{-1}$ ) and the use of a more alkaline electrolyte, which decreased the zeta potential and enhanced migration of larger particles toward the anode. In the present study, the average particle sizes were comparable to those reported; however, EDX analysis suggests that adjusting particle crystallinity can serve as an effective strategy to control the amount of CaP phases incorporated into the surface region of PEO coatings.

#### 4.2.6. Raman spectroscopy analysis

Raman spectroscopy was employed to further investigate the structural characteristics of oxide layers formed on Ti and TAV substrates (Figure 20). When compared with literature data [370], the Raman spectrum of the b-Ti coating closely resembled that of anatase, with major fitted bands observed at  $145 \text{ cm}^{-1}$  (Eg),  $392 \text{ cm}^{-1}$  (B1g),  $518 \text{ cm}^{-1}$  (A1g), and  $636 \text{ cm}^{-1}$  (Eg). The position and linewidth of the dominant Eg mode suggest the presence of nanometric anatase particles, indicating well-developed long-range order within the crystal lattice. Notable differences between the literature-reported and experimentally measured band positions likely stem from the crystallization pathway of anatase in this study, which was influenced by the Ti substrate. This process is hypothesized to induce internal stresses within the Ti–O framework, causing slight deviations from the ideal bulk anatase structure [371]. Additional spectral discrepancies, including splitting of the main E1g mode and the appearance of extra bands during fitting, are attributed to structural point defects introduced by interactions between  $\text{K}^+$  and  $\text{PO}_4^{3-}$  ions and the unsaturated bonds of titanium oxide [372].

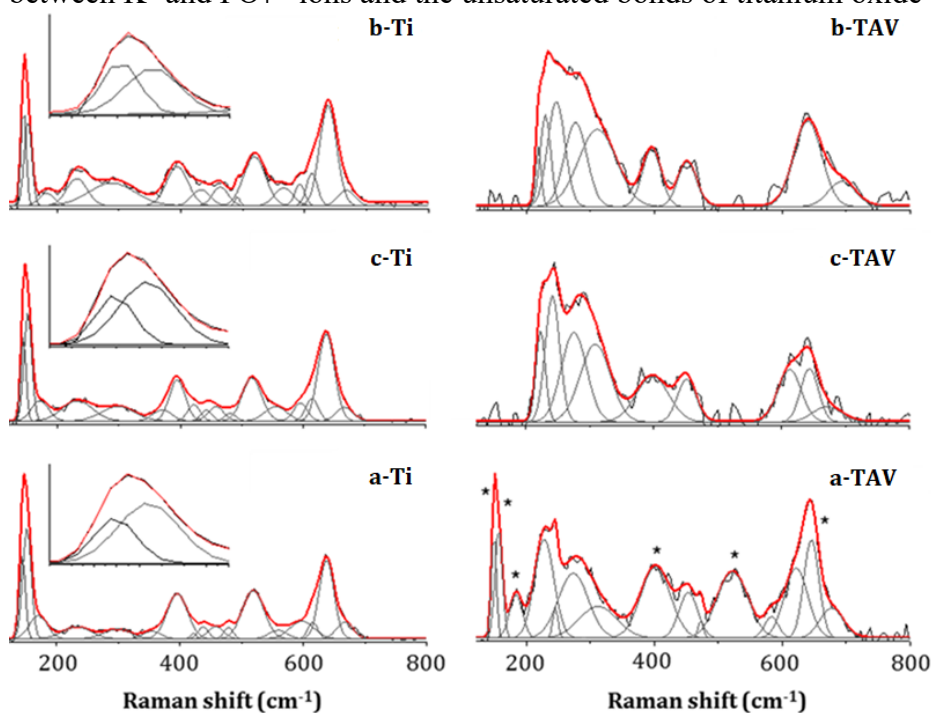


**Figure 20.** Raman spectra of oxide coating surfaces formed on Ti and TAV substrates using different electrolytes.

The remaining Ti coatings exhibited Raman spectra similar to b-Ti, with characteristic anatase bands appearing at nearly identical positions and intensities. However, the addition of crystalline HAP or amorphous TCP particles influenced the spectra by increasing the intensity of the  $153 \text{ cm}^{-1}$  band, as well as the number of detectable bands and their FWHM values. These changes suggest an increased presence of phosphate groups interacting with unsaturated anatase bonds, indirectly confirming particle incorporation. A further distinction between c-Ti and a-Ti coatings was related to the type of particle fraction added. Coatings formed with crystalline

HAP showed narrower FWHM values, indicative of a more ordered structure, whereas those prepared with amorphous TCP exhibited broader bands, consistent with a less ordered, defect-rich structure.

A markedly different Raman spectral profile was observed for b-TAV coatings. Unlike the Ti-based coatings, no characteristic anatase bands were detected. Instead, the spectrum exhibited broad bands with relatively high FWHM, indicative of non-stoichiometric titanium oxide formation. Literature reports on TAV alloys describe similar spectra as a mixture of locally ordered and disordered Ti–O structures with potassium incorporated into the titanium oxide lattice [372]. This incorporation likely promoted Ti–O–K bond formation through Ti–O bond disruption, generating a pronounced Raman signal below 400 cm<sup>-1</sup>. However, in contrast to this interpretation, the spectrum also contained typical Ti–O stretching modes (400–800 cm<sup>-1</sup>), characteristic of defect-rich structures. Additional spectral anomalies may result from aluminum and/or vanadium migration from the substrate into the oxidized Ti layer. Such isomorphic substitution of Al and/or V into Ti lattice sites could activate Ti–O–X (X = Al, V) vibrational modes, leading to increased structural distortion of the titanium oxide network and the emergence of a greater number of low-frequency bands compared to Ti substrates [373].

The addition of crystalline HAP and amorphous TCP particles to the electrolyte caused noticeable structural modifications in the oxide layers formed on TAV substrates. Similar to b-TAV coatings, the Raman spectra of c-TAV and a-TAV exhibited atypical band arrangements, primarily indicative of Ti–O–K and Ti–O–X (X = Al, V) bond formation, with potassium occupying interstitial sites within the titanium oxide lattice. Introduction of crystalline HAP slightly altered the number, intensity, and FWHM of the main Raman bands, effects likely attributed to an excess of phosphate groups originating from the particles. In contrast, amorphous TCP addition resulted in a more complex oxide structure. The Raman spectra revealed coexistence of defect-rich titanium oxide containing Ti–O–K and Ti–O–X bonds alongside anatase-like phases with characteristic Ti–O–Ti vibrations. Notably, these anatase bands were shifted to higher frequencies, consistent with literature reports [370], suggesting the presence of point defects or structural dislocations caused by Al or V migration into the titanium oxide lattice or interactions between phosphate ions and the oxide. Another contributing factor may be the relatively low thickness of the anatase layer. The observed coexistence of two oxide types is unconventional and may be explained by the formation of a microporous or multilayered titanium oxide system, where a thin anatase layer overlays a more defect-rich titanium oxide phase formed directly on the substrate.

In summary, Raman spectroscopy revealed both similarities and differences in the structural characteristics of the fabricated coatings, primarily reflected in the phase composition of titanium oxides. On Ti substrates, anatase was the sole TiO<sub>2</sub> phase detected, whereas coatings on TAV substrates consisted of non-stoichiometric titanium oxides with less consistent phase formation across different electrolytes. The analysis also indirectly confirmed particle incorporation in all Ti and TAV coatings, as evidenced by the increased number of Raman bands. These findings help explain the previously observed lower thickness uniformity of a-TAV coatings (Figure 15) and the presence of non-uniform surface microstructures, including large pores and sintered particles (Figure 11). However, the precise mechanism underlying these structural variations remains unclear. When compared with literature data, no strong correlation between the relative amounts of different TiO<sub>2</sub> phases was observed, likely due to differences in oxidation conditions among studies. Nevertheless, the incorporation of CaP particles into PEO coatings formed on titanium-based substrates generally favors anatase formation [292], [368], which was also partially confirmed by the present results.

#### 4.2.7. Bioactivity tests

Simulated body fluid (SBF) immersion tests were conducted as a preliminary evaluation of the *in vivo* behavior of the coatings [374]. In this method, samples were immersed in a physiologically relevant medium for several weeks, and the rate and uniformity of HAP crystal

formation on the coating surfaces were assessed. The process is known to strongly depend on the physicochemical properties of the coating [375], [376]. The total test duration was 4 weeks, with crystal growth monitored at 7-day intervals. However, only data from weeks 1 and 3 are presented (Figure 21), as these best illustrate the observed trends. Figure 21 also includes average Ca/P molar ratios of the surface-grown crystals after 3 weeks of immersion in SBF.

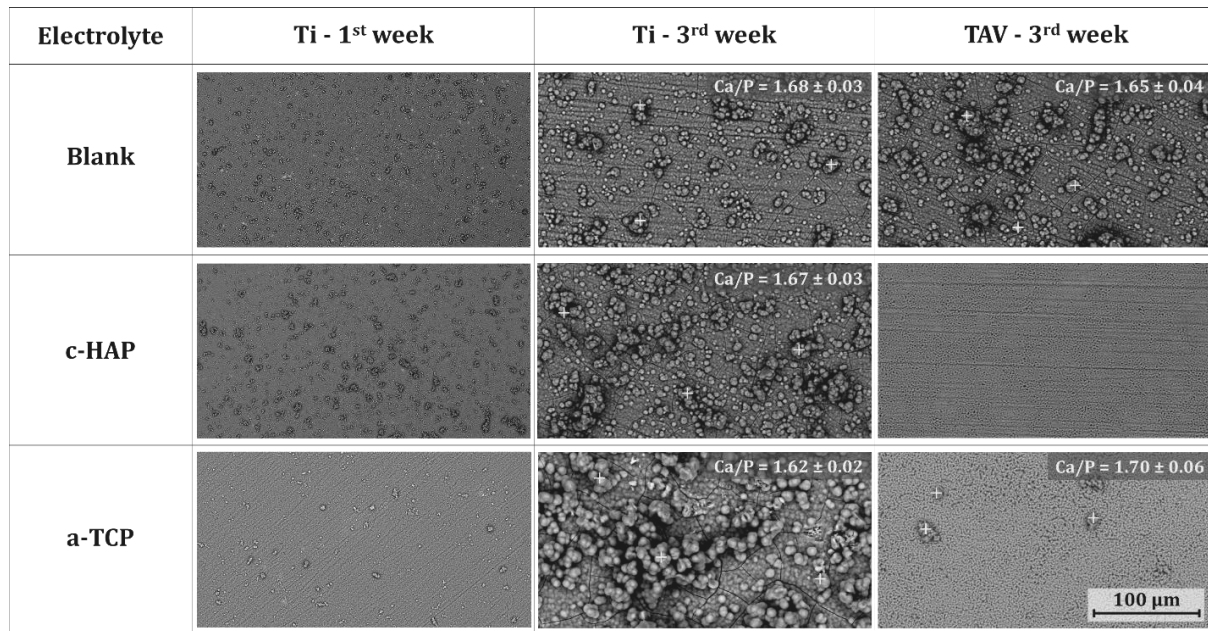


**Figure 21.** SEM images of oxide coating surfaces after 1 and 3 weeks of immersion in SBF solution. Average Ca/P molar ratios of the surface-grown crystals were determined by EDX spot analysis at three different locations (indicated by ‘+’ marks).

Over the three-week immersion period, all coatings on Ti substrates exhibited varying degrees of bioactivity. For the TAV alloy, only the b-coating demonstrated notable bioactivity, whereas the c- and a-coatings were non-bioactive or weakly bioactive.

Based on chronological observations of crystalline layer development on bioactive coatings (b-Ti, c-Ti, a-Ti, and b-TAV), three distinct stages of formation were identified:

1. Nucleation: Appearance of isolated, non-accreted crystals and initial agglomerate formation.
2. Growth and Coalescence: Enlargement of agglomerates through merging with smaller crystals, while new nucleation centers continue to form on exposed coating areas.
3. Full Coverage: Complete masking of the oxide surface due to coalescence of the crystalline layer, followed by uniform thickening and deposition of additional crystals.

After three weeks, the Ca/P molar ratios of the formed crystals (Figure 21) ranged narrowly from 1.62 to 1.70, with consistent values across different surface regions. These results confirm the formation of a homogeneous HA layer chemically identical to stoichiometric HAP (Ca/P = 1.67) on all coatings where visible crystallization occurred.

By the end of the third week, it was evident that the addition of both crystalline HAP and amorphous TCP particles enhanced the HAP growth rate on Ti coatings. However, crystal density observations at earlier stages were less straightforward. After the first week, c-Ti demonstrated the highest bioactivity, slightly exceeding b-Ti and significantly outperforming a-Ti. Yet, after three weeks, the thickest and densest crystalline layer was observed on a-Ti. These discrepancies can be rationalized by considering insights from previous analyses, which highlight the influence of particle type and incorporation behavior on coating structure and subsequent bioactivity.

Experimental results confirmed that the a-Ti coating surface exhibited smaller average pore sizes compared to c-Ti. This explains the slower HAP layer growth during the first week, as nucleation within smaller pores requires higher energy [376]. Although a-Ti had a greater

number of pores per unit area, its overall two-dimensional porosity was lower than that of c-Ti (Figure 12), further hindering initial crystal growth. Additionally, the larger spacing between pore centers relative to their diameter on a-Ti likely impeded the subsequent coalescence of individual crystallization centers during the early stages of immersion in SBF. Once the initial physical and energetic barriers were overcome, HAP growth on a-Ti coatings accelerated significantly. This increase was facilitated by the coating's higher microscale roughness (Figure 14) and its greater CaP content in the outer layers (Figure 17, Table 8). It is well established that a higher mass fraction of CaP phases enhances bioactivity by promoting hydrolysis and generating locally elevated calcium ion concentrations near the surface [377]. Additionally, differences in particle solubility likely contributed to the observed SBF results [378]. Amorphous TCP particles, with higher solubility and larger surface area (Figure 10), more readily released calcium ions and gradually transformed into HAP, accelerating layer formation. While Ca/P ratio is frequently cited as another bioactivity-related factor, its difference between crystalline HAP and amorphous TCP was relatively small and is generally considered secondary [379]. Overall, the slower initial nucleation followed by rapid apatite layer thickening observed for a-Ti coatings could favor a more uniform and higher-quality osteointegration process. This behavior may ultimately have a beneficial impact on the long-term performance of *implants in vivo*.

As previously discussed, coatings fabricated on Ti and TAV substrates demonstrated similar surface property modifications and vertical calcium distribution following particle incorporation (Section 4.2.5). Based on this similarity, and considering the higher roughness of TAV coatings (Table 7), their bioactivity was expected to match or surpass that of Ti coatings. Contrary to this expectation, c-TAV and a-TAV coatings showed negligible HAP growth. Because this lack of bioactivity occurred with both crystalline and amorphous particle additions, the underlying cause is most likely related to phase composition rather than particle crystallinity (Section 4.2.6). The formation of non-stoichiometric titanium oxides on TAV coatings appears to be a decisive factor. During PEO treatment of c-TAV and a-TAV coatings, specific oxide phases likely interacted with CaPs, hindering subsequent HAP precipitation. Aluminum- and vanadium-containing phases may also contribute to this inhibition, albeit to a lesser extent, as their combined atomic ratio relative to Ti in the surface regions was approximately 1:7 (Figure 17). It is plausible that bioactivity improvements similar to those observed for Ti coatings could be achieved on TAV substrates by adjusting PEO parameters or applying different current modes. Supporting this, Wei et al. [292] reported bioactive CaP particle-incorporated oxide coatings on TAV prepared via pulsed-current PEO in a basic electrolyte, while Hong et al. [351] achieved even greater bioactivity than blank coatings under different conditions. Notably, both studies resulted in coatings dominated by anatase and rutile titanium oxide phases.

Despite some conflicting reports, it is generally recognized that crystalline CaPs are preferable in implantology due to their superior cell adhesion and proliferation properties [380] and slower degradation rate [381]. Although assessing the crystallinity of CaP phases incorporated into the coatings was beyond the scope of this study, our findings indicate that amorphous CaP particles may actually yield more favorable outcomes for biomedical applications. This effect is primarily reflected in the increased CaP content within PEO coatings. Moreover, SBF test results for Ti coatings demonstrated that amorphous particle addition enhances oxide coating bioactivity. However, further studies are necessary to confirm whether this conclusion applies universally to substrates with different elemental compositions and to PEO processes under varied conditions.

This study contributes to advancing the understanding and development of the PEO process in suspensions as a versatile approach for fabricating functional coatings. It identifies particle crystallinity as an additional parameter for tailoring PEO coating properties, complementing established factors such as particle size, elemental and phase composition, thermal stability, and electrolyte concentration. In implantology, the most significant benefit of



incorporating amorphous particles into the PEO electrolyte is the substantial increase in calcium content within oxide coatings [185], [382], [383]. Beyond biomedical applications, utilizing amorphous particles in PEO processes could also enhance coating performance in other fields—for example, by improving corrosion resistance through reduced surface porosity [384] or increasing heat resistance via oxide layer thickening [336].

### **4.3. Part III – Fabrication and characterization of CC-HA coatings**

This section presents the research results on the fabrication of CC-HA coatings, addressing all related aspects, including optimization of the PEO process parameters, comprehensive characterization of the final coatings produced according to the developed procedure, preparation and characterization of the PEO baths, and a detailed analysis of the coating growth mechanism. As outlined in the literature review (Section 1.4.2), the strategy of synthesizing CC particles and their subsequent interaction with a phosphate-based electrolyte was identified as the most promising and relatively straightforward approach for co-depositing HA within the PEO bath. This strategy eliminates the need for the separate synthesis, purification, and suspension of individual HA particles, thereby serving as the primary basis for designing operational electrolyte baths. Among the available synthesis techniques for CC particles, the carbonation method was identified as the most advantageous. Carbonation enables the production of CC particles across a wide size range—from several tens of nanometers to several tens of micrometers—while generating neutral suspensions free of ionic impurities typically associated with conventional wet precipitation reactions (e.g.,  $\text{CaCl}_2 + (\text{NH}_4)_2\text{CO}_3$ ). Additionally, this method minimizes the concentration of conducting species in the electrolyte, limited only by the natural dissolution of  $\text{CO}_2$ . For these reasons, carbonation was selected as the preferred method for preparing PEO baths in this study.

#### **4.3.1. Basic interrelations**

The first step in the study on the fabrication of CC-HA coatings was to establish the relationships between key process parameters and the resulting coating properties. The parameters selected for investigation included the concentration of the phosphate-based electrolyte, the concentration of suspended CC particles, and the applied processing voltage. These factors were identified as having a primary influence not only on the characteristics of the final coatings but also on the feasibility of their successful formation. This subsection presents the findings primarily from a practical perspective, without delving deeply into the underlying mechanisms responsible for the observed variations in coating properties caused by changes in processing conditions. Consequently, the use of advanced coating characterization techniques—particularly those aimed at evaluating functional properties—was intentionally omitted at this stage. Instead, the analysis was limited to surface morphology, elemental composition, and, in selected cases, coating thickness and surface roughness. Although the stages of coating growth were briefly outlined as a function of the applied voltage, a more comprehensive investigation of the PEO coating growth mechanism, including the analysis of structural features and comprehensive characterization, is provided in subsequent sections for the optimized CC-HA coating configuration (Sections 4.3.4–4.3.7). Similarly, aspects related to the preparation of the PEO bath, with particular emphasis on the optimal duration of interaction between CC particles and the phosphate electrolyte, are discussed and analyzed in detail later (Section 4.3.2).

The optimal concentration of the base electrolyte was selected in conjunction with the applied voltage, as these parameters collectively govern the size and intensity of micro-discharges during PEO processing. This, in turn, influences coating thickness, internal porosity, surface morphology, and the mechanism of particle incorporation. At the same time, the electrolyte concentration was adjusted to control the molar ratio of phosphates to carbonates in the bath and to regulate the extent of physicochemical transformations that CC particles



undergo upon addition (Section 4.3.2). The concentration of suspended particles was used as an additional tool to achieve the desired calcium content in the final coating.

**Base electrolyte concentration** is the primary factor determining the conductivity of the suspension and is therefore of critical importance to both the progression and the outcome of the PEO process. To select an appropriate concentration, a series of blank  $\text{Na}_2\text{HPO}_4$  solutions with concentrations ranging from 28 to 60 mM were prepared and analyzed based on various surface characteristics of the resulting coatings (Figure 22). Considering the physicochemical transformations that occur in the working suspension after preparation [19]—specifically, the release of carbonate ions into the solution and the chemical adsorption of phosphates onto the CC particle surface (Section 4.3.2)—it would be more objective to include a proportional amount of carbonate ions in the blank solutions. However, the minor conductivity changes associated with the interactions between CC particles and phosphate ions (Section 4.3.2) justifies neglecting these compositional adjustments for the purpose of this analysis. It is important to note that the data obtained from this specific experiment primarily serve to demonstrate the adopted methodological approach, as they isolate the effect of a single variable—the  $\text{Na}_2\text{HPO}_4$  concentration—while omitting the influence of electrical PEO process parameters such as voltage and current density. The separate effect of voltage on surface morphology and elemental composition is addressed later in terms of the current Section 4.3.1.

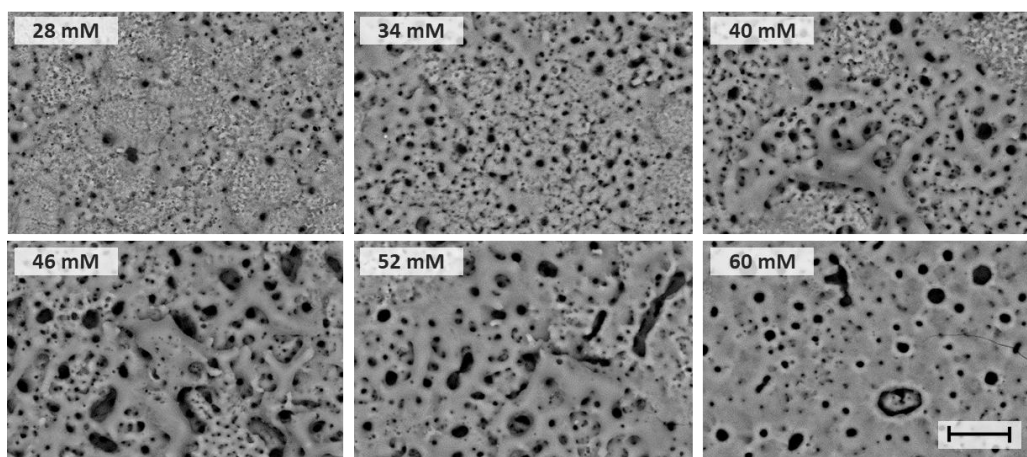


**Figure 22.** Influence of  $\text{Na}_2\text{HPO}_4$  base electrolyte concentration on the surface morphology of Blank coatings under selected electrical parameters (scale bar: 10  $\mu\text{m}$ ).

Increasing the  $\text{Na}_2\text{HPO}_4$  concentration from 28 mM to 46 mM resulted in progressively more porous coatings, with large pores several micrometers in diameter appearing more frequently (Figure 22). In contrast, further increases in electrolyte concentration led to the opposite effect, reducing surface porosity due to the formation of progressively fewer nanopores. The initial increase in porosity can be attributed to the growing intensity and spatial coverage of micro-discharges [237], [286]. However, beyond a certain threshold, the energy of individual sparks becomes sufficiently high to melt larger surrounding areas. Upon solidification, the molten oxide spreads laterally, partially filling adjacent pores and creating localized regions of reduced porosity [289], [385]. This phenomenon was first observed at a  $\text{Na}_2\text{HPO}_4$  concentration of 40 mM and became particularly pronounced at 46 and 52 mM. At 60 mM, surface melting and pore filling became dominant across the entire coating, leading to the formation of a smoother surface. The elevated spark temperatures combined with rapid solidification introduced substantial internal stresses, which ultimately resulted in cracking of the oxide layer. From a processing standpoint, excessively high temperatures during PEO are undesirable for the thermally unstable CC phase, as intensified oxide layer melting promotes particle engulfment by the molten mass. Conversely, excessively low suspension conductivity produces thinner coatings and hinders efficient particle incorporation due to low-intensity discharges [106], [386]. Within this context, the 46 mM  $\text{Na}_2\text{HPO}_4$  blank electrolyte provides an

optimal conductivity level, enabling moderately pronounced surface melting and the development of a homogeneously distributed surface with alternating regions of high and low porosity. Moreover, the increased porosity achieved at 46 mM is advantageous from the perspective of enhancing particle entrapment and physical uptake during coating formation [32], [120], [213].

**Concentration of CC particles.** When selecting the concentration of CC particles, several factors were considered—namely, the molar ratio of carbonates to phosphates in the working suspension (both in the liquid phase and in the suspended particle fraction) and the overall particle concentration. In terms of the molar ratio, an excessive imbalance toward either phosphates or carbonates was deemed undesirable. Regarding particle concentration, it needed to be sufficiently high to impart bioactive and biocompatible properties to the coating, yet not so high as to disrupt oxide layer growth, compromise its structural integrity, or render the coating overly brittle [223]. The experiments were based on empirical observations obtained from a series of PEO coatings fabricated in working suspensions containing 46 mM  $\text{Na}_2\text{HPO}_4$  and CC particle concentrations ranging from 0 to 84 mM. The resulting coatings were analyzed for elemental composition and surface morphological features, and chemical analyses of the suspensions were also conducted (Figure 23).

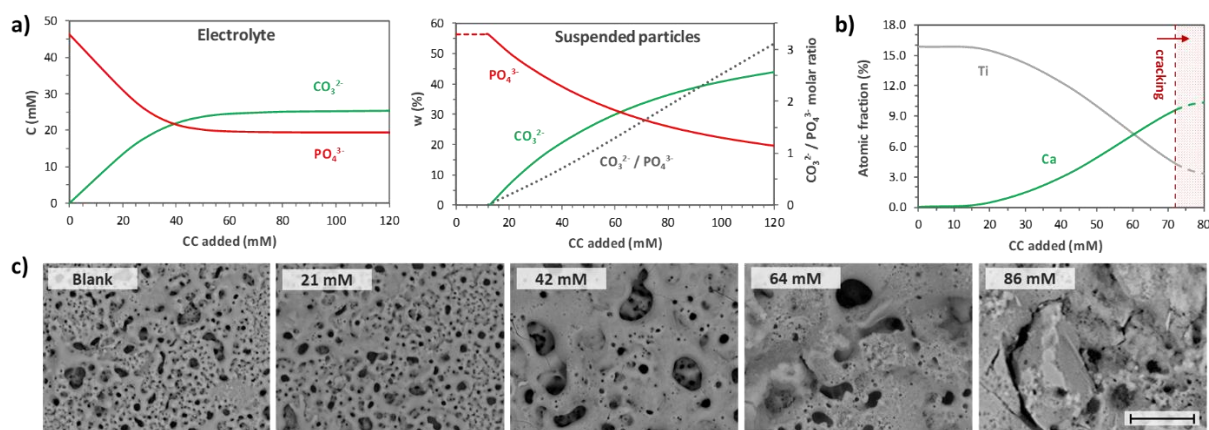


**Figure 23.** Summary of the effects of varying CC particle concentration in the working PEO bath containing 46 mM  $\text{Na}_2\text{HPO}_4$  and aged for 7 days after preparation: (a) composition of the suspension medium and dispersed phase; (b) Ti and Ca content determined by EDX analysis of coating surface regions (dotted line indicates the concentration above which intensive cracking occurs); (c) coating surface morphology (scale bar: 20  $\mu\text{m}$ ).

From the plots shown in Figure 23a, it can be observed that the concentrations of carbonate and phosphate ions in the electrolyte change linearly as the CC particle concentration increases from 0 to approximately 25 mM. Beyond this point, the rate of change gradually slows until reaching around 50 mM, after which the ion concentrations remain constant regardless of additional CC particle content. These observations indicate the establishment of a thermodynamic equilibrium between the CC particles and the dissolved carbonate ions, which suppresses further chemisorption and phosphate–carbonate ion exchange [202], [209]. As a result, large deviations in the concentration of dissolved species are effectively prevented. Changes in the mass fraction of phosphates and carbonates within the suspended particles exhibit more complex behavior but remain consistent with the trends observed for ionic concentrations. Specifically, when the concentration of CC particles is below approximately 12 mM, their interaction with phosphate ions likely follows the mechanisms illustrated in Figure 29(1), Section 4.3.2. However, this amount of CC appears insufficient to saturate the electrolyte with carbonate ions and to prevent the complete transformation of the suspended phase into HA. This also explains the strictly linear regions observed on the ion concentration plot. Correspondingly, a rapid increase in the carbonate mass fraction within the particles is observed when the CC concentration in suspension is raised above ~12 mM, followed by a gradual slowdown as the solution approaches saturation at approximately 50 mM. Increasing the CC

particle concentration beyond this saturation point does not induce additional physicochemical changes in the suspension and merely results in the “dilution” of HA.

From the perspective of particle chemical composition, the use of CC concentrations in the range of 30–80 mM can be considered practical, corresponding to a carbonate-to-phosphate ratio of 0.5–2.0. Analysis of the coatings revealed a slow increase in calcium content (Figure 23b) and no significant differences in surface morphology (Figure 23c) compared with the Blank coating when suspensions with CC concentrations up to ~30 mM were used. However, beyond this threshold, pronounced changes were observed, manifested by increased porosity and a higher number of incorporated particles. It appears that preparing more concentrated working suspensions results in a smaller fraction of CC particles undergoing physicochemical transformations, including particle size modification. As described later in Section 4.3.2, the as-synthesized CC particles had an initial size of ~175 nm (Figure 28), and this size reduction during processing could facilitate their incorporation into the growing oxide layer. This effect, in turn, promotes a disproportionately higher coating growth rate compared with the nominal increase in CC concentration. At CC concentrations above 60 mM, calcium becomes the dominant element in the outer layers of the coating. Nevertheless, further increases in its atomic fraction gradually slow down, which can be attributed to approaching a critical particle concentration beyond which stable oxide growth cannot be maintained. A critical transition occurs when the CC concentration exceeds 70 mM, where widespread cracking appears across the surface (Figure 23c). At this point, the Ca/Ti ratio surpasses 2 (Figure 23b), indicating excessive incorporation of CC and HA phases, which leads to increased coating brittleness [314], [387]. From a practical standpoint, such cracks are highly undesirable because they compromise implant integrity through potential surface flaking and simultaneously reduce the corrosion resistance of the final product. Therefore, a “safe” CC concentration in the suspension that ensures both high calcium incorporation and crack-free coatings should not exceed 60–65 mM.

**Limiting voltage and coating growth mechanism.** Figure 24 illustrates the evolution of surface morphology as the limiting voltage of the PEO process was increased from 320 to 480 V in 20 V increments, with distinct surface features observed at each voltage level. At 320 V, the coating exhibited low porosity and retained periodic traces of sandpaper polishing, a characteristic typically associated with coatings formed just above the dielectric breakdown potential [323]. This coating demonstrated the lowest thickness and roughness, the highest titanium content, and negligible calcium incorporation (Figure 25a-c). Nonetheless, small amounts of phosphorus and carbon were detected, indicating limited incorporation of dissolved phosphate and carbonate species into the oxide layer. Notable particle incorporation into the oxide coating commenced at 340 V, where the atomic fraction of incorporated particles exceeded 1%, accompanied by a sharp decrease in the C/Ca ratio. At this voltage, polishing marks on the surface were no longer apparent, and medium-sized pores appeared along with clusters of solidified oxide forming the pore walls [127]. These structural features likely correspond to localized sites of CC-HA particle incorporation. However, at this stage, such features remained spatially confined and alternated with more prevalent nanoporous regions across the surface.

At 360 V, the increased size of micro-discharges facilitated the formation of medium-sized pores distributed uniformly across the entire surface, contributing to further surface roughening and a more pronounced thickening of the oxide layer (Figure 25d). Beyond 360 V, the atomic fraction of phosphorus ceased to increase and even showed a slight decreasing trend, while the carbon content continued to rise, albeit at a slower rate. Concurrently, despite the nearly constant phosphorus level, the Ca/P ratio increased sharply (Figure 25c). Following the voltage increase beyond 360 V, a rapid growth in pore size was observed, persisting up to 420 V, where the largest pores reached approximately 10  $\mu\text{m}$  in diameter. However, the overall porosity appeared to plateau after 380 V, accompanied by a decrease in the number of small and medium-sized pores. Notably, starting from 380 V, the coating surface began to exhibit a bilayer

structure, consisting of a basal layer with smaller pores ( $\sim 1\text{--}2\ \mu\text{m}$ ) and a top layer characterized by larger pores. Another distinctive feature of all coatings formed at voltages of 380 V and above is the presence of discrete concave pores on the surface of the solidified oxide layer.

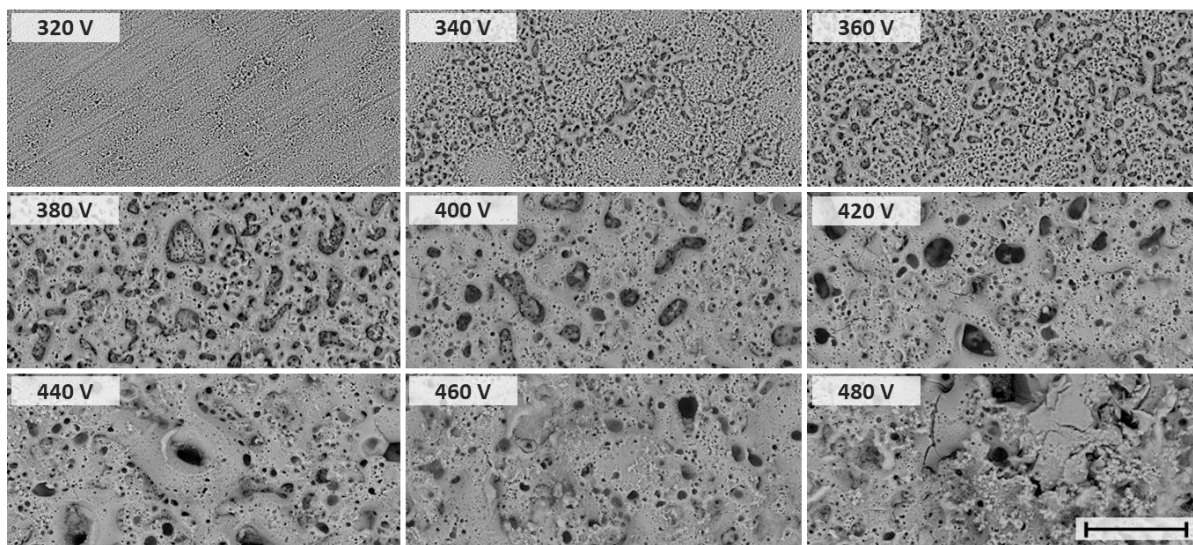


**Figure 24.** Effect of the limiting voltage in the PEO process on the surface morphology of coatings prepared in a 64 mM CC suspension aged for 7 days after the addition of 46 mM  $\text{Na}_2\text{HPO}_4$  (scale bar: 50  $\mu\text{m}$ ).

Beyond 420 V, the overall surface porosity continued to decline, further promoted by the disappearance of large pores. Simultaneously, at 440 V, prominent particulate inclusions appeared on the surface, most likely representing localized agglomerations of incorporated CC-HA particles. These structures likely contributed to the reduction in porosity by filling available pore volume. The particulate features became progressively larger and more abundant at 460 V and, by 480 V, covered approximately half of the surface area. Meanwhile, an accelerated increase in the calcium atomic fraction and a decrease in the oxygen atomic fraction took place at voltages above 440 V, leading to a pronounced rise in both the O/Ti and Ca/Ti ratios. In this context, the observed slowdown in the growth of the Ca/P ratio indicates that CC-HA particles became the dominant building material for newly formed upper coating layers after 440 V.

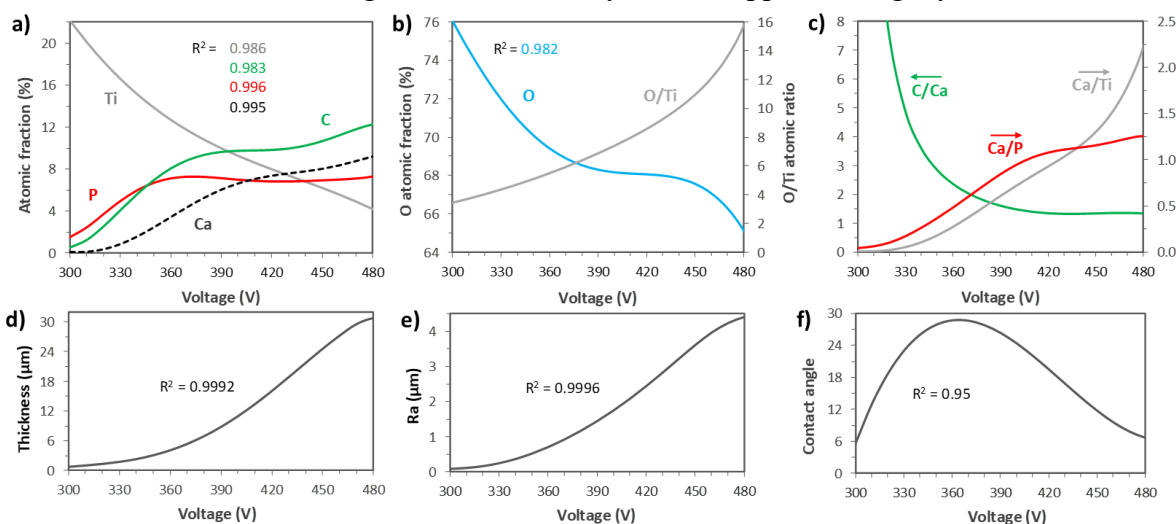


**Figure 25.** Summary of the effects of varying the limiting voltage of the PEO process on the properties of coatings prepared in a 64 mM CC suspension containing 46 mM  $\text{Na}_2\text{HPO}_4$ : elemental composition determined by EDX analysis of coating surface regions; (a) titanium, carbon, calcium, phosphorus; (b) oxygen content and O/Ti ratio; (c) C/Ca, Ca/P, and Ca/Ti ratios (vertical axis directions are indicated by bullets); (d) oxide layer thickness; (e) average surface roughness; (f) water contact angle.



Analysis of coating thickness evolution (Figure 25d) reveals three distinct growth stages: (i) slow thickening up to 360 V, associated with initial particle incorporation and the formation of a simple monolayer structure; (ii) accelerated thickening between 360 and 460 V, where successive particle-rich layers formed atop the existing oxide as discharge activity intensified; and (iii) a slowdown in thickness growth beyond 460 V, indicating the approach of a critical voltage. At 480 V, the coating thickness reached its maximum achievable value, while further discharge intensification compromised the integrity of the oxide layer, leading to crack formation. Surface roughness (Figure 25e) exhibited a similar trend, increasing proportionally to coating thickness across the entire voltage range. In contrast, the contact angle displayed a more complex behavior: at 320 V, the coating consisted of a thin titanium dioxide layer with a relatively flat surface and fine porosity, allowing water to spread easily and rendering the surface superhydrophilic [305]. With increasing voltage, the formation of larger pores and local elevations acted as physical barriers to droplet spreading, causing a rise in contact angle (Figure 25f). However, beginning at 360 V, this effect was gradually offset by the growing mass fraction of CC and HA phases in the surface layers, leading to a progressive decrease in contact angle and ultimately resulting in a hydrophilic surface at 480 V. Considering these findings, the optimal voltage for the fabrication of CC-HA coatings lies within a relatively narrow range of 440–460 V. This interval satisfies three critical conditions simultaneously: (1) a high degree of particle incorporation into the coating, as evidenced by a Ca/Ti ratio exceeding 1.0; (2) partially reactive incorporation of CC-HA particles forming the outer layer of the coating; and (3) the absence of structural defects such as cracking.

#### 4.3.2. Preparation and characterization of PEO baths

This section addresses the preparation and characterization of the working PEO baths, whose optimal compositions were identified in Section 4.3.1, and which were later utilized for fabricating the final CC-HA PEO coatings. The Blank bath preparation followed a simple procedure (Section 3.1), resulting in a stable  $\text{Na}_2\text{HPO}_4$  solution that showed no detectable changes in pH, conductivity, or phosphate concentration over time. In contrast, preparing the CC-HA bath required multiple additional steps, including the synthesis of CC particles and their coprecipitation with HA—processes that are considerably more complex and demand precise control of several parameters [196], [209]. Therefore, this section is devoted primarily to the preparation and detailed characterization of the CC-HA bath.

**CC particle synthesis.** One of the essential components of the CC-HA electrolyte bath, the CC stock suspension, was synthesized via a carbonation process. Throughout the reaction, electrical conductivity, temperature, and pH were monitored and recorded on a unified timeline (Figure 26). Among these parameters, pH variation provided the most reliable indication of the stoichiometric point, which occurred 19.6 minutes after initiating  $\text{CO}_2$  introduction, corresponding to a pH of 7.0. Initially, the pH remained steady (12.5–12.7) up to approximately 12 minutes, reflecting a rapid release of  $\text{OH}^-$  ions as the dissolution of  $\text{Ca}(\text{OH})_2$  exceeded the rates of  $\text{CO}_2$  adsorption and CC precipitation [275], [388]. Conductivity showed a comparable trend, with a measurable decline beginning around 9 minutes due to its linear scale of measurement compared to the logarithmic pH scale. Between 0–17 minutes, dissolved  $\text{Ca}^{2+}$  concentration decreased gradually, while conductivity reduction indicated a relatively constant CC formation rate.

Once the pH dropped below 12, only trace amounts of  $\text{Ca}(\text{OH})_2$  remained, and a sharp pH decrease signaled a slowdown in reaction kinetics. This deceleration is likely linked to both reduced  $\text{CO}_2$  solubility/adsorption and diminished collision probability between  $\text{Ca}^{2+}$  and  $\text{CO}_3^{2-}$  ions [275], [388]. At approximately pH 10, conductivity reached its minimum; subsequent  $\text{CO}_2$  introduction caused a slight conductivity rise, possibly due to (i) conversion of carbonates to bicarbonates, (ii) changes in the electrical double layer of CC particles, or (iii) increased ionic concentration caused by enhanced CC solubility at lower pH levels.

Following completion, conductivity stabilized at  $\sim 0.3 \text{ mS}\cdot\text{cm}^{-1}$ , while pH required several additional hours to fully stabilize at 7.22 (Table 9). The reaction medium exhibited a  $\sim 2^\circ\text{C}$  temperature increase, consistent with the exothermic nature of CC formation [277], [388], [389]. The overall temperature profile was linear, suggesting a uniform reaction rate, with slight deviations early on likely reflecting  $\text{CO}_2$  saturation of the solution. Near the stoichiometric point, temperature stabilization further supported the observed kinetic slowdown.

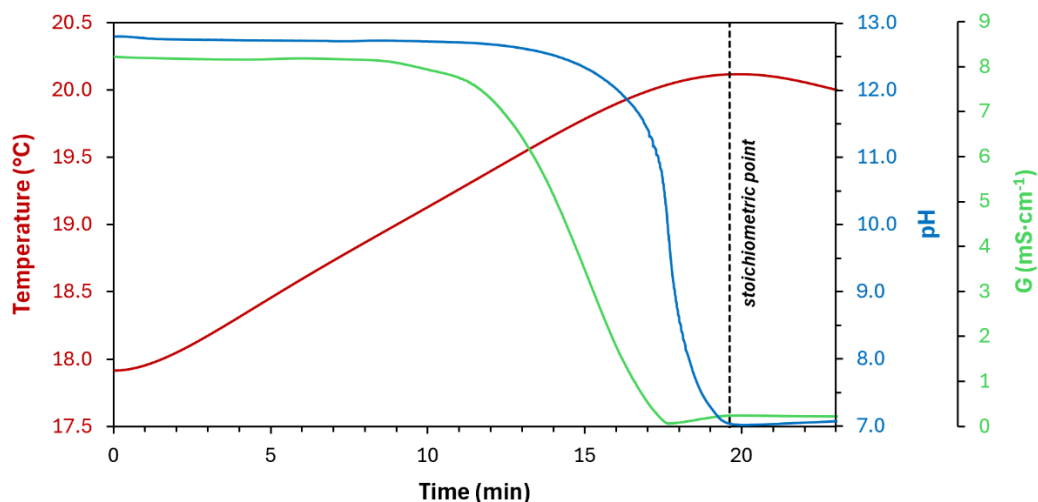


**Figure 26.** Variations in electrical conductivity, temperature, and pH during the carbonation process used to synthesize the CC stock suspension.

**Preparation and characterization of PEO baths.** For the characterization process, all solutions and suspensions used during different stages of PEO coating preparation were analyzed, including the CC stock suspension, Blank bath, and CC-HA bath. Their properties were evaluated from multiple perspectives, with results summarized in Figure 27, Figure 28, Figure 29 and Table 9, Table 10, Table 11. Following carbonation synthesis, part of the CC stock suspension was introduced into a  $\text{Na}_2\text{HPO}_4$  solution, yielding the CC-HA precursor bath. This bath contained 46 mM phosphate ions and 64 mM CC, corresponding to a CC mass fraction of  $6.4 \text{ g}\cdot\text{L}^{-1}$ . This concentration falls within the typical particle loading range ( $1\text{--}20 \text{ g}\cdot\text{L}^{-1}$ ) commonly employed in PEO processes [30].

The literature contains extensive data on the interactions between CC and phosphate-based electrolytes. However, reported studies differ substantially in reaction conditions, which strongly influence outcomes, particularly reaction time. Factors likely governing the reaction pathway include the pH and temperature of the medium, mixing efficiency, CC particle size and morphology, the molar ratio of CC to phosphate species, and the presence of auxiliary additives. Within the CC–phosphate system, multiple physicochemical processes—such as dissolution–precipitation, chemisorption, and heterocoagulation—can occur simultaneously. Consequently, reported reaction kinetics vary significantly, with complete transformations ranging from a few minutes to several weeks. To date, no comprehensive study has systematically established kinetic relationships for CC–phosphate interactions while accounting for multiple influential variables.

To some degree, the optimal maturation time can be inferred through multifactorial analysis of discrete data reported under varying experimental conditions. A relevant reference is the study by Ishikawa et al. [206], who used  $\text{Na}_2\text{HPO}_4$  to react with CC—an electrolyte component also employed in this work for preparing the CC-HA bath. Based on XRD phase analysis, they concluded that full transformation required 14 days, although the CC phase was no longer detectable on XRD patterns after just 4 days. It is important to note that their experimental setup differed from the present study, involving a higher temperature ( $60^\circ\text{C}$ ), no mixing, and bulk CC. Further insights are provided by Yanyan et al. [204], who demonstrated a strong pH dependence of the transformation kinetics. In their experiments, submicron- and

nanosized CC particles were exposed to phosphate species in the presence of amino acids at 37 °C for 10 days. The conversion to HA was most rapid at pH 3, slower at pH 6, and markedly reduced at pH  $\geq 7$  under otherwise comparable conditions.

Another study demonstrated that increasing phosphate concentration can significantly accelerate the reaction [210]. When the phosphate concentration was four times lower than that of CC, most of the transformation occurred within 7 hours, reaching near-complete conversion after 24 hours under otherwise comparable conditions. Similar findings were reported by Yoshimura et al. [197] and Eliassi et al. [196]. A particularly illustrative example is provided by Ashokan et al. [211], who examined micron-sized CC reacting with diammonium hydrogen phosphate at pH 10 over periods of 30 minutes to 2 hours, investigating the effects of temperature and stirring. In stirred suspensions, full conversion was achieved within this short timeframe regardless of stirring intensity, whereas non-stirred systems exhibited only minor transformation, retaining most of the suspended CC. Temperature also played a key role: reaction rates increased significantly at 80 °C and even more under hydrothermal conditions at 160 °C, compared to 50 °C or room temperature. Yoshimura et al. [197] likewise concluded that elevated temperatures promote the CC–phosphate reaction.

Considering the findings reported in the literature [196], [197], [204], [206], [210], [211] and the specific conditions applied in this study—alkaline pH, moderate mechanical stirring, CC particles of  $\sim 100$  nm, a carbonate-to-phosphate molar ratio of 1.4, and relatively low reaction temperature—a moderate maturation period is most likely. Under these conditions, the reaction is expected to reach completion within several days and, with higher certainty, within one week. However, certain factors may have a stronger impact on the transformation process and may also interact synergistically or antagonistically. To validate these assumptions and more accurately determine the optimal maturation duration, an empirical approach was adopted. The evolution of the CC-HA bath was monitored by tracking pH changes, dissolved phosphate and carbonate concentrations, particle size distribution, and the mass fractions of phosphate and carbonate phases in the resulting solids.

Based on the results shown in Figure 27, a maturation period of 48 hours was determined to be the minimum required for completing all physicochemical interactions between CC particles and the phosphate electrolyte. This duration was selected by analyzing the temporal evolution of key parameters: although a rapid increase in reaction dynamics occurred within the first six hours, only minor changes were observed after 24 hours, and full stabilization was reached at 48 hours. Notably, the monitored parameters exhibited strong synchronicity. Particle size changes closely mirrored the increase in phosphate mass fraction within the suspended solids, while pH variations correlated with the release of carbonate ions. Overall, these experimental observations are consistent with trends previously reported in the literature on CC–phosphate reactions [196], [197], [204], [206], [210], [211].

The observed pH increase from 9.24 to 9.82 (Table 9) is consistent with findings reported by Yanyan et al. [204] and can be attributed to the conversion of  $\text{CO}_3^{2-}$  ions into  $\text{HCO}_3^-$  through proton capture, with the protons originating from water dissociation. This observation supports the overall reaction stoichiometry proposed in [204], which is also valid under the conditions of this study and can be expressed as shown in Eq. 5. At the start of the maturation process (5 minutes after preparation), the CC-HA bath exhibited a slightly lower pH compared to the Blank bath (Table 9), primarily due to dilution caused by introducing the neutral CC suspension. Conductivity was the only parameter that remained largely unchanged throughout the 48-hour maturation period, decreasing by just 2.5% from its initial value. The conductivity of the PEO bath is governed by ions such as  $\text{PO}_4^{3-}$ ,  $\text{HPO}_4^{2-}$ ,  $\text{CO}_3^{2-}$ ,  $\text{HCO}_3^-$ ,  $\text{OH}^-$ ,  $\text{H}^+$ , and  $\text{Na}^+$ , with sodium concentration remaining constant throughout the reaction (Eq. 5). These results confirm that the selected CC-HA bath composition provides a stable suspension comparable to the Blank bath. Consequently, no corrective measures—such as additional dilution or the inclusion of conductive additives—are necessary to match the conductivity of the two baths. As summarized in Table 9, the final conductivity difference between the CC-HA and Blank

baths is only about 1%, which is sufficient to maintain comparable plasma temperatures and thus enable a fair assessment of the resulting coating properties.

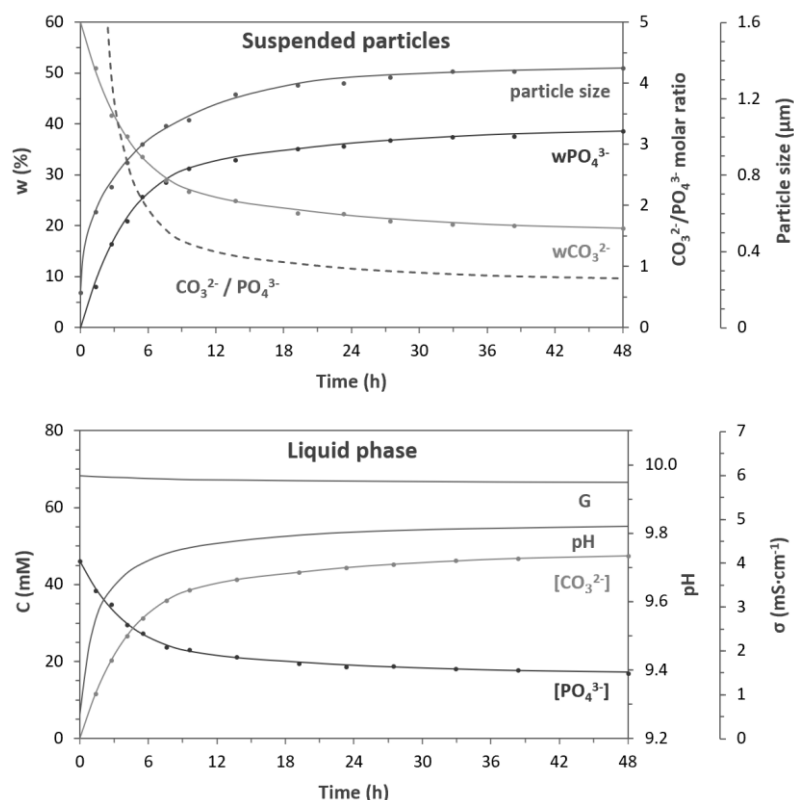


**Figure 27.** Observed trends in the CC-HA PEO bath over 48 hours following component mixing, maintained at 10°C with 300 rpm stirring.

**Table 9.** Comparative overview of the CC stock suspension and PEO bath compositions employed for coating fabrication.

Parameter	CC stock suspension	Blank bath	CC-HA bath	
			As-prepared <sup>a</sup>	After 48 h
G (mS·cm <sup>-1</sup> )	0.28	5.88	5.97	5.82
pH	7.22	9.31	9.24	9.82
Zeta potential (mV)	16.3 ± 0.4	n/a	3.7 ± 0.9	-21.8 ± 0.3
Particle size (nm)	175 ± 10	n/a	335 ± 20	1350 ± 40

<sup>a</sup> 5 minutes after mixing CC stock suspension with phosphate electrolyte



Table 10 provides a more detailed overview of the chemical composition changes in the PEO bath during maturation. When the mass fractions of carbonates and phosphates ( $w\text{CO}_3^{2-}$  and  $w\text{PO}_4^{3-}$ ) were recalculated as wCC and wHA, their combined value (wCC+HA, %) remained close to 100% throughout the reaction, indicating stoichiometric co-precipitation of the HA phase. At later stages, however, a slight upward deviation in wCC+HA suggests that a minor fraction of phosphate may have also precipitated as other CaP phases, such as TCP. The chemical transformations in the liquid phase were inversely related to those in the suspended particles. As more phosphate ions precipitated into HA, dissolved carbonate concentration increased. After 48 hours, this ion exchange reduced phosphate content in solution by more than 50%, leaving 36.96% of the initial amount, while the dissolved carbonate-to-phosphate ratio ( $\text{CO}_3^{2-}/\text{PO}_4^{3-}$ ) reached approximately 2.8. Concurrently, the final wCC fraction in the solids dropped to 32.55%. Variations in calcium mass fraction were not analyzed, as theoretical Ca contents for CC (40.0%), HA (39.9%), and TCP (38.8%) are nearly identical, providing limited insight into phase transformation dynamics.

According to the stoichiometry of HA, the formation of one molecule requires 10  $\text{Ca}^{2+}$  ions and 6  $\text{PO}_4^{3-}$  ions (Eq. 5), yielding a characteristic Ca/P molar ratio of 1.667 [390]. In the

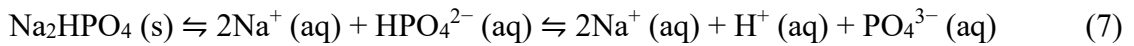


CC-HA system,  $\text{Ca}^{2+}$  is supplied via the dissociation of poorly soluble CC (Eq. 6), while phosphate originates from the dissociation of  $\text{Na}_2\text{HPO}_4$  (Eq. 7). As 6  $\text{PO}_4^{3-}$  ions are incorporated into HA, 10  $\text{CO}_3^{2-}$  ions are released into the solution. Throughout the reaction, the measured ratio of released carbonate to adsorbed phosphate ( $\text{CO}_3^{2-}/\text{PO}_4^{3-}$  ads., Table 10) remained close to 1.667, indirectly confirming the near-stoichiometric nature of HA co-precipitation. However, considering the initial bath composition, it is evident that the solid-phase transformation remained incomplete. Theoretically, 46 mM of phosphate could dissolve up to 76.7 mM of CC, derived by applying the 10:6 Ca/P ratio (i.e.,  $46 \text{ mM} \times 10 / 6$ ). This value exceeds the actual CC concentration in the bath by 12.7 mM, suggesting that complete conversion was chemically feasible. In practice, though, only partial CC transformation was observed. The final carbonate-to-phosphate molar ratio ( $x\text{CO}_3^{2-}/x\text{PO}_4^{3-}$ ) was  $\sim 0.8$ , corresponding to phase molar fractions of  $x\text{CC} = 0.828$  and  $x\text{HA} = 0.172$ . This indicates that approximately 4.8 CC molecules remain for every HA molecule formed. This limited conversion can likely be attributed to secondary physicochemical processes, particularly the chemisorption of phosphate species onto CC particle surfaces. This surface interaction likely forms a passivating layer that inhibits further CC dissolution. Literature data [209] support this mechanism, with chemisorption reactions described by Eqs. 8 and 9.

**Table 10.** Summary of chemical transformations occurring within the CC-HA bath.

Parameter	Time (hours)				
	0*	2	4	8	48
Suspended particles					
wCO <sub>3</sub> <sup>2-</sup> (%)	59.98	46.46	37.67	28.77	19.51
wPO <sub>4</sub> <sup>3-</sup> (%)	-	12.86	21.24	29.72	38.57
wCC (%)	100.00	77.49	62.83	47.99	32.55
wHA (%)	-	22.67	37.44	52.39	68.00
wCC+HA (%)	100.00	100.17	100.27	100.38	100.55
xCO <sub>3</sub> <sup>2-</sup>	1.000	0.851	0.737	0.605	0.445
xPO <sub>4</sub> <sup>3-</sup>	-	0.149	0.263	0.395	0.555
xCO <sub>3</sub> <sup>2-</sup> /xPO <sub>4</sub> <sup>3-</sup>	-	5.718	2.808	1.532	0.801
xCC	1.000	0.972	0.944	0.902	0.828
xHA	-	0.028	0.056	0.098	0.172
xCC/HA	-	34.3	16.8	9.2	4.8
Composition	CaCO <sub>3</sub>	Ca <sub>10</sub> (PO <sub>4</sub> ) <sub>6</sub> (OH) <sub>2</sub>	Ca <sub>10</sub> (PO <sub>4</sub> ) <sub>6</sub> (OH) <sub>2</sub>	Ca <sub>10</sub> (PO <sub>4</sub> ) <sub>6</sub> (OH) <sub>2</sub>	Ca <sub>10</sub> (PO <sub>4</sub> ) <sub>6</sub> (OH) <sub>2</sub>
		+	+	+	+
		34.3 CaCO <sub>3</sub>	16.8 CaCO <sub>3</sub>	9.2 CaCO <sub>3</sub>	4.8 CaCO <sub>3</sub>
Liquid phase					
CO <sub>3</sub> <sup>2-</sup> (mM)	-	15.85	26.17	36.62	47.53
PO <sub>4</sub> <sup>3-</sup> (mM)	46.00	36.42	30.23	23.93	17.00
CO <sub>3</sub> <sup>2-</sup> / PO <sub>4</sub> <sup>3-</sup>	-	0.435	0.866	1.530	2.795
PO <sub>4</sub> <sup>3-</sup> left (%)	100.00	79.17	65.72	52.03	36.96
PO <sub>4</sub> <sup>3-</sup> ads. (mM)	-	9.58	15.77	22.07	29.00
CO <sub>3</sub> <sup>2-</sup> / PO <sub>4</sub> <sup>3-</sup> ads.	-	1.654	1.660	1.659	1.639

\*theoretical values calculated for infinitely small time after mixing the reactants; “-” not detected



where  $2r = n(m-3)$

To better capture the physicochemical changes occurring during the interaction of CC with  $\text{Na}_2\text{HPO}_4$  electrolyte, several additional particle characteristics were analyzed, including surface morphology, size distribution, zeta potential, functional groups, phase composition, and crystallinity (Figure 28, Table 9). TEM images showed that CC particles synthesized via carbonation had a cubic morphology typical of calcite crystals, with individual particle sizes around 50 nm. These findings were corroborated by XRD, which displayed all characteristic

peaks of calcite, and by FTIR, where carbonate vibrational modes ( $v_2$ ,  $v_3$ , and  $v_4$ ) appeared at  $\sim 875$ ,  $1400$ , and  $715\text{ cm}^{-1}$ , respectively—consistent with literature data (Table 11). Dynamic light scattering measurements revealed a larger average particle size of  $175\text{ nm}$  in suspension, primarily due to optical scattering effects from cubic crystals and, to a lesser extent, mild agglomeration. The measured zeta potential of  $16\text{ mV}$  (Table 9) suggests moderate electrostatic repulsion, preventing significant aggregation. The absence of additional XRD peaks, such as those for  $\text{Ca}(\text{OH})_2$  [391], further confirms that the carbonation process was successfully completed without by-product formation.

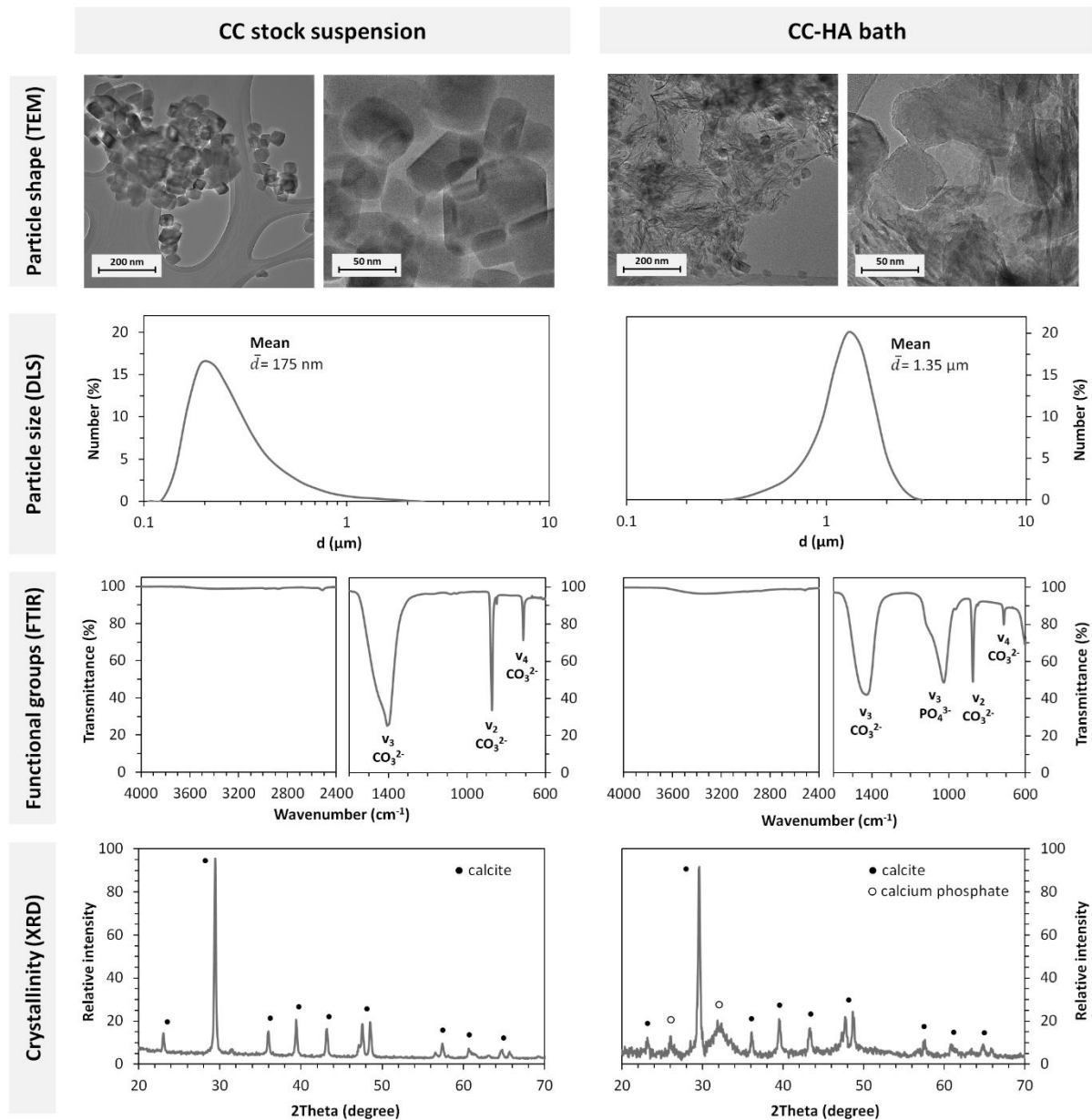


**Figure 28.** Properties of synthesized CC particles and the CC-HA bath analyzed 48 hours after combining  $64\text{ mM}$  CC stock suspension with  $46\text{ mM}$  phosphate solution.

After 48 hours of reaction, notable changes in particle morphology were observed. Some cubic CC crystals transformed into whisker-like or acicular structures, while others exhibited surface roughening. The formation of elongated particles likely resulted from CC dissolution and subsequent HA precipitation in the bulk solution [196], whereas surface roughening may be attributed to phosphate adsorption on CC crystal surfaces [209]. A significant portion of CC particles largely retained their original cubic shape, likely because their smooth, defect-free surfaces limited phosphate penetration and protected inner layers from transformation. XRD

analysis revealed two additional peaks at  $\sim 26^\circ$  and  $32^\circ$ , characteristic of HA, confirming partial CC conversion. The broad and low-intensity nature of these peaks indicates that the newly formed HA phase possesses low crystallinity, approaching an amorphous state. This observation aligns with previous reports on CC-to-HA conversion in phosphate electrolytes [196], [204], [211]. FTIR spectra provided further evidence: the appearance of the  $\nu_3\text{PO}_4^{3-}$  band at  $1025\text{ cm}^{-1}$  and a shift of the  $\nu_3\text{CO}_3^{2-}$  band to  $1435\text{ cm}^{-1}$  (Table 11) support the formation of HA or carbonate-substituted HA ( $\text{CO}_3\text{-HA}$ ). Since the  $\nu_4\text{CO}_3^{2-}$  vibration is absent in carbonate-substituted apatite, the observed  $\sim$ twofold decrease in the  $715\text{ cm}^{-1}$  band intensity compared to the initial CC signal indicates partial HA formation. However, the lack of a detectable O–H vibration near  $3570\text{ cm}^{-1}$  [392] suggests a low hydroxyl content in the co-precipitated phase, implying that the product may consist of a mixture of HA and TCP.

**Table 11.** Characteristic FTIR peak positions ( $\pm 5\text{ cm}^{-1}$ ) and their corresponding vibrational modes for compounds identified from literature and experiments.

Compounds	Phosphate		Carbonate		Reference
	$\nu_3$	$\nu_2$	$\nu_3$	$\nu_4$	
CC	-	875	1420	715	[393]
HA	1045	-	-	-	[394]
$\text{CO}_3\text{-HA}$	1035	875	1455	-	[395]
CC <sup>a</sup>	-	870	1405	715	Figure 28
CC-HA <sup>a</sup>	1025	875	1435	715	Figure 28

<sup>a</sup> synthesized in the present study

During the reaction between CC and the phosphate electrolyte, suspended particles progressively agglomerated, resulting in an average hydrodynamic diameter of  $1.35\text{ }\mu\text{m}$ . This increase is partly due to the co-precipitation of irregularly shaped HA but is also strongly influenced by the electrokinetic properties of CC and HA. The isoelectric point (IEP) of HA is typically around 7 [396], though it can range from  $\sim 4$  to 9 depending on synthesis conditions and ionic substitutions [397], [398]. Carbonate-rich HA is known to shift its IEP toward higher pH values [397]. CC, on the other hand, generally exhibits IEPs near 10 [109]–[111], occasionally exceeding 11 [399]. Consequently, in the phosphate electrolyte, where pH rises from 9.24 to 9.82 (Table 9), CC particles are expected to remain slightly positively charged, while HA maintains a negative charge [181]. This charge disparity promotes electrostatic attraction between CC and HA, driving heterocoagulation [179], [400].

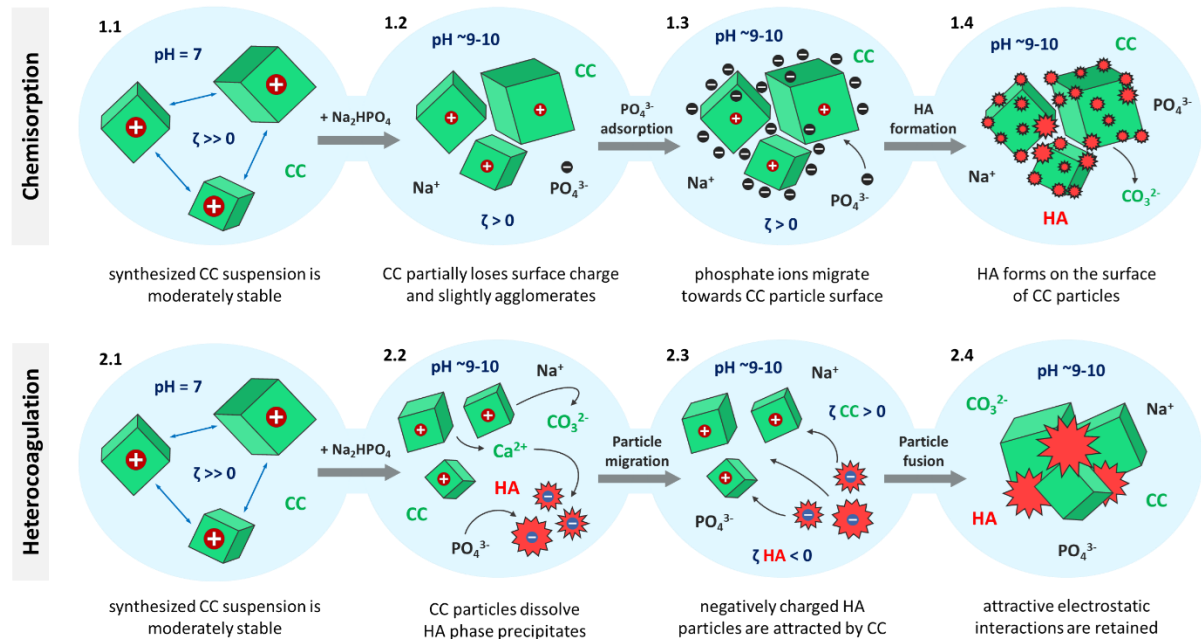


**Figure 29.** Schematic representation of two potential mechanisms influencing interactions between CC particles and phosphate electrolyte during CC-HA PEO bath preparation ( $\zeta$  – zeta potential).

Particle geometry further facilitates this process: whisker-like HA structures (Figure 28) can entrap cubic CC particles, forming compact aggregates [401]. Experimentally, CC displayed a near-neutral zeta potential (3.7 mV) immediately after CC-HA bath preparation, leading to a twofold increase in particle size. At one stage of the reaction, zeta potential reached 0 mV (Table 9), likely weakening electrostatic repulsion and promoting further agglomeration. After 48 hours, HA co-precipitation rendered the zeta potential moderately negative ( $-21.8 \pm 0.3$  mV), improving bath stability and enhancing particle mobility during PEO processing by facilitating electrophoretic migration toward the anode [180]. The final particle size of  $1.35 \mu\text{m}$  is likely well-suited for the PEO process, matching typical pore dimensions on PEO coating surfaces [186], [189], [212].

Based on the results discussed in this section, it can be asserted that interactions between CC and phosphates are inherently complex, but primarily driven by two parallel mechanisms: chemisorption on the CC particle surface and dissolution-precipitation, with the latter further driving heterocoagulation of CC with co-precipitated HA particles. A visual representation of these two mechanisms is presented in Figure 29.

#### 4.3.3. Characterization of the PEO process

PEO treatments were performed in both Blank and CC-HA baths, producing coatings referred to as Blank and CC-HA layers, respectively. The process evolution was assessed by monitoring voltage and current profiles over time (Figure 30). Vertical dashed lines denote the point at which the limiting voltage ( $V_{\text{lim}} = 450$  V) was reached, marking the transition from galvanostatic to potentiostatic control and initiating the potentiostatic aging stage [402]. Due to the pulsed power supply, current–time and voltage–time responses are displayed as shaded regions rather than continuous traces typical of DC PEO [129], [403], [404]. Throughout the process, the current dropped to zero during each off-phase, whereas voltage partially decreased before the next pulse. For both coatings, the amplitude of this transient voltage drop increased progressively until reaching  $V_{\text{lim}}$  and then gradually diminished toward the end of oxidation. This behavior reflects the increased energy required to achieve higher voltages as the oxide layer thickens, elevating the potential difference between the substrate and electrolyte. Upon reaching  $V_{\text{lim}}$ , coating growth approached its maximum thickness under the applied conditions, and the subsequent stage primarily involved structural ordering and stabilization of the oxide layer [405].

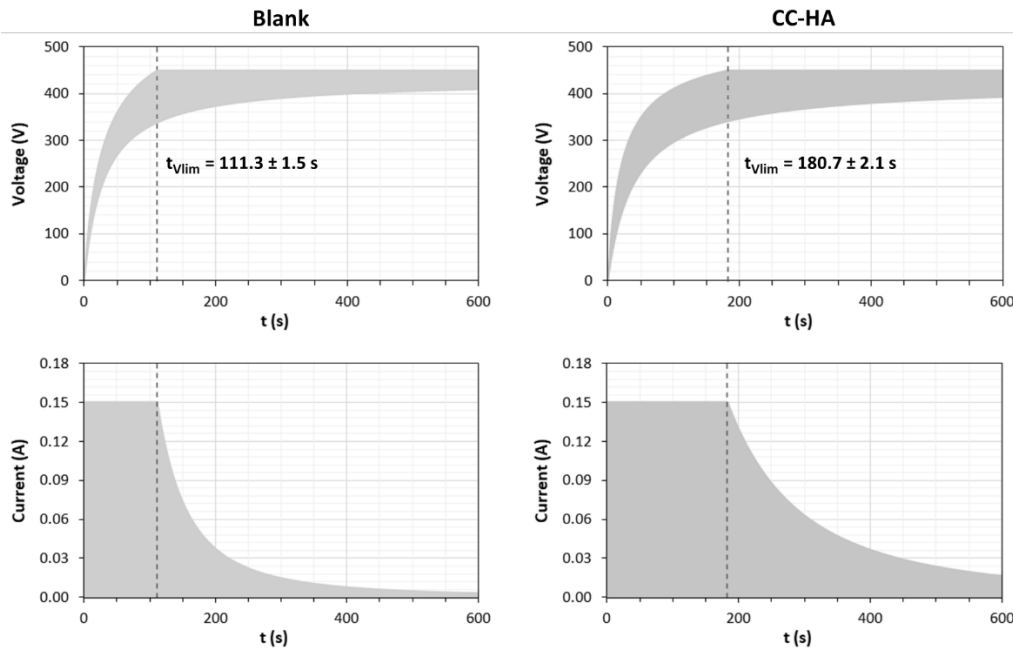


**Figure 30.** Average time–voltage and time–current profiles during the PEO treatment, with dashed lines marking the point at which the limiting voltage ( $V_{\text{lim}}$ ) is achieved.

The Blank coating reached  $V_{lim}$  in  $111.3 \pm 1.5$  s, whereas the CC-HA coating required  $180.7 \pm 2.1$  s—approximately 1.6 times longer. This difference is statistically significant ( $p = 1.28 \times 10^{-6}$ ), indicating substantial variation in coating formation between the two baths. Following  $V_{lim}$ , the CC-HA bath also exhibited a slower current decay and higher voltage amplitudes. These findings suggest a more complex growth mechanism for particle-containing coatings. Since the oxidation conditions were identical, this behavior is attributed to the contribution of CC-HA particles. Additional differences in current and voltage may stem from the distinct dielectric properties of the phases incorporated into the growing oxide [117], [232], [237], while dissolved carbonates in the CC-HA bath could also influence microdischarge behavior and breakdown dynamics [153]. Ultimately, the altered progression of the PEO process resulted in coatings with distinct surface morphology, thickness, and elemental composition, as detailed in Sections 4.3.4 and 4.3.5.

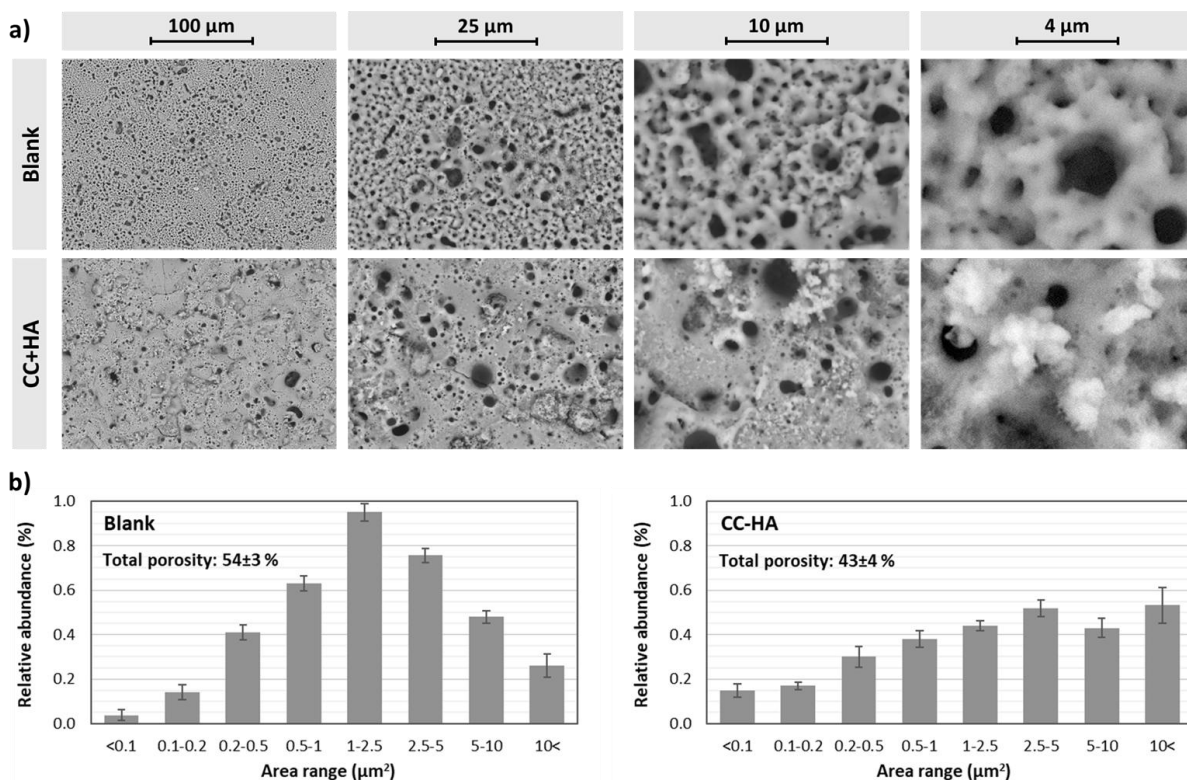
#### 4.3.4. Coating surface characteristics

Figure 31a shows the surface morphology of the fabricated coatings at different magnifications. The Blank coating exhibited a typical PEO surface formed in a phosphate-based electrolyte [340], [406], [407], [408], characterized by high porosity, numerous uniformly distributed pores, and an alternating pattern of micro- and submicropores. The pores were predominantly round or slightly elongated, with smooth walls and no visible inclusions or surface irregularities. At lower magnification, the surface displayed a uniform distribution of regions ( $\sim 30 \times 30 \mu\text{m}$ ) featuring either larger or finer pores, consistent across the entire coating. Incorporating CC-HA particles into the bath noticeably altered the surface features. A reduction in overall porosity, changes in pore structure, and the presence of larger micropores were observed. The pores remained mostly circular, but the surrounding areas were densely packed with particle-like deposits. Such inclusions are commonly reported when particulate additives are introduced into PEO baths [180], [186], [213], [215], [409], suggesting partial reactivity or inert entrapment of particles within the oxide layer, and confirming that the selected particle concentration was sufficiently high to influence coating formation. Localized areas of partially closed pores and relatively large non-porous regions ( $\sim 10 \times 10 \mu\text{m}$ ) were also identified. Additionally, coatings formed with CC-HA particles exhibited slight surface cracking, likely caused by the brittle nature of CC and HA phases [410], [411] and their relatively high incorporation into the oxide layer, reflected by a Ca/Ti molar ratio greater than 1 (Figure 33).

Porosity was further analyzed using contrast enhancement, with the results presented in Figure 31b. The graphs show the relative contributions of different pore size ranges to the total porosity, allowing comparison both within and between the coatings. For the Blank coating, pore size distribution followed a near-normal pattern, which can be attributed to the simpler ionic composition of the electrolyte. In contrast, the CC-HA coating displayed a less defined dominant pore size and showed increased contributions from both very small pores ( $< 0.2 \mu\text{m}^2$ ) and large pores ( $> 10 \mu\text{m}^2$ ). Intermediate-sized pores were less prevalent, leading to a 9% reduction in total porosity compared to the Blank coating ( $54 \pm 3\%$  vs.  $43 \pm 4\%$ ). This difference was statistically significant ( $p = 7.15 \times 10^{-5}$ , two-tailed Student's t-test), indicating a consistent porosity reduction following CC-HA incorporation. Additionally, the narrower standard error observed for the Blank coating suggests greater uniformity in pore distribution and microstructure. In contrast, the CC-HA coating exhibited slightly larger error bars across most pore size ranges—especially for the largest pores—pointing to higher microstructural variability.

According to Hao et al. [412], PEO coatings generally exhibit porosities ranging from 5% to 40%, depending on process parameters and bath composition. Both the Blank and CC-HA coatings produced in this study fall within the high-porosity category. In certain cases, such as with fluoride-containing electrolytes, porosities as low as 1% have been reported [412]. However, in many practical applications, high porosity is advantageous. In implantology, not only high overall porosity but also a broad pore size distribution—such as that observed in CC-

HA coatings—plays a critical role. This structural diversity simultaneously provides nucleation sites for chemical bonding and protein adsorption while facilitating cell adhesion and attachment [413], [414], [415], [416]. Similarly, in photocatalytic applications, porous PEO coatings enhance surface area and increase the number of active sites for light-induced reactions, improving both light absorption and mass transport of reactants and products, thereby boosting photocatalytic efficiency [417]. Although dedicated studies on PEO coatings as adsorbents are lacking, their naturally porous architecture suggests strong potential for sorption applications, including phosphate removal [418]. The CC-HA coating, with its lower porosity compared to the Blank coating, is also expected to offer improved corrosion resistance. Reduced porosity minimizes pathways for corrosive agents (e.g., water and aggressive ions) to reach the substrate, an effect further strengthened by the significantly greater thickness of the CC-HA coating (Section 4.3.5). If further porosity reduction is required, it can be achieved by tuning electrical parameters [419] or optimizing particle size [31]. Previous studies, including that of Keyvani et al. [420], have consistently shown that increased coating thickness and lower porosity enhance corrosion protection.



**Figure 31.** (a) SEM micrographs depicting surface morphology of Blank and CC-HA coatings at various magnifications; (b) surface porosity analysis showing the proportion of pores across different size ranges.

Figure 32 shows the surface roughness analysis results obtained via contact profilometry and 3D SEM profilometry. Overall,  $R_a$  and  $R_z$  values measured by 3D SEM were lower than those from contact profilometry, with a particularly reduced  $R_z$  observed for the CC-HA coating. This discrepancy likely stems from the smaller scanned area in 3D SEM analysis ( $\sim 100 \times 100$  nm for the Blank coating and  $0.5 \times 0.5$  μm for the CC-HA coating), whereas contact profilometry covered several millimeters, increasing the likelihood of capturing a broader range of surface elevations and depressions. The average roughness values for the Blank coating were typical of PEO coatings produced under similar conditions, rarely exceeding 1–2 μm [386], [406], [421]. Roughness profiles and height maps revealed small, periodically distributed elevations and flat regions, corresponding to clusters of large and small pores observed in SEM images (Figure 31a). Incorporation of CC-HA particles significantly increased surface roughness—approximately fivefold—accompanied by the formation of large,

irregular elevations across the coating surface. This effect suggests localized particle incorporation at the microscale. The resulting 3D topographies closely resemble those reported for PEO coatings on Ti-based substrates by other researchers [422], [423].

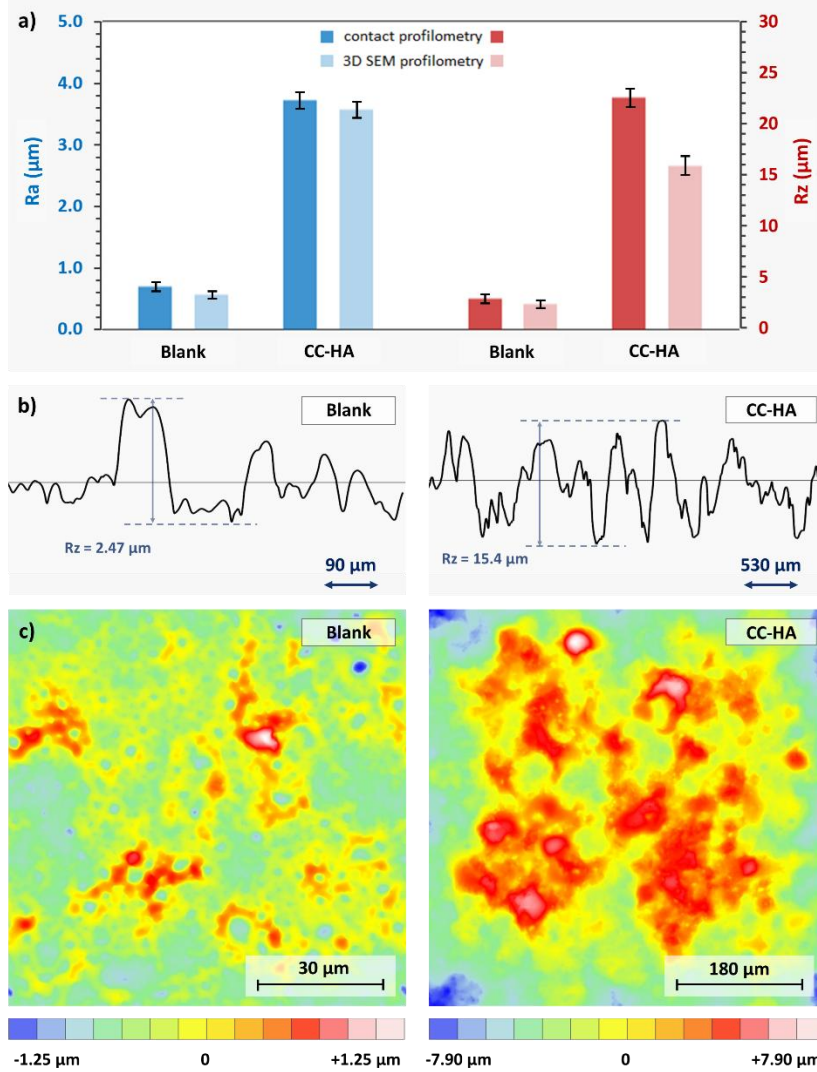


**Figure 32.** Surface roughness analysis results: (a) comparison of  $R_a$  and  $R_z$  values obtained via contact profilometry and 3D SEM profilometry; (b) representative surface profiles captured by 3D SEM profilometry; (c) corresponding 3D topography maps.

Elemental surface composition was analyzed by averaging measurements from three distinct regions of each coating ( $\overline{A_3}$ ) for O, Ti, Ca, P, and C (Figure 33). Additionally, point analyses were performed at four specific locations (x1–x4), and elemental mapping was conducted at two magnifications to further assess elemental distribution in the CC-HA coating (Figure 34). The Blank coating displayed a relatively uniform elemental distribution, though moderate variations were observed for O, Ti, and P [424], which likely correspond to local differences in coating thickness and internal porosity. Specifically, elevated Ti content and a less pronounced decrease in O were detected in the walls of larger pores. The detected C signal in the Blank coating is attributed mainly to artificial EDX artifacts and atmospheric  $\text{CO}_2$  adsorption. This adsorption may be enhanced by the presence of phosphate groups on the coating surface, as suggested by the positive correlation between P and C fractions.

In the CC-HA coating, elemental distribution was generally more uniform compared to the Blank coating, with one notable exception: a region along a wide pore wall (spot 2) exhibited increased concentrations of Ti, Ca, and P, and reduced O and C levels relative to surrounding areas. The origins of these local compositional variations are further analyzed in Section 4.3.7. The averaged surface elemental fractions ( $\overline{A_3}$ ) revealed a relatively high calcium



content in the CC-HA coating, with Ca exceeding Ti by a factor of 1.36. The average surface Ca/P ratio, determined from area analysis, was 1.20. Phosphorus content was similar for both coatings ( $\bar{A}_3 = 6.1\%$  for Blank and  $6.9\%$  for CC-HA), although the difference was statistically significant ( $p = 0.0068$ ). This similarity is expected since both baths contained equal total phosphorus concentrations; however, in the Blank bath, phosphorus was entirely dissolved, while in the CC-HA bath, it was largely introduced in particulate form (Figure 27). Other elemental differences were more pronounced and statistically significant ( $p < 0.01$  for all comparisons). Overall, the surface Ca and P fractions in the CC-HA coating were consistent with values reported by Nahum and Lugovskoy [175], who employed a bath with 0.25 M CA and 0.06 M calcium BGP in AC mode to produce HA coatings on Ti6Al4V alloy.

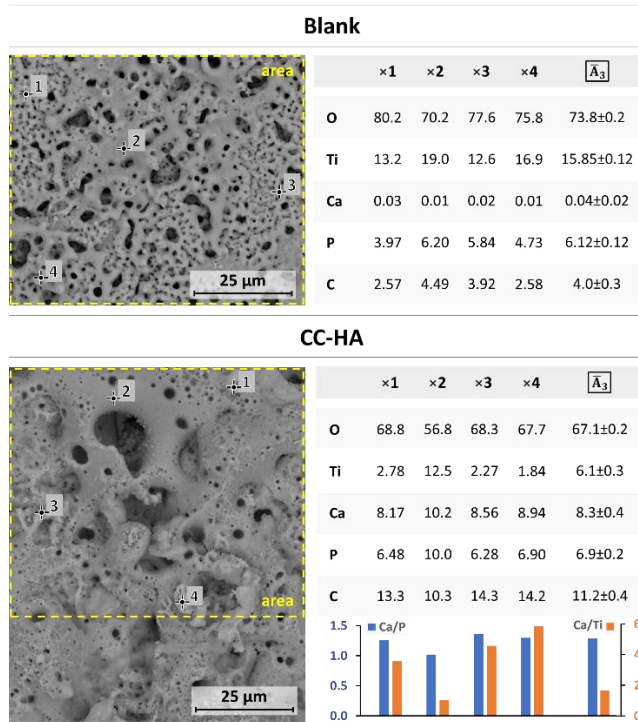


**Figure 33.** EDX-based elemental composition of coatings: spot analysis at indicated positions and averaged data from scans of three regions.

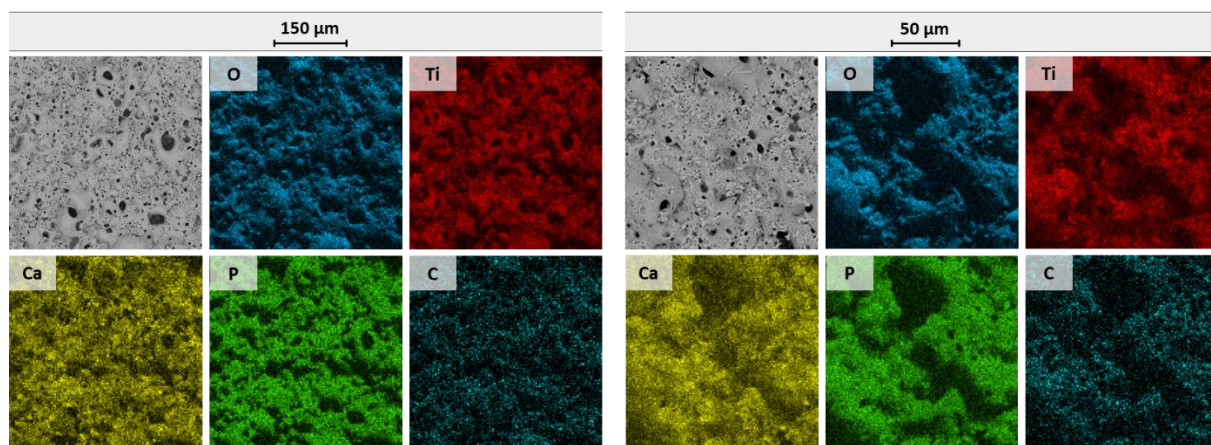


**Figure 34.** EDX elemental mapping of the CC-HA coating at various magnification levels.

Elemental mapping at lower magnification (Figure 34) showed a generally homogeneous distribution of all analyzed elements, consistent with the overall surface topography. In the Ca map, localized brighter spots were observed, likely corresponding to accumulations of incorporated CC-HA particles. At higher magnification, noticeable contrast between colored and dark regions appeared; however, this contrast primarily resulted from



surface roughness effects. Areas at lower elevations were outside the focal plane, which could misleadingly suggest elemental absence. The maps also revealed an alternating Ti distribution and indicated that Ca and P were not always co-located, suggesting that some incorporated particles consisted exclusively of CC or HA phases. Although EDX mapping provides only approximate compositional data, a more detailed phase distribution analysis was performed using Raman spectroscopy (Section 4.3.6).

#### 4.3.5. Coating cross-section

Cross-sectional imaging (Figure 35) revealed that the incorporation of CC-HA particles led to a substantial increase in oxide layer thickness, from approximately 7  $\mu\text{m}$  for the Blank coating to about 25  $\mu\text{m}$  for the CC-HA coating—a more than threefold enhancement. To highlight these differences, microstructural features of both coatings are shown at multiple magnifications. Typically, PEO coatings formed in phosphate baths without particle additives and under DC oxidation do not exceed 4–5  $\mu\text{m}$  in thickness [340], [425]. Interruption of voltage and current pulses is known to prolong the solidification cycle of the molten oxide, thereby promoting thicker coating growth [29], [232]. In this study, the relatively low pulse frequency produced an oxidation regime similar to DC, which limited the thickness of the Blank coating. The pronounced thickening observed for the CC-HA coating is unusual for particle-containing PEO processes. In most reported cases, particle addition increases coating thickness by up to 50% compared to particle-free coatings [186], [190], [213], with occasional reports of thickness reduction [133]. When incorporating CaP phases specifically, thickness changes relative to Blank coatings have been inconsistent, ranging from negligible differences [31], to  $\sim 20\%$  reduction [224], or  $\sim 10\%$  increase [426]. Current literature has not established a clear correlation between coating thickness and particle size or other suspended particle properties [31], [224], [426]. Instead, thickness variations appear primarily governed by the electrical parameters of the PEO process and strongly influenced by bath chemistry and substrate properties. Potential mechanisms explaining the exceptional coating thickening observed here are discussed in Section 4.3.7.

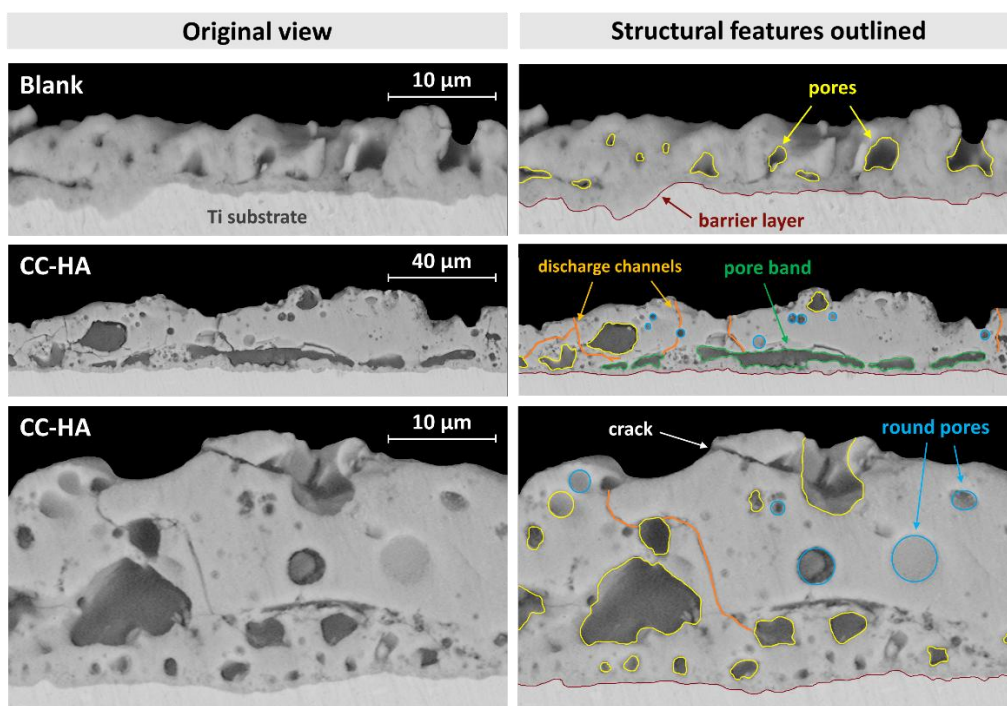


**Figure 35.** Cross-sectional morphology of Blank and CC-HA coatings with highlighted key microstructural features.

Based on visual inspection, the internal structure of the CC-HA coating can be described as bilayered, consisting of a relatively compact inner layer a few micrometers thick and a

thicker, more porous outer layer containing both closed and open pores—features typical of PEO coatings [26], [224], [427], [428]. However, an additional, often-overlooked component is also present: the barrier layer. This thin, dense layer forms at the metal/oxide interface during the initial stages of oxidation and typically measures a few hundred nanometers in thickness [429]. Due to its compact nature and the overall thickness of the coating, it is not easily discernible in SEM images. A pronounced curvature at the substrate–coating interface was also observed—a common feature in PEO systems [430], [431], [432]. This curvature results from uneven oxide growth into the substrate, driven by spatially variable discharge activity and local thermal gradients during the process [433]. Additionally, the inner and outer layers were separated by an elongated porous band, a less frequently reported but well-documented structural feature [419]. Horizontal cracks observed in the CC-HA coating likely formed during mechanical polishing but may have been exacerbated by increased brittleness due to high CC and HA content [410], [411]. The CC-HA coating exhibited a more complex microstructure overall, with features such as round pores, visible discharge channels, and a broader internal pore size distribution. These features may arise from different formation mechanisms, some of which could be influenced by particle incorporation. Potential explanations for the observed internal porosity patterns and structural differences are further discussed in Section 4.3.7 as part of the proposed growth mechanisms.

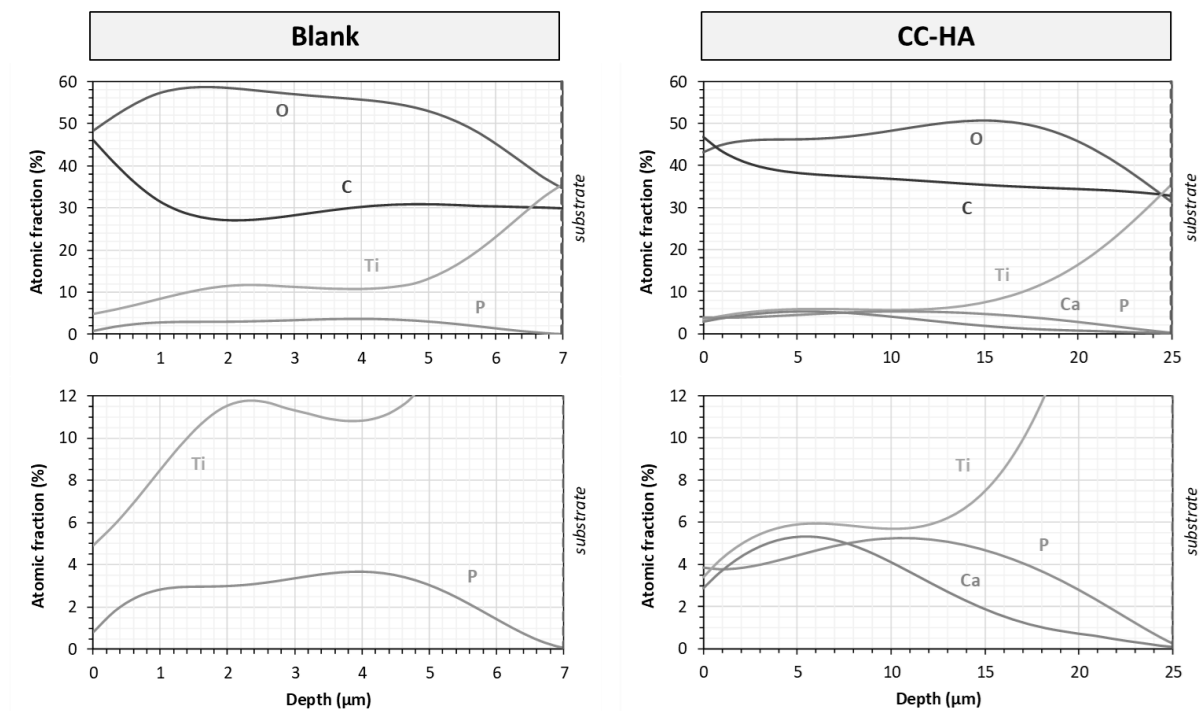


**Figure 36.** Elemental distribution across coating cross-sections, showing atomic fraction gradients from surface to substrate based on measurements at five vertical positions.

Figure 36 presents the elemental composition profiles of the coatings as a function of depth. While replicate measurements were performed, these profiles were primarily intended to visualize compositional trends across the coating thickness rather than provide detailed statistical comparisons of elemental concentrations at specific depths. The left vertical axis (zero argument value) corresponds to the coating surface, while the right axis indicates the oxide–substrate transition. Both Blank and CC-HA coatings showed similar overall growth patterns, particularly in the comparable shapes of Ti and P curves. In the CC-HA coating, calcium and phosphorus were detected throughout the entire thickness, with small amounts even near the substrate interface. The relatively low concentrations of Ca, P, and Ti in the upper and middle layers are likely associated with the frequent occurrence of surface and closed pores. The upper layers of the CC-HA coating were enriched in calcium, with a consistently high Ca/Ti

ratio up to a depth of  $\sim 10\ \mu\text{m}$ . In both coatings, oxygen content decreased and titanium content gradually increased toward the deeper layers, suggesting an increase in coating density and reduced porosity closer to the substrate. This trend also indicates the transition into the oxide/metal interface. Carbon contributed limited compositional insight because of its presence in the resin used for cross-sectional preparation. Nevertheless, the substantially higher carbon fraction in the upper layers of the CC-HA coating compared to the Blank coating clearly results from incorporated particles. The elevated carbon content throughout the depth profile also explains why the Ti signal at the coating–substrate boundary did not reach 100%. Additionally, to confirm the uniformity of CC–HA particle incorporation, calcium distribution profiles were provided for different locations of the coating cross-section (Figure 37). As can be seen, despite slight differences in absolute mass fractions, the trends were consistent in all cases.

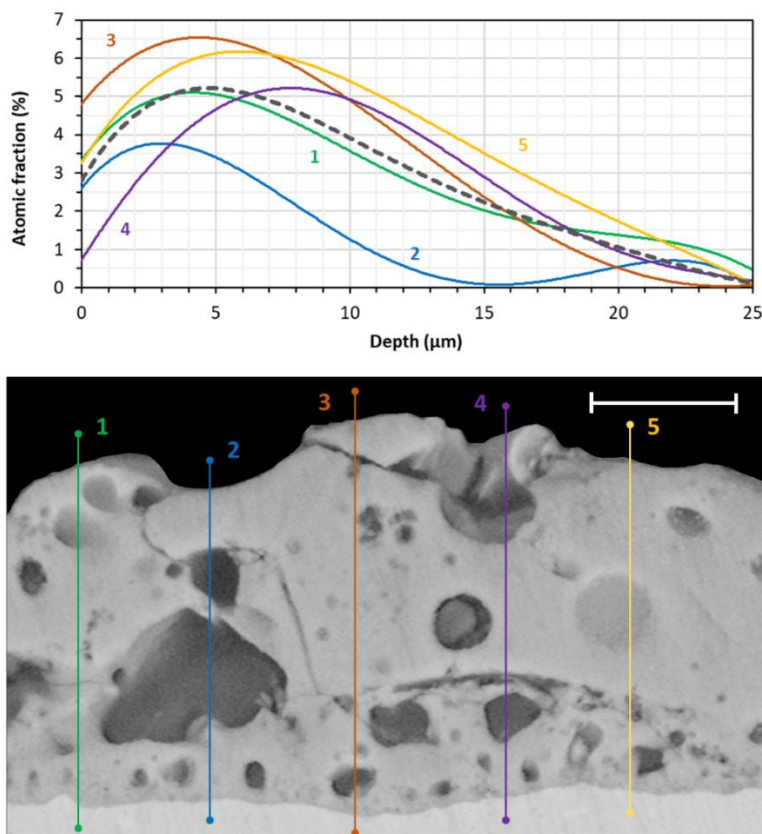
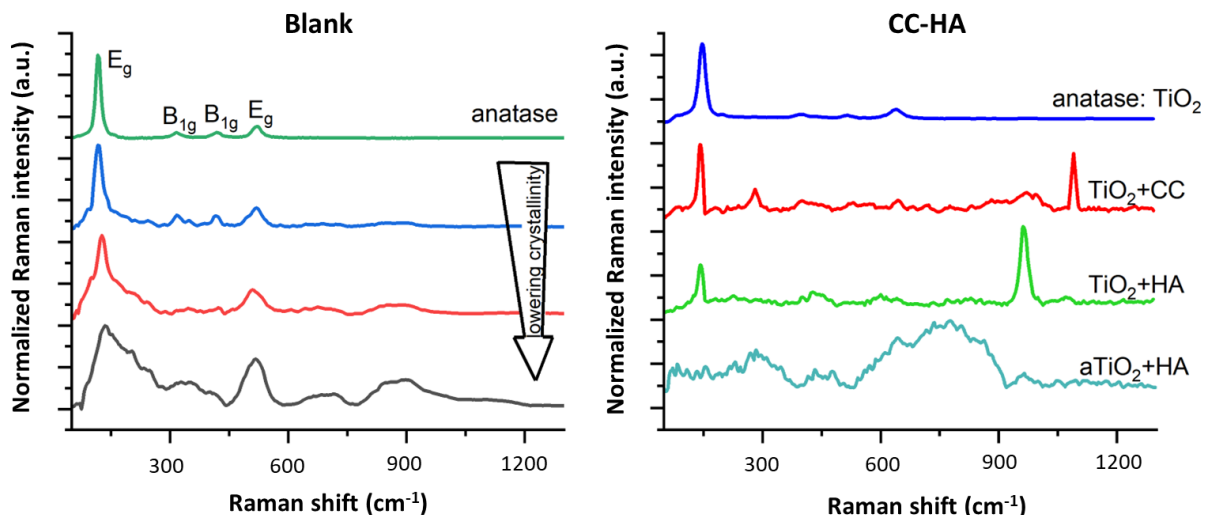


**Figure 37.** Depth-wise calcium distribution across five distinct regions of the CC-HA coating, with individual profiles shown as colored vertical lines (scale bar:  $10\ \mu\text{m}$ ).

#### 4.3.6. Raman spectroscopy analysis

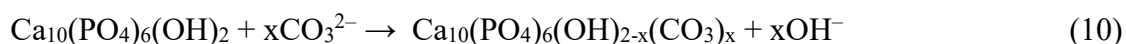
Raman spectroscopy was used to investigate the surface phase composition of both Blank and CC-HA coatings. Measurements were conducted across five regions on each coating, and representative spectra were extracted using True Component Analysis for the  $50\text{--}1300\ \text{cm}^{-1}$  range (Figure 38). Analysis of the Blank coating revealed four structural forms of anatase, each displaying different levels of crystallinity. Highly crystalline anatase exhibited well-defined Raman bands at  $150$ ,  $395$ ,  $515$ , and  $640\ \text{cm}^{-1}$  [318]. Defective anatase showed slightly shifted and broadened peaks, while highly disordered anatase presented weak, broad bands indicative of severe lattice defects. The CC-HA coating displayed a similar overall Raman pattern, with both crystalline and defective anatase phases present across the surface. The prevalence of structurally disordered anatase suggests shorter solidification cycles of molten oxide during coating formation compared to the Blank sample. The observed crystallinity variations, together with surface porosity and roughness (Figure 31, Figure 32), likely result from localized temperature fluctuations during oxidation, as further discussed in Section 4.3.7. Typically, PEO-

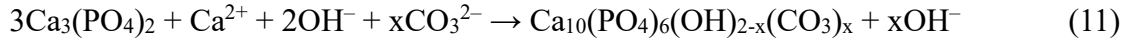
formed TiO<sub>2</sub> coatings exhibit both anatase and rutile phases, with rutile formation favored at higher process voltages [319], [320]. The anatase-to-rutile ratio can therefore serve as an indirect indicator of the surface temperature during PEO treatment. Tubío et al. [434] demonstrated that amorphous TiO<sub>2</sub> nanoparticles undergo crystallization with rutile formation initiating near 600 °C and becoming dominant around 700 °C. The absence of rutile on the surfaces of both coatings suggests that the oxidation temperature remained below 600 °C, conditions favorable for stabilizing the anatase phase. This lack of rutile formation may also be associated with enhanced heat dissipation during coating growth due to the thermostated PEO bath.



**Figure 38.** Raman spectra of phases formed in Blank and CC-HA coatings.

In addition to anatase-related features, the CC-HA coating displayed distinct Raman bands associated with the incorporated CC and HA phases. Prominent peaks at 1090 cm<sup>-1</sup> and 710 cm<sup>-1</sup> correspond to the  $\nu_1$  and  $\nu_4$  vibrational modes of the carbonate ion, confirming the presence of crystalline CC [277]. The narrow width of the  $\nu_1(\text{CO}_3^{2-})$  band at 1090 cm<sup>-1</sup> indicates a highly ordered structure, consistent with the XRD data for CC particles filtered from the stock suspension (Figure 28) and suggesting high crystallinity [435]. HA was identified by a strong phosphate  $\nu_1$  band at 964 cm<sup>-1</sup>, attributed to the symmetric stretching of  $\text{PO}_4^{3-}$  groups [436]. Additional HA-related features were observed at 1030 cm<sup>-1</sup> ( $\nu_3$ ), 580 cm<sup>-1</sup> ( $\nu_4$ ), and 425 cm<sup>-1</sup> ( $\nu_2$ ), corresponding to asymmetric stretching and bending vibrations. Compared to CC, the phosphate bands were broader, indicating the formation of HA with a more disordered structure—likely related to the 48-hour in-bath reaction process (Section 4.3.2). However, partial thermal crystallization during coating growth is suggested by the measured full width at half maximum (FWHM) values. To explore potential carbonate substitution into the HA lattice (i.e.,  $\text{CO}_3$ -HA formation), Raman spectra were deconvoluted to assess both carbonate signals and structural impurities. The simultaneous presence of the strong phosphate  $\nu_1$  band at 964 cm<sup>-1</sup> and a carbonate-related band near 1075 cm<sup>-1</sup> supports the formation of A-type  $\text{CO}_3$ -substituted HA, where carbonate replaces hydroxyl groups [437], [438], [439]. This conclusion is further supported by the absence of a distinct hydroxyl-related Raman band typical of stoichiometric HA (Figure 39). Additional weak bands between 860–750 cm<sup>-1</sup> were assigned to  $\nu_2$  and  $\nu_4(\text{CO}_3^{2-})$  modes [437], [440], reinforcing evidence of carbonate incorporation. This substitution likely occurred due to the high concentration of dissolved carbonate in the CC-HA bath (Figure 27) and localized high-temperature conditions produced by plasma discharges. The substitution could proceed either via a reaction with stoichiometric HA (Eq. 10) or through the transformation of TCP (Eq. 11)—the latter pathway being supported by XRD results (Figure 28, Section 4.3.8).





where  $0 \leq x \leq 1$

This comprehensive Raman analysis highlights the structural complexity of both Blank and CC-HA coatings, particularly emphasizing the variation in anatase crystallinity. The presence of CC particles during oxidation confirmed that surface temperatures in the outer layers of the CC-HA coating remained below 750 °C [88], [441]. While Raman spectra confirmed the incorporation of CC and HA phases, they did not indicate the formation of  $\text{CO}_3$ -HA. This outcome aligns with the study's primary objective—successful incorporation of the CC phase—while still introducing carbonate as an additional chemical constituent. From a structural and chemical perspective,  $\text{CO}_3$ -HA can be considered analogous to both CC and HA, representing an intermediate transitional form between these phases. This interpretation is supported by previous findings showing that HA solubility increases with higher levels of carbonate substitution [442]. Moreover, the absence of other crystalline impurities demonstrates the high phase purity of the fabricated coatings, further validating the effectiveness of the applied PEO process.

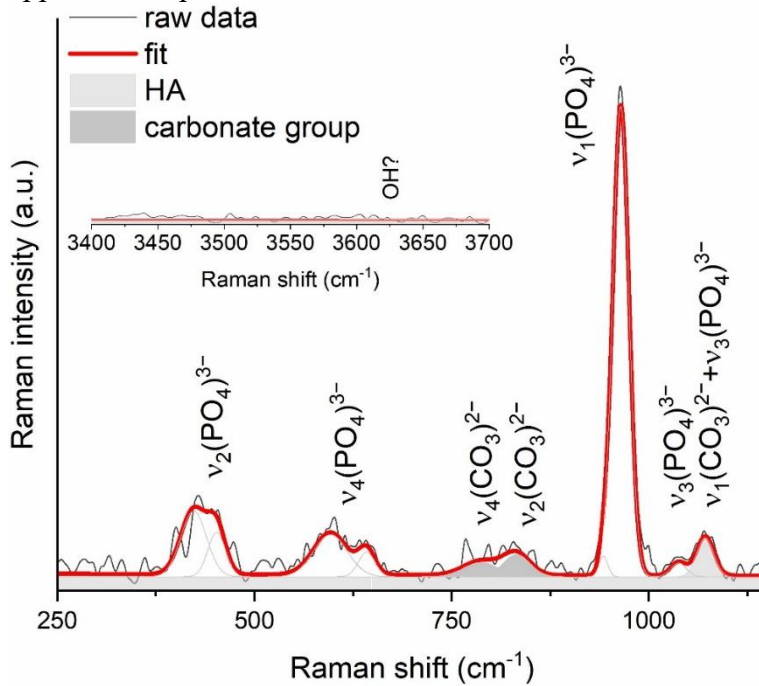


**Figure 39.** Deconvoluted Raman spectrum of the HA phase indicating carbonate incorporation.

For phase mapping, the most intense and non-overlapping Raman bands of CC and HA were selected as integration ranges. Interpretation of the strongest band near 145  $\text{cm}^{-1}$  [318] was complicated by the presence of a nearby calcite band at  $\sim 155 \text{ cm}^{-1}$  [277]. Similarly, anatase bands at 395 and 640  $\text{cm}^{-1}$  partially overlapped with HA bands at 425 and 580  $\text{cm}^{-1}$  [436]. To avoid spectral ambiguity, the anatase band at  $\sim 515 \text{ cm}^{-1}$  was chosen for analysis, along with the amorphous  $\text{TiO}_2$  region spanning 700–900  $\text{cm}^{-1}$ . Given the difficulty of defining integration regions unambiguously, an alternative, more robust approach was employed: True Component Analysis (TCA). Using both integrated phase-specific bands and TCA, the spatial distribution of anatase, HA, and CC was analyzed across the coating surface while accounting for depth variations caused by surface roughness (Figure 40). The coating's deepest layer was set as the zero reference plane (“0  $\mu\text{m}$ ”), while focal planes labeled “+2  $\mu\text{m}$ ,” “+4  $\mu\text{m}$ ,” and “+6  $\mu\text{m}$ ” corresponded to progressively higher surface layers.

True Component Analysis revealed the coexistence of anatase and amorphous  $\text{TiO}_2$  phases, both broadly distributed across the coating surface. Amorphous  $\text{TiO}_2$  was mainly localized along pore walls, while HA displayed a distribution partially overlapping with anatase. At the chosen magnification, HA appeared moderately uniform, forming agglomerates up to



~20  $\mu\text{m}$  in size. Its consistent detection at all coating depths suggests relatively uniform deposition throughout the layer. In contrast, CC exhibited a distinct distribution pattern. Although it often co-localized with HA-rich regions, CC primarily appeared as isolated, rounded particles 1–5  $\mu\text{m}$  in diameter and was less abundant than HA, likely due to its lower thermal stability during plasma oxidation. Larger CC agglomerates were less common in deeper coating layers, while the brighter background observed in the CC map at the “0  $\mu\text{m}$ ” plane indicated the presence of nanoscale carbonate particles (Figure 40). These nanoparticles likely originated from dissolution–precipitation reactions releasing carbonate ions into the electrolyte (Figure 27), followed by  $\text{Na}_2\text{CO}_3$  adsorption onto the coating surface. Overall, this phase-distribution analysis underscores the structural and compositional variability of the CC-HA coating and provides insight into how plasma conditions and thermal effects influence the incorporation and spatial arrangement of anatase, HA, and CC phases [443].

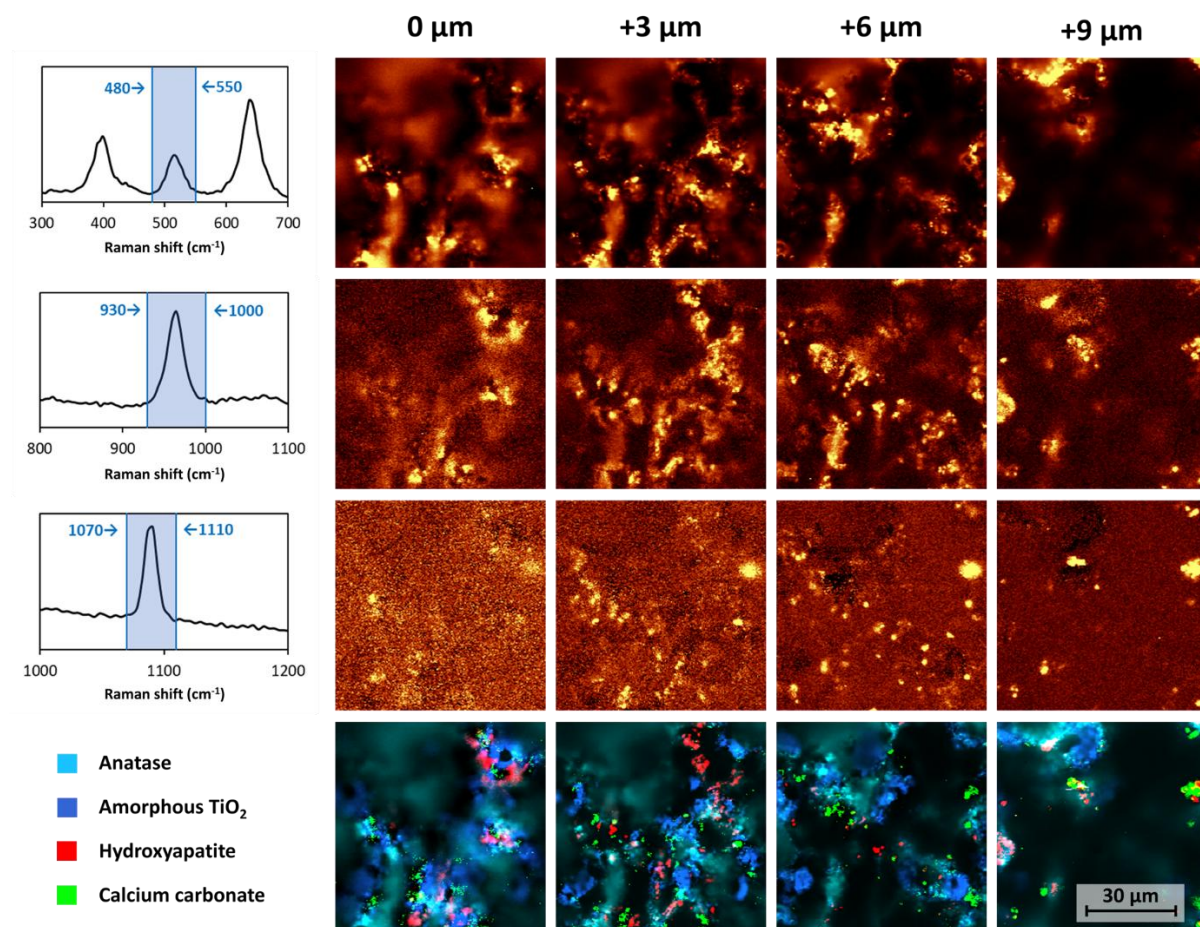


**Figure 40.** Raman spectra with phase-mapping of anatase, HA, and CC phases at various depths, accounting for the high surface roughness of CC-HA coatings.

#### 4.3.7. Coating growth mechanism

As demonstrated in the Introduction part (Section 1.4.1), no previous studies have successfully incorporated a carbonate phase directly into a PEO coating in the form of solid particles. The current research is, therefore, among the first to employ a carbonation-based particle synthesis approach specifically tailored for PEO applications (Figure 2). A further distinguishing feature of this work is the use of microscale CC particles, as opposed to the nanosized Si/CC composites utilized by Tan et al. [167]. Given these novel aspects, a detailed description of the mechanism underlying the formation of CC-HA composite coatings is warranted. Such a discussion will also help to systematize the observed results (Sections 4.3.4–4.3.6) and provide a foundation for future studies on carbonate-related PEO processes. The

conclusions and interpretations presented in this section are based on the fundamental principles of PEO coating formation outlined in the Introduction (Section 1.3.3).

The growth mechanism of PEO coatings in the presence of suspended particulate matter is inherently more intricate than that observed in electrolytes containing only soluble components. The inclusion of solid-phase particles introduces additional pathways and interactions that can significantly affect discharge behavior and chemical incorporation within the evolving oxide layer [32], [213], [444]. Therefore, before advancing to a detailed discussion of the formation mechanism of CC-HA composite coatings, it is essential to first describe the coating development in the Blank bath and determine whether any non-standard structural features are present.

**Blank coating growth mechanism.** The PEO treatment of titanium substrates initiates with a conventional anodizing stage, during which a thin, compact oxide layer develops at the metal surface (Eqs. 12 and 13). As the applied voltage approaches a substrate- and electrolyte-specific breakdown threshold [445], [446], localized dielectric breakdown occurs, giving rise to micro-discharges across the surface [340]. These transient plasma channels briefly bridge the electrolyte and substrate, promoting oxidation and rapid solidification of molten oxide (Eq. 14) [26], [447] (see Section 1.3.3 for a detailed discussion of plasma-assisted coating formation). Even during these breakdown events, a compact barrier layer [158] persists at the metal/oxide interface, maintaining strong adhesion and corrosion protection. Concurrent gas evolution (Eqs. 15, 16) and plasma reactions generate reactive oxygen species [448], [449], [450], while the discharge channels—typically on the micrometer scale and ending in surface pores—produce the characteristic porous morphology of PEO coatings [451], [118], [452]. Such standard discharge features are also observed in the Blank coating (Figure 31, Figure 35).



As the oxide layer grows thicker, its electrical resistance increases, necessitating progressively higher voltages to maintain the PEO process. This shift results in fewer but more energetic micro-discharges, which either initiate new plasma channels or further extend existing ones [125], [237], [340], [385] (see Section 1.3.3 for a detailed mechanism). The repeated occurrence of these discharge events accounts for the variation in pore sizes typically observed in Blank coatings (Figure 31). In the present study, the comparatively large surface pores (Figure 35) are likely a consequence of the low pulse frequency and the near-DC oxidation regime, both of which promote the formation of intense, deeply penetrating discharges [453], [454].

PEO coatings form through a combination of inward and outward growth processes occurring simultaneously [452]. The inward growth, driven by electrochemical oxidation (Eqs. 12–16), generates a dense inner barrier layer, whereas the outward growth involves ejection of molten oxide onto the surface, where it rapidly solidifies, giving rise to the characteristic porous structure [451] (see Section 1.3.3). The internal porosity observed in the Blank coatings (Figure 35) is likely a result of incomplete solidification of molten material or the entrapment of oxygen bubbles during discharge events [455], [91]. The relatively low final thickness of the Blank coating indicates efficient heat dissipation, which may have promoted repeated re-melting of the oxide and contributed to the masking or closure of finer discharge channels.

At elevated voltages, the PEO process induces strong electrophoretic forces that propel negatively charged species (e.g.,  $\text{PO}_4^{3-}$ ,  $\text{SiO}_3^{2-}$ ,  $\text{CO}_3^{2-}$ ) toward the anode. These species tend to

accumulate near discharge sites, where they can be incorporated into the growing oxide layer either through capture within molten material or by penetrating plasma channels (Section 1.3.3). Subsequent chemical reactions may yield bonded phases, complex oxides, or insoluble salts [151], [165], [456]. While previous studies have reported limited cation incorporation under AC conditions [457], and  $\text{Na}^+$  uptake has been linked to capillary-driven transport [458], [459], no sodium was detected in either the Blank or CC-HA coatings in this work (Figure 33, Figure 36), suggesting that such incorporation pathways are negligible under the near-DC processing regime used here.

Elemental analysis (Figure 33, Figure 36) revealed that the Blank coating contained a substantial amount of phosphorus. However, Raman spectroscopy (Figure 38, Figure 40) identified anatase as the only crystalline phase, with no evidence of phosphate-containing compounds. This indicates that phosphorus was incorporated predominantly as amorphous species [460], [461]. Within the discharge channels, phosphate ions likely reacted with molten titanium (Eq. 17) or molten  $\text{TiO}_2$  (Eq. 18), or interacted directly with  $\text{Ti}^{4+}$  ions at the metal/oxide interface (Eq. 19), leading to the formation of amorphous  $\text{TiPO}_4$  [462]. Under plasma conditions, phosphate or hydrogen phosphate ions may also undergo thermal conversion to pyrophosphate species (Eq. 20), which can incorporate into the coating through mechanisms analogous to those of orthophosphates (Eqs. 17–19). Additionally, the formation of mixed non-stoichiometric oxides and crosslinked Ti–P–O networks is plausible (Eq. 21) [110], [463]. In these amorphous structures,  $\text{Ti}^{4+}$  typically forms octahedral  $[\text{TiO}_6]$  units, while  $\text{PO}_4^{3-}$  groups form tetrahedral  $[\text{PO}_4]^{3-}$  units. Oxygen sharing between these units results in Ti–O–P bridges and extended network motifs ( $\cdots\text{Ti}-\text{O}-\text{P}-\text{O}-\text{Ti}\cdots$ ) characteristic of glassy or amorphous PEO coatings [154], [464]. Such behavior—where only  $\text{TiO}_2$  appears as the crystalline phase despite significant phosphorus incorporation—is common in PEO treatments of titanium using electrolytes containing only soluble phosphate salts, as further confirmed by XRD analysis [458].



Localized EDX surface analysis (Figure 33) and Raman spectroscopy results (Figure 38) provide additional insights into the fundamental mechanisms of PEO coating formation. The observed variations in oxygen, titanium, and phosphorus content likely arise from localized fluctuations in temperature and discharge intensity during processing [138], factors known to influence both coating thickness and internal porosity. Notably, the increased titanium content detected in the walls of larger pores—accompanied by only a minor reduction in oxygen concentration—suggests that these pores were formed by the eruption of significant amounts of molten titanium from the substrate [139]. The rapid quenching of the ejected material prevented complete oxidation. This same rapid solidification also explains the variation in anatase crystallinity observed in the Blank coating (Figure 38).

**CC-HA coating growth mechanism.** Unlike the Blank coating, the CC-HA layer developed in an electrolyte containing suspended particulate matter, introducing additional processes beyond the fundamental PEO mechanisms outlined in Section 1.3.3 [30], [180], [213], [465]. The markedly greater thickness of the CC-HA coating (Figure 35), along with its higher calcium content relative to titanium and phosphorus (Figure 33), demonstrates significant particle incorporation into the oxide matrix. The CC-HA particles, carrying a negative surface charge with a measured zeta potential of  $-21.8 \pm 0.3$  mV (Table 9), were electrophoretically attracted to the positively polarized titanium anode during the PEO process



[180], [460], [466], [467]. Due to their micron-scale size and sufficient mobility, these particles were continuously transported to active discharge sites, where they became entrained within molten oxide and were subsequently incorporated into the growing coating either through physical embedding or chemical reactions [31], [32].

The influence of CC-HA particle morphology—encompassing particle size and structural features—was evaluated using several datasets, including pore size distribution (Figure 31), calcium depth profiles (Figure 36), calcium distribution repeatability (Figure 37), and particle characterization (Figure 28). In the Blank coating, pores ranged from 0.2 to 10  $\mu\text{m}$ , with the majority measuring 1–2  $\mu\text{m}$  in diameter. Although these values represent the final pore dimensions, they provide a useful reference for understanding particle incorporation behavior, with the Blank surface serving as a control matrix produced in the absence of suspended particles. The CC-HA particles exhibited sizes between 300 nm and 3  $\mu\text{m}$ , with a predominant peak at approximately 1.35  $\mu\text{m}$ —comparable to the most frequent pore sizes. While pore penetration is widely recognized as a primary mechanism for particle uptake during PEO [444], [31] (Section 1.3.3), the calcium depth profiles (Figure 36) show a sharp decrease in calcium concentration beyond  $\sim 10 \mu\text{m}$ . This observation is reinforced by the high repeatability of the calcium distribution data (Figure 37). These findings suggest that deeper particle incorporation via pore penetration was limited, likely confined to smaller particles ( $\sim 500$  nm or less), particularly during the early stages of coating growth when micro-discharge intensity was relatively low [93]. As the coating thickened and discharge events became more energetic, pore widening likely facilitated the entrapment of larger particles within the evolving oxide layer [213], [468].

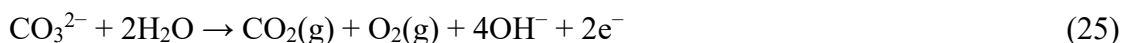
Even for particles similar in size to surface pores, the probability of full penetration may be limited by spatial constraints. Particles can become trapped at the pore entrance or obstructed within the pore by its walls, particularly when the pore is in an active discharge state surrounded by molten oxide [30], [31], [213]. Additionally, some particles may be captured directly from the electrolyte by plasma discharges without first contacting the coating surface [166], [469]. Evidence supporting these alternative incorporation routes—rather than classical pore penetration—comes from the structural characteristics of the CC-HA particles. These particles are actually micron-sized agglomerates composed of numerous nanoparticles (Figure 28). Owing to their relatively low density and high specific surface area, these agglomerates are more likely to undergo “productive” interactions with plasma events and surface features, leading to entrapment in molten oxide or adsorption at discharge-active zones [444]. Since their dimensions are comparable to both the pores and the sparks, full embedding into the oxide likely occurs gradually. The process may begin with partial capture of the agglomerate’s outer surface, while the remaining portion—loosely bound by electrostatic interactions (as illustrated in Figure 29)—remains temporarily mobile. With continued discharges and coating growth, the agglomerate progressively integrates into the oxide matrix. Another factor facilitating this incorporation is the low crystallinity of one of the suspension’s components: HA. These HA particles form *in situ* through interactions between CC and phosphate ions in the electrolyte (Section 4.3.2). Acting as a binding phase, the amorphous HA stabilizes cubic CC nanoparticles within the agglomerates (Figure 29). Moreover, its high surface area further enhances collision efficiency with molten oxide, promoting particle entrapment. Similar behavior was observed in Section 4.2, where amorphous TCP particles with high specific surface area produced thicker PEO coatings compared to their crystalline counterparts.

In summary, the factors discussed above were likely key contributors to the pronounced thickening of the CC-HA coating (Figure 35). The negative zeta potential of the suspension promoted continuous electrophoretic transport of fresh particles toward the anode surface (Table 9), while the size, morphology, and dispersion characteristics of the synthesized CC-HA particles (Figure 28) were well-suited for efficient incorporation of solid additives into the developing PEO layer [31], [213]. Consequently, the process dynamics shifted significantly toward outward coating growth. The outer regions of the coating became progressively enriched

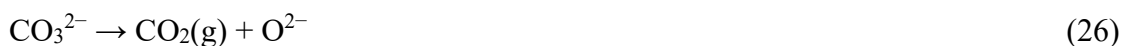
with incorporated particles, with larger particles preferentially embedded closer to the surface. Raman spectroscopy mapping (Figure 40) indicated particle sizes of up to 5  $\mu\text{m}$ , which is likely comparable to the maximum discharge diameter reached during the later stages of coating formation. Additional evidence for the high particle concentration in the upper layers includes the elevated calcium content and slightly reduced oxygen levels observed in the EDX depth profiles (Figure 36). The latter is consistent with the lower intrinsic oxygen content of CC and HA relative to  $\text{TiO}_2$ .

Similar to dissolved ions, suspended particles can undergo different incorporation pathways depending on factors such as size, chemical composition, thermal stability, and discharge intensity (which is influenced by voltage and electrolyte composition) [19], [32], [444]. Based on these factors, three primary incorporation modes are generally recognized: inert, reactive, and partially reactive [30]. Raman spectroscopy confirmed the widespread presence of both CC and HA phases on the coating surface (Figure 38, Figure 40), suggesting predominantly inert or partially reactive incorporation, where particles are embedded with little or no formation of chemical bonds with the oxide matrix. The persistence of CC within the interfacial layers is likely linked to its thermal stability, enhanced by efficient heat dissipation through direct contact with the electrolyte bath. Furthermore, rapid cooling of these layers likely contributed to the pronounced amorphous character of the coating (Figure 38, Figure 40) [460]. Nonetheless, several indirect observations—derived from surface morphology, internal structure of the CC-HA coating, and elemental analysis—indicate that reactive incorporation may also have occurred, particularly for the CC phase, which is thermally less stable than HA [441]. The overall lower porosity of CC-HA coatings compared to Blank coatings (Figure 31), along with the presence of highly compact surface regions exhibiting closed porosity and lacking visible particulate inclusions (Figure 31), suggests that particles may have filled surface pores and subsequently decomposed under plasma exposure [470], [31]. Such interactions could give rise to a heterogeneous, amorphous or nanocrystalline oxide-ceramic composite, such as  $\text{TiO}_2\text{-Ca-P-O}$  [460], [461]. This process likely began with thermal decomposition of the CC phase within the particles (Eq. 22), producing  $\text{CaO}$ , which could then react with molten  $\text{TiO}_2$  to form a  $\text{Ca-Ti-O}$  composite (Eq. 23). The absence of Raman peaks corresponding to perovskite-type phases (e.g.,  $\text{CaTiO}_3$ ) in CC-HA coatings (Figure 38) suggests that crystalline  $\text{CaTiO}_3$  did not form on the surface [471], likely due to rapid cooling rates or insufficient thermal conditions to support crystallization.

Another distinctive feature of the CC-HA coatings is the presence of multiple small- and medium-sized spherical inner pores (Figure 35), which likely result from thermal decomposition of the CC phase incorporated within the oxide during the later stages of coating growth. The  $\text{CO}_2$  released during this decomposition (Eq. 22) would rapidly expand, displacing the surrounding molten oxide uniformly in all directions and leaving behind spherical cavities as it solidified. Additionally, the surface of CC-HA coatings exhibits small, round nanopores (Figure 31), which may originate from localized decomposition of CC nanostructures embedded in the surface layers. These nanopores could form through the attachment of  $\text{CO}_2$  bubbles that subsequently rupture under the high-energy conditions of micro-discharges or through indentation of the softened oxide caused by associated shock waves [412]. Alternatively, bubble rupture might be initiated by a rapid chemical reaction between  $\text{CO}_2$  and hydroxide ions in the PEO electrolyte (Eq. 24) [137], [472]. Apart from decomposition of incorporated CC particles (Eq. 22),  $\text{CO}_2$  bubble formation could also arise from electrochemical conversion of carbonate ions at the anode surface (Eq. 25). Another plausible mechanism involves  $\text{CO}_2$  bubbles adhering to the oxide surface and temporarily insulating localized regions [226], [473], thereby suppressing or displacing micro-arc discharges in those areas [447], [474]. This effect could contribute to the observed non-uniform thickness of CC-HA coatings (Figure 35) and may help explain the delayed onset of sparking detected during their formation (Figure 30).

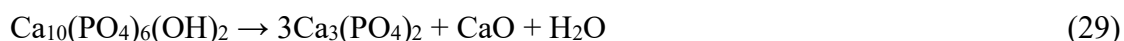


Phosphate ions may have similarly influenced the chemical composition of the CC-HA coatings through reactions described in Eqs. 17–21. The slightly elevated phosphorus content in the CC-HA coating compared to the Blank coating suggests that phosphates actively participated in the coating growth process. As observed in the Blank coating, phosphorus was relatively evenly distributed throughout the CC-HA layer (Figure 36), including the inner regions. This uniform distribution indicates that, unlike solid particles, phosphate ions were incorporated during the early stages of coating formation—likely beginning almost immediately after reaching the breakdown voltage [452], [460]. In addition to phosphates, the matured CC-HA bath contained a notable concentration of carbonate ions (Figure 27), whose potential role also warrants consideration. Like phosphates, carbonate ions migrate toward the anode under electrophoretic forces [180], where several reaction pathways are possible. Analogous to anodic oxygen evolution in alkaline electrolytes (Eq. 14), carbonate ions may contribute to  $\text{CO}_2$  generation (Eq. 25) [475]. However, given their relatively low concentration compared to water, the resulting increase in gas evolution is likely insufficient to cause significant structural changes in the CC-HA coating [92], [449]. From a plasma chemistry standpoint, the most probable interaction involves thermal decomposition of carbonate ions with  $\text{CO}_2$  release (Eq. 26). A hypothetical reaction between Ti or  $\text{TiO}_2$  and carbonate ions—producing  $\text{Ti}(\text{CO}_3)_2$  through a mechanism similar to phosphate incorporation (Eqs. 17–19)—is unlikely to be significant, as the compound is thermally unstable and would readily decompose under PEO conditions (Eq. 27) [476]. Furthermore, in the alkaline environment of the CC-HA bath, any  $\text{CO}_2$  generated—whether from particle decomposition (Eq. 22) or electrochemical reactions (Eq. 25)—would rapidly reconvert into carbonate ions via Eq. 24 [475]. Therefore, the most plausible role of carbonate ions in surface chemical modification is their contribution to amorphous phase formation through a mechanism akin to that described in Eq. 21. This process could lead to the incorporation of carbon within Ti–P–O–C network structures. As previously noted, the intentional addition of soluble carbonate salts to PEO electrolytes is relatively uncommon; nonetheless, literature reports [157], [158], [159], [160], [161], [477] support the conclusion that carbonate ions have only a minor influence on phase formation during PEO of relatively inert metals such as titanium. Achieving direct incorporation of crystalline carbonate-containing phases via dissolved carbonate ions remains particularly challenging.



Analysis of other structural features of the CC-HA coatings—particularly external porosity and internal, non-spherical pores—suggests that they formed through mechanisms similar to those in the Blank coating, involving eruption, melting, and re-solidification of molten oxide [468], [478], [479]. However, distinct structural characteristics are evident and can be attributed to the presence and participation of CC-HA particles. As the CC-HA coatings thickened and reached substantial dimensions, the relatively low porosity observed in the upper layers—likely resulting from partial or complete blockage of surface pores by particles (Figure 31)—may have impeded the escape of anodically generated oxygen from the metal/oxide interface into the surrounding electrolyte. This obstruction likely promoted the development of internal voids and contributed to localized delamination within the coating (Figure 35). In the literature, elongated networks of interconnected voids are commonly referred to as pore bands, a well-documented microstructural feature in PEO coatings produced under DC [186], [425],

[480], AC [213], [406], [412], [481], and pulsed current regimes [419]. The positioning of the pore band within the inner regions of the CC-HA coatings—specifically near the metal/oxide interface and adjacent to the barrier layer—is likely not coincidental. It may reflect a mechanically weaker boundary separating the calcium-poor lower layers from the calcium-rich upper layers (Figure 36), the latter formed through active particle incorporation. Additionally, some inner pores (Figure 35) may have originated from phase transformations accompanied by volumetric shrinkage [482], such as crystallization or thermal decomposition of HA within the incorporated particles. Representative examples include the formation of oxyapatite (Eq. 28) or TCP (Eq. 29). However, Raman spectroscopy (Figure 38, Figure 40) and spectral deconvolution (Figure 39) did not detect these phases, indicating that such decomposition processes, if they occurred, did not manifest at the surface level.



A distinctive characteristic of the CC-HA coating is the presence of well-defined discharge channels and their remnants [451], [452], [483], features much less evident in the thinner Blank coating. This difference can be attributed to the greater thickness of the CC-HA layer, which broadens the electric field distribution, reducing the likelihood of repeated discharges at the same locations and allowing discharge channels to remain intact (see Section 1.3.3 for the underlying mechanism). Furthermore, the increased thickness of the CC-HA coating diminishes heat dissipation efficiency [484], limiting the extent of molten oxide reflow and preventing complete closure of channels through post-discharge melting and resolidification. Additionally, higher discharge energy [125] promoted the formation of deeper and wider channels, contributing to the relatively large pores—up to 10  $\mu\text{m}$ —observed both internally and on the surface of the coating (Figure 31, Figure 35). Some of the internal pores were likely open during earlier stages of coating growth but were subsequently sealed due to localized re-melting and resolidification of  $\text{TiO}_2$  [485].

The thickened walls surrounding surface pores appear to have formed as a result of particularly intense eruptions of molten oxide, consistent with the high concentration of amorphous  $\text{TiO}_2$  detected in these regions (Figure 40). The elevated calcium content measured in the same pore walls (Figure 33) indicates substantial particle entrapment, likely facilitated by direct interaction with molten oxide or plasma-assisted incorporation during discharge events [486] (see Section 1.3.3 for details on molten oxide dynamics). Variations in the surface concentrations of Ti and O (Figure 33) can be attributed to differences in micro-discharge size and energy, similar to the mechanisms discussed earlier for the Blank coating. Raman spectroscopy (Figure 38, Figure 40) supports this interpretation, showing that HA distribution on the CC-HA surface partially coincided with that of anatase. This correlation, consistent with findings reported by Lavrushin et al. [487], suggests preferential HA incorporation in regions subjected to higher plasma temperatures or areas where crystallization of previously embedded HA had taken place.

**CC-HA coating formation stages.** Based on the conditions and phenomena described in this section, the formation of CC-HA coatings during the PEO process can be segmented into distinct chronological stages. This stage-wise classification is supported by the voltage evolution profile recorded during coating growth (Figure 30), along with observable changes in surface morphology and oxide layer thickness. The key events and transformations associated with each stage are illustrated schematically in Figure 41.

**Stage I – breakdown and initial layer formation.** The process commenced with the appearance of micro-discharges [93], initiated upon reaching a critical voltage threshold that led to dielectric breakdown of the thin anodic  $\text{TiO}_2$  layer formed during the initial anodizing phase [323]. Concurrently, phosphorus incorporation into the growing oxide layer began, driven by the high electrophoretic mobility of phosphate ions present in the electrolyte [31]. At this early stage, anodic gas evolution was also initiated—primarily involving oxygen release, with

minor contributions from carbon dioxide—and continued throughout the process. The early growth behavior likely resembled that of the coating produced in the Blank bath, characterized by limited or no particle incorporation and the absence of medium or large pores. The oxide layer formed during this phase is estimated to reach a thickness of approximately 1  $\mu\text{m}$ . This initial stage likely spanned the first  $\sim 30$  seconds of treatment, during which the applied voltage rose sharply to around 320 V (Figure 30).

Stage II – onset of particle incorporation. The second stage marked the initiation of particle involvement in the coating formation process, as indicated by the first detectable traces of particulate incorporation at an applied voltage of approximately 340 V (Figure 24). During this period, the smallest CC-HA particles were likely fully embedded within the growing oxide matrix, while larger particles began to attach to or partially penetrate the surface. However, complete incorporation of these larger particles was likely limited by the still moderate discharge energy at this stage. This phase likely extended to approximately 80 seconds into the process and was characterized by a noticeable deceleration in the voltage increase, culminating at around 380–400 V (Figure 30). A significant increase in coating thickness occurred during this time, potentially reaching several micrometers. The evolving microstructure began to diverge distinctly from that of the Blank coating, reflecting the influence of the suspended particles. By the end of this stage, a continuous network of large surface pores had developed (Figure 24), accompanied by the appearance of small, rounded pores along their inner walls.

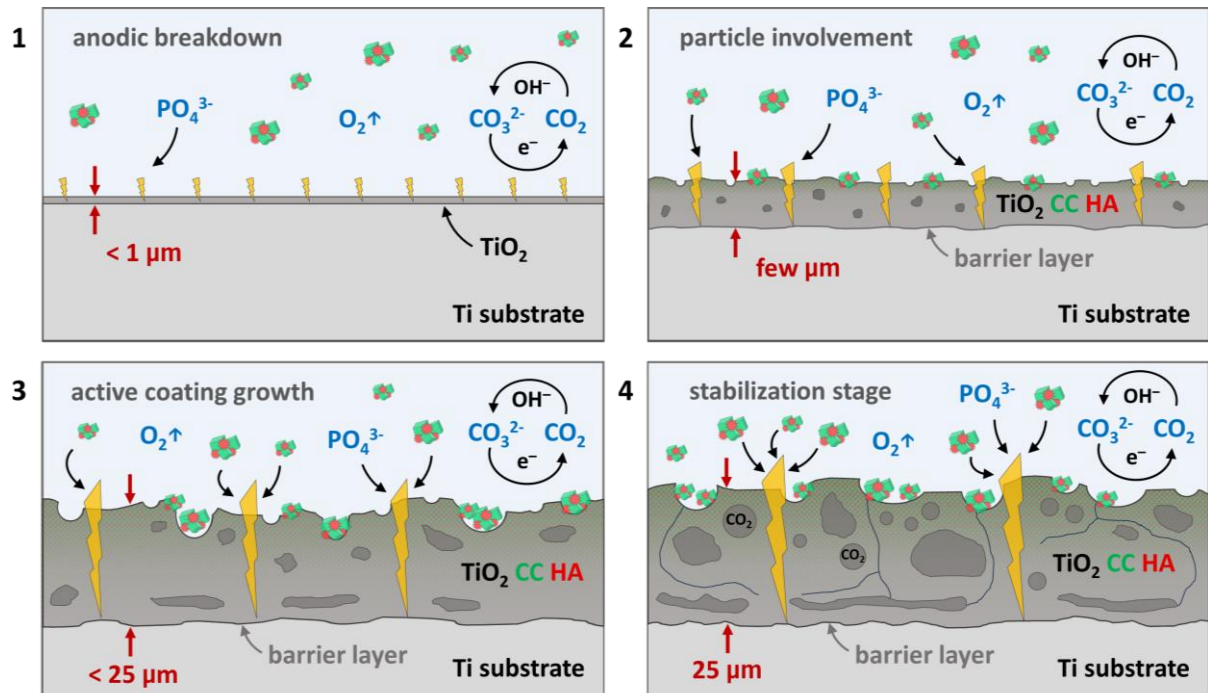


**Figure 41.** Main stages and processes contributing to CC-HA coating formation.

Stage III – full-scale particle incorporation and structural diversification. This stage, extending to approximately 180 seconds and concluding with the attainment of the limiting voltage of 450 V, was characterized by a more linear and steady increase in voltage (Figure 30). By this point, micro-discharges had intensified sufficiently to enable the incorporation of suspended CC-HA particles across the full size spectrum, overcoming previous energy-related limitations. Consequently, even larger agglomerates were successfully embedded within the growing oxide matrix. This stage likely contributed the most to the final coating thickness, with outward growth proceeding at a notably enhanced rate. Concurrently, the size of the large surface pores increased, accompanied by thickening of their surrounding walls (Figure 24). In parallel, secondary processes became increasingly prominent—most notably, the local thermal decomposition of previously incorporated CC particles. This decomposition likely contributed to both surface and internal porosity, especially in the form of rounded pores formed via the

release and expansion of CO<sub>2</sub>. These features became considerably more pronounced than in the preceding stage.

Stage IV – structural maturation. The fourth and final stage likely played a critical role in the development of the characteristic pore band, as anodically generated gases exerted pressure on the mid- and upper regions of the now substantially thickened coating. This phase was distinguished by the appearance of the largest—albeit least frequent—sparks. Despite the intensity of these discharge events, there was little to no further increase in coating thickness, indicating that the growth process had largely reached a plateau. Instead, secondary processes became more prominent. Among them was the formation of large, persistent discharge channels that remained visible after PEO treatment, along with partial closure of surface pores caused by localized re-melting and re-solidification [485]. Additionally, partial thermal decomposition of HA may have taken place, potentially accompanied by phase transformations, resulting in volumetric shrinkage and structural rearrangement within the coating. These combined effects marked the final stage in the structural evolution of the CC-HA coating.

The analysis presented in Section 4.3.7 demonstrates that the addition of CC to the electrolyte introduces several new dimensions to the PEO coating formation process and significantly influences the resulting chemical composition. Beyond the confirmed capability for direct incorporation of the CC phase into the oxide layer, evidence suggests that CC particles may also undergo reactive incorporation. This could occur either during their interaction with active discharge sites or subsequently, after their partial or full integration into the coating, thereby further altering the morphology and chemistry of the developing oxide structure. The presence of CC in the bath led to several notable structural effects, including a substantial increase in coating thickness, the formation of characteristic inner and outer rounded pores, and a general reduction in open surface porosity. These findings offer preliminary insight into the role of carbonate-containing particles in PEO processing and provide a foundation for further investigation into the mechanisms by which such particles are incorporated and influence coating development. However, more definitive and quantitatively precise data are required to fully understand the origin of the observed structural features. Ideally, future work should include time-resolved analyses of coating evolution at different stages, along with concurrent measurements of gas evolution, acoustic emissions, plasma temperature, and electrolyte properties. In parallel, attention should also be directed toward understanding the influence of soluble carbonate salts, particularly since the use of CC in phosphate-based baths leads to the release of carbonate ions into the electrolyte, potentially contributing to coating chemistry and behavior.

#### 4.3.8. XRD analysis

XRD offers complementary advantages to Raman spectroscopy for phase identification, particularly in distinguishing between various CaP phases due to their distinct crystallographic signatures. Unlike Raman spectroscopy, which is more surface-sensitive, conventional XRD typically probes several tens of micrometers into the material. As a result, XRD provides insight into the deeper regions of the CC-HA coating, extending down to the metal substrate, rather than being confined to the surface or interfacial layers. Although the outer layers of PEO coatings are more relevant to *in vivo* interactions, the deeper regions examined by XRD remain largely sealed and protected from the external environment due to the coating's mechanical integrity and the limited, non-uniform presence of outer pores. Therefore, the bulk composition revealed by XRD may not directly reflect surface bioactivity, but the data are nonetheless valuable for confirming earlier observations regarding coating structure and formation mechanisms, while also contributing to a more comprehensive understanding of the PEO process, especially from the point of view of phase transformations.

XRD analysis confirmed that the Blank coating consisted exclusively of anatase (Figure 42), in agreement with previous findings [313]. In contrast, the incorporation of CC-HA particles into the PEO bath led to a more complex phase composition. The resulting CC-HA

coating contained both anatase and rutile, along with five calcium-containing phases: CC, HA, TCP, calcium titanate (perovskite), and brushite (Figure 42). The coexistence of anatase and rutile is common in PEO coatings on titanium-based substrates [126], [186], [406], [488], although coatings composed solely of anatase [180], [425] or rutile [489] have also been reported. The anatase-to-rutile ratio is primarily governed by the temperature of plasma discharges but may also be influenced by factors such as particle concentration [186] and pulse current frequency [386]. Given that rutile is the high-temperature polymorph of  $\text{TiO}_2$ , its appearance suggests that the formation of the CC-HA coating involved more intense sparking. This could have been promoted by dissolved carbonates in the CC-HA bath, previously shown to enhance surface discharge activity [153]. Additionally, several interrelated factors—such as particle-induced surface modification, altered dielectric properties, and significant coating thickening—may have collectively contributed to rutile formation.

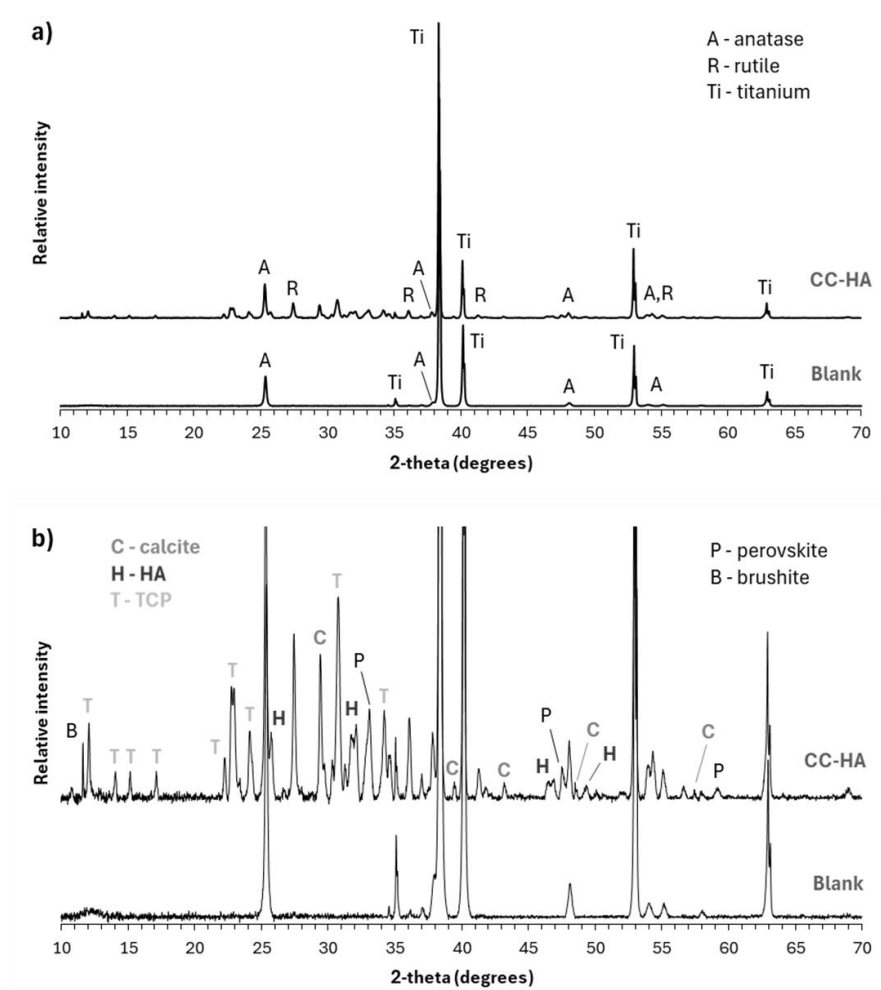
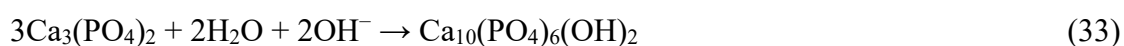
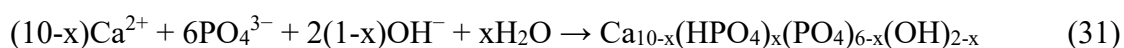


**Figure 42.** XRD analysis results of Blank and CC-HA coatings: (a) complete diffraction patterns with anatase, rutile, and Ti peaks; (b) zoomed-in regions highlighting calcium-containing phases.

The identification of multiple calcium-containing phases in the CC-HA coating—beyond the originally targeted CC and HA—is a notable outcome but remains entirely acceptable within the context of this study. Several of the additional phases, such as TCP, brushite, and calcium titanate ( $\text{CaTiO}_3$ ), are well-established as biocompatible materials. TCP, in particular, shares structural and solubility characteristics with HA [490] and is similarly valued for bone and dental tissue regeneration [491]. Moreover, TCP can readily convert to HA through hydrothermal treatment [175]. Brushite and  $\text{CaTiO}_3$  also contribute positively to osteogenesis and bone regeneration [492], [493]. The presence of  $\text{CaTiO}_3$  in PEO coatings has been reported to promote *in vitro* HA precipitation when immersed in SBF [494]. In coatings

formed from fully soluble baths—such as those containing CA and calcium BGP—various combinations of Ca-containing phases have been reported, including HA with TCP and CaTiO<sub>3</sub> [424], [495], HA alone [477], [496], HA with CaTiO<sub>3</sub> [494], or TCP alone [185]. In these systems, CaTiO<sub>3</sub> formation is attributed to the reaction of Ca<sup>2+</sup> ions with molten TiO<sub>2</sub> (Eq. 30), while HA formation results from the simultaneous ionization of Ca<sup>2+</sup>, HPO<sub>4</sub><sup>2-</sup>, PO<sub>4</sub><sup>3-</sup>, and OH<sup>-</sup> near the coating–electrolyte interface (Eq. 31). TCP formation, in turn, is linked to the thermal decomposition or partial transformation of HA under high-temperature plasma discharge conditions (Eq. 28) [168], [169], [170].

In most studies involving HA particle addition to PEO baths, HA is typically reported as the sole CaP phase incorporated into the coating [31], [180], [489]. However, the formation of HA–TCP mixtures has also been documented [497]. In contrast to these trends, the current study additionally identified CaTiO<sub>3</sub> within the CC-HA coatings. One contributing factor may be the inherent solubility of CC, which supplies Ca<sup>2+</sup> ions to the bath, enabling their reaction with molten TiO<sub>2</sub> as described in Eq. 30. A more plausible explanation, however, lies in the microstructure of the CC-HA particles used. These particles are agglomerates composed of nanocrystalline CC and HA whiskers (Figure 28). Due to their nanoscale size and high specific surface area, CC crystals are particularly susceptible to thermal interaction with molten TiO<sub>2</sub>. This could occur either through surface alloying or via a two-step process: thermal decomposition of CC into CaO and CO<sub>2</sub> (Eq. 22), followed by a reaction between CaO and molten TiO<sub>2</sub> to form CaTiO<sub>3</sub> (Eq. 32). The low crystallinity and whisker-like morphology of the HA particles (Figure 28) also suggest a high surface area, which may have facilitated their partial decomposition into TCP (Eq. 28) [498]. In contrast, Kim et al. [180] used HA particles pre-treated via calcination at 900 °C to enhance crystallinity, and reported no formation of additional CaP phases. This comparison supports the hypothesis that particle crystallinity correlates with thermal stability during PEO treatment [499]. An alternative explanation should also be considered: the initially co-precipitated HA in the CC-HA particles (Figure 28) exhibited low crystallinity and may have been structurally similar to TCP [500]. In this case, HA formation in the coating could have occurred through a secondary transformation of TCP via reaction with water and hydroxyl ions at elevated temperatures (Eq. 33).



There is currently no consensus on the optimal crystallinity of HA for implant coatings, with reported ideal values ranging from 50% to 90% [501]. Importantly, the desired degree of crystallinity varies depending on the anatomical site and application—for example, tooth enamel has significantly higher crystallinity than dentin [502]. Therefore, the ability to tailor HA crystallinity should be considered a critical parameter of the coating technology. In the present study, the sharp diffraction peaks observed in the XRD pattern of the CC-HA coating (Figure 42) suggest that the incorporated phases exhibited a high degree of crystallinity. This level of ordering may limit the ability to reduce crystallinity via post-treatment. However, given that the initially co-precipitated HA was nearly amorphous, it is reasonable to propose that the final crystallinity could be tuned by modifying PEO process parameters. Specifically, employing milder oxidation conditions—such as higher pulse frequencies and duty cycles—may allow better control over plasma temperatures and enable *in situ* HA crystallization “on demand” [503].

#### 4.3.9. XPS analysis

XPS was employed to further investigate the surface composition and chemical bonding states in the CC-HA coating. Due to the microscale heterogeneity of surface features (Figure



31, Figure 32), measurements were performed at three distinct locations to ensure representative and accurate data. The survey spectra (Figure 43) show clearly identifiable peaks for Ti2p, O1s, Ca2p, P2p, and C1s, confirming the presence of all expected elements within the CC-HA coating. These core-level signals appear at binding energies of approximately 458 eV (Ti2p), 530 eV (O1s), 348 eV (Ca2p), 134 eV (P2p), and 285 eV (C1s). High-resolution spectra for these elements are presented in Figure 44, while semi-quantitative elemental data are summarized in Table 12.

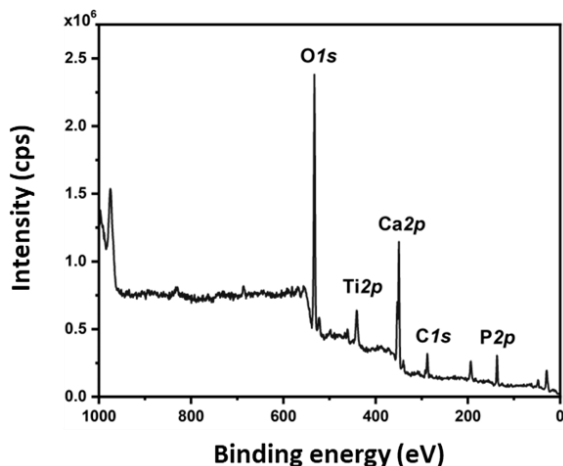


**Figure 43.** Survey XPS spectrum of CC-HA coatings.

High-resolution XPS spectra revealed one primary component along with its spin–orbit splitting pair in both the Ca2p and P2p regions. The Ca2p peaks appeared at 346.8 eV and 350.4 eV, while P2p peaks were observed at 133.7 eV and 134.5 eV. These binding energies confirm the presence of  $\text{Ca}^{2+}$  and  $\text{PO}_4^{3-}$  ions within the coating matrix [407], [426], [504]. The Ti 2p<sub>3/2</sub> peak at 457.8 eV and its spin–orbit counterpart at 463.0 eV (2p<sub>1/2</sub>) indicate the formation of titanium oxide on the CC-HA coating surface [488]. The C1s signal likely corresponds to a combination of carbonate species and adventitious carbon, the latter being commonly found in air-exposed samples [505]. The O1s spectrum similarly reflects contributions from both  $\text{TiO}_2$  and adsorbed carbon-containing species, further confirming surface oxidation. As shown in Table 12, the XPS results demonstrated good reproducibility across three measured locations, with only minor deviation observed in the second scan. This particular region showed a slightly higher Ti and lower Ca content, possibly due to local sampling of a Ti-rich zone—such as an intense discharge site or an area where CC experienced thermal decomposition. Such regions were also visible in Figure 31 and previously identified via EDX analysis (Figure 33) [313]. Overall, the semi-quantitative data in Table 12 are favorable from a biomedical perspective. The high surface concentrations of Ca and P—both in absolute terms and relative to Ti—reflect the composition of the coating’s outermost atomic layers (a few nanometers thick [506]). Upon implantation, these surface layers are expected to release  $\text{Ca}^{2+}$  and  $\text{PO}_4^{3-}$  ions in moderate amounts (Section 4.3.10), promoting bioactivity at the implant–tissue interface.

**Table 12.** Semi-quantitative elemental composition from high-resolution XPS spectra at three surface locations of the CC-HA coating, including averaged values. Data presented as element mass fractions (%).

Element (%)	Position			Average
	1	2	3	
Ti	1.3	2.5	1.2	1.7
O	53.7	53.1	54.0	53.6
Ca	18.0	14.6	18.3	17.0
P	13.3	15.3	12.7	13.8
C	13.7	14.5	13.8	14.0

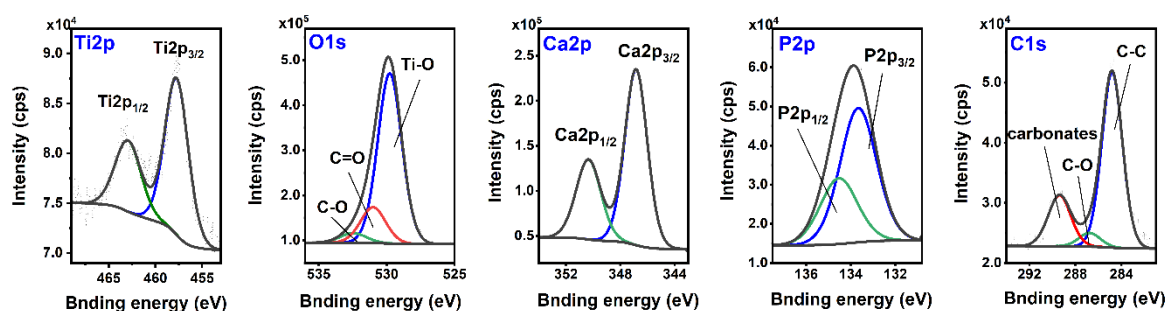


**Figure 44.** High-resolution XPS spectra for Ti2p, O1s, Ca2p, P2p, and C1s.

#### 4.3.10. Ion release tests and surface wettability

Figure 45a presents the results of calcium ion release from the coating surface, evaluated under both static and simulated dynamic conditions over a 30-day period. In the dynamic setup, PBS was refreshed every three days. Under static conditions, the cumulative release curve plateaued at approximately  $21 \text{ mg} \cdot \text{L}^{-1}$  around day 20, which reflects the solubility limit of CC in PBS. Initially, the release rate was rapid, with calcium ion concentrations reaching  $\sim 2 \text{ mg} \cdot \text{L}^{-1}$  after 1 hour and  $\sim 13 \text{ mg} \cdot \text{L}^{-1}$  after 3 days. The subsequent deceleration of the curve is attributed to the progressive approach toward thermodynamic equilibrium, where the solution becomes saturated with  $\text{Ca}^{2+}$  ions, thereby slowing further dissolution. In contrast, the dynamic release profile showed a steep decline during the first 10 days, followed by a slower decrease that stabilized around  $2.5 \text{ mg} \cdot \text{L}^{-1}$  from day 20 onward, likely reflecting the balance between ion release and removal through PBS replacement.

Given that two calcium-containing phases are present within the surface layers of the coating, the sharp decrease in calcium release during the early immersion period is likely attributed to the rapid and nearly complete dissolution of the more soluble CC phase. In the later stages, the release is primarily governed by the slower dissolution kinetics of HA, which exhibits considerably lower solubility. As the dynamic test involved periodic replacement of PBS, a higher cumulative calcium release was anticipated compared to the static setup, where only a fraction of the total calcium content was able to diffuse into the medium. The profiles of both release modes reflect typical calcium release behavior in physiological environments and align well with trends reported in the literature [507], [508]. Furthermore, titanium concentrations were assessed in all collected samples. In every case, the measured Ti levels were below the detection threshold ( $<0.1 \text{ mg} \cdot \text{L}^{-1}$ ), consistent with findings by Mohedano et al. [189], who observed similar  $\text{Ti}^{4+}$  release levels—between  $0.1$  and  $0.2 \text{ mg} \cdot \text{L}^{-1}$ —after immersing PEO-coated titanium in SBF for 1 to 4 weeks.

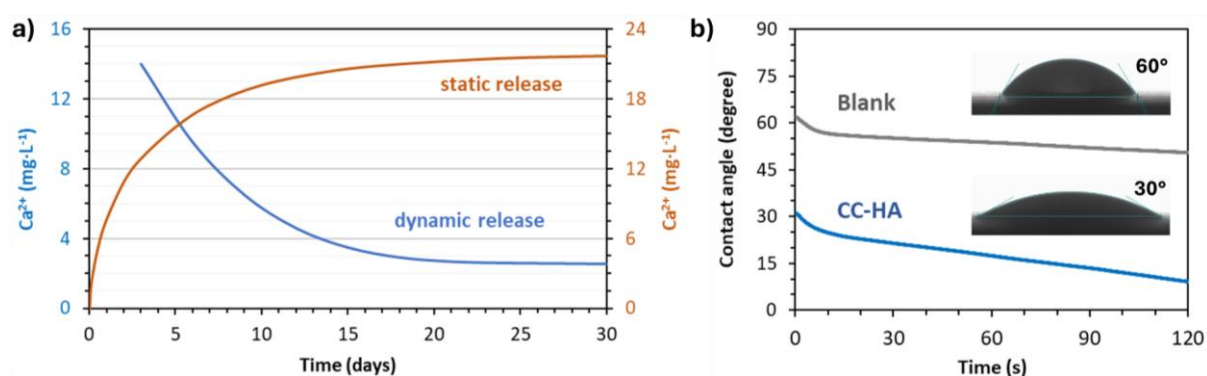


**Figure 45.** (a) Dynamic and static  $\text{Ca}^{2+}$  ion release profiles from CC-HA coatings into PBS; (b) dynamic water contact angle measurements for Blank and CC-HA coatings with as-deposited droplet images.

The continuous presence of calcium ions in the extracellular environment plays a pivotal role during all phases of osteointegration. In the early inflammatory phase,  $\text{Ca}^{2+}$  ions facilitate

leukocyte activation and the formation of a provisional extracellular matrix. Subsequently, they support osteoblast function, induce apoptosis in osteoclasts, and bind to calcium-affinitive macromolecules such as glycosaminoglycans and proteoglycans, thereby creating supersaturated conditions that initiate HA nucleation [509], [510], [511], [512]. Calcium ions localized at the implant surface also influence the local zeta potential, establishing an electrostatic environment that attracts both cells and biomolecules crucial for biomineralization [513]. The obtained release profiles confirm a sustained calcium ion release lasting at least one month, indicating that the coatings can maintain an ion-rich microenvironment across all key stages of bone-implant interaction. This sustained delivery may be particularly beneficial during the initial phase of osteointegration, due to the presence and dissolution of the CC phase, which enables a rapid increase in  $\text{Ca}^{2+}$  concentration [514]. For example, on days 5 and 10, the measured calcium levels were approximately four and 2.5 times higher, respectively, than those recorded on day 20. Early-stage calcium release has been widely recognized as beneficial [515], [516]. One notable example is the study by Anitua et al. [509], in which titanium coatings capable of releasing two-thirds of their calcium content within one minute were shown to significantly enhance osteoblast proliferation—doubling cell numbers within 7 days compared to Ca-free surfaces. In addition to promoting proliferation, calcium also supported osteoblast adhesion and differentiation, and after 12 weeks in a sheep tibia model, enhanced bone formation in the 1 mm zone surrounding the implant.

An alternative explanation for the calcium ion release behavior may be proposed by considering *in vivo* conditions following implant placement. In particular, osteoclasts – which are primarily responsible for the resorption of mineralized bone – can also interact with synthetic surfaces, modulating them for subsequent osteoblastic activity and contributing to remodeling processes [517], [518]. This interaction involves acid secretion that promotes the dissolution of mineral components, especially HA [519]. As reported in a prior study [313] and supported by the findings in Section 4.3.2, CC-HA particles synthesized for this work exhibit a bilayer structure, where HA forms an outer layer chemisorbed onto the surface of CC. It is therefore plausible that upon incorporation into the PEO coating and immersion in PBS, a substantial portion of CC remains shielded beneath this HA shell, limiting its direct contact with the solution. However, under physiological conditions, the HA layer may be gradually degraded by osteoclasts, enabling access to the underlying CC core. This biological mechanism could potentially trigger a more pronounced calcium ion release than observed under PBS-based test conditions.

Based on the established classification model [520], both types of coatings demonstrated hydrophilic behavior, with initial water contact angles measured at approximately  $60^\circ$  for the Blank coating and around  $30^\circ$  for the CC-HA coating (Figure 45b). Within 2 minutes of contact, these angles further decreased to  $50^\circ$  and  $10^\circ$ , respectively, indicating faster droplet dispersion and enhanced wettability in the CC-HA sample. Such an increase in hydrophilicity is a common phenomenon observed when particles are introduced into PEO coatings [110], [178], though the extent of this effect is largely governed by the physicochemical characteristics and concentration of the incorporated particles [226]. Both CC and HA, in their unmodified, pure forms, are inherently hydrophilic due to the presence of functional groups such as  $\text{PO}_4^{3-}$ ,  $\text{OH}^-$ , and  $\text{CO}_3^{2-}$  [20], [521], [522], which reasonably accounts for the notable difference in surface wettability between the Blank and CC-HA coatings. XRD results confirmed that only anatase was present in the Blank coating, while the CC-HA variant exhibited both anatase and rutile phases. Nevertheless, previous Raman spectroscopy data [313] indicated an absence of rutile near the outermost surface, implying that  $\text{TiO}_2$  polymorphs may not be the primary contributors to the observed wettability trends. Even assuming rutile's presence at the surface, it would likely improve hydrophilicity — a phenomenon not evident in these experiments. This assumption aligns with atomic-level simulations by Zhu et al. [523], where rutile and anatase displayed theoretical contact angles of  $73.9^\circ$  and  $43.7^\circ$ , respectively. Beyond composition, surface topography also influences wettability. The increased surface roughness observed in

CC-HA coatings [524] likely enhanced water spreading. In biomedical applications, particularly for dental and orthopedic implants, hydrophilic surfaces are generally favored due to their role in promoting protein adsorption, cell adhesion, and efficient wetting by physiological fluids — all of which are essential for successful osteointegration [525]. Nonetheless, the clinical advantages of superhydrophilicity and the identification of an ideal contact angle remain subjects of ongoing investigation [520].

#### 4.3.11. Corrosion resistance tests

EIS and PDP techniques were employed to evaluate the corrosion behavior of both Blank and CC-HA coatings. Bare titanium substrates, referred to hereafter as the Ref sample, served as the control group. The obtained impedance data are presented in Figure 46. Examination of the Nyquist (Figure 46a,b) and Bode (Figure 46c) plots for the Ref sample revealed the presence of a single RC time constant, as evidenced by one capacitive semicircle. To interpret this response, a basic equivalent electrical circuit (EEC), described by the R(QR) model, was applied (Figure 47a). In this model, the symbol Q denotes a constant-phase element (CPE), the impedance (Z) of which is defined according to the following expression [526], [527]:

$$Z_Q^{-1} = Y_Q = Y_0(j\omega)^n \quad (34)$$

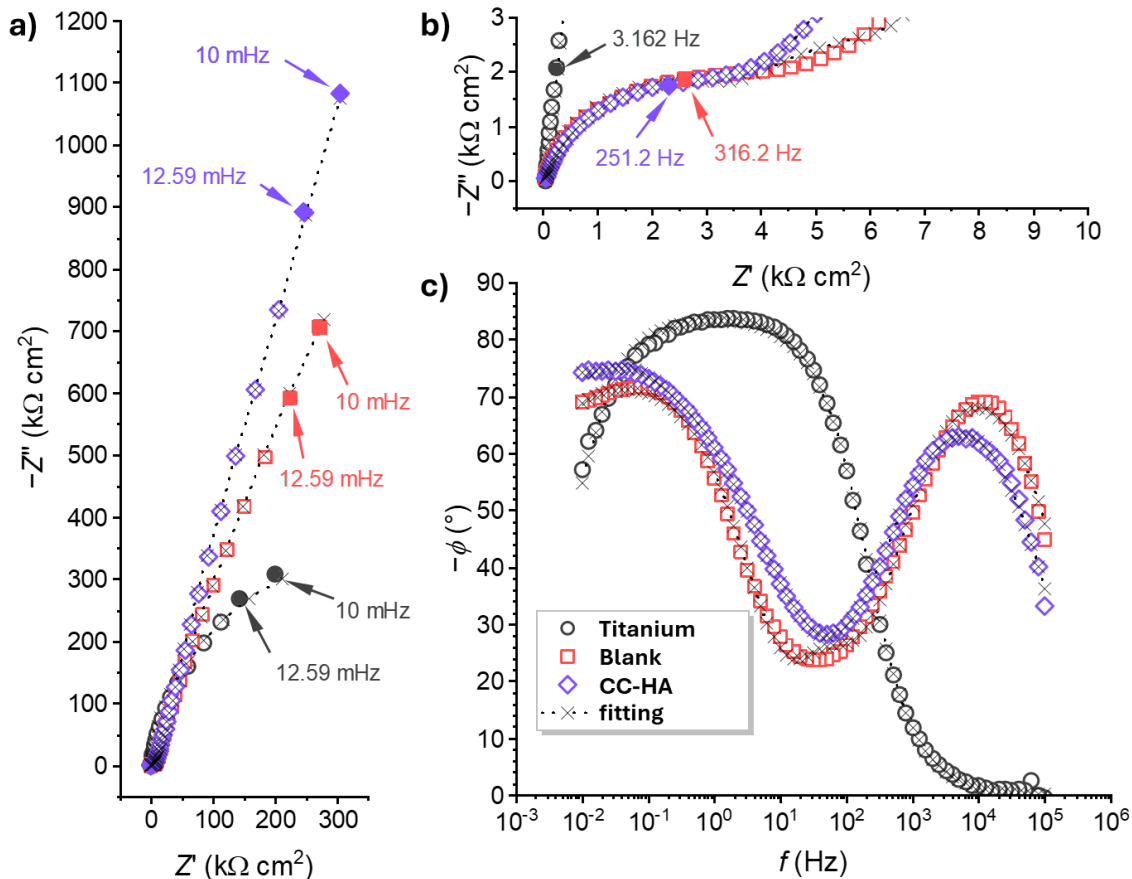


**Figure 46.** Nyquist plots at (a) low and (b) high magnifications for bare Ti (Ref), Blank, and CC-HA coatings. Cross symbols and dashed lines indicate fitted circuit data, also presented as (c) Bode phase angle plots.

In the above expression,  $Y_Q$  represents the admittance of the constant-phase element (CPE),  $j$  is the imaginary unity,  $\omega$  denotes the angular frequency, and  $Y_0$  along with  $n$  are characteristic parameters defining the behavior of the CPE. When  $n$  approaches one,  $Y_0$  approximates the behavior of a pure capacitor, and the CPE can be considered a non-ideal or "leaky" capacitor. In the equivalent electrical circuit (EEC) used for modeling the Ref sample

(Figure 47a),  $R_s$  corresponds to the electrolyte resistance,  $Q_{dl}$  describes the capacitive behavior of the electrical double layer, and  $R_{ct}$  represents the charge transfer resistance, indicative of corrosion activity. For the PEO-treated samples (Blank and CC-HA coatings), the impedance response proved more complex, as evidenced by both high-frequency and low-frequency loops in the Nyquist and Bode plots (Figure 46a-c). Initial fitting attempts using a standard  $R(Q(R(QR)))$  model resulted in poor agreement with experimental data. Therefore, alternative circuit configurations incorporating an additional time constant were evaluated. Through iterative fitting, the circuit configuration depicted in Figure 47b yielded significantly improved accuracy. However, assigning clear physical meaning to the added  $R_?$  and  $Q_?$  components was initially challenging. Further analysis revealed that the  $n$  values for these CPEs were approximately  $0.472 \pm 0.105$  for the Blank and  $0.469 \pm 0.147$  for the CC-HA coating. Such values are close to the theoretical value of 0.5, typically associated with Warburg impedance, which models diffusion-limited processes in electrochemical systems [526], [527], [528]. Based on this observation, the ambiguous  $R_?Q_?$  pair was replaced with a Warburg impedance element (Figure 47b). Both finite-length (FL) and finite-space (FS) forms were evaluated, with the former providing the best fit. This choice is also consistent with the expected physical behavior of diffusion-controlled processes in coatings. The expression describing the impedance of the finite-length Warburg element ( $W_{FL}$ ) is given in [526], [528]:

$$Z_{W_{FL}}^{-1} = Y_{W_{FL}} = Y_o(j\omega)^{0.5} \coth[B(j\omega)^{0.5}] \quad (35)$$

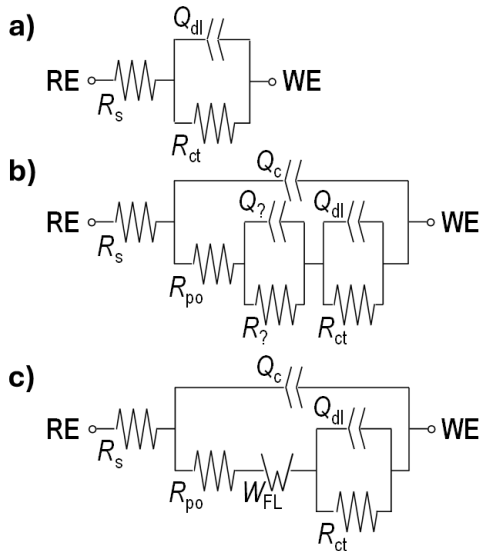


**Figure 47.** Equivalent electrical circuit models used to fit EIS data for (a) Ref samples, (b) Blank coatings, and (c) CC-HA coatings.

In this formulation,  $Y_o$  and  $B$  are the defining parameters of the finite-length Warburg element ( $W_{FL}$ ). This element accounts for ion diffusion phenomena and is characterized by a finite impedance at zero frequency, described as follows [526], [528]:

$$\lim_{f \rightarrow 0} Z_{W_{FL}} = \frac{B}{Y_o} = R_d \quad (36)$$

Here,  $R_d$  denotes the diffusion resistance, capturing the hindrance to mass transport within the porous structure of the coating. In the equivalent circuit presented in Figure 47c, two additional components are introduced to reflect the specific features of PEO coatings. The element  $R_{po}$  represents the resistance offered by the electrolyte confined within the open pores of the oxide layer, while  $Q_c$  captures the overall capacitive behavior of the coating structure as a whole.

The numerical results obtained from fitting the impedance data to the selected model are summarized in Table 13.

**Table 13.** Results of corrosion resistance testing.

Parameter	Ti Ref	Blank	CC-HA
$Q_c-Y_o, s^n M\Omega^{-1} cm^{-2}$	—	0.196±0.054	0.614±0.187
$Q_c-n$	—	0.87±0.02	0.79±0.02
$R_{po}, k\Omega cm^2$	—	4.52±1.44	4.43±1.09
$W_{FL}-Y_o, s^{0.5} M\Omega^{-1} cm^{-2}$	—	35.9±13.5	33.6±5.3
$W_{FL}-B, s^{0.5}$	—	0.0986±0.0206	3.80±0.80
$R_d, k\Omega cm^2$	—	2.88±0.54	113±4
$Q_{dl}-Y_o, s^n M\Omega^{-1} cm^{-2}$	26.7±2.6	12.4±1.2	12.6±4.4
$Q_{dl}-n$	0.94±0.01	0.80±0.05	0.94±0.03
$R_{ct}, M\Omega cm^2$	0.830±0.115	10.986±4.135	13.695±5.711
$R_{tot}, M\Omega cm^2$	0.830±0.115	10.993±4.137	13.812±5.714
$\chi^2$	$< 1.22 \cdot 10^{-3}$	$< 9.97 \cdot 10^{-4}$	$< 2.79 \cdot 10^{-4}$
$E_{OC}, mV$	-180.5±39.6	506.0±49.7	643.6±35.4
$E_{cor}, mV$	-144.6±35.8	365.5±33.7	524.2±47.0
$i_{pass}, nA cm^{-2}$	657±28	8.30±3.20	1.39±0.41

As demonstrated by the data in Figure 46 and Table 13, the model provides a highly satisfactory fit to the experimental EIS spectra, with  $\chi^2$  values below  $1.22 \times 10^{-3}$ . Additionally, the nnn values obtained for the CPE elements are generally above 0.8, indicating that the constant phase elements used in the equivalent circuit appropriately capture the capacitive characteristics of the system's electrochemical interfaces. To facilitate a comparative assessment of overall corrosion resistance, a cumulative parameter— $R_{tot}$ —was calculated by summing all relevant resistive components (i.e.,  $R_s$ ,  $R_{po}$ ,  $R_{ct}$  and  $R_d$ ). This analysis revealed that the PEO-treated samples provided significantly enhanced resistance—by at least one order of magnitude—compared to the untreated titanium reference, which possesses only its natural passive oxide layer (Table 13). Among the coatings, the samples fabricated with carbonate-containing particles exhibited a marginally higher corrosion resistance on average; however, this difference was not statistically significant. Interestingly, the values of  $R_{po}$  for both PEO-modified coatings were nearly identical, despite notable differences in their microstructure (Figure 35). This observation suggests that, although the CC-HA coatings were thicker and embedded with particulate matter, they offered a comparable permeable volume to the corrosion medium as the thinner Blank coatings. The most notable distinction was observed in the Warburg element values: specifically, the diffusion resistance ( $R_d$ ) for the CC-HA coating was found to be approximately two orders of magnitude greater than that of the Blank variant. This is likely a result of the substantially increased coating thickness and structural complexity, which may have introduced longer and more tortuous diffusion pathways, thereby impeding oxygen transport to the metal interface. To further evaluate this effect, the diffusion length ( $\delta$ ) for oxygen species was estimated using the following expression [526], [528]:

$$\delta = B\sqrt{D} \quad (37)$$

In this equation,  $D$  represents the diffusion coefficient for oxygen within the corrosive environment. Assuming a  $D$  value of  $2620 \mu m^2 \cdot s^{-1}$ , which corresponds to oxygen in pure water, the diffusion length ( $\delta$ ) was estimated to be approximately  $5.04 \pm 1.06 \mu m$  for the Blank coating and  $194 \pm 29 \mu m$  for the CC-HA coating. These estimates should be considered approximate, as specific diffusion coefficients for oxygen in PBS were not available in the literature. Nonetheless, the derived  $\delta$  for the Blank sample is of the same order of magnitude as the actual coating thickness, lending credibility to the validity of the equivalent circuit model (Figure 35). In contrast, the significantly longer diffusion length observed for the CC-HA coating—nearly an order of magnitude greater than its physical thickness—suggests the presence of a more intricate pore network. This enhanced complexity likely results in increased tortuosity and restricted oxygen transport through the oxide layer.

Following the completion of EIS measurements, PDP tests were conducted. The resulting representative polarization curves are displayed in Figure 48, and the key electrochemical parameters derived from these plots are summarized in Table 13. A noticeable discrepancy was observed between the measured corrosion potential  $E_{\text{cor}}$  and the open-circuit potential  $E_{\text{OC}}$ , particularly for the samples with PEO coatings. For the untreated titanium reference specimens (Ref), the  $E_{\text{cor}}$  value—recorded after approximately 200 minutes of immersion—was slightly higher than  $E_{\text{OC}}$ , which was measured just prior to the EIS experiment (after 120 minutes of immersion). This shift can be attributed to the natural passivation process occurring on the titanium surface in contact with the PBS environment [529]. In contrast, for both PEO-coated samples, the  $E_{\text{cor}}$  values were shifted by approximately 120–140 mV relative to  $E_{\text{OC}}$ . This deviation is primarily a consequence of the capacitive nature of the coatings, which leads to a measurable charging current during the potential sweep. Despite these differences, the measurements were sufficiently consistent across replicates to enable meaningful comparisons. As anticipated, the application of PEO treatment resulted in a positive shift in  $E_{\text{cor}}$ , indicating enhanced corrosion resistance. This shift was more pronounced in the coating containing CC particles. Notably, even at the reversal point of the polarization scan (2 V), all samples remained in a passive state, as evidenced by a decrease in current density, suggesting no coating breakdown occurred under test conditions. To further assess the protective behavior of the coatings, passivation current density ( $i_{\text{pas}}$ ) was measured at a potential of 0.8 V. This voltage was selected to avoid interference from competing reactions, such as oxygen evolution, which typically becomes significant at higher potentials [530]. The  $i_{\text{pas}}$  value for the untreated Ti sample was approximately two orders of magnitude higher than that for the PEO-treated surfaces, reinforcing the superior corrosion resistance provided by these coatings. Among them, the CC-HA coatings exhibited the lowest passivation current, consistent with the trends observed in the EIS measurements.

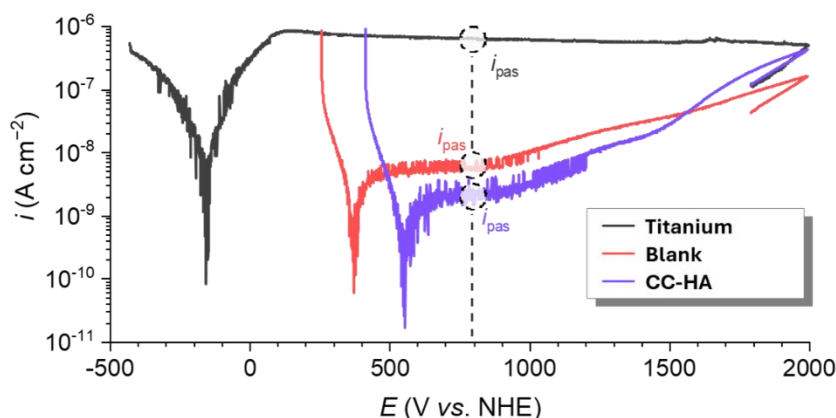


**Figure 48.** PDP curves for bare Ti (Ref), Blank, and CC-HA coatings.

In summary, the corrosion studies confirmed a substantial enhancement in the corrosion resistance of titanium upon application of PEO coatings. This protective effect was further amplified when the coatings were synthesized using CC-HA particles, resulting in higher corrosion resistance compared to the coatings formed in the particle-free (Blank) electrolyte. Among the PEO-treated samples, corrosion processes were modestly influenced by the diffusion of oxygen from the bulk electrolyte to the underlying metal interface. Notably, the coating derived from the CC-HA-enriched electrolyte exhibited a markedly higher diffusion resistance, indicating more effective hindrance to mass transport within its porous structure.

Only a limited number of publications have systematically evaluated the influence of particulate additives—especially HA—on the corrosion performance of PEO coatings formed on titanium substrates. This may be due to titanium's inherently high corrosion resistance, which, unlike more reactive metals such as magnesium, often makes it suitable for biomedical applications even in its uncoated form [531]. Nonetheless, the work by Bai et al. [532], who

used HA particles ( $0\text{--}20\text{ g}\cdot\text{L}^{-1}$ ) in a NaOH–ethanol-based electrolyte for PEO processing, indicated that particle addition can enhance the corrosion resistance of PEO coatings. However, the outcome was highly concentration-dependent and, in some cases, led to increased corrosion current densities compared to coatings without particle reinforcement. A more consistently beneficial effect is often observed when HA is used in PEO coatings on Mg substrates, where corrosion resistance can improve significantly—sometimes by an order of magnitude relative to particle-free coatings [353], [215]. Even so, such improvements are not guaranteed, as particle incorporation can also negatively affect key coating properties such as thickness, porosity, and structural integrity [533]. Taking these observations into account, the improved corrosion resistance of the CC-HA coatings in the present study likely reflects a well-optimized combination of processing parameters and particle concentration tailored for this specific system.

#### 4.3.12. Surface scratch tests

Scratch testing offers essential insights into how implant coatings behave under practical conditions involving mechanical wear, surface contact, and friction [534]. One of the critical requirements for coatings used in biomedical applications is sufficient adhesion to the underlying substrate, which ensures mechanical stability once implanted [535]. In the present study, scratch tests were employed not only to evaluate the mechanical durability of the coatings but also to compare the impact of incorporating CC-HA particles on adhesion-related performance. The outcomes are summarized in Figure 49, which includes data on the critical loads (Lc1 and Lc2), as well as representative optical and SEM images of the damage patterns observed along the scratch paths.

The first critical load, Lc1, corresponds to the initial onset of coating degradation under increasing mechanical stress. In optical micrographs (Figure 49b,c), this is manifested by a sequence of bright, localized spots distributed along the scratch trajectory, contrasting with the darker, undisturbed coating surface. These spots mark the initiation of partial delamination and localized substrate exposure. In reality, structural damage begins at much lower loads—as soon as the diamond stylus makes contact with the surface—leading to gradual breakdown of the porous morphology and progressive broadening of the scratch path. Such early mechanical response has been previously described by Cheng et al. [536] and Chen et al. [537], who reported visible deformation at loads as low as  $0.1\text{--}0.2\text{ N}$ . The second critical load, Lc2, denotes the point at which the coating suffers major damage—ranging from deep furrows and extended cracking to full delamination. In the micrographs, this damage is visible as a continuous, bright line tracing the scratch, indicating a severe loss of coating integrity. According to the results presented in a, the CC-HA-modified coatings consistently demonstrate higher Lc1 and Lc2 values, implying improved mechanical robustness, resistance to surface damage, and higher adhesion strength. A review by Sharifi et al. [23] emphasizes that multiple parameters—including electrolyte composition, processing time, and electrical conditions—affect adhesion performance in PEO coatings. Since the electrical parameters were standardized in this study, the observed improvement can be directly attributed to the influence of the incorporated CC-HA particles and the resulting modifications to the coating microstructure.

CC and HA are intrinsically brittle materials [410], [538], so it was initially anticipated that their incorporation into the CC-HA coating would reduce its resistance to mechanical loading, reflected in lower Lc1 and Lc2 values. Contrary to this expectation, the CC-HA coating demonstrated enhanced adhesion strength, largely due to the substantial increase in its thickness compared to the Blank coating (Section 4.3.5). This positive effect of coating thickness on mechanical performance is not only characteristic of PEO layers [539], but is also observed across various surface engineering techniques [540]. A greater volume of coating material provides an extended pathway for dissipating mechanical stress, thereby reducing the likelihood of premature detachment. One distinguishing feature observed in the scratch profiles of CC-HA coatings is the irregular pattern of damage progression under increasing load—visible as



alternating zones of bright and dark contrast. Such features indicate a non-uniform penetration depth of the stylus and are likely linked to the higher surface roughness of CC-HA coatings relative to the Blank variant (Section 4.3.4), consistent with prior findings by Cheng et al. [536] for PEO-treated Ti surfaces using pulsed current modes. It is worth noting, however, that while both Lc1 and Lc2 values increased for the CC-HA coating, the magnitude of this improvement is relatively modest considering the threefold increase in thickness. This suggests that the mechanical robustness of the outermost layers may be lower than that of the inner regions. In fact, the assumption that higher thickness always yields greater mechanical integrity is not universally valid. Durdu et al. [541] demonstrated this by extending the PEO treatment time on Ti6Al4V substrates from 20 to 60 minutes, which increased the coating thickness by 1.5 times, yet resulted in only a ~25% rise in the critical load for total failure (6.7 N vs. 5.2 N). Additionally, our observations align with the findings of Mandelli et al. [542], who reported that the deeper layers of PEO coatings tend to exhibit superior adhesion. This phenomenon can be linked to the formation of a compact barrier layer near the substrate interface, which is a fundamental feature of PEO-generated oxide films [429].

In principle, critical loads Lc1 and Lc2 can be used for cross-study comparisons. However, when it comes to PEO coatings, the objectivity of such comparisons is often compromised due to several interrelated factors: (1) significant variability in PEO process parameters, electrolyte compositions, and substrate types—especially among titanium alloys—all of which heavily influence the resulting coating characteristics [539], [543]; (2) a limited number of publications reporting scratch resistance for PEO-based implant coatings, reducing the availability of data with matching parameters such as thickness; (3) sensitivity of scratch test outcomes to experimental settings, including scratch speed, loading rate, and stylus geometry [544]; and (4) the diversity of failure mechanisms observed during scratching, which leads to variability in data interpretation and comparison frameworks [545]. Among the limited studies that enable meaningful benchmarking, the work by Yeung et al. [31] offers the most direct comparison. Their PEO process employed Na<sub>2</sub>HPO<sub>4</sub>-based electrolytes and pulsed current treatment on a Ti6Al4V alloy, resulting in coatings similar to the Blank variant in this study—composed of anatase and rutile phases with thicknesses around 7.5–9.5 μm. While there were slight differences in test parameters, their reported Lc1 and Lc2 values (3.0 N and 5.5 N, respectively) are in good agreement with those of the Blank coating (Figure 49a). Despite the usefulness of Lc values in controlled studies, their absolute magnitudes are not always predictive of *in vivo* behavior. This is particularly relevant for PEO coatings formed in conventional baths (like the phosphate-based solution used here), which are known to provide strong interfacial adhesion—often outperforming techniques such as sol-gel or thermal spray deposition [23]. Such coatings have consistently shown favorable performance in biological environments [546], [547], [548]. Given that the CC-HA coatings demonstrated higher Lc1 and Lc2 values than the Blank reference, it is reasonable to infer that their mechanical integrity under physiological conditions will be at least comparable, if not superior. Importantly, the absence of reduced scratch resistance following CC-HA incorporation suggests that mechanical performance is preserved, supporting their potential suitability for implant applications.

While optical microscopy alone can offer a general understanding of coating scratch resistance [31], [543], it lacks the resolution needed to uncover finer structural changes or subtle failure mechanisms. Therefore, combining optical observations (Figure 49b,c) with SEM analysis of the scratch tracks (Figure 49d) provides a more comprehensive view. As shown in the SEM images, the outer layers of the CC-HA coating tend to fracture when in contact with the diamond indenter. This is evident from the appearance of microcracks and localized detachment of fine particles along the scratch edges—features absent in the Blank coating. These phenomena are likely due to surface regions enriched in CC and HA phases, which can locally increase the coating's brittleness [410], [538]. Similar effects were noted by Kozelskaya et al. [126] for CaP-containing coatings produced via pulsed current PEO. Despite this local degradation, the bulk of the CC-HA coating remains well adhered to the substrate, with no

evidence of delamination or interfacial failure, even at higher loads [545]. The absence of large-scale detachment is especially notable given that such damage is commonly reported in PEO coatings subjected to extended oxidation times [223]. Both the Blank and CC-HA coatings exhibit fine, shallow cracking dispersed across the scratch path—an effect also reported for Ti6Al4V substrates treated with alternating current in phosphate-based electrolytes [549]. However, more serious defect types, such as arc tensile or chevron cracks [126], were not observed in either sample. Overall, the SEM data affirm strong coating-substrate adhesion. The lack of large cracks or delamination along the scratch path also supports the presence of sufficient cohesive strength within the coatings. Should further enhancement of adhesion be required, strategies such as increasing cathodic voltages in AC PEO modes [550] or applying post-treatment thermal processing [536] could be considered.

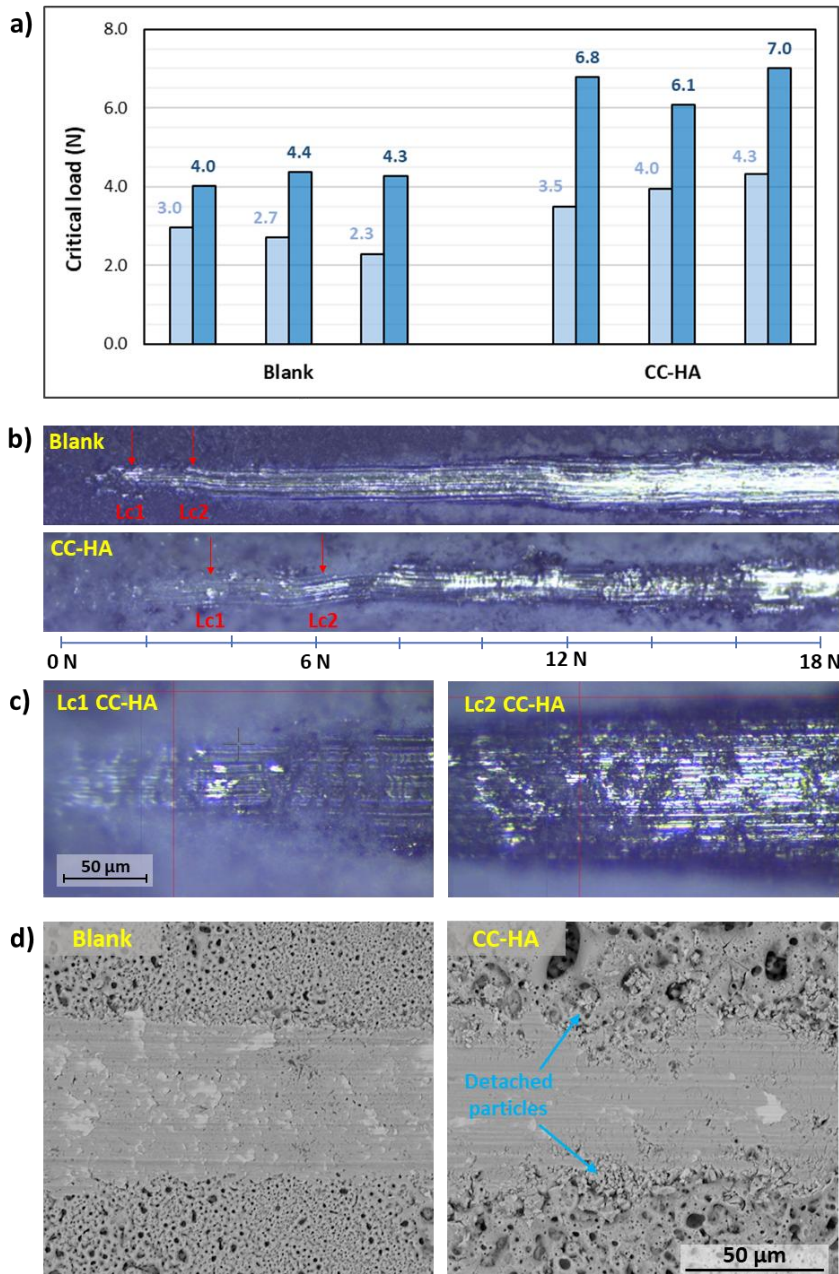


**Figure 49.** Scratch resistance testing results: (a) comparison of Lc1 and Lc2 values for Blank and CC-HA coatings (three repetitions); (b) optical scratch paths with indicated critical loads; (c) optical images of CC-HA coatings near Lc1 and Lc2; (d) SEM images of Blank and CC-HA coatings between Lc1 and Lc2.

#### 4.3.13. Assessment of biocompatibility and antibacterial performance

Figure 50 presents the evaluation of cellular interactions with polished Ti, PEO-Blank, and PEO-CC-HA surfaces. While all samples supported initial cell proliferation up to day 3, both the polished titanium and Blank coatings exhibited a notable decline by day 7, suggesting insufficient biochemical stimulation and suboptimal adhesion. In contrast, the CC-HA-modified surface displayed continuous enhancement in cell proliferation from day 1 through day 7 (Figure 50, diagram). This behavior is consistent with previous findings that calcium-based inorganic materials, such as CC, can stimulate cell adhesion and growth [501], [551]. The steady release of calcium and phosphate ions from the surface (as demonstrated in Section 4.3.10) likely contributes to the improved cellular activity observed on the CC-HA coatings.

Fluorescence staining performed on day 7 further emphasized morphological differences among the samples. Cells cultured on polished Ti exhibited notable heterogeneity in nuclear shape—ranging from oval and elongated to round nuclei—signs often associated with cellular stress or early apoptosis (Figure 50a). Additionally, the irregular Actin Red staining of the cytoplasm indicated impaired metabolic function. In contrast, both PEO-treated surfaces supported more favorable cellular morphologies. The Blank and CC-HA coatings were fully covered with adherent cells exhibiting uniformly oval nuclei and well-developed cytoplasm (Figure 50b,c). Particularly on the CC-HA surface, cell clustering and intercellular connectivity were more pronounced, resembling a symplastic structure (Figure 50c, insertion).

Taken together, these observations confirm that CC-HA incorporation into PEO coatings enhances surface biocompatibility by promoting cell viability and adherence. Previous literature shows that PEO treatments can have variable effects on biocompatibility, depending on electrolyte composition and process parameters—with outcomes ranging from improved [552], unchanged [553], to diminished [554] cell performance. However, when bioactive ceramic phases like HA, TCP, or  $\text{CaTiO}_3$  are integrated into the coating, the tendency leans toward enhanced or preserved cell behavior relative to untreated titanium surfaces [185], [424], [488]. The current findings are in alignment with this general trend.

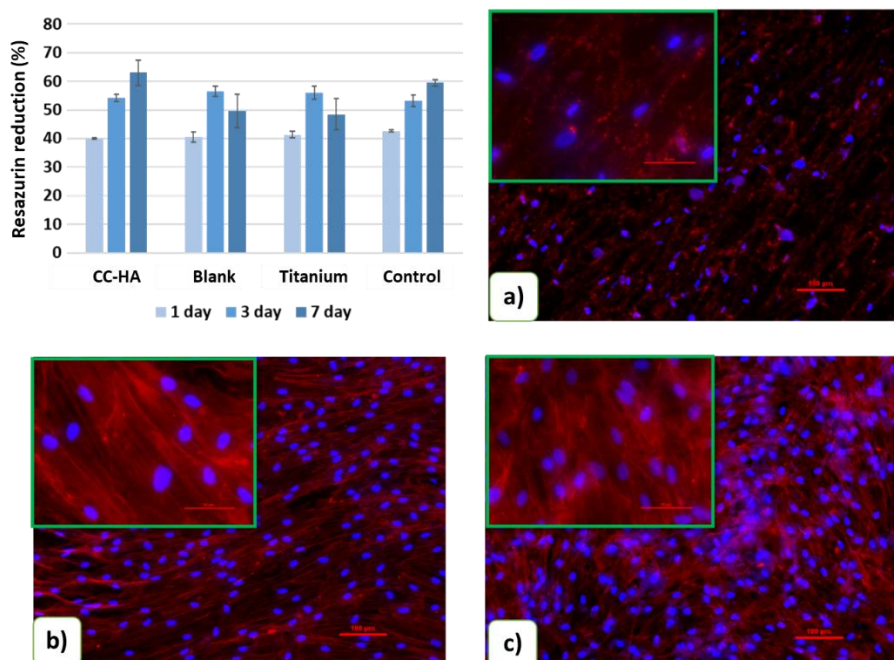


**Figure 50.** Resazurin reduction assay results after 7 days of D6P10 cell cultivation on various test surfaces, accompanied by fluorescence images showing nuclei (blue) and cytoskeleton (red) staining on day 7 for (a) polished Ti, (b) Blank, and (c) CC-HA surfaces. Main images captured at  $\times 100$  magnification (scale bar = 100  $\mu\text{m}$ ); insets at  $\times 400$  magnification (scale bar = 50  $\mu\text{m}$ ).

Bacterial biofilms represent a major challenge in clinical settings, contributing to device-associated and nosocomial infections. These structured microbial communities adhere

to implant and instrument surfaces, exhibiting significant resistance to conventional antibiotics and disinfectants, thus complicating treatment efforts. Biofilm development is strongly influenced by material surface properties such as topography, wettability, and intrinsic antimicrobial activity. Consequently, many preventive strategies aim to interrupt the initial bacterial adhesion phase, which is critical in mitigating subsequent biofilm establishment [555], [556]. Surfaces that inherently reduce microbial attachment are therefore of particular interest in medical device design. Titanium-based materials, while widely used, have been shown to allow bacterial adherence through a combination of physicochemical and biological mechanisms. These include long-range forces like Lifshitz–van der Waals interactions, hydrogen bonding, and electrostatic forces (Section 4.3.14), as well as short-range interactions driven by Brownian motion [557], [558]. Additionally, specific binding events involving bacterial surface proteins and titanium surfaces, alongside surface wettability characteristics at the solid–liquid interface, play a crucial role in microbial adhesion [559], [560].

Bacterial adhesion assays were performed to investigate how surface characteristics influence microbial colonization over time. Initial evaluations at the 2-hour mark showed that all tested surfaces—polished titanium, Blank, and CC-HA coatings—supported early-stage bacterial attachment. At this point, both *S. aureus* and *E. coli* exhibited comparable adhesion levels, reaching approximately 4 log CFU·mL<sup>-1</sup> and 5 log CFU·mL<sup>-1</sup>, respectively. However, the subsequent growth patterns diverged significantly depending on the surface type. The polished Ti specimens supported the most rapid bacterial proliferation, with colony-forming units increasing over time to peak values of ~10<sup>8</sup> CFU·mL<sup>-1</sup> for *S. aureus* and ~10<sup>7</sup> CFU·mL<sup>-1</sup> for *E. coli*. In contrast, the Blank coatings demonstrated only modest bacterial development. This relatively limited growth may be associated with the distinct surface features imparted by the PEO process, including specific surface chemistry, microtopography, and enhanced hydrophilicity. These factors likely contributed to a less favorable environment for bacterial attachment and multiplication, as visualized in Figure 51.

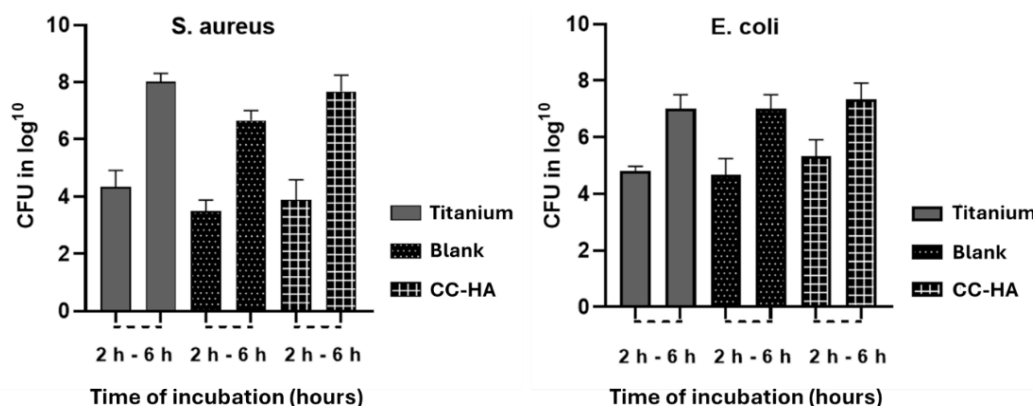


**Figure 51.** Bacterial adhesion to coatings as a function of time.

The incorporation of CC-HA particles into the coating appeared to slightly increase bacterial adhesion, which may be attributed to the influence of CC and HA on the surface charge characteristics (as discussed in Section 4.3.14), thereby diminishing the surface’s natural resistance to microbial attachment. Both CC and HA seemed to contribute to a more favorable environment for initial bacterial contact. However, this effect did not lead to a statistically significant enhancement in bacterial growth compared to the polished titanium or Blank PEO coatings. While the CC-HA surface demonstrated a marginal tendency to inhibit bacterial adhesion, the observed differences in colony formation and surface colonization remained statistically insignificant across all tested surfaces. Interestingly, for *S. aureus*, a slight decrease in the number of adherent cells was observed on the CC-HA surface at both 2 and 6 hours post-inoculation. Although overall biofilm formation by *S. aureus* and *E. coli* increased over time, no notable differences in bacterial load were detected between the tested groups ( $p > 0.05$ ), as

shown in the corresponding growth profiles. These findings suggest that CC-HA-modified coatings do not exacerbate bacterial colonization compared to uncoated or conventionally coated surfaces, thus confirming their suitability for biomedical use. Nonetheless, for applications requiring explicitly antibacterial functionality, the integration of silver—either in ionic form [561] or as nanoparticles [562]—remains a widely adopted strategy in PEO-based systems [563].

#### 4.3.14. Surface zeta potential measurements

Zeta potential measurements were employed to further characterize the surface properties of the Blank and CC-HA coatings and to better understand their potential behavior in physiological environments. This parameter reflects the net surface charge polarity, dictated by the balance of ionizable groups on the surface, while its absolute value depends on the density of surface charges [564]. Notably, both of these aspects are sensitive to the pH of the surrounding medium—typically, a rise in pH leads to a more negative zeta potential. As illustrated in Figure 52, this expected trend was confirmed for both coating types. When the pH was raised from approximately 5–6 to around 9, the zeta potential dropped from -40 mV to -47 mV for the Blank samples, and from -20 mV to -27 mV for the CC-HA samples. In general, the results exhibited high consistency, although measurements above pH 7.5 showed minor deviations. These fluctuations are likely linked to CO<sub>2</sub> uptake from ambient air by the NaOH-containing KCl solution, forming carbonate and bicarbonate species that could adsorb onto the surface and modulate its charge—an effect also observed in earlier work by Szweczyk et al. [565] on electrospun cellulose acetate fibers. Leaving aside the contributions of environmental conditions such as pH, ionic strength, or temperature, and focusing solely on intrinsic surface characteristics, the primary factor determining zeta potential is the surface chemical composition. In this context, the CC-HA coatings consistently showed zeta potential values that were approximately 20 mV higher than those of the Blank coatings (Figure 52), indicating a shift toward less negative surface charge. This behavior likely stems from the incorporation of CC, as it is the only phase among those identified in the CC-HA system—namely anatase, rutile, CC, HA, TCP, and CaTiO<sub>3</sub> (Section 4.3.8)—that carries a net positive electrokinetic charge even under alkaline conditions (up to pH 10–11) [396], [566], [567], [568]. Therefore, these results offer further evidence supporting the presence of exposed CC on the outer surface of the coating in appreciable amounts.

Although surface features such as roughness and porosity are often discussed in the context of surface interactions, their influence on zeta potential tends to be minimal or even negligible in most cases [569], [570]. Nonetheless, certain types of topographical structures—particularly those that are poorly streamlined and oriented perpendicular to fluid flow—can affect the accuracy of zeta potential measurements. These features, which include sharp protrusions or trench-like formations, may disrupt local hydrodynamics by acting as physical obstructions, causing backflow, restricting liquid-surface contact, and creating partially unwetted regions. As a result, the effective zeta potential captured during measurement may be underestimated, yielding values that appear less positive or less negative than the true surface charge would suggest [571]. An illustrative case was reported by Drechsler et al. [569], who studied polyvinylidene fluoride (PVDF) substrates with varying surface topographies. They observed that introducing trenches perpendicular to the flow increased the mean square roughness from 0.1  $\mu\text{m}$  (flat surface) to 0.6  $\mu\text{m}$ , which in turn led to a substantial decrease in the measured zeta potential at pH 7—from -50 mV for the smooth surface to -75 mV for the rough one, highlighting a 25 mV difference. This discrepancy could become even more pronounced if the excluded regions possess differing phase compositions, contributing further to surface charge heterogeneity. In our case, although the Blank and CC-HA coatings exhibited similar disparities in surface roughness, the overall surface morphology was characterized by evenly distributed topographic features—namely, gently alternating hills and valleys, as observed in Figure 32. Moreover, previous investigations involving identically fabricated

coatings demonstrated that the horizontal distribution of phases across the surface remained uniform down to a scale of several tens of micrometers, with consistent presence of CC, HA, and TiO<sub>2</sub> at all elevations [313]. These findings support the assumption that fluid flow remained well-distributed across the coating surface and that all compositional phases were uniformly wetted by the KCl solution. Hence, the recorded zeta potential values primarily reflect the inherent surface chemistry rather than being significantly influenced by topographical effects.

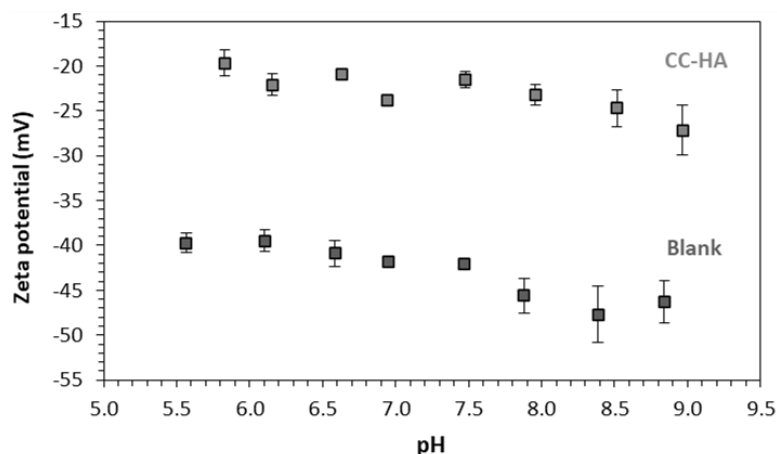


**Figure 52.** Surface zeta potential of Blank and CC-HA coatings as a function of pH.

Although surface zeta potential is considered a reliable indicator of how well a biomaterial may attract osteoblasts and integrate with bone tissue [572], it is still not routinely included in biomaterial surface characterization workflows [573]. This is particularly evident in the case of PEO-derived coatings and implants, where such measurements are rarely reported. However, the limited body of relevant literature does provide some comparative insights that align—either directly or indirectly—with the present findings [167], [574], [575], [576]. For example, Lorenzetti et al. [576] synthesized TiO<sub>2</sub> coatings in the anatase form through a hydrothermal route, wherein titanium substrates were treated at 200 °C for 48 hours in a solution containing Ti(IV) isopropoxide. Their measured zeta potential of −52 mV closely matched the values observed for our Blank coating at elevated pH levels (Figure 52). In another study by Tan et al. [167], PEO coatings were created on titanium using a Na<sub>2</sub>HPO<sub>4</sub>-based electrolyte supplemented with silicon-encapsulated CC (Si/CC) particles. Although all resulting coatings had a net negative surface charge—similar to the Blank and CC-HA coatings discussed here—the changes in zeta potential due to particle incorporation followed an opposite trend. Their data showed a zeta potential of −15.95 mV for particle-free coatings, dropping further to values between −20.98 and −34.67 mV depending on the concentration of added Si/CC particles. However, direct comparison is complicated by the use of composite particles in which the CC core was isolated from the surrounding environment by a silicon shell, thus likely preventing any meaningful interaction between the carbonate phase and the electrolyte during testing. Closer alignment with our results was seen in a study by Wei et al. [575], who measured a zeta potential of −47 mV for anatase-containing PEO coatings produced from a bath containing only soluble salts. These coatings were later modified with Si-doped HA nanorods using microwave hydrothermal treatment, which resulted in a decrease in the magnitude of the negative charge, yielding a zeta potential of −29 mV. Among works focusing specifically on CC coatings on titanium, the most similar zeta potential values to those obtained for our CC-HA coatings were reported by Tovani et al. [574]. Their layer-by-layer fabricated coatings exhibited a surface charge of approximately −19 mV, closely matching the average values recorded in our study.

When evaluating the surface zeta potential of implant coatings, no universally agreed-upon optimal range exists, largely due to differences in experimental protocols and material surface characteristics. Nonetheless, a commonly shared viewpoint in the literature suggests



that surfaces possessing a moderate surface charge—whether positive or negative—are generally more favorable than those exhibiting near-neutral zeta potentials or extremely high or low values. This idea is exemplified by the work of Szewczyk et al. [565], where cellulose acetate fibers generated via electrospinning showed improved attachment and proliferation of MG-63 osteoblast-like cells at a zeta potential of  $-12.2$  mV. Similarly, Gruening et al. [577] observed that Ti surfaces modified with various functional groups (e.g., amino polymers, ECM proteins, or polyelectrolytes) achieved the highest intracellular calcium responses when the surface zeta potential was moderately positive (ranging from  $+1$  mV to  $+10$  mV). Conversely, more negatively charged surfaces ( $-90$  to  $-3$  mV) elicited a lower cellular response, while highly positive surfaces ( $\sim +50$  mV) were found to be cytotoxic—marked by impaired membrane integrity and a significant decline in cell proliferation and calcium mobilization.

However, these general observations are not without exceptions. Some research findings reveal preferential osteoblast adhesion on negatively charged surfaces, while their positively charged counterparts showed minimal or even inhibitory effects on cell attachment [578]. A plausible explanation for this inconsistency lies in the inherent negative surface charge of osteoblasts and fibroblasts [578], [579], which could result in electrostatic repulsion from highly negative surfaces. In the case of the CC-HA coatings examined in this study, enhanced cell viability and proliferation may be attributed not solely to electrostatic attraction but also to synergistic effects involving bioactive surface composition, increased roughness, and improved wettability (Sections 4.3.4 and 4.3.10). Additionally, rather than interacting directly with cells, negatively charged surfaces may initially attract cationic proteins from body fluids, which can act as intermediaries in cell adhesion [580]. Since protein adsorption is known to occur within seconds after an implant is exposed to blood [581], the kinetics of cell attachment is unlikely to confer any major advantage to positively charged surfaces over their negatively charged counterparts. This understanding supports the practical effectiveness of both surface charge polarities in promoting osteointegration. On the other hand, extreme zeta potential values—regardless of polarity—tend to have detrimental consequences. Such surfaces may excessively anchor segments of the cell membrane, thereby restricting cellular expansion and ultimately limiting the spread of the osteointegration front [580].

Similar to osteoblasts and fibroblasts, most bacterial species also exhibit a net negative surface charge, primarily due to the presence of ionized functional groups such as phosphate and carboxyl moieties within their outer membranes [582]. As a result, negatively charged biomaterial surfaces are generally thought to repel bacteria through electrostatic interactions. This concept was demonstrated by Smith et al. [583], who systematically adjusted the zeta potential of silica substrates—from  $-81.0$  mV to  $-13.4$  mV—using various surface treatments. When exposed to *Mycobacterium smegmatis*, a clear inverse relationship emerged: substrates with more negative zeta potentials exhibited reduced bacterial coverage. This was consistent with the measured zeta potential of *M. smegmatis*, which was  $-29$  mV at physiological pH (7.42). A similar rationale can be applied to the bacterial adhesion results presented for the Blank and CC-HA coatings (Section 4.3.13), as both *Escherichia coli* and *Staphylococcus aureus* possess negatively charged outer membranes [584], [585]. Given that the CC-HA coating had a comparatively less negative zeta potential (Figure 52), it may have exhibited slightly reduced repulsion, allowing marginally more *S. aureus* adhesion (Figure 51). Interestingly, repulsive effects are not limited to negatively charged surfaces. For instance, Kao et al. [586] reported reduced bacterial attachment of *Pseudomonas aeruginosa* on titanium screws coated with positively charged polyelectrolyte multilayers fabricated via a layer-by-layer deposition method. Despite these trends, no universal agreement has been reached concerning which surface charge polarity is optimal for minimizing bacterial colonization. Several factors may contribute to the conflicting outcomes observed across studies, including variations in surface chemistry, differences in bacterial envelope properties across species, and adaptive mechanisms by which certain bacteria can modulate their surface charge in response to environmental stimuli [586]. Beyond microbial adhesion, zeta potential measurements also

serve as valuable predictors for a surface's capacity to induce HA precipitation, both *in vitro* (e.g., SBF tests) and potentially *in vivo*. Generally, negatively charged surfaces are considered more favorable for HA nucleation, as they facilitate the initial attraction of  $\text{Ca}^{2+}$  ions from the surrounding medium [587], [588], [374]. In contrast, surfaces with a strong positive charge are often less conducive to HA formation, as the increased adsorption of  $\text{Cl}^-$  ions may interfere with crystal growth [588].

In summary, the zeta potential of the CC-HA coating—approximately  $-22$  mV at physiological pH (Figure 52)—can be characterized as moderately negative, a range generally considered favorable for biomedical implants. Under physiological conditions, such a surface charge is likely to attract osteoblasts through electrostatic interaction without being so strong as to induce adverse effects like membrane flattening or cellular entrapment [580]. This moderately negative potential may also be sufficient to exert a repelling force against bacterial cells [583], while simultaneously indicating a surface enriched in negatively charged groups such as  $\text{Ti-OH}$ , which are known to enhance HA nucleation [494]. These surface charge characteristics align with earlier findings from cell adhesion and antibacterial assays (Section 4.3.13), reinforcing the conclusion that the CC-HA coating supports improved fibroblast proliferation compared to Blank coatings, while exhibiting comparable antibacterial behavior. However, it is important to acknowledge that surface zeta potential does not act in isolation. Biological interactions are also modulated by additional surface parameters such as chemical composition, micro/nanoroughness, and wettability [589].



## 5. SUMMARY AND OUTLOOK

The work presented in this dissertation set out to address the challenge of incorporating calcium carbonate (CC) and hydroxyapatite (HA) into plasma electrolytic oxidation (PEO) coatings on titanium implants—an objective motivated by the combined potential of CC's bioresorbability and HA's bone-mimetic stability to enhance implant bioactivity and osteointegration. Central to this aim was the hypothesis that conventional electrolyte preparation methods offer limited applicability for carbonate-phase incorporation, and that a particle-assisted route could provide a practical and versatile solution. The research also sought to broaden the fundamental understanding of particle incorporation mechanisms in PEO and to develop a reproducible, optimized coating process suitable for biomedical application.

The preliminary investigations established foundational knowledge regarding how electrolyte composition and parameters affect coating formation in phosphate–carbonate systems. Systematic variation of phosphate salt type and concentration revealed measurable yet generally moderate influences on coating morphology and composition. Among the three sodium phosphates tested, tribasic sodium phosphate produced slightly more distinct morphological features and higher sodium incorporation compared to mono- and dibasic forms, but these differences did not translate into major functional advantages. The dibasic form emerged as the most practical choice due to its chemical stability toward CC and HA, moderate alkalinity (reducing the need for intensive post-treatment rinsing), and compatibility with biomedical contexts. In carbonate–phosphate mixed electrolytes of equal conductivity, carbonate ions up to ~75% of total anion content did not inhibit PEO layer formation, though they caused a slight decrease in pore size and, at higher proportions, reduced phosphorus incorporation. These effects were more pronounced for  $\text{Na}_2\text{CO}_3$  than  $\text{NaHCO}_3$ , suggesting a role of pH and carbonate source in modifying discharge behavior. Complete substitution of phosphates with carbonates prevented microarc initiation, yielding non-porous anodic oxide surfaces and confirming the hypothesis that soluble carbonates alone cannot sustain the PEO process on titanium. Collectively, these findings confirmed that carbonates do not inherently preclude PEO in phosphate-containing baths but subtly influence microstructure and composition, underscoring the need for precise control over electrolyte composition and electrical parameters when targeting CC–HA co-incorporation.

In the second stage investigated particle crystallinity as an independent variable—a factor previously unexamined in PEO studies but hypothesized to influence incorporation efficiency and coating biofunctionality alongside particle size, shape, and composition. Using crystalline and amorphous calcium phosphate particles as model systems, it was demonstrated that crystallinity strongly affects both coating physicochemical properties and biological potential. In all cases, particle addition resulted in thicker oxide layers, enhanced wettability, and increased surface roughness compared to particle-free coatings, while maintaining macroscopic homogeneity. However, the crystallinity-dependent effects were clear: amorphous particles promoted higher calcium content in the outer coating layers, plausibly due to their higher surface area and roughness enhancing particle retention within the porous oxide structure during growth. They also influenced surface topography—affecting pore shape, size distribution, porosity, and pore density—and accelerated the formation of HA-like layers during *in vitro* bioactivity tests. Notably, these trends held true across both commercially pure titanium (Ti) and titanium alloy (TAV) substrates, despite differences in oxide phase composition, indicating that crystallinity effects are substrate-independent. The data supported the hypothesis that particle crystallinity is a critical parameter in PEO incorporation and suggested that amorphous TCP particles offer the most advantageous combination of wettability, micro-roughness, CaP content, and bioactivity for biomedical applications. These results introduced crystallinity control as a promising tool for fine-tuning PEO coatings for targeted performance.

The final stage of the research translated these insights into an optimized fabrication route for CC–HA composite coatings. A modified electrolyte was developed by synthesizing CC nanoparticles via a controlled carbonation process, then allowing them to react partially

with a dibasic phosphate solution ( $\text{Na}_2\text{HPO}_4$ ). This physicochemical interaction produced CC–HA microagglomerates (1–2  $\mu\text{m}$ ) in a stable suspension free from conductive impurities, eliminating the need for purification or redispersion—one of the practical limitations of conventional suspension-assisted PEO. The particle size and morphology of these agglomerates were found to correlate positively with coating thickness and spark-assisted incorporation efficiency. Using this optimized bath, PEO produced coatings with the typical microstructure of spark-anodized oxides, an average thickness of  $\sim 25 \mu\text{m}$ , and a dual-layer architecture (dense inner layer, porous outer layer) enriched in calcium and phosphorus. Raman spectroscopy confirmed the homogeneous distribution of CC, HA, anatase, and amorphous  $\text{TiO}_2$ , and indicated carbonate substitution within HA—a finding of particular relevance for tuning bioresorption behavior. XRD analysis additionally detected rutile, perovskite, and brushite phases, highlighting the multi-phase complexity achievable through this approach.

Functionally, CC–HA-enriched coatings demonstrated multiple improvements. Electrochemical testing showed their enhanced corrosion resistance, while mechanical adhesion tests confirmed stronger coating–substrate bonding. The coatings were hydrophilic, exhibited a moderately negative zeta potential, and released calcium ions in a sustained manner over at least one month in PBS. Biological evaluations revealed increased fibroblast viability after 7 days and bacteriostatic effects against relevant microbial strains, suggesting potential for reducing implant-associated infection risk. These outcomes align directly with the aim of producing bioactive, corrosion-resistant, and mechanically robust coatings with controlled phase composition, and they confirm the final hypothesis that CC–HA incorporation positively influences functional properties of PEO coatings.

Taken together, the results of all three stages validate the central premise of this work: that carbonate phases can be effectively introduced into PEO coatings via a particle-assisted route, and that controlling particle characteristics—particularly crystallinity—provides a means to tailor coating performance. To the best of current knowledge, the study demonstrates, for the first time, the successful direct incorporation of a carbonate phase as solid particles into a PEO coating on titanium and the first application of carbonation-based particle synthesis designed specifically for PEO electrolytes. From a practical perspective, the optimized CC–HA coating system satisfies several key requirements for *in vivo* use: biocompatibility, corrosion resistance, favorable surface chemistry for osteointegration, and a surface charge and topography conducive to cell attachment while not promoting bacterial adhesion. Beyond the biomedical scope, the approach developed here extends the versatility of the PEO technique for advanced surface engineering, opening possibilities for tailored carbonate-containing coatings in diverse applications.

Looking ahead, future research should focus on refining electrolyte composition for even more precise control over particle incorporation, testing coating performance under clinically relevant mechanical and biological conditions, further elucidating the role of carbonates in discharge formation and plasma–particle interactions, and exploring alternative particle chemistries for standalone or synergistic incorporation with CC. Such efforts will not only deepen the understanding of particle-assisted PEO but also broaden the applicability of this method for creating multifunctional, application-specific oxide coatings.

## 6. LITERATURE

- [1] M. Liu *et al.*, ‘Global, regional, and national burden of musculoskeletal disorders, 1990–2021: an analysis of the global burden of disease study 2021 and forecast to 2035’, *Front. Public Health*, vol. 13, p. 1562701, Aug. 2025, doi: 10.3389/fpubh.2025.1562701.
- [2] C. M. Naso, S.-Y. Lin, G. Song, and H. Xue, ‘Time trend analysis of osteoporosis prevalence among adults 50 years of age and older in the USA, 2005–2018’, *Osteoporos. Int.*, vol. 36, no. 3, pp. 547–554, Mar. 2025, doi: 10.1007/s00198-025-07395-3.
- [3] Y. A. Al-Ajlouni *et al.*, ‘The burden of musculoskeletal disorders in the Middle East and North Africa (MENA) region: a longitudinal analysis from the global burden of disease dataset 1990–2019’, *BMC Musculoskelet. Disord.*, vol. 24, no. 1, p. 439, May 2023, doi: 10.1186/s12891-023-06556-x.
- [4] V. P. Leifer, J. N. Katz, and E. Losina, ‘The burden of OA-health services and economics’, *Osteoarthritis Cartilage*, vol. 30, no. 1, pp. 10–16, Jan. 2022, doi: 10.1016/j.joca.2021.05.007.
- [5] R. De Pace, S. Molinari, E. Mazzoni, and G. Perale, ‘Bone Regeneration: A Review of Current Treatment Strategies’, *J. Clin. Med.*, vol. 14, no. 6, p. 1838, Mar. 2025, doi: 10.3390/jcm14061838.
- [6] C. I. Codrea *et al.*, ‘Advances in Osteoporotic Bone Tissue Engineering’, *J. Clin. Med.*, vol. 10, no. 2, p. 253, Jan. 2021, doi: 10.3390/jcm10020253.
- [7] N. Filip *et al.*, ‘Biomaterials in Orthopedic Devices: Current Issues and Future Perspectives’, *Coatings*, vol. 12, no. 10, p. 1544, Oct. 2022, doi: 10.3390/coatings12101544.
- [8] R. Zhao, R. Yang, P. R. Cooper, Z. Khurshid, A. Shavandi, and J. Ratnayake, ‘Bone Grafts and Substitutes in Dentistry: A Review of Current Trends and Developments’, *Molecules*, vol. 26, no. 10, p. 3007, May 2021, doi: 10.3390/molecules26103007.
- [9] D. C. Carrascal-Hernández, J. P. Martínez-Cano, J. D. Rodríguez Macías, and C. D. Grande-Tovar, ‘Evolution in Bone Tissue Regeneration: From Grafts to Innovative Biomaterials’, *Int. J. Mol. Sci.*, vol. 26, no. 9, p. 4242, Apr. 2025, doi: 10.3390/ijms26094242.
- [10] C. M. Abraham, ‘A Brief Historical Perspective on Dental Implants, Their Surface Coatings and Treatments’, *Open Dent. J.*, vol. 8, no. 1, pp. 50–55, May 2014, doi: 10.2174/1874210601408010050.
- [11] N. Walter, T. Stich, D. Docheva, V. Alt, and M. Rupp, ‘Evolution of implants and advancements for osseointegration: A narrative review’, *Injury*, vol. 53, pp. S69–S73, Nov. 2022, doi: 10.1016/j.injury.2022.05.057.
- [12] E. Marin and A. Lanzutti, ‘History of Metallic Orthopedic Materials’, *Metals*, vol. 15, no. 4, p. 378, Mar. 2025, doi: 10.3390/met15040378.
- [13] G. Wei *et al.*, ‘An overview of surface modification, A way toward fabrication of nascent biomedical Ti–6Al–4V alloys’, *J. Mater. Res. Technol.*, vol. 24, pp. 5896–5921, May 2023, doi: 10.1016/j.jmrt.2023.04.046.
- [14] K. Homa *et al.*, ‘Surface Functionalization of Titanium-Based Implants with a Nanohydroxyapatite Layer and Its Impact on Osteoblasts: A Systematic Review’, *J. Funct. Biomater.*, vol. 15, no. 2, p. 45, Feb. 2024, doi: 10.3390/jfb15020045.
- [15] H. Ghodrati *et al.*, ‘A narrative review of recent developments in osseointegration and anti-corrosion of titanium dental implants with nano surface’, *Bone Rep.*, vol. 25, p. 101846, June 2025, doi: 10.1016/j.bonr.2025.101846.
- [16] M. M. Farag, ‘Recent trends on biomaterials for tissue regeneration applications: review’, *J. Mater. Sci.*, vol. 58, no. 2, pp. 527–558, Jan. 2023, doi: 10.1007/s10853-022-08102-x.
- [17] S. M. Sadati Tilebon *et al.*, ‘Intelligent modeling and optimization of titanium surface etching for dental implant application’, *Sci. Rep.*, vol. 12, no. 1, p. 7184, May 2022, doi: 10.1038/s41598-022-11254-0.
- [18] M. S. Safavi, F. C. Walsh, M. A. Surmeneva, R. A. Surmenev, and J. Khalil-Allafi, ‘Electrodeposited Hydroxyapatite-Based Biocoatings: Recent Progress and Future Challenges’, *Coatings*, vol. 11, no. 1, p. 110, Jan. 2021, doi: 10.3390/coatings11010110.
- [19] V. Grebnevs, A. Viksna, and W. Simka, ‘Toward bioactive calcium carbonate and hydroxyapatite-based coatings via plasma electrolytic oxidation – A review of challenges and current state-of-

- the-art', *Surf. Coat. Technol.*, vol. 506, p. 132135, June 2025, doi: 10.1016/j.surfcoat.2025.132135.
- [20] M. A. E. Cruz *et al.*, 'Calcium carbonate hybrid coating promotes the formation of biomimetic hydroxyapatite on titanium surfaces', *Appl. Surf. Sci.*, vol. 370, pp. 459–468, May 2016, doi: 10.1016/j.apsusc.2015.12.250.
- [21] S. Umemoto, T. Furusawa, H. Unuma, T. Goto, and T. Sekino, 'Evaluation of resorption rate-controlled calcium carbonate ceramics as a substitute bone material', *Dent. Mater. J.*, vol. 44, no. 1, pp. 9–16, Jan. 2025, doi: 10.4012/dmj.2024-120.
- [22] K. H. Min, D. H. Kim, K. H. Kim, J.-H. Seo, and S. P. Pack, 'Biomimetic Scaffolds of Calcium-Based Materials for Bone Regeneration', *Biomimetics*, vol. 9, no. 9, p. 511, Aug. 2024, doi: 10.3390/biomimetics9090511.
- [23] H. Sharifi, M. Aliofkhazraei, G. B. Darband, and S. Shrestha, 'A REVIEW ON ADHESION STRENGTH OF PEO COATINGS BY SCRATCH TEST METHOD', *Surf. Rev. Lett.*, vol. 25, no. 03, p. 1830004, Apr. 2018, doi: 10.1142/S0218625X18300046.
- [24] C. Batchelor-McAuley, M. Yang, R. E. M. Rickaby, and R. G. Compton, 'Calcium Carbonate Dissolution from the Laboratory to the Ocean: Kinetics and Mechanism', *Chem. – Eur. J.*, vol. 28, no. 68, p. e202202290, Dec. 2022, doi: 10.1002/chem.202202290.
- [25] N. Spanos and P. G. Koutsoukos, 'Kinetics of Precipitation of Calcium Carbonate in Alkaline pH at Constant Supersaturation. Spontaneous and Seeded Growth', *J. Phys. Chem. B*, vol. 102, no. 34, pp. 6679–6684, Aug. 1998, doi: 10.1021/jp981171h.
- [26] F. Simchen, M. Sieber, A. Kopp, and T. Lampke, 'Introduction to Plasma Electrolytic Oxidation—An Overview of the Process and Applications', *Coatings*, vol. 10, no. 7, p. 628, June 2020, doi: 10.3390/coatings10070628.
- [27] V. S. Saji, 'Plasma electrolytic oxidation (PEO) layers grown on metals and alloys as supported photocatalysts', *Energy*, vol. 8, p. 100259, July 2025, doi: 10.1016/j.nxener.2025.100259.
- [28] M. Pavarini, M. Moscatelli, and R. Chiesa, 'Plasma Electrolytic Oxidation: A Versatile Tool to Modulate the Degradation of Biodegradable Metals in Medical Applications', *JOM*, vol. 77, no. 6, pp. 4456–4472, June 2025, doi: 10.1007/s11837-025-07312-3.
- [29] T. Wu *et al.*, 'Role of phosphate, silicate and aluminate in the electrolytes on PEO coating formation and properties of coated Ti6Al4V alloy', *Appl. Surf. Sci.*, vol. 595, p. 153523, Sept. 2022, doi: 10.1016/j.apsusc.2022.153523.
- [30] X. Lu *et al.*, 'Plasma electrolytic oxidation coatings with particle additions – A review', *Surf. Coat. Technol.*, vol. 307, pp. 1165–1182, Dec. 2016, doi: 10.1016/j.surfcoat.2016.08.055.
- [31] W. K. Yeung *et al.*, 'Characteristics and in vitro response of thin hydroxyapatite–titania films produced by plasma electrolytic oxidation of Ti alloys in electrolytes with particle additions', *RSC Adv.*, vol. 6, no. 15, pp. 12688–12698, 2016, doi: 10.1039/C5RA22178A.
- [32] A. Fattah-alhosseini, R. Chaharmahali, and K. Babaei, 'Effect of particles addition to solution of plasma electrolytic oxidation (PEO) on the properties of PEO coatings formed on magnesium and its alloys: A review', *J. Magnes. Alloys*, vol. 8, no. 3, pp. 799–818, Sept. 2020, doi: 10.1016/j.jma.2020.05.001.
- [33] M. Geetha, A. K. Singh, R. Asokamani, and A. K. Gogia, 'Ti based biomaterials, the ultimate choice for orthopaedic implants – A review', *Prog. Mater. Sci.*, vol. 54, no. 3, pp. 397–425, May 2009, doi: 10.1016/j.pmatsci.2008.06.004.
- [34] A. T. and J. C., 'Osteoinduction, osteoconduction and osseointegration', *Eur. Spine J.*, vol. 10, no. 0, pp. S96–S101, Oct. 2001, doi: 10.1007/s005860100282.
- [35] Q. Chen and G. A. Thouas, 'Metallic implant biomaterials', *Mater. Sci. Eng. R Rep.*, vol. 87, pp. 1–57, Jan. 2015, doi: 10.1016/j.mser.2014.10.001.
- [36] S. V. Dorozhkin, 'Bioceramics of calcium orthophosphates', *Biomaterials*, vol. 31, no. 7, pp. 1465–1485, Mar. 2010, doi: 10.1016/j.biomaterials.2009.11.050.
- [37] J. E. Davies, 'Understanding peri-implant endosseous healing', *J. Dent. Educ.*, vol. 67, no. 8, pp. 932–949, Aug. 2003.
- [38] J. V. Calazans Neto, C. A. S. Celles, C. S. A. F. De Andrade, C. R. M. Afonso, B. E. Nagay, and V. A. R. Barão, 'Recent Advances and Prospects in  $\beta$ -type Titanium Alloys for Dental Implants Applications', *ACS Biomater. Sci. Eng.*, vol. 10, no. 10, pp. 6029–6060, Oct. 2024, doi: 10.1021/acsbiomaterials.4c00963.

- [39] M. Özcan and C. Hämmerle, 'Titanium as a Reconstruction and Implant Material in Dentistry: Advantages and Pitfalls', *Materials*, vol. 5, no. 9, pp. 1528–1545, Aug. 2012, doi: 10.3390/ma5091528.
- [40] E. Marin and A. Lanzutti, 'Biomedical Applications of Titanium Alloys: A Comprehensive Review', *Materials*, vol. 17, no. 1, p. 114, Dec. 2023, doi: 10.3390/ma17010114.
- [41] R. Davis *et al.*, 'A comprehensive review on metallic implant biomaterials and their subtractive manufacturing', *Int. J. Adv. Manuf. Technol.*, vol. 120, no. 3–4, pp. 1473–1530, May 2022, doi: 10.1007/s00170-022-08770-8.
- [42] V. Tsakiris, C. Tardei, and F. M. Clicinschi, 'Biodegradable Mg alloys for orthopedic implants – A review', *J. Magnes. Alloys*, vol. 9, no. 6, pp. 1884–1905, Nov. 2021, doi: 10.1016/j.jma.2021.06.024.
- [43] S. Bencharit *et al.*, 'Development and Applications of Porous Tantalum Trabecular Metal-Enhanced Titanium Dental Implants', *Clin. Implant Dent. Relat. Res.*, vol. 16, no. 6, pp. 817–826, Dec. 2014, doi: 10.1111/cid.12059.
- [44] S. Najeib, M. S. Zafar, Z. Khurshid, and F. Siddiqui, 'Applications of polyetheretherketone (PEEK) in oral implantology and prosthodontics', *J. Prosthodont. Res.*, vol. 60, no. 1, pp. 12–19, Jan. 2016, doi: 10.1016/j.jpor.2015.10.001.
- [45] S. Bose, M. Roy, and A. Bandyopadhyay, 'Recent advances in bone tissue engineering scaffolds', *Trends Biotechnol.*, vol. 30, no. 10, pp. 546–554, Oct. 2012, doi: 10.1016/j.tibtech.2012.07.005.
- [46] T. K. Dash and V. B. Konkimalla, 'Poly-ε-caprolactone based formulations for drug delivery and tissue engineering: A review', *J. Controlled Release*, vol. 158, no. 1, pp. 15–33, Feb. 2012, doi: 10.1016/j.jconrel.2011.09.064.
- [47] H. L. Ornaghi, F. M. Monticeli, and L. D. Agnol, 'A Review on Polymers for Biomedical Applications on Hard and Soft Tissues and Prosthetic Limbs', *Polymers*, vol. 15, no. 19, p. 4034, Oct. 2023, doi: 10.3390/polym15194034.
- [48] A. M. Inchingolo *et al.*, 'Surface Coatings of Dental Implants: A Review', *J. Funct. Biomater.*, vol. 14, no. 5, p. 287, May 2023, doi: 10.3390/jfb14050287.
- [49] A. A. Daniyan, T. L. Akpomejoro, O. O. Ige, and P. A. Olubambi, 'Corrosion Prevention of Biomedical Implants: Surface Coating Techniques Perspective', *ChemistrySelect*, vol. 8, no. 40, p. e202300223, Oct. 2023, doi: 10.1002/slct.202300223.
- [50] G. Zhang, J. Liu, Y. Zhu, T. Shen, and D. Yang, 'Enhanced antibacterial efficacies, corrosion resistance, and cytocompatibility of ZnO/CuO composite coatings through designed sputtering orders', *Appl. Surf. Sci.*, vol. 635, p. 157724, Oct. 2023, doi: 10.1016/j.apsusc.2023.157724.
- [51] V. Vishwakarma, G. Kaliaraj, and K. Amirtharaj Mosas, 'Multifunctional Coatings on Implant Materials—A Systematic Review of the Current Scenario', *Coatings*, vol. 13, no. 1, p. 69, Dec. 2022, doi: 10.3390/coatings13010069.
- [52] Y. Fu, M. Zhu, A. Shi, B. Zhang, and P. Xu, 'Stimulus-responsive antibacterial strategies for construction of anti-infection bone implants', *Mater.*, vol. 8, p. 100554, July 2025, doi: 10.1016/j.nxmate.2025.100554.
- [53] N. Maher, A. Mahmood, M. A. Fareed, N. Kumar, D. Rokaya, and M. S. Zafar, 'An updated review and recent advancements in carbon-based bioactive coatings for dental implant applications', *J. Adv. Res.*, vol. 72, pp. 265–286, June 2025, doi: 10.1016/j.jare.2024.07.016.
- [54] A. W. Zia, I. Anestopoulos, M. I. Panayiotidis, and M. Birkett, 'Soft diamond-like carbon coatings with superior biocompatibility for medical applications', *Ceram. Int.*, vol. 49, no. 11, pp. 17203–17211, June 2023, doi: 10.1016/j.ceramint.2023.02.085.
- [55] J. Adhikari, P. Saha, and A. Sinha, 'Surface modification of metallic bone implants—Polymer and polymer-assisted coating for bone in-growth', in *Fundamental Biomaterials: Metals*, Elsevier, 2018, pp. 299–321. doi: 10.1016/B978-0-08-102205-4.00014-3.
- [56] M. Saleem, Z. Khurshid, and M. S. Zafar, 'Proteins and peptides coatings on the dental implant surface', in *Dental Implants*, Elsevier, 2020, pp. 117–132. doi: 10.1016/B978-0-12-819586-4.00007-X.
- [57] M. Mozafari, S. Banijamali, F. Baino, S. Kargozar, and R. G. Hill, 'Calcium carbonate: Adored and ignored in bioactivity assessment', *Acta Biomater.*, vol. 91, pp. 35–47, June 2019, doi: 10.1016/j.actbio.2019.04.039.
- [58] Y.-L. Yang, X.-W. Guo, Y.-F. Meng, W.-Z. Zhang, L.-B. Mao, and S.-H. Yu, 'Biomimetic calcium carbonate-calcium phosphate composite films with tunable cytological behaviors', *Nano Res.*, vol. 18, no. 1, p. 94907055, Jan. 2025, doi: 10.26599/NR.2025.94907055.

- [59] Y.-Q. Niu *et al.*, 'Calcium carbonate: controlled synthesis, surface functionalization, and nanostructured materials', *Chem. Soc. Rev.*, vol. 51, no. 18, pp. 7883–7943, 2022, doi: 10.1039/D1CS00519G.
- [60] B. Le Thi *et al.*, 'Biological responses of MC3T3-E1 on calcium carbonate coatings fabricated by hydrothermal reaction on titanium', *Biomed. Mater.*, vol. 15, no. 3, p. 035004, Mar. 2020, doi: 10.1088/1748-605X/ab6939.
- [61] N. A. J. M. Sommerdijk, E. N. M. V. Leeuwen, M. R. J. Vos, and J. A. Jansen, 'Calcium carbonate thin films as biomaterial coatings using DNA as crystallization inhibitor', *CrystEngComm*, vol. 9, no. 12, p. 1209, 2007, doi: 10.1039/b710277a.
- [62] C. Tan *et al.*, 'Advanced CaCO<sub>3</sub>-derived delivery systems for bioactive compounds', *Adv. Colloid Interface Sci.*, vol. 309, p. 102791, Nov. 2022, doi: 10.1016/j.cis.2022.102791.
- [63] F. He, J. Zhang, F. Yang, J. Zhu, X. Tian, and X. Chen, 'In vitro degradation and cell response of calcium carbonate composite ceramic in comparison with other synthetic bone substitute materials', *Mater. Sci. Eng. C*, vol. 50, pp. 257–265, May 2015, doi: 10.1016/j.msec.2015.02.019.
- [64] Y. Liu, Y. Zhou, T. Jiang, Y.-D. Liang, Z. Zhang, and Y.-N. Wang, 'Evaluation of the osseointegration of dental implants coated with calcium carbonate: an animal study', *Int. J. Oral Sci.*, vol. 9, no. 3, pp. 133–138, Sept. 2017, doi: 10.1038/ijos.2017.13.
- [65] A.-L. Vasiliu, M.-M. Zaharia, M.-M. Bazarghideanu, I. Rosca, D. Peptanariu, and M. Mihai, 'Hydrophobic Composites Designed by a Nonwoven Cellulose-Based Material and Polymer/CaCO<sub>3</sub> Patterns with Biomedical Applications', *Biomacromolecules*, vol. 23, no. 1, pp. 89–99, Jan. 2022, doi: 10.1021/acs.biomac.1c01036.
- [66] R. Donate, R. Paz, Á. Quintana, P. Bordón, and M. Monzón, 'Calcium Carbonate Coating of 3D-Printed PLA Scaffolds Intended for Biomedical Applications', *Polymers*, vol. 15, no. 11, p. 2506, May 2023, doi: 10.3390/polym15112506.
- [67] A. S. I. Ahmed *et al.*, 'Calcium released by osteoclastic resorption stimulates autocrine/paracrine activities in local osteogenic cells to promote coupled bone formation', *Am. J. Physiol.-Cell Physiol.*, vol. 322, no. 5, pp. C977–C990, May 2022, doi: 10.1152/ajpcell.00413.2021.
- [68] K. Ishikawa and K. Hayashi, 'Carbonate apatite artificial bone', *Sci. Technol. Adv. Mater.*, vol. 22, no. 1, pp. 683–694, Dec. 2021, doi: 10.1080/14686996.2021.1947120.
- [69] C. A. Schmidt *et al.*, 'Myriad Mapping of nanoscale minerals reveals calcium carbonate hemihydrate in forming nacre and coral biominerals', *Nat. Commun.*, vol. 15, no. 1, p. 1812, Feb. 2024, doi: 10.1038/s41467-024-46117-x.
- [70] A. Ressler, A. Žužić, I. Ivanišević, N. Kamboj, and H. Ivanković, 'Ionic substituted hydroxyapatite for bone regeneration applications: A review', *Open Ceram.*, vol. 6, p. 100122, June 2021, doi: 10.1016/j.oceram.2021.100122.
- [71] Y. Wang *et al.*, 'Corrosion resistance of a calcium carbonate coating prepared by ultrasound-assisted chemical conversion in calcium disodium edetate solution', *J. Magnes. Alloys*, p. S2213956722003097, May 2023, doi: 10.1016/j.jma.2022.11.022.
- [72] O. Gibert, C. Valderrama, M. M. Martínez, R. M. Darbra, J. O. Moncunill, and V. Martí, 'Hydroxyapatite Coatings on Calcite Powder for the Removal of Heavy Metals from Contaminated Water', *Water*, vol. 13, no. 11, p. 1493, May 2021, doi: 10.3390/w13111493.
- [73] J. L. Paris, N. Lafuente-Gomez, M. V. Cabanas, J. Roman, J. Pena, and M. Vallet-Regi, 'Fabrication of a nanoparticle-containing 3D porous bone scaffold with proangiogenic and antibacterial properties', 2021, doi: 10.48550/ARXIV.2103.09559.
- [74] C. Montoya, Y. Du, A. L. Gianforcaro, S. Orrego, M. Yang, and P. I. Lelkes, 'On the road to smart biomaterials for bone research: definitions, concepts, advances, and outlook', *Bone Res.*, vol. 9, no. 1, p. 12, Feb. 2021, doi: 10.1038/s41413-020-00131-z.
- [75] H. Bahrom *et al.*, 'Controllable synthesis of calcium carbonate with different geometry: comprehensive analysis of particles formation, their cellular uptake and biocompatibility', 2021, *arXiv*. doi: 10.48550/ARXIV.2106.15974.
- [76] F. A. Shah, 'Revisiting the physical and chemical nature of the mineral component of bone', *Acta Biomater.*, vol. 196, pp. 1–16, Apr. 2025, doi: 10.1016/j.actbio.2025.01.055.
- [77] S. Umemoto, T. Furusawa, H. Unuma, M. Tajika, and T. Sekino, 'In vivo bioresorbability and bone formation ability of sintered highly pure calcium carbonate granules', *Dent. Mater. J.*, vol. 40, no. 5, pp. 1202–1207, Sept. 2021, doi: 10.4012/dmj.2020-254.

- [78] M. A. Abdulghafor, M. K. Mahmood, H. Tassery, D. Tardivo, A. Falguiere, and R. Lan, 'Biomimetic Coatings in Implant Dentistry: A Quick Update', *J. Funct. Biomater.*, vol. 15, no. 1, p. 15, Dec. 2023, doi: 10.3390/jfb15010015.
- [79] W. Tang, N. G. Fischer, X. Kong, T. Sang, and Z. Ye, 'Hybrid coatings on dental and orthopedic titanium implants: Current advances and challenges', *BMEMat*, vol. 2, no. 4, p. e12105, Dec. 2024, doi: 10.1002/bmm2.12105.
- [80] K. Kuroda and M. Okido, 'Hydroxyapatite Coating of Titanium Implants Using Hydroprocessing and Evaluation of Their Osteoconductivity', *Bioinorg. Chem. Appl.*, vol. 2012, pp. 1–7, 2012, doi: 10.1155/2012/730693.
- [81] K. A. Kravanja and M. Finšgar, 'A review of techniques for the application of bioactive coatings on metal-based implants to achieve controlled release of active ingredients', *Mater. Des.*, vol. 217, p. 110653, May 2022, doi: 10.1016/j.matdes.2022.110653.
- [82] K. Safin Kaosar Saad, T. Saba, and A. Bin Rashid, 'Application of PVD coatings in medical implantology for enhanced performance, biocompatibility, and quality of life', *Heliyon*, vol. 10, no. 16, p. e35541, Aug. 2024, doi: 10.1016/j.heliyon.2024.e35541.
- [83] T. Saba, K. S. K. Saad, and A. B. Rashid, 'Precise surface engineering: Leveraging chemical vapor deposition for enhanced biocompatibility and durability in biomedical implants', *Heliyon*, vol. 10, no. 18, p. e37976, Sept. 2024, doi: 10.1016/j.heliyon.2024.e37976.
- [84] J. P. Fernández-Hernán, B. Torres, A. J. López, and J. Rams, 'The Role of the Sol-Gel Synthesis Process in the Biomedical Field and Its Use to Enhance the Performance of Bioabsorbable Magnesium Implants', *Gels*, vol. 8, no. 7, p. 426, July 2022, doi: 10.3390/gels8070426.
- [85] Z. Hadzhieva and A. R. Boccaccini, 'Recent developments in electrophoretic deposition (EPD) of antibacterial coatings for biomedical applications - A review', *Curr. Opin. Biomed. Eng.*, vol. 21, p. 100367, Mar. 2022, doi: 10.1016/j.cobme.2021.100367.
- [86] A. Ritwik, K. K. Saju, A. Vengellur, and P. P. Saipriya, 'Development of thin-film hydroxyapatite coatings with an intermediate shellac layer produced by dip-coating process on Ti6Al4V implant materials', *J. Coat. Technol. Res.*, vol. 19, no. 2, pp. 597–605, Mar. 2022, doi: 10.1007/s11998-021-00549-y.
- [87] S. Bajda *et al.*, 'Laser cladding of bioactive glass coating on pure titanium substrate with highly refined grain structure', *J. Mech. Behav. Biomed. Mater.*, vol. 119, p. 104519, July 2021, doi: 10.1016/j.jmbbm.2021.104519.
- [88] K. S. P. Karunadasa, C. H. Manoratne, H. M. T. G. A. Pitawala, and R. M. G. Rajapakse, 'Thermal decomposition of calcium carbonate (calcite polymorph) as examined by in-situ high-temperature X-ray powder diffraction', *J. Phys. Chem. Solids*, vol. 134, pp. 21–28, Nov. 2019, doi: 10.1016/j.jpcs.2019.05.023.
- [89] J. V. Rau *et al.*, 'Physicochemical Investigation of Pulsed Laser Deposited Carbonated Hydroxyapatite Films on Titanium', *ACS Appl. Mater. Interfaces*, vol. 1, no. 8, pp. 1813–1820, Aug. 2009, doi: 10.1021/am900356e.
- [90] M. Aliofkhazraei *et al.*, 'Review of plasma electrolytic oxidation of titanium substrates: Mechanism, properties, applications and limitations', *Appl. Surf. Sci. Adv.*, vol. 5, p. 100121, Sept. 2021, doi: 10.1016/j.apsadv.2021.100121.
- [91] M. Kaseem, S. Fatimah, N. Nashrah, and Y. G. Ko, 'Recent progress in surface modification of metals coated by plasma electrolytic oxidation: Principle, structure, and performance', *Prog. Mater. Sci.*, vol. 117, p. 100735, Apr. 2021, doi: 10.1016/j.pmatsci.2020.100735.
- [92] L. O. Snizhko *et al.*, 'Anodic processes in plasma electrolytic oxidation of aluminium in alkaline solutions', *Electrochimica Acta*, vol. 49, no. 13, pp. 2085–2095, May 2004, doi: 10.1016/j.electacta.2003.11.027.
- [93] S. Sikdar, P. V. Menezes, R. Maccione, T. Jacob, and P. L. Menezes, 'Plasma Electrolytic Oxidation (PEO) Process—Processing, Properties, and Applications', *Nanomaterials*, vol. 11, no. 6, p. 1375, May 2021, doi: 10.3390/nano11061375.
- [94] D. Dogadkin, A. Sagidugumar, D. Kaliyev, N. Dmitriev, and Y. Kozhakhmetov, 'The Role of Signal Waveforms in Plasma Electrolytic Oxidation', *Coatings*, vol. 15, no. 1, p. 36, Jan. 2025, doi: 10.3390/coatings15010036.
- [95] X. Yang, L. Chen, Y. Qu, R. Liu, K. Wei, and W. Xue, 'Optical emission spectroscopy of plasma electrolytic oxidation process on 7075 aluminum alloy', *Surf. Coat. Technol.*, vol. 324, pp. 18–25, Sept. 2017, doi: 10.1016/j.surfcoat.2017.05.005.

- [96] M. Molaei, M. Atapour, and E. Mohammadi Zahrani, 'Plasma Electrolytic Oxidation (PEO) Coatings for Biomedical Implants: A Review on Enhancing Antibacterial Efficacy Through Controlled Antibiotic Release', *Coatings*, vol. 15, no. 8, p. 925, Aug. 2025, doi: 10.3390/coatings15080925.
- [97] R. R. Lucas, R. C. M. Sales-Contini, F. J. G. Da Silva, E. C. Botelho, and R. P. Mota, 'Plasma electrolytic oxidation (PEO): An alternative to conventional anodization process', *AIMS Mater. Sci.*, vol. 11, no. 4, pp. 684–711, 2024, doi: 10.3934/matensci.2024035.
- [98] V. Dehnavi, X. Y. Liu, B. L. Luan, D. W. Shoesmith, and S. Rohani, 'Phase transformation in plasma electrolytic oxidation coatings on 6061 aluminum alloy', *Surf. Coat. Technol.*, vol. 251, pp. 106–114, July 2014, doi: 10.1016/j.surfcoat.2014.04.010.
- [99] C. A. Vargas *et al.*, 'Morphological analysis of plasma electrolytic oxidation coatings formed on Ti6Al4V alloys manufactured by electron beam powder bed fusion', *Heliyon*, vol. 9, no. 9, p. e19289, Sept. 2023, doi: 10.1016/j.heliyon.2023.e19289.
- [100] L. Zhu, W. Zhang, H. Liu, L. Liu, F. Wang, and Z. Qiao, 'Single Dense Layer of PEO Coating on Aluminum Fabricated by "Chain-like" Discharges', *Materials*, vol. 15, no. 13, p. 4635, July 2022, doi: 10.3390/ma15134635.
- [101] L. Qiu, C. Zhang, X. Yang, F. Peng, Y. Huang, and Y. He, 'A SiO<sub>2</sub> layer on PEO-treated Mg for enhanced corrosion resistance and bone regeneration', *Front. Bioeng. Biotechnol.*, vol. 10, p. 1053944, Dec. 2022, doi: 10.3389/fbioe.2022.1053944.
- [102] G. C. Cardoso, C. R. Grandini, and J. V. Rau, 'Comprehensive review of PEO coatings on titanium alloys for biomedical implants', *J. Mater. Res. Technol.*, vol. 31, pp. 311–328, July 2024, doi: 10.1016/j.jmrt.2024.06.068.
- [103] A. Kopp *et al.*, 'Long-term in vivo observations show biocompatibility and performance of ZX00 magnesium screws surface-modified by plasma-electrolytic oxidation in Göttingen miniature pigs', *Acta Biomater.*, vol. 157, pp. 720–733, Feb. 2023, doi: 10.1016/j.actbio.2022.11.052.
- [104] X. Wen, Y. Liu, F. Xi, X. Zhang, and Y. Kang, 'Micro-arc oxidation (MAO) and its potential for improving the performance of titanium implants in biomedical applications', *Front. Bioeng. Biotechnol.*, vol. 11, p. 1282590, Nov. 2023, doi: 10.3389/fbioe.2023.1282590.
- [105] M. Thukkaram *et al.*, 'Antibacterial activity of a porous silver doped TiO<sub>2</sub> coating on titanium substrates synthesized by plasma electrolytic oxidation', *Appl. Surf. Sci.*, vol. 500, p. 144235, Jan. 2020, doi: 10.1016/j.apsusc.2019.144235.
- [106] P. Fernández-López *et al.*, 'Data-Driven Optimization of Plasma Electrolytic Oxidation (PEO) Coatings with Explainable Artificial Intelligence Insights', *Coatings*, vol. 14, no. 8, p. 979, Aug. 2024, doi: 10.3390/coatings14080979.
- [107] K. Yang, J. Zeng, H. Huang, J. Chen, and B. Cao, 'A Novel Self-Adaptive Control Method for Plasma Electrolytic Oxidation Processing of Aluminum Alloys', *Materials*, vol. 12, no. 17, p. 2744, Aug. 2019, doi: 10.3390/ma12172744.
- [108] L. Liu, S. Dong, X.-Bo Chen, F. Wang, F. Wang, and J. Dong, 'Improving energy efficiency and corrosion resistance of PEO coating on Zr alloys through a two-frequency stepped strategy', *Corros. Commun.*, p. S2667266925000635, Aug. 2025, doi: 10.1016/j.corcom.2024.12.003.
- [109] X.-Y. Liu *et al.*, 'Electrode materials matching PEO electrolyte in lithium batteries: Progress and perspectives', *J. Power Sources*, vol. 623, p. 235422, Dec. 2024, doi: 10.1016/j.jpowsour.2024.235422.
- [110] V. Grebņevs *et al.*, 'Modification of physicochemical properties and bioactivity of oxide coatings formed on Ti substrates via plasma electrolytic oxidation in crystalline and amorphous calcium phosphate particle suspensions', *Appl. Surf. Sci.*, vol. 598, p. 153793, Oct. 2022, doi: 10.1016/j.apsusc.2022.153793.
- [111] X. Lu, C. Blawert, N. Scharnagl, and K. U. Kainer, 'Influence of incorporating Si<sub>3</sub>N<sub>4</sub> particles into the oxide layer produced by plasma electrolytic oxidation on AM50 Mg alloy on coating morphology and corrosion properties', *J. Magnes. Alloys*, vol. 1, no. 4, pp. 267–274, Dec. 2013, doi: 10.1016/j.jma.2013.11.001.
- [112] Y. Cheng, X. Shi, Y. Lv, and X. Zhang, 'Effect of Electrolyte Temperature on Plasma Electrolytic Oxidation of Pure Aluminum', *Metals*, vol. 14, no. 6, p. 615, May 2024, doi: 10.3390/met14060615.
- [113] M. Kaseem and B. Dikici, 'Optimization of Surface Properties of Plasma Electrolytic Oxidation Coating by Organic Additives: A Review', *Coatings*, vol. 11, no. 4, p. 374, Mar. 2021, doi: 10.3390/coatings11040374.



- [114] G. Zhang *et al.*, 'Dual-structured oxide coatings with enhanced wear and corrosion resistance prepared by plasma electrolytic oxidation on Ti-Nb-Ta-Zr-Hf high-entropy alloy', *Surf. Coat. Technol.*, vol. 456, p. 129254, Mar. 2023, doi: 10.1016/j.surfcoat.2023.129254.
- [115] S. Lashkarara, A. Fazlali, K. Ghaseminezhad, C. Fleck, and M. Salavati, 'Mechanism of plasma electrolytic oxidation in Mg<sub>3</sub>ZnCa implants: a study of double-layer formation and properties through nanoindentation', *Sci. Rep.*, vol. 14, no. 1, p. 7380, Mar. 2024, doi: 10.1038/s41598-024-58008-8.
- [116] Y. Ye, L. Wang, X. Hu, and Z. Bu, 'Studies on the Coating Formation and Structure Property for Plasma Electrolytic Oxidation of AZ31 Magnesium Alloy', *Coatings*, vol. 15, no. 7, p. 846, July 2025, doi: 10.3390/coatings15070846.
- [117] P. Fernández-López, S. A. Alves, J. T. San-Jose, E. Gutierrez-Berasategui, and R. Bayón, 'Plasma Electrolytic Oxidation (PEO) as a Promising Technology for the Development of High-Performance Coatings on Cast Al-Si Alloys: A Review', *Coatings*, vol. 14, no. 2, p. 217, Feb. 2024, doi: 10.3390/coatings14020217.
- [118] P. Karlova *et al.*, 'Comparison of 2D and 3D Plasma Electrolytic Oxidation (PEO)-Based Coating Porosity Data Obtained by X-ray Tomography Rendering and a Classical Metallographic Approach', *Materials*, vol. 15, no. 18, p. 6315, Sept. 2022, doi: 10.3390/ma15186315.
- [119] A. Nominé *et al.*, 'The Evidence of Cathodic Micro-discharges during Plasma Electrolytic Oxidation Process', 2019, doi: 10.48550/ARXIV.1902.09828.
- [120] F. Ceriani, L. Casanova, L. Massimini, A. Brenna, and M. Ormellese, 'TiO<sub>2</sub> Microparticles Incorporation in Coatings Produced by Plasma Electrolytic Oxidation (PEO) on Titanium', *Coatings*, vol. 13, no. 10, p. 1718, Sept. 2023, doi: 10.3390/coatings13101718.
- [121] D. Zhai, T. Qiu, J. Shen, and K. Feng, 'Growth kinetics and mechanism of microarc oxidation coating on Ti-6Al-4V alloy in phosphate/silicate electrolyte', *Int. J. Miner. Metall. Mater.*, vol. 29, no. 11, pp. 1991–1999, Nov. 2022, doi: 10.1007/s12613-022-2413-8.
- [122] H. Zhang, J. Zhu, J. Xia, S. Sun, and J. Han, 'Wear and Optical Properties of MoSi<sub>2</sub> Nanoparticles Incorporated into Black PEO Coating on TC4 Alloy', *Coatings*, vol. 15, no. 1, p. 21, Dec. 2024, doi: 10.3390/coatings15010021.
- [123] S. Grigoriev *et al.*, 'Investigation of Tribological Characteristics of PEO Coatings Formed on Ti6Al4V Titanium Alloy in Electrolytes with Graphene Oxide Additives', *Materials*, vol. 16, no. 11, p. 3928, May 2023, doi: 10.3390/ma16113928.
- [124] A. Lugovskoy and M. Zinigr, 'Plasma Electrolytic Oxidation of Valve Metals', in *Materials Science - Advanced Topics*, Y. Mastai, Ed., InTech, 2013. doi: 10.5772/54827.
- [125] X. Nie, R. Cai, C. Zhao, J. Sun, J. Zhang, and D. T. A. Matthews, 'Advancement of plasma electrolytic oxidation towards non-valve metals', *Surf. Coat. Technol.*, vol. 442, p. 128403, July 2022, doi: 10.1016/j.surfcoat.2022.128403.
- [126] A. I. Kozelskaya *et al.*, 'Surface Modification of Additively Fabricated Titanium-Based Implants by Means of Bioactive Micro-Arc Oxidation Coatings for Bone Replacement', *J. Funct. Biomater.*, vol. 13, no. 4, p. 285, Dec. 2022, doi: 10.3390/jfb13040285.
- [127] F. Xi, Y. Huang, Y. Zhao, Y. Liu, W. Dai, and Y. Tian, 'Effects of Substrate Roughness on Microstructure and Fatigue Behavior of Plasma Electrolytic Oxidation-Coated Ti-6Al-4V Alloy', *Materials*, vol. 15, no. 12, p. 4256, June 2022, doi: 10.3390/ma15124256.
- [128] G. Wu *et al.*, 'Effect of laser texturing on the antiwear properties of micro-arc oxidation coating formed on Ti-6Al-4V', *Surf. Coat. Technol.*, vol. 453, p. 129114, Jan. 2023, doi: 10.1016/j.surfcoat.2022.129114.
- [129] F. Hou, R. Gorthy, I. Mardon, D. Tang, and C. Goode, 'Low voltage environmentally friendly plasma electrolytic oxidation process for titanium alloys', *Sci. Rep.*, vol. 12, no. 1, p. 6037, Apr. 2022, doi: 10.1038/s41598-022-09693-w.
- [130] B. Jaleh, A. Nasri, R. Chaharmahali, M. Kaseem, and A. Fattah-alhosseini, 'Exploring wear, corrosion, and microstructure in PEO coatings via laser surface treatments on aluminum substrates', *Opt. Laser Technol.*, vol. 181, p. 111958, Feb. 2025, doi: 10.1016/j.optlastec.2024.111958.
- [131] Q. Zhao *et al.*, 'Osteogenic activity of a titanium surface modified with silicon-doped titanium dioxide', *Mater. Sci. Eng. C*, vol. 110, p. 110682, May 2020, doi: 10.1016/j.msec.2020.110682.
- [132] X. Zhang, W. Zhou, and W. Xi, 'Advancements in incorporating metal ions onto the surface of biomedical titanium and its alloys via micro-arc oxidation: a research review', *Front. Chem.*, vol. 12, p. 1353950, Feb. 2024, doi: 10.3389/fchem.2024.1353950.

- [133] X. Lu, C. Blawert, Y. Huang, H. Ovri, M. L. Zheludkevich, and K. U. Kainer, 'Plasma electrolytic oxidation coatings on Mg alloy with addition of SiO<sub>2</sub> particles', *Electrochimica Acta*, vol. 187, pp. 20–33, Jan. 2016, doi: 10.1016/j.electacta.2015.11.033.
- [134] H. Zhang, J. Zhu, B. Wang, J. Xia, K. Fu, and J. Han, 'The Incorporation of Nano-MoSi<sub>2</sub> Particles into a Black PEO Coating on Ti Alloy and Its Corrosion Performance', *Coatings*, vol. 15, no. 2, p. 145, Jan. 2025, doi: 10.3390/coatings15020145.
- [135] B. Shi *et al.*, 'Advances in amelioration of plasma electrolytic oxidation coatings on biodegradable magnesium and alloys', *Heliyon*, vol. 10, no. 4, p. e24348, Feb. 2024, doi: 10.1016/j.heliyon.2024.e24348.
- [136] A. Sobolev, M. Zinigrad, and K. Borodianskiy, 'Ceramic coating on Ti-6Al-4V by plasma electrolytic oxidation in molten salt: Development and characterization', *Surf. Coat. Technol.*, vol. 408, p. 126847, Feb. 2021, doi: 10.1016/j.surfcoat.2021.126847.
- [137] L. Yu *et al.*, 'Effect of CO<sub>2</sub> on the microstructure and corrosion mechanism of Mg-Nd-Zn-Ca plasma electrolytic oxidation coatings', *Mater. Today Commun.*, vol. 34, p. 105081, Mar. 2023, doi: 10.1016/j.mtcomm.2022.105081.
- [138] J. R. F. Neto *et al.*, 'Effect of Bulk Phase Composition on the Growth of PEO Coatings on the Biomedical Ti-6Al-4V Alloy', *Materials*, vol. 18, no. 5, p. 955, Feb. 2025, doi: 10.3390/ma18050955.
- [139] X. Ming, Y. Wu, Z. Zhang, and Y. Li, 'Micro-Arc Oxidation in Titanium and Its Alloys: Development and Potential of Implants', *Coatings*, vol. 13, no. 12, p. 2064, Dec. 2023, doi: 10.3390/coatings13122064.
- [140] F. Ceriani, L. Casanova, and M. Ormellese, 'Use of Organic Acids as Additives for Plasma Electrolytic Oxidation (PEO) of Titanium', *Coatings*, vol. 14, no. 6, p. 703, June 2024, doi: 10.3390/coatings14060703.
- [141] L. Wang, W. Fu, G. Yi, Z. Chen, Z. Gao, and Q. Pan, 'Discharge Characteristics, Plasma Electrolytic Oxidation Mechanism and Properties of ZrO<sub>2</sub> Membranes in K<sub>2</sub>ZrF<sub>6</sub> Electrolyte', *Membranes*, vol. 12, no. 5, p. 516, May 2022, doi: 10.3390/membranes12050516.
- [142] X. Liu, L. Liu, S. Dong, X.-B. Chen, and J. Dong, 'Towards dense corrosion-resistant plasma electrolytic oxidation coating on Mg-Gd-Y-Zr alloy by using ultra-high frequency pulse current', *Surf. Coat. Technol.*, vol. 447, p. 128881, Oct. 2022, doi: 10.1016/j.surfcoat.2022.128881.
- [143] G. Yeshmanova *et al.*, 'Effect of electrolyte composition on the formation of PEO coatings on AA2024 aluminium alloy', *Surf. Interfaces*, vol. 44, p. 103797, Jan. 2024, doi: 10.1016/j.surf.2023.103797.
- [144] X. Xu *et al.*, 'Characterization of the ceramic coating formed on 2024 al alloy by scanning plasma electrolytic oxidation', *Sci. Rep.*, vol. 15, no. 1, p. 8044, Mar. 2025, doi: 10.1038/s41598-025-93028-y.
- [145] S. G. Moga *et al.*, 'The Influence of Processing Time on Morphology, Structure and Functional Properties of PEO Coatings on AZ63 Magnesium Alloy', *Appl. Sci.*, vol. 12, no. 24, p. 12848, Dec. 2022, doi: 10.3390/app122412848.
- [146] T. A. Aljohani, S. Aljadaan, M. T. Bin Rubayan, and F. Khoshnaw, 'Impact of processing parameters in plasma electrolytic oxidation on corrosion resistance of magnesium alloy type AZ91', *Eng. Rep.*, vol. 4, no. 2, p. e12459, Feb. 2022, doi: 10.1002/eng2.12459.
- [147] A. Fattah-alhosseini, M. Molaei, and K. Babaei, 'The effects of nano- and micro-particles on properties of plasma electrolytic oxidation (PEO) coatings applied on titanium substrates: A review', *Surf. Interfaces*, vol. 21, p. 100659, Dec. 2020, doi: 10.1016/j.surf.2020.100659.
- [148] G. Li *et al.*, 'Review of micro-arc oxidation of titanium alloys: Mechanism, properties and applications', *J. Alloys Compd.*, vol. 948, p. 169773, July 2023, doi: 10.1016/j.jallcom.2023.169773.
- [149] F. C. Walsh *et al.*, 'Plasma electrolytic oxidation (PEO) for production of anodised coatings on lightweight metal (Al, Mg, Ti) alloys', *Trans. IMF*, vol. 87, no. 3, pp. 122–135, May 2009, doi: 10.1179/174591908X372482.
- [150] K. Babaei, A. Fattah-alhosseini, and M. Molaei, 'The effects of carbon-based additives on corrosion and wear properties of Plasma electrolytic oxidation (PEO) coatings applied on Aluminum and its alloys: A review', *Surf. Interfaces*, vol. 21, p. 100677, Dec. 2020, doi: 10.1016/j.surf.2020.100677.

- [151] S. Jin *et al.*, 'Effect of carbonate additive on the microstructure and corrosion resistance of plasma electrolytic oxidation coating on Mg-9Li-3Al alloy', *Int. J. Miner. Metall. Mater.*, vol. 29, no. 7, pp. 1453–1463, July 2022, doi: 10.1007/s12613-021-2377-0.
- [152] R. F. Zhang, Y. Q. Zhang, S. F. Zhang, B. Qu, S. B. Guo, and J. H. Xiang, 'Formation process of micro arc oxidation coatings obtained in a sodium phytate containing solution with and without CaCO<sub>3</sub> on binary Mg-1.0Ca alloy', *Appl. Surf. Sci.*, vol. 325, pp. 79–85, Jan. 2015, doi: 10.1016/j.apsusc.2014.10.127.
- [153] Z. Liu, H. Lu, X. Dai, B. Cheng, and A. Zhou, 'Study on micro-arc oxidation coating of copper pretreated at high temperature', *J. Alloys Compd.*, vol. 1003, p. 175627, Oct. 2024, doi: 10.1016/j.jallcom.2024.175627.
- [154] A. Anawati, H. Labibah, and S. Purwanto, 'Characteristics of non-crystalline thin oxide films formed on aluminum by plasma electrolytic oxidation', *Int. J. Corros. Scale Inhib.*, vol. 10, no. 2, June 2021, doi: 10.17675/2305-6894-2020-10-2-20.
- [155] T. Kikuchi, T. Taniguchi, R. O. Suzuki, and S. Natsui, 'Fabrication of a plasma electrolytic oxidation/anodic aluminum oxide multi-layer film via one-step anodizing aluminum in ammonium carbonate', *Thin Solid Films*, vol. 697, p. 137799, Mar. 2020, doi: 10.1016/j.tsf.2020.137799.
- [156] S. He *et al.*, 'Ceramic oxide coating formed on beryllium by micro-arc oxidation', *Corros. Sci.*, vol. 122, pp. 108–117, July 2017, doi: 10.1016/j.corsci.2017.04.001.
- [157] Y. Han, S.-H. Hong, and K. Xu, 'Structure and in vitro bioactivity of titania-based films by micro-arc oxidation', *Surf. Coat. Technol.*, vol. 168, no. 2–3, pp. 249–258, May 2003, doi: 10.1016/S0257-8972(03)00016-1.
- [158] X. Jiang, Y. Wang, and C. Pan, 'High Concentration Substitutional N -Doped TiO<sub>2</sub> Film: Preparation, Characterization, and Photocatalytic Property', *J. Am. Ceram. Soc.*, vol. 94, no. 11, pp. 4078–4083, Nov. 2011, doi: 10.1111/j.1551-2916.2011.04692.x.
- [159] K. Venkateswarlu *et al.*, 'Role of electrolyte additives on in-vitro electrochemical behavior of micro arc oxidized titania films on Cp Ti', *Appl. Surf. Sci.*, vol. 258, no. 18, pp. 6853–6863, July 2012, doi: 10.1016/j.apsusc.2012.03.118.
- [160] C. L. Chu *et al.*, 'Micro-nano hierarchical porous titania modified with ZnO nanorods for biomedical applications', *Surf. Coat. Technol.*, vol. 232, pp. 68–74, Oct. 2013, doi: 10.1016/j.surfcoat.2013.04.054.
- [161] Y. Han, S.-H. Hong, and K. W. Xu, 'Porous nanocrystalline titania films by plasma electrolytic oxidation', *Surf. Coat. Technol.*, vol. 154, no. 2–3, pp. 314–318, May 2002, doi: 10.1016/S0257-8972(02)00036-1.
- [162] A. Sobolev, A. Kossenko, and K. Borodianskiy, 'Study of the Effect of Current Pulse Frequency on Ti-6Al-4V Alloy Coating Formation by Micro Arc Oxidation', *Materials*, vol. 12, no. 23, p. 3983, Dec. 2019, doi: 10.3390/ma12233983.
- [163] A. Mamaeva *et al.*, 'Influence of Current Duty Cycle and Voltage of Micro-Arc Oxidation on the Microstructure and Composition of Calcium Phosphate Coating', *Coatings*, vol. 14, no. 6, p. 766, June 2024, doi: 10.3390/coatings14060766.
- [164] V. V. Chebodaeva, M. B. Sedelnikova, O. V. Bakina, and Yu. P. Sharkeev, 'Formation of Structural, Physical and Adhesion Properties in Calcium-Phosphate Biocoatings in the Course of Microarc Oxidation Using Fe–Cu Nanocomposite Particles', *Russ. Phys. J.*, vol. 64, no. 8, pp. 1435–1442, Dec. 2021, doi: 10.1007/s11182-021-02476-2.
- [165] N. Salami, M. R. Bayati, F. Golestani-Fard, and H. R. Zargar, 'UV and visible photodecomposition of organic pollutants over micro arc oxidized Ag-activated TiO<sub>2</sub> nanocrystalline layers', *Mater. Res. Bull.*, vol. 47, no. 4, pp. 1080–1088, Apr. 2012, doi: 10.1016/j.materresbull.2011.12.022.
- [166] M. Shokouhfar, C. Dehghanian, and A. Baradaran, 'Preparation of ceramic coating on Ti substrate by Plasma electrolytic oxidation in different electrolytes and evaluation of its corrosion resistance', *Appl. Surf. Sci.*, vol. 257, no. 7, pp. 2617–2624, Jan. 2011, doi: 10.1016/j.apsusc.2010.10.032.
- [167] L. Tan *et al.*, 'Osteogenic differentiation of mesenchymal stem cells by silica/calcium micro-galvanic effects on the titanium surface', *J. Mater. Chem. B*, vol. 8, no. 11, pp. 2286–2295, 2020, doi: 10.1039/D0TB00054J.

- [168] J. Sun, Y. Han, and X. Huang, 'Hydroxyapatite coatings prepared by micro-arc oxidation in Ca and P-containing electrolyte', *Surf. Coat. Technol.*, vol. 201, no. 9–11, pp. 5655–5658, Feb. 2007, doi: 10.1016/j.surfcoat.2006.07.052.
- [169] W. Zhu, Y.-J. Fang, H. Zheng, G. Tan, H. Cheng, and C. Ning, 'Effect of applied voltage on phase components of composite coatings prepared by micro-arc oxidation', *Thin Solid Films*, vol. 544, pp. 79–82, Oct. 2013, doi: 10.1016/j.tsf.2013.04.121.
- [170] S.-D. Wu, H. Zhang, X.-D. Dong, C.-Y. Ning, A. S. L. Fok, and Y. Wang, 'Physicochemical properties and in vitro cytocompatibility of modified titanium surfaces prepared via micro-arc oxidation with different calcium concentrations', *Appl. Surf. Sci.*, vol. 329, pp. 347–355, Feb. 2015, doi: 10.1016/j.apsusc.2014.12.039.
- [171] M. C. Rossi, R. F. Dos Santos, P. A. B. Kuroda, and C. R. M. Afonso, 'Characteristics of ceramic-like coatings obtained by plasma electrolyte oxidation on different Ti alloys', *Bol. Soc. Esp. Cerámica Vidr.*, vol. 63, no. 1, pp. 33–46, Jan. 2024, doi: 10.1016/j.bsecv.2023.04.002.
- [172] P. A. B. Kuroda, C. R. Grandini, and C. R. M. Afonso, 'Surface Characterization of New  $\beta$  Ti-25Ta-Zr-Nb Alloys Modified by Micro-Arc Oxidation', *Materials*, vol. 16, no. 6, p. 2352, Mar. 2023, doi: 10.3390/ma16062352.
- [173] J. Chen, Y. Shi, L. Wang, F. Yan, and F. Zhang, 'Preparation and properties of hydroxyapatite-containing titania coating by micro-arc oxidation', *Mater. Lett.*, vol. 60, no. 20, pp. 2538–2543, Sept. 2006, doi: 10.1016/j.matlet.2006.01.035.
- [174] M. Montazeri, C. Dehghanian, M. Shokouhfar, and A. Baradaran, 'Investigation of the voltage and time effects on the formation of hydroxyapatite-containing titania prepared by plasma electrolytic oxidation on Ti-6Al-4V alloy and its corrosion behavior', *Appl. Surf. Sci.*, vol. 257, no. 16, pp. 7268–7275, June 2011, doi: 10.1016/j.apsusc.2011.03.103.
- [175] E. Nahum and S. Lugovskoy, 'A Comparative Study of Hydroxyapatite Coating Produced with Plasma Electrolytic Oxidation and Hydrothermal Treatment on Titanium Alloys: Ti6Al4V and Ti6Al7Nb for Dental Implants', Dec. 13, 2018. doi: 10.20944/preprints201810.0694.v2.
- [176] H.-C. Wu, J. Jiang, and E. I. Meletis, 'Microstructure of BaCO<sub>3</sub> and BaTiO<sub>3</sub> coatings produced on titanium by plasma electrolytic oxidation', *Appl. Surf. Sci.*, vol. 506, p. 144858, Mar. 2020, doi: 10.1016/j.apsusc.2019.144858.
- [177] Y. Wang, D. Yu, K. Ma, C. Dai, D. Wang, and J. Wang, 'Self-healing performance and corrosion resistance of a bilayer calcium carbonate coating on microarc-oxidized magnesium alloy', *Corros. Sci.*, vol. 212, p. 110927, Mar. 2023, doi: 10.1016/j.corsci.2022.110927.
- [178] R. Askarnia, M. Sobhani, M. Zare, H. Aghamohammadi, and H. Staji, 'Incorporation of Al<sub>2</sub>O<sub>3</sub> and ZrO<sub>2</sub> ceramics to AZ31 magnesium alloys composite coating using micro-arc oxidation method', *J. Mech. Behav. Biomed. Mater.*, vol. 141, p. 105784, May 2023, doi: 10.1016/j.jmbbm.2023.105784.
- [179] B. V. Derjaguin, 'A theory of the heterocoagulation, interaction and adhesion of dissimilar particles in solutions of electrolytes', *Discuss. Faraday Soc.*, vol. 18, p. 85, 1954, doi: 10.1039/df9541800085.
- [180] D.-Y. Kim, M. Kim, H.-E. Kim, Y.-H. Koh, H.-W. Kim, and J.-H. Jang, 'Formation of hydroxyapatite within porous TiO<sub>2</sub> layer by micro-arc oxidation coupled with electrophoretic deposition', *Acta Biomater.*, vol. 5, no. 6, pp. 2196–2205, July 2009, doi: 10.1016/j.actbio.2009.02.021.
- [181] R. Chaharmahali, A. Fattah-Alhosseini, and H. Esfahani, 'Increasing the in-vitro corrosion resistance of AZ31B-Mg alloy via coating with hydroxyapatite using plasma electrolytic oxidation', *J. Asian Ceram. Soc.*, vol. 8, no. 1, pp. 39–49, Jan. 2020, doi: 10.1080/21870764.2019.1698143.
- [182] R. Firdous, T. Hirsch, D. Klimm, B. Lothenbach, and D. Stephan, 'Reaction of calcium carbonate minerals in sodium silicate solution and its role in alkali-activated systems', *Miner. Eng.*, vol. 165, p. 106849, May 2021, doi: 10.1016/j.mineng.2021.106849.
- [183] P. P. Fedorov, A. A. Luginina, A. A. Alexandrov, and E. V. Chernova, 'Transformation of calcite CaCO<sub>3</sub> to fluorite CaF<sub>2</sub> by action of KF solution', *J. Fluor. Chem.*, vol. 251, p. 109898, Nov. 2021, doi: 10.1016/j.jfluchem.2021.109898.
- [184] M. Yoo, S.-J. Han, and J.-H. Wee, 'Carbon dioxide capture capacity of sodium hydroxide aqueous solution', *J. Environ. Manage.*, vol. 114, pp. 512–519, Jan. 2013, doi: 10.1016/j.jenvman.2012.10.061.

- [185] M. Mohedano, R. Guzman, R. Arrabal, J. -L. López Lacomba, and E. Matykina, 'Bioactive plasma electrolytic oxidation coatings—The role of the composition, microstructure, and electrochemical stability', *J. Biomed. Mater. Res. B Appl. Biomater.*, vol. 101, no. 8, pp. 1524–1537, Nov. 2013, doi: 10.1002/jbm.b.32974.
- [186] M. Roknian, A. Fattah-alhosseini, S. O. Gashti, and M. K. Keshavarz, 'Study of the effect of ZnO nanoparticles addition to PEO coatings on pure titanium substrate: Microstructural analysis, antibacterial effect and corrosion behavior of coatings in Ringer's physiological solution', *J. Alloys Compd.*, vol. 740, pp. 330–345, Apr. 2018, doi: 10.1016/j.jallcom.2017.12.366.
- [187] J.-Y. Cho, D.-Y. Hwang, D.-H. Lee, B. Yoo, and D.-H. Shin, 'Influence of potassium pyrophosphate in electrolyte on coated layer of AZ91 Mg alloy formed by plasma electrolytic oxidation', *Trans. Nonferrous Met. Soc. China*, vol. 19, no. 4, pp. 824–828, Aug. 2009, doi: 10.1016/S1003-6326(08)60358-1.
- [188] Z. Yang *et al.*, 'An interesting anodic oxidation behavior of plasma electrolytic oxidation coatings fabricated on aluminum in alkaline phosphate electrolyte', *Surf. Interfaces*, vol. 16, pp. 199–205, Sept. 2019, doi: 10.1016/j.surf.2018.10.004.
- [189] M. Mohedano, E. Matykina, R. Arrabal, A. Pardo, and M. C. Merino, 'Metal release from ceramic coatings for dental implants', *Dent. Mater.*, vol. 30, no. 3, pp. e28–e40, Mar. 2014, doi: 10.1016/j.dental.2013.12.011.
- [190] A. Kazek-Kęsik, D. Djurado, S. Pouget, A. Blacha-Grzechnik, I. Kalembe-Rec, and W. Simka, 'Analysis of the Calcium Phosphate-Based Hybrid Layer Formed on a Ti-6Al-7Nb Alloy to Enhance the Osseointegration Process', *Materials*, vol. 13, no. 23, p. 5468, Nov. 2020, doi: 10.3390/ma13235468.
- [191] G. Tang *et al.*, 'Combustion properties and thermal degradation behaviors of biobased polylactide composites filled with calcium hypophosphite', *RSC Adv.*, vol. 4, no. 18, p. 8985, 2014, doi: 10.1039/c3ra44537b.
- [192] M. A. Gol'dberg *et al.*, 'Hydroxyapatite-calcium carbonate ceramic composite materials', *Inorg. Mater.*, vol. 46, no. 11, pp. 1269–1273, Nov. 2010, doi: 10.1134/S0020168510110208.
- [193] J. Kiehl *et al.*, 'Grafting process of ethyltrimethoxysilane and polyphosphoric acid on calcium carbonate surface', *Appl. Surf. Sci.*, vol. 264, pp. 864–871, Jan. 2013, doi: 10.1016/j.apsusc.2012.10.166.
- [194] S. V. Sirkä *et al.*, 'Physicochemical and biological characterization of functionalized calcium carbonate', *Materialia*, vol. 28, p. 101742, May 2023, doi: 10.1016/j.mtla.2023.101742.
- [195] A. M. Bernhardt, S. C. Kunigelis, and K. M. Wilbur, 'Effects of phosphates on shell growth and calcium carbonate crystal formation', *Aquat. Toxicol.*, vol. 7, no. 1–2, pp. 1–13, Oct. 1985, doi: 10.1016/0166-445X(85)90032-3.
- [196] M. D. Eliassi, W. Zhao, and W. F. Tan, 'Effect of carbonate and phosphate ratios on the transformation of calcium orthophosphates', *Mater. Res. Bull.*, vol. 55, pp. 114–120, July 2014, doi: 10.1016/j.materresbull.2014.03.037.
- [197] M. Yoshimura, P. Sujaridworakun, F. Koh, T. Fujiwara, D. Pongkao, and A. Ahniyaz, 'Hydrothermal conversion of calcite crystals to hydroxyapatite', *Mater. Sci. Eng. C*, vol. 24, no. 4, pp. 521–525, June 2004, doi: 10.1016/j.msec.2004.01.005.
- [198] H. Guo and M. An, 'Effect of surfactants on surface morphology of ceramic coatings fabricated on magnesium alloys by micro-arc oxidation', *Thin Solid Films*, vol. 500, no. 1–2, pp. 186–189, Apr. 2006, doi: 10.1016/j.tsf.2005.11.045.
- [199] J.-H. Lee, H.-E. Kim, and Y.-H. Koh, 'Highly porous titanium (Ti) scaffolds with bioactive microporous hydroxyapatite/TiO<sub>2</sub> hybrid coating layer', *Mater. Lett.*, vol. 63, no. 23, pp. 1995–1998, Sept. 2009, doi: 10.1016/j.matlet.2009.06.023.
- [200] S. S. Zumdahl, S. L. Zumdahl, and D. J. DeCoste, *World of chemistry*. Princeton, N.J.: Recording for the Blind & Dyslexic, 2007.
- [201] V. Yanamadala, 'Calcium Carbonate Phosphate Binding Ion Exchange Filtration and Accelerated Denitrification Improve Public Health Standards and Combat Eutrophication in Aquatic Ecosystems', *Water Environ. Res.*, vol. 77, no. 7, pp. 3003–3012, Nov. 2005, doi: 10.2175/106143005X73884.
- [202] K. Benataya, M. Lakrat, L. L. Elansari, and E. Mejdoubi, 'Synthesis of B-type carbonated hydroxyapatite by a new dissolution-precipitation method', *Mater. Today Proc.*, vol. 31, pp. S83–S88, 2020, doi: 10.1016/j.matpr.2020.06.100.

- [203] K. Ishikawa, 'Bone Substitute Fabrication Based on Dissolution-Precipitation Reactions', *Materials*, vol. 3, no. 2, pp. 1138–1155, Feb. 2010, doi: 10.3390/ma3021138.
- [204] S. Yanyan, W. Guangxin, L. Wuhui, W. Yaming, S. Hayakawa, and A. Osaka, 'Conversion of sub- $\mu\text{m}$  calcium carbonate (calcite) particles to hollow hydroxyapatite agglomerates in  $\text{K}_2\text{HPO}_4$  solutions', *Nanotechnol. Rev.*, vol. 9, no. 1, pp. 945–960, Sept. 2020, doi: 10.1515/ntrev-2020-0070.
- [205] J. Barralet, S. Best, and W. Bonfield, 'Carbonate substitution in precipitated hydroxyapatite: An investigation into the effects of reaction temperature and bicarbonate ion concentration', *J. Biomed. Mater. Res.*, vol. 41, no. 1, pp. 79–86, July 1998, doi: 10.1002/(SICI)1097-4636(199807)41:1%3C79::AID-JBM10%3E3.0.CO;2-C.
- [206] K. Ishikawa, S. Matsuya, X. Lin, Z. Lei, T. Yuasa, and Y. Miyamoto, 'Fabrication of low crystalline B-type carbonate apatite block from low crystalline calcite block', *J. Ceram. Soc. Jpn.*, vol. 118, no. 1377, pp. 341–344, 2010, doi: 10.2109/jcersj2.118.341.
- [207] C. Verwilghen, M. Chkir, S. Rio, A. Nzihou, P. Sharrock, and G. Depelsenaire, 'Convenient conversion of calcium carbonate to hydroxyapatite at ambient pressure', *Mater. Sci. Eng. C*, vol. 29, no. 3, pp. 771–773, Apr. 2009, doi: 10.1016/j.msec.2008.07.007.
- [208] A. C. Tas and F. Aldinger, 'Formation of apatitic calcium phosphates in a Na-K-phosphate solution of pH 7.4', *J. Mater. Sci. Mater. Med.*, vol. 16, no. 2, pp. 167–174, Jan. 2005, doi: 10.1007/s10856-005-5919-5.
- [209] T. Suzuki, S. Inomata, and K. Sawada, 'Adsorption of phosphate on calcite', *J. Chem. Soc. Faraday Trans. 1 Phys. Chem. Condens. Phases*, vol. 82, no. 6, p. 1733, 1986, doi: 10.1039/f19868201733.
- [210] S. Yanyan, W. Guangxin, S. Guoqing, W. Yaming, L. Wuhui, and A. Osaka, 'Effects of amino acids on conversion of calcium carbonate to hydroxyapatite', *RSC Adv.*, vol. 10, no. 61, pp. 37005–37013, 2020, doi: 10.1039/D0RA07636H.
- [211] A. Ashokan, T. S. S. Kumar, and G. Jayaraman, 'Process optimization for the rapid conversion of calcite into hydroxyapatite microspheres for chromatographic applications', *Sci. Rep.*, vol. 12, no. 1, p. 12164, July 2022, doi: 10.1038/s41598-022-16579-4.
- [212] J.-M. Yu and H.-C. Choe, 'Morphology changes and bone formation on PEO-treated Ti-6Al-4V alloy in electrolyte containing Ca, P, Sr, and Si ions', *Appl. Surf. Sci.*, vol. 477, pp. 121–130, May 2019, doi: 10.1016/j.apsusc.2017.11.223.
- [213] M. O'Hara, S. C. Troughton, R. Francis, and T. W. Clyne, 'The incorporation of particles suspended in the electrolyte into plasma electrolytic oxidation coatings on Ti and Al substrates', *Surf. Coat. Technol.*, vol. 385, p. 125354, Mar. 2020, doi: 10.1016/j.surfcoat.2020.125354.
- [214] F. Wang *et al.*, 'Simultaneous incorporation of gallium oxide and tantalum microparticles into micro-arc oxidation coating of titanium possessing antibacterial effect and stimulating cellular response', *Biomater. Adv.*, vol. 135, p. 212736, Apr. 2022, doi: 10.1016/j.bioadv.2022.212736.
- [215] A. Seyfoori, Sh. Mirdamadi, Z. S. Seyedraoufi, A. Khavandi, and M. Aliofkhazraei, 'Synthesis of biphasic calcium phosphate containing nanostructured films by micro arc oxidation on magnesium alloy', *Mater. Chem. Phys.*, vol. 142, no. 1, pp. 87–94, Oct. 2013, doi: 10.1016/j.matchemphys.2013.06.045.
- [216] A. Declat, S. Reyes, and O. M. Suárez, 'Calcium Carbonate Precipitation: A Review Of The Carbonate Crystallization Process And Applications In Bioinspired Composites', *Rev. Adv. Mater. Sci.*, vol. 44, no. 1, pp. 87–107, 2016.
- [217] L. Addadi, J. Aizenberg, S. Albeck, G. Falini, and S. Weiner, 'Structural Control Over The Formation Of Calcium Carbonate Mineral Phases In Biomineralization', in *Supramolecular Stereochemistry*, Kluwer Academic Publishers, 1995, p. 127.
- [218] T. Ogino, T. Suzuki, and K. Sawada, 'The rate and mechanism of polymorphic transformation of calcium carbonate in water', *J. Cryst. Growth*, vol. 100, no. 1–2, pp. 159–167, Feb. 1990, doi: 10.1016/0022-0248(90)90618-U.
- [219] B. Majhy, P. Priyadarshini, and A. K. Sen, 'Effect of surface energy and roughness on cell adhesion and growth – facile surface modification for enhanced cell culture', *RSC Adv.*, vol. 11, no. 25, pp. 15467–15476, 2021, doi: 10.1039/D1RA02402G.
- [220] Y. Hou *et al.*, 'Surface Roughness Gradients Reveal Topography-Specific Mechanosensitive Responses in Human Mesenchymal Stem Cells', *Small*, vol. 16, no. 10, p. 1905422, Mar. 2020, doi: 10.1002/smll.201905422.

- [221] P. Fadia *et al.*, 'Calcium carbonate nano- and microparticles: synthesis methods and biological applications', *3 Biotech*, vol. 11, no. 11, p. 457, Nov. 2021, doi: 10.1007/s13205-021-02995-2.
- [222] O. A. Jimoh, K. S. Ariffin, H. B. Hussin, and A. E. Temitope, 'Synthesis of precipitated calcium carbonate: a review', *Carbonates Evaporites*, vol. 33, no. 2, pp. 331–346, June 2018, doi: 10.1007/s13146-017-0341-x.
- [223] X. Lu *et al.*, 'Influence of SiO<sub>2</sub> Particles on the Corrosion and Wear Resistance of Plasma Electrolytic Oxidation-Coated AM50 Mg Alloy', *Coatings*, vol. 8, no. 9, p. 306, Aug. 2018, doi: 10.3390/coatings8090306.
- [224] J. Yang, X. Lu, C. Blawert, S. Di, and M. L. Zheludkevich, 'Microstructure and corrosion behavior of Ca/P coatings prepared on magnesium by plasma electrolytic oxidation', *Surf. Coat. Technol.*, vol. 319, pp. 359–369, June 2017, doi: 10.1016/j.surfcoat.2017.04.001.
- [225] Q. Chen, Z. Jiang, S. Tang, W. Dong, Q. Tong, and W. Li, 'Influence of graphene particles on the micro-arc oxidation behaviors of 6063 aluminum alloy and the coating properties', *Appl. Surf. Sci.*, vol. 423, pp. 939–950, Nov. 2017, doi: 10.1016/j.apsusc.2017.06.202.
- [226] E. Nikoomanzari, A. Fattah-alhosseini, M. R. Pajohi Alamoti, and M. K. Keshavarz, 'Effect of ZrO<sub>2</sub> nanoparticles addition to PEO coatings on Ti–6Al–4V substrate: Microstructural analysis, corrosion behavior and antibacterial effect of coatings in Hank's physiological solution', *Ceram. Int.*, vol. 46, no. 9, pp. 13114–13124, June 2020, doi: 10.1016/j.ceramint.2020.02.084.
- [227] L. Qi, J. Fresnais, P. Muller, O. Theodoly, J.-F. Berret, and J.-P. Chapel, 'Interfacial activity of phosphonated-polyethylene glycol functionalized cerium oxide nanoparticles', 2013, doi: 10.48550/ARXIV.1305.0898.
- [228] M. Iijima and H. Kamiya, 'Surface Modification for Improving the Stability of Nanoparticles in Liquid Media', *KONA Powder Part. J.*, vol. 27, no. 0, pp. 119–129, 2009, doi: 10.14356/kona.2009012.
- [229] R. P. Bagwe, L. R. Hilliard, and W. Tan, 'Surface Modification of Silica Nanoparticles to Reduce Aggregation and Nonspecific Binding', *Langmuir*, vol. 22, no. 9, pp. 4357–4362, Apr. 2006, doi: 10.1021/la052797j.
- [230] J. Q. Qi, R. Guo, Y. Wang, X. W. Liu, and H. L. W. Chan, 'Electric Field-Controlled Crystallizing CaCO<sub>3</sub> Nanostructures from Solution', *Nanoscale Res. Lett.*, vol. 11, no. 1, p. 120, Dec. 2016, doi: 10.1186/s11671-016-1338-4.
- [231] A. Strach *et al.*, 'Multifaceted Assessment of Porous Silica Nanocomposites: Unraveling Physical, Structural, and Biological Transformations Induced by Microwave Field Modification', *Nanomaterials*, vol. 14, no. 4, p. 337, Feb. 2024, doi: 10.3390/nano14040337.
- [232] P. Wang *et al.*, 'Effect of MgO MicroParticles on Characteristics of Microarc Oxidation Coatings Fabricated on Pure Titanium', *Int. J. Electrochem. Sci.*, vol. 14, no. 1, pp. 287–300, Jan. 2019, doi: 10.20964/2019.01.16.
- [233] P. Wang *et al.*, 'Effect of Nd<sub>2</sub>O<sub>3</sub> Particles Addition on the Crack Resistance of Micro-arc Oxidation Coatings on Cast Aluminum Alloy', *Int. J. Electrochem. Sci.*, vol. 14, no. 6, pp. 5161–5173, June 2019, doi: 10.20964/2019.06.60.
- [234] P. Moulin and H. Roques, 'Zeta potential measurement of calcium carbonate', *J. Colloid Interface Sci.*, vol. 261, no. 1, pp. 115–126, May 2003, doi: 10.1016/S0021-9797(03)00057-2.
- [235] S. Knez, D. Klinar, and J. Golob, 'Stabilization of PCC dispersions prepared directly in the mother-liquid after synthesis through the carbonation of (hydrated) lime', *Chem. Eng. Sci.*, vol. 61, no. 17, pp. 5867–5880, Sept. 2006, doi: 10.1016/j.ces.2006.05.016.
- [236] M. Kaseem, H. W. Yang, and Y. G. Ko, 'Toward a nearly defect-free coating via high-energy plasma sparks', *Sci. Rep.*, vol. 7, no. 1, p. 2378, May 2017, doi: 10.1038/s41598-017-02702-3.
- [237] T. W. Clyne and S. C. Troughton, 'A review of recent work on discharge characteristics during plasma electrolytic oxidation of various metals', *Int. Mater. Rev.*, vol. 64, no. 3, pp. 127–162, Apr. 2019, doi: 10.1080/09506608.2018.1466492.
- [238] S. Xin, L. Song, R. Zhao, and X. Hu, 'Influence of cathodic current on composition, structure and properties of Al<sub>2</sub>O<sub>3</sub> coatings on aluminum alloy prepared by micro-arc oxidation process', *Thin Solid Films*, vol. 515, no. 1, pp. 326–332, Sept. 2006, doi: 10.1016/j.tsf.2005.12.087.
- [239] V. Raj and M. Mubarak Ali, 'Formation of ceramic alumina nanocomposite coatings on aluminium for enhanced corrosion resistance', *J. Mater. Process. Technol.*, vol. 209, no. 12–13, pp. 5341–5352, July 2009, doi: 10.1016/j.jmatprotec.2009.04.004.
- [240] B. Wendrow and K. A. Kobe, 'The System Sodium Oxide–Phosphorus Pentoxide–Water', *Ind. Eng. Chem.*, vol. 44, no. 6, pp. 1439–1448, June 1952, doi: 10.1021/ie50510a065.

- [241] W. L. Bourcier, J. K. Stolaroff, M. M. Smith, and R. D. Aines, 'Achieving Supercritical Fluid CO<sub>2</sub> Pressures Directly from Thermal Decomposition of Solid Sodium Bicarbonate', *Energy Procedia*, vol. 114, pp. 2545–2551, July 2017, doi: 10.1016/j.egypro.2017.03.1412.
- [242] C. Ramakrishna, T. Thenepalli, J.-H. Huh, and J. W. Ahn, 'Precipitated Calcium Carbonate Synthesis by Simultaneous Injection to Produce Nano Whisker Aragonite', *J. Korean Ceram. Soc.*, vol. 53, no. 2, pp. 222–226, Mar. 2016, doi: 10.4191/kcers.2016.53.2.222.
- [243] Y. Shen *et al.*, 'Controllable Synthesis of Nano-Micro Calcium Carbonate Mediated by Additive Engineering', *Crystals*, vol. 13, no. 10, p. 1432, Sept. 2023, doi: 10.3390/cryst13101432.
- [244] R. Febrida, E. Herda, A. Cahyanto, and I. M. Joni, 'Effect of drying technique on the synthesis of calcium carbonate by simple solution method', presented at the 3RD INTERNATIONAL CONFERENCE ON CONDENSED MATTER AND APPLIED PHYSICS (ICC-2019), Bikaner, India, 2020, p. 080012. doi: 10.1063/5.0003073.
- [245] Y.-H. Won, H. S. Jang, D.-W. Chung, and L. A. Stanciu, 'Multifunctional calcium carbonate microparticles: Synthesis and biological applications', *J. Mater. Chem.*, vol. 20, no. 36, p. 7728, 2010, doi: 10.1039/c0jm01231a.
- [246] R. Ševčík, M. Pérez-Estébanez, A. Viani, P. Šašek, and P. Mácová, 'Characterization of vaterite synthesized at various temperatures and stirring velocities without use of additives', *Powder Technol.*, vol. 284, pp. 265–271, Nov. 2015, doi: 10.1016/j.powtec.2015.06.064.
- [247] F. Munawaroh, M. Ahied, and L. K. Muharrami, 'The effect of Ca(OH)<sub>2</sub> slurry concentration on precipitated CaCO<sub>3</sub> product', presented at the INTERNATIONAL CONFERENCE ON SCIENCE AND APPLIED SCIENCE (ICSAS) 2019, Surakarta, Indonesia, 2019, p. 020017. doi: 10.1063/1.5141630.
- [248] J. Ahn *et al.*, 'Synthesis of Precipitated Calcium Carbonate in Ca(OH)<sub>2</sub>-CO<sub>2</sub>-H<sub>2</sub>O System by the Continuous Drop Method of Ca(OH)<sub>2</sub> Slurry', *J. Korean Ceram. Soc.*, vol. 39, no. 4, pp. 327–335, 2002.
- [249] M. Kogo, N. Uzawa, A. Nasu, T. Umegaki, and Y. Kojima, 'Synthesis of colored calcium carbonate and its color', *J. Ceram. Soc. Jpn.*, vol. 130, no. 1, pp. 94–99, Jan. 2022, doi: 10.2109/jcersj.2.21106.
- [250] L. Xiang, Y. Xiang, Y. Wen, and F. Wei, 'Formation of CaCO<sub>3</sub> nanoparticles in the presence of terpineol', *Mater. Lett.*, vol. 58, no. 6, pp. 959–965, Feb. 2004, doi: 10.1016/j.matlet.2003.07.034.
- [251] L. Xiang, Y. Xiang, Z. G. Wang, and Y. Jin, 'Influence of chemical additives on the formation of super-fine calcium carbonate', *Powder Technol.*, vol. 126, no. 2, pp. 129–133, July 2002, doi: 10.1016/S0032-5910(02)00047-5.
- [252] A. Barhoum *et al.*, 'Effect of Cationic and Anionic Surfactants on the Application of Calcium Carbonate Nanoparticles in Paper Coating', *ACS Appl. Mater. Interfaces*, vol. 6, no. 4, pp. 2734–2744, Feb. 2014, doi: 10.1021/am405278j.
- [253] G. Montanari *et al.*, 'Effect of Aspartic Acid and Glycine on Calcite Growth', *Cryst. Growth Des.*, vol. 16, no. 9, pp. 4813–4821, Sept. 2016, doi: 10.1021/acs.cgd.5b01635.
- [254] K. K. Sand *et al.*, 'Binding of Ethanol on Calcite: The Role of the OH Bond and Its Relevance to Biomineralization', *Langmuir*, vol. 26, no. 19, pp. 15239–15247, Oct. 2010, doi: 10.1021/la101136j.
- [255] M. Yang, S. L. S. Stipp, and J. Harding, 'Biological Control on Calcite Crystallization by Polysaccharides', *Cryst. Growth Des.*, vol. 8, no. 11, pp. 4066–4074, Nov. 2008, doi: 10.1021/cg800508t.
- [256] S. Görgen, K. Benzerara, F. Skouri-Panet, M. Gugger, F. Chauvat, and C. Cassier-Chauvat, 'The diversity of molecular mechanisms of carbonate biomineralization by bacteria', *Discov. Mater.*, vol. 1, no. 1, p. 2, Dec. 2021, doi: 10.1007/s43939-020-00001-9.
- [257] N. Kamennaya, C. Ajo-Franklin, T. Northen, and C. Jansson, 'Cyanobacteria as Biocatalysts for Carbonate Mineralization', *Minerals*, vol. 2, no. 4, pp. 338–364, Oct. 2012, doi: 10.3390/min2040338.
- [258] G. Aloisi, A. Gloter, M. Krüger, K. Wallmann, F. Guyot, and P. Zuddas, 'Nucleation of calcium carbonate on bacterial nanoglobules', *Geology*, vol. 34, no. 12, p. 1017, 2006, doi: 10.1130/G22986A.1.
- [259] R. S. Chaurasiya and H. U. Hebbar, 'Reverse Micelles for Nanoparticle Synthesis and Biomolecule Separation', in *Nanoscience in Food and Agriculture 4*, vol. 24, S. Ranjan, N.



- Dasgupta, and E. Lichtfouse, Eds, in *Sustainable Agriculture Reviews*, vol. 24. , Cham: Springer International Publishing, 2017, pp. 181–211. doi: 10.1007/978-3-319-53112-0\_5.
- [260] T. M. Stawski, T. Roncal-Herrero, A. Fernandez-Martinez, A. Matamoros-Veloza, R. Kröger, and L. G. Benning, “‘On demand’ triggered crystallization of  $\text{CaCO}_3$  from solute precursor species stabilized by the water-in-oil microemulsion’, *Phys. Chem. Chem. Phys.*, vol. 20, no. 20, pp. 13825–13835, 2018, doi: 10.1039/C8CP00540K.
- [261] A. H. Kshash and A. S. Ismail, ‘Minimizing Evaporation of Light Hydrocarbons for Iraqi Gasoline by using D-Glucitol Fatty Acid Esters as Reduced Pressure Agents, Synthesis and Characterization’, *Pet. Coal*, vol. 61, no. 1, pp. 100–109, 2019.
- [262] R. Atchudan, N. Lone, and J. Joo, ‘Preparation of  $\text{CaCO}_3$  and  $\text{CaO}$  Nanoparticles via Solid-State Conversion of Calcium Oleate Precursor’, *J. Nanosci. Nanotechnol.*, vol. 18, no. 3, pp. 1958–1964, Mar. 2018, doi: 10.1166/jnn.2018.14208.
- [263] D. Neumeyer, C. Venturini, N. Ratel-Ramond, M. Verelst, and A. Gourdon, ‘Simple and economic elaboration of high purity  $\text{CaCO}_3$  particles for bone graft applications using a spray pyrolysis technique’, *J. Mater. Chem. B*, vol. 5, no. 33, pp. 6897–6907, 2017, doi: 10.1039/C7TB00586E.
- [264] M. Huber, W. J. Stark, S. Loher, M. Maciejewski, F. Krumeich, and A. Baiker, ‘Flame synthesis of calcium carbonate nanoparticles’, *Chem. Commun.*, no. 5, p. 648, 2005, doi: 10.1039/b411725e.
- [265] G. Meng *et al.*, ‘Controllable synthesis and characterization of high purity calcium carbonate whisker-like fibers by electrochemical cathodic reduction method’, *J. Clean. Prod.*, vol. 342, p. 130923, Mar. 2022, doi: 10.1016/j.jclepro.2022.130923.
- [266] D. Zhou, E. V. Anoishkina, V. H. Desai, and K. J. Casey, ‘ChemInform Abstract: Synthesis and Characterization of Calcium Carbonate Whiskers.’, *ChemInform*, vol. 29, no. 42, p. chin.199842262, Oct. 1998, doi: 10.1002/chin.199842262.
- [267] H. K. Chahal, S. Matthews, and M. I. Jones, ‘Effect of process conditions on spray dried calcium carbonate powders for thermal spraying’, *Ceram. Int.*, vol. 47, no. 1, pp. 351–360, Jan. 2021, doi: 10.1016/j.ceramint.2020.08.140.
- [268] K. Cho, Y. J. Suh, H. Chang, D. S. Kil, B. G. Kim, and H.-D. Jang, ‘Synthesis of mesoporous  $\text{CaCO}_3$  particles by a spray drying method from the stable suspensions achieved in a beads mill’, *Adv. Powder Technol.*, vol. 21, no. 2, pp. 145–149, Mar. 2010, doi: 10.1016/j.apt.2010.02.016.
- [269] A. Dusanter, K. Saleh, and P. Guigon, ‘Formulation of Highly Concentrated Suspensions for Spray Drying in a Fluidized Bed’, *KONA Powder Part. J.*, vol. 26, no. 0, pp. 215–226, 2008, doi: 10.14356/kona.2008019.
- [270] Z. Liu *et al.*, ‘Crosslinking ionic oligomers as conformable precursors to calcium carbonate’, *Nature*, vol. 574, no. 7778, pp. 394–398, Oct. 2019, doi: 10.1038/s41586-019-1645-x.
- [271] Y. I. Svenskaya *et al.*, ‘Key Parameters for Size- and Shape-Controlled Synthesis of Vaterite Particles’, *Cryst. Growth Des.*, vol. 18, no. 1, pp. 331–337, Jan. 2018, doi: 10.1021/acs.cgd.7b01328.
- [272] X. Luo, X. Song, C. Lai, J. Wang, and Y. Cao, ‘Sonochemical Synthesis of Vaterite-Type Calcium Carbonate Using Steamed Ammonia Liquid Waste without Additives’, *ACS Omega*, vol. 6, no. 37, pp. 23846–23854, Sept. 2021, doi: 10.1021/acsomega.1c02772.
- [273] T. Yang *et al.*, ‘Biomimetic synthesis of calcium carbonate under phenylalanine: Control of polymorph and morphology’, *Mater. Sci. Eng. C*, vol. 114, p. 111019, Sept. 2020, doi: 10.1016/j.msec.2020.111019.
- [274] Y. Liu, Y. Chen, X. Huang, and G. Wu, ‘Biomimetic synthesis of calcium carbonate with different morphologies and polymorphs in the presence of bovine serum albumin and soluble starch’, *Mater. Sci. Eng. C*, vol. 79, pp. 457–464, Oct. 2017, doi: 10.1016/j.msec.2017.05.085.
- [275] E. Ulkeryildiz, S. Kilic, and E. Ozdemir, ‘Nano- $\text{CaCO}_3$  synthesis by jet flow’, *Colloids Surf. Physicochem. Eng. Asp.*, vol. 512, pp. 34–40, Jan. 2017, doi: 10.1016/j.colsurfa.2016.10.037.
- [276] M. Altiner, S. Top, and B. Kaymakoglu, ‘Ultrasonic-assisted production of precipitated calcium carbonate particles from desulfurization gypsum’, *Ultrason. Sonochem.*, vol. 72, p. 105421, Apr. 2021, doi: 10.1016/j.ultsonch.2020.105421.
- [277] F. C. Donnelly, F. Purcell-Milton, V. Framont, O. Cleary, P. W. Dunne, and Y. K. Gun’ko, ‘Synthesis of  $\text{CaCO}_3$  nano- and micro-particles by dry ice carbonation’, *Chem. Commun.*, vol. 53, no. 49, pp. 6657–6660, 2017, doi: 10.1039/C7CC01420A.

- [278] Y. Liang *et al.*, ‘Controllable preparation of nano-CaCO<sub>3</sub> in a microporous tube-in-tube microchannel reactor’, *Chem. Eng. Process. Process Intensif.*, vol. 79, pp. 34–39, May 2014, doi: 10.1016/j.cep.2014.03.006.
- [279] X. Liu *et al.*, ‘Density-dependent microbial calcium carbonate precipitation by drinking water bacteria via amino acid metabolism and biosorption’, *Water Res.*, vol. 202, p. 117444, Sept. 2021, doi: 10.1016/j.watres.2021.117444.
- [280] C. Y. Lin, A. V. Turchyn, Z. Steiner, P. Bots, G. I. Lampronti, and N. J. Tosca, ‘The role of microbial sulfate reduction in calcium carbonate polymorph selection’, *Geochim. Cosmochim. Acta*, vol. 237, pp. 184–204, Sept. 2018, doi: 10.1016/j.gca.2018.06.019.
- [281] R. Warthmann, Y. Van Lith, C. Vasconcelos, J. A. McKenzie, and A. M. Karpoff, ‘Bacterially induced dolomite precipitation in anoxic culture experiments’, *Geology*, vol. 28, no. 12, p. 1091, 2000, doi: 10.1130/0091-7613(2000)28%3C1091:BIDPIA%3E2.0.CO;2.
- [282] R. E. Martinez, E. Gardés, O. S. Pokrovsky, J. Schott, and E. H. Oelkers, ‘Do photosynthetic bacteria have a protective mechanism against carbonate precipitation at their surfaces?’, *Geochim. Cosmochim. Acta*, vol. 74, no. 4, pp. 1329–1337, Feb. 2010, doi: 10.1016/j.gca.2009.11.025.
- [283] N. Wang, X. Wang, L. Yang, and H. Chen, ‘Morphology and size control of nanocalcium carbonate crystallised in reverse micelle system with cationic surfactant cetyltrimethylammonium bromide’, *Micro Nano Lett.*, vol. 8, no. 2, pp. 94–98, Feb. 2013, doi: 10.1049/mnl.2012.0831.
- [284] Y. Shen *et al.*, ‘Controlled synthesis of calcium carbonate nanocrystals with multi-morphologies in different bicontinuous microemulsions’, *Mater. Sci. Eng. A*, vol. 443, no. 1–2, pp. 95–100, Jan. 2007, doi: 10.1016/j.msea.2006.08.105.
- [285] X. Meng, M. Lu, W. Yin, A. Benecer, and K. J. Kirk, ‘Evaluation of Coating Thickness Using Lift-Off Insensitivity of Eddy Current Sensor’, *Sensors*, vol. 21, no. 2, p. 419, Jan. 2021, doi: 10.3390/s21020419.
- [286] G. Li, G. Li, and Y. Xia, ‘Study on Discharge Characteristics and Microstructural Evolution of PEO Coatings Based on an Al/Ti Tracer Substrate’, *Coatings*, vol. 13, no. 9, p. 1507, Aug. 2023, doi: 10.3390/coatings13091507.
- [287] K. Mojsilović, S. Stojadinović, and R. Vasilčić, ‘The Plasma Electrolytic Oxidation of Aluminum Using Microsecond-Range DC Pulsing’, *Metals*, vol. 13, no. 12, p. 1931, Nov. 2023, doi: 10.3390/met13121931.
- [288] J. Sovík *et al.*, ‘The Effect of Mechanical Pretreatment on the Electrochemical Characteristics of PEO Coatings Prepared on Magnesium Alloy AZ80’, *Materials*, vol. 16, no. 16, p. 5650, Aug. 2023, doi: 10.3390/ma16165650.
- [289] J. A. Curran and T. W. Clyne, ‘Porosity in plasma electrolytic oxide coatings’, *Acta Mater.*, vol. 54, no. 7, pp. 1985–1993, Apr. 2006, doi: 10.1016/j.actamat.2005.12.029.
- [290] R. Muntean, M. Brîndușoiu, D. Buzdugan, N. S. Nemeș, A. Kellenberger, and I. D. Uțu, ‘Characteristics of Hydroxyapatite-Modified Coatings Based on TiO<sub>2</sub> Obtained by Plasma Electrolytic Oxidation and Electrophoretic Deposition’, *Materials*, vol. 16, no. 4, p. 1410, Feb. 2023, doi: 10.3390/ma16041410.
- [291] K. Rokosz, T. Hryniewicz, and Ł. Dudek, ‘Phosphate Porous Coatings Enriched with Selected Elements via PEO Treatment on Titanium and Its Alloys: A Review’, *Materials*, vol. 13, no. 11, p. 2468, May 2020, doi: 10.3390/ma13112468.
- [292] D. Wei, Y. Zhou, D. Jia, and Y. Wang, ‘Chemical treatment of TiO<sub>2</sub>-based coatings formed by plasma electrolytic oxidation in electrolyte containing nano-HA, calcium salts and phosphates for biomedical applications’, *Appl. Surf. Sci.*, vol. 254, no. 6, pp. 1775–1782, Jan. 2008, doi: 10.1016/j.apsusc.2007.07.144.
- [293] K. Rokosz *et al.*, ‘Characterization of Porous Phosphate Coatings Enriched with Calcium, Magnesium, Zinc and Copper Created on CP Titanium Grade 2 by Plasma Electrolytic Oxidation’, *Metals*, vol. 8, no. 6, p. 411, June 2018, doi: 10.3390/met8060411.
- [294] T. O. B. Polo *et al.*, ‘Plasma Electrolytic Oxidation as a Feasible Surface Treatment for Biomedical Applications: an in vivo study’, *Sci. Rep.*, vol. 10, no. 1, p. 10000, June 2020, doi: 10.1038/s41598-020-65289-2.
- [295] K. Leśniak-Ziółkowska *et al.*, ‘Antibacterial and cytocompatible coatings based on poly(adipic anhydride) for a Ti alloy surface’, *Bioact. Mater.*, vol. 5, no. 3, pp. 709–720, Sept. 2020, doi: 10.1016/j.bioactmat.2020.04.020.

- [296] I. A. J. Van Hengel, M. W. A. M. Tierolf, L. E. Fratila-Apachitei, I. Apachitei, and A. A. Zadpoor, 'Antibacterial Titanium Implants Biofunctionalized by Plasma Electrolytic Oxidation with Silver, Zinc, and Copper: A Systematic Review', *Int. J. Mol. Sci.*, vol. 22, no. 7, p. 3800, Apr. 2021, doi: 10.3390/ijms22073800.
- [297] A. Han and S.-Y. Lee, 'An overview of various methods for in vitro biofilm formation: a review', *Food Sci. Biotechnol.*, vol. 32, no. 12, pp. 1617–1629, Oct. 2023, doi: 10.1007/s10068-023-01425-8.
- [298] B. A. Jerri Al-Bakhsh, F. Shafiei, A. Hashemian, K. Shekofteh, B. Bolhari, and M. Behroozibakhsh, 'In-vitro bioactivity evaluation and physical properties of an epoxy-based dental sealer reinforced with synthesized fluorine-substituted hydroxyapatite, hydroxyapatite and bioactive glass nanofillers', *Bioact. Mater.*, vol. 4, pp. 322–333, Dec. 2019, doi: 10.1016/j.bioactmat.2019.10.004.
- [299] R. Drevet, J. Fauré, and H. Benhayoune, 'Bioactive Calcium Phosphate Coatings for Bone Implant Applications: A Review', *Coatings*, vol. 13, no. 6, p. 1091, June 2023, doi: 10.3390/coatings13061091.
- [300] R. Luo *et al.*, 'Fabrication, properties and biological activity of a titanium surface modified with zinc via plasma electrolytic oxidation', *Front. Mater.*, vol. 10, p. 1202110, July 2023, doi: 10.3389/fmats.2023.1202110.
- [301] R. Farrakhov *et al.*, 'Comparison of Biocompatible Coatings Produced by Plasma Electrolytic Oxidation on cp-Ti and Ti-Zr-Nb Superelastic Alloy', *Coatings*, vol. 11, no. 4, p. 401, Mar. 2021, doi: 10.3390/coatings11040401.
- [302] L. Pezzato, K. Brunelli, S. Diodati, M. Pigato, M. Bonesso, and M. Dabalà, 'Microstructural and Corrosion Properties of Hydroxyapatite Containing PEO Coating Produced on AZ31 Mg Alloy', *Materials*, vol. 14, no. 6, p. 1531, Mar. 2021, doi: 10.3390/ma14061531.
- [303] M. Molaei, M. Nouri, K. Babaei, and A. Fattah-Alhosseini, 'Improving surface features of PEO coatings on titanium and titanium alloys with zirconia particles: A review', *Surf. Interfaces*, vol. 22, p. 100888, Feb. 2021, doi: 10.1016/j.surf.2020.100888.
- [304] L. Chen *et al.*, 'Characterization of plasma electrolytic oxidation film on biomedical high niobium-containing  $\beta$ -titanium alloy', *Surf. Coat. Technol.*, vol. 352, pp. 295–301, Oct. 2018, doi: 10.1016/j.surfcoat.2018.08.025.
- [305] S. S. Farhadi, M. Aliofkhaezai, Gh. Barati Darband, A. Abolhasani, and A. Sabour Rouhaghdam, 'Wettability and Corrosion Behavior of Chemically Modified Plasma Electrolytic Oxidation Nanocomposite Coating', *J. Mater. Eng. Perform.*, vol. 26, no. 10, pp. 4797–4806, Oct. 2017, doi: 10.1007/s11665-017-2931-0.
- [306] M. Echeverry-Rendón, O. Galvis, R. Aguirre, S. Robledo, J. G. Castaño, and F. Echeverría, 'Modification of titanium alloys surface properties by plasma electrolytic oxidation (PEO) and influence on biological response', *J. Mater. Sci. Mater. Med.*, vol. 28, no. 11, p. 169, Nov. 2017, doi: 10.1007/s10856-017-5972-x.
- [307] M. Serdechnova *et al.*, 'Properties of ZnO/ZnAl<sub>2</sub>O<sub>3</sub> composite PEO coatings on zinc', 2022, doi: 10.48550/ARXIV.2210.15443.
- [308] M. Karbasi *et al.*, 'A review on plasma electrolytic oxidation coatings for organic pollutant degradation: How to prepare them and what to expect of them?', *J. Environ. Chem. Eng.*, vol. 11, no. 3, p. 110027, June 2023, doi: 10.1016/j.jece.2023.110027.
- [309] S. Stojadinović, M. Perković, and N. Radić, 'Photocatalytic and photoluminescent properties of Er<sup>3+</sup> doped TiO<sub>2</sub>/Al<sub>2</sub>TiO<sub>5</sub> coatings formed by plasma electrolytic oxidation of titanium', *Opt. Mater.*, vol. 162, p. 116873, May 2025, doi: 10.1016/j.optmat.2025.116873.
- [310] S. Aliasghari *et al.*, 'Communication—Formation of a Superconducting MgB<sub>2</sub> -Containing Coating on Niobium by Plasma Electrolytic Oxidation', *ECS J. Solid State Sci. Technol.*, vol. 8, no. 3, pp. N39–N41, 2019, doi: 10.1149/2.0071903jss.
- [311] Z. Yu *et al.*, 'Incorporation mechanism of ZnO nanoparticles in PEO coating on 1060 Al alloy', *Surf. Coat. Technol.*, vol. 412, p. 127068, Apr. 2021, doi: 10.1016/j.surfcoat.2021.127068.
- [312] F. Simchen, R. Morgenstern, S. Clauß, T. Mehner, and T. Lampke, 'Dissolution Behavior of Different Alumina Phases within Plasma Electrolytic Oxidation Coatings', *Coatings*, vol. 12, no. 8, p. 1205, Aug. 2022, doi: 10.3390/coatings12081205.
- [313] V. Grebnevs *et al.*, 'Advancements in plasma electrolytic oxidation with particle suspensions: a novel approach for the first-ever incorporation of calcium carbonate', *Appl. Surf. Sci.*, vol. 713, p. 164360, 2025, doi: 10.1016/j.apsusc.2025.164360.

- [314] Y. Q. Almajidi *et al.*, 'Unveiling the Effect of Particle Incorporation in PEO Coatings on the Corrosion and Wear Performance of Magnesium Implants', *Lubricants*, vol. 11, no. 12, p. 519, Dec. 2023, doi: 10.3390/lubricants11120519.
- [315] Y. Li and W. Weng, 'In vitro synthesis and characterization of amorphous calcium phosphates with various Ca/P atomic ratios', *J. Mater. Sci. Mater. Med.*, vol. 18, no. 12, pp. 2303–2308, Nov. 2007, doi: 10.1007/s10856-007-3132-4.
- [316] S. Somrani, M. Banu, M. Jemal, and C. Rey, 'Physico-chemical and thermochemical studies of the hydrolytic conversion of amorphous tricalcium phosphate into apatite', *J. Solid State Chem.*, vol. 178, no. 5, pp. 1337–1348, May 2005, doi: 10.1016/j.jssc.2004.11.029.
- [317] T. Christison and J. Rohrer, 'AU159: Determination of Volcanic Gases as Anions in Caustic Solutions Using AutoNeutralization, Automated Dilutions, and a Reagent-Free Ion Chromatography System'. Thermo Fischer Scientific, 2017. [Online]. Available: <https://apps.lab.thermofisher.com/ViewApplication/DownloadAttachment/375f48fb-a5d6-46e8-b89b-dee3da37d302>
- [318] O. Frank, M. Zukalova, B. Laskova, J. Kürti, J. Koltai, and L. Kavan, 'Raman spectra of titanium dioxide (anatase, rutile) with identified oxygen isotopes (16, 17, 18)', *Phys. Chem. Chem. Phys.*, vol. 14, no. 42, p. 14567, 2012, doi: 10.1039/c2cp42763j.
- [319] S. Franz *et al.*, 'Exploiting Direct Current Plasma Electrolytic Oxidation to Boost Photoelectrocatalysis', *Catalysts*, vol. 10, no. 3, p. 325, Mar. 2020, doi: 10.3390/catal10030325.
- [320] L.-H. Li *et al.*, 'Improved biological performance of Ti implants due to surface modification by micro-arc oxidation', *Biomaterials*, vol. 25, no. 14, pp. 2867–2875, June 2004, doi: 10.1016/j.biomaterials.2003.09.048.
- [321] K. Suchanek, A. Bartkowiak, M. Perzanowski, M. Marszałek, M. Sowa, and W. Simka, 'Electrochemical properties and bioactivity of hydroxyapatite coatings prepared by MEA/EDTA double-regulated hydrothermal synthesis', *Electrochimica Acta*, vol. 298, pp. 685–693, Mar. 2019, doi: 10.1016/j.electacta.2018.12.140.
- [322] V. Deineka *et al.*, 'Hemostatic and Tissue Regeneration Performance of Novel Electrospun Chitosan-Based Materials', *Biomedicines*, vol. 9, no. 6, p. 588, May 2021, doi: 10.3390/biomedicines9060588.
- [323] H. Mora-Sanchez *et al.*, 'Hard Anodizing and Plasma Electrolytic Oxidation of an Additively Manufactured Al-Si alloy', *Surf. Coat. Technol.*, vol. 420, p. 127339, Aug. 2021, doi: 10.1016/j.surfcoat.2021.127339.
- [324] M. Su, J. Han, Y. Li, J. Chen, Y. Zhao, and K. Chadwick, 'Ultrasonic Crystallization of Calcium Carbonate in Presence of Seawater Ions', *Desalination*, vol. 369, pp. 85–90, Aug. 2015, doi: 10.1016/j.desal.2015.05.001.
- [325] W. Xue, X. Liu, X. Zheng, and C. Ding, 'Effect of hydroxyapatite coating crystallinity on dissolution and osseointegration *in vivo*', *J. Biomed. Mater. Res. A*, vol. 74A, no. 4, pp. 553–561, Sept. 2005, doi: 10.1002/jbm.a.30323.
- [326] L. Xia, Y. Xie, B. Fang, X. Wang, and K. Lin, 'In situ modulation of crystallinity and nano-structures to enhance the stability and osseointegration of hydroxyapatite coatings on Ti-6Al-4V implants', *Chem. Eng. J.*, vol. 347, pp. 711–720, Sept. 2018, doi: 10.1016/j.cej.2018.04.045.
- [327] A. F. V. Recum, C. E. Shannon, C. E. Cannon, K. J. Long, T. G. V. Kooten, and J. Meyle, 'Surface Roughness, Porosity, and Texture as Modifiers of Cellular Adhesion', *Tissue Eng.*, vol. 2, no. 4, pp. 241–253, Dec. 1996, doi: 10.1089/ten.1996.2.241.
- [328] S. V. Dorozhkin, 'Calcium orthophosphates: Occurrence, properties, biomineralization, pathological calcification and biomimetic applications', *Biomatter*, vol. 1, no. 2, pp. 121–164, Oct. 2011, doi: 10.4161/biom.18790.
- [329] G. D. Cole *et al.*, 'High-performance near- and mid-infrared crystalline coatings', *Optica*, vol. 3, no. 6, p. 647, June 2016, doi: 10.1364/OPTICA.3.000647.
- [330] M. A. Giardina and M. A. Fanovich, 'Synthesis of nanocrystalline hydroxyapatite from Ca(OH)<sub>2</sub> and H<sub>3</sub>PO<sub>4</sub> assisted by ultrasonic irradiation', *Ceram. Int.*, vol. 36, no. 6, pp. 1961–1969, Aug. 2010, doi: 10.1016/j.ceramint.2010.05.008.
- [331] N. A. S. Mohd Pu'ad, R. H. Abdul Haq, H. Mohd Noh, H. Z. Abdullah, M. I. Idris, and T. C. Lee, 'Synthesis method of hydroxyapatite: A review', *Mater. Today Proc.*, vol. 29, pp. 233–239, 2020, doi: 10.1016/j.matpr.2020.05.536.

- [332] M. Shi and H. Li, 'A Mathematical interpretation model of Ti alloy micro-arc oxidation (MAO) process and its experimental study', *Surf. Eng. Appl. Electrochem.*, vol. 51, no. 5, pp. 468–477, Sept. 2015, doi: 10.3103/S1068375515050142.
- [333] I. Han, J. H. Choi, B. H. Zhao, H. K. Baik, and I.-S. Lee, 'Micro-arc oxidation in various concentration of KOH and structural change by different cut off potential', *Curr. Appl. Phys.*, vol. 7, pp. e23–e27, Apr. 2007, doi: 10.1016/j.cap.2006.11.008.
- [334] R. Sun *et al.*, 'Amorphous Calcium Carbonate Constructed from Nanoparticle Aggregates with Unprecedented Surface Area and Mesoporosity', *ACS Appl. Mater. Interfaces*, vol. 10, no. 25, pp. 21556–21564, June 2018, doi: 10.1021/acsami.8b03939.
- [335] E. D. Eanes, 'Amorphous Calcium Phosphate: Thermodynamic and Kinetic Considerations', in *Calcium Phosphates in Biological and Industrial Systems*, Z. Amjad, Ed., Boston, MA: Springer US, 1998, pp. 21–39. doi: 10.1007/978-1-4615-5517-9\_2.
- [336] M. A. Vargas and J. E. Rodríguez-Páez, 'Amorphous TiO<sub>2</sub> nanoparticles: Synthesis and antibacterial capacity', *J. Non-Cryst. Solids*, vol. 459, pp. 192–205, Mar. 2017, doi: 10.1016/j.jnoncrysol.2017.01.018.
- [337] K. M. Lee, B. U. Lee, S. I. Yoon, E. S. Lee, B. Yoo, and D. H. Shin, 'Evaluation of plasma temperature during plasma oxidation processing of AZ91 Mg alloy through analysis of the melting behavior of incorporated particles', *Electrochimica Acta*, vol. 67, pp. 6–11, Apr. 2012, doi: 10.1016/j.electacta.2012.01.053.
- [338] X. Li and B. L. Luan, 'Discovery of Al<sub>2</sub>O<sub>3</sub> particles incorporation mechanism in plasma electrolytic oxidation of AM60B magnesium alloy', *Mater. Lett.*, vol. 86, pp. 88–91, Nov. 2012, doi: 10.1016/j.matlet.2012.07.032.
- [339] S. V. Gnedenkov *et al.*, 'Formation and properties of bioactive surface layers on titanium', *Inorg. Mater. Appl. Res.*, vol. 2, no. 5, pp. 474–481, Oct. 2011, doi: 10.1134/S2075113311050133.
- [340] E. Matykina, A. Berkani, P. Skeldon, and G. E. Thompson, 'Real-time imaging of coating growth during plasma electrolytic oxidation of titanium', *Electrochimica Acta*, vol. 53, no. 4, pp. 1987–1994, Dec. 2007, doi: 10.1016/j.electacta.2007.08.074.
- [341] C. Rey, O. Marsan, C. Combes, C. Drouet, D. Grossin, and S. Sarda, 'Characterization of Calcium Phosphates Using Vibrational Spectroscopies', in *Advances in Calcium Phosphate Biomaterials*, vol. 2, B. Ben-Nissan, Ed., in Springer Series in Biomaterials Science and Engineering, vol. 2, Berlin, Heidelberg: Springer Berlin Heidelberg, 2014, pp. 229–266. doi: 10.1007/978-3-642-53980-0\_8.
- [342] J. P. Lafon, E. Champion, D. Bernache-Assollant, R. Gibert, and A. M. Danna, 'Thermal decomposition of carbonated calcium phosphate apatites', *J. Therm. Anal. Calorim.*, vol. 72, no. 3, pp. 1127–1134, June 2003, doi: 10.1023/A:1025036214044.
- [343] D. Farlay, G. Panczer, C. Rey, P. D. Delmas, and G. Boivin, 'Mineral maturity and crystallinity index are distinct characteristics of bone mineral', *J. Bone Miner. Metab.*, vol. 28, no. 4, pp. 433–445, July 2010, doi: 10.1007/s00774-009-0146-7.
- [344] T. I. Ivanova, O. V. Frank-Kamenetskaya, A. B. Kol'tsov, and V. L. Ugolkov, 'Crystal Structure of Calcium-Deficient Carbonated Hydroxyapatite. Thermal Decomposition', *J. Solid State Chem.*, vol. 160, no. 2, pp. 340–349, Sept. 2001, doi: 10.1006/jssc.2000.9238.
- [345] T. Kanazawa, T. Umegaki, and N. Uchiyama, 'Thermal crystallisation of amorphous calcium phosphate to  $\alpha$ -tricalcium phosphate', *J. Chem. Technol. Biotechnol.*, vol. 32, no. 2, pp. 399–406, Jan. 1982, doi: 10.1002/jctb.5030320206.
- [346] H. Keh and W. Hsu, 'Electric conductivity of a suspension of charged colloidal spheres with thin but polarized double layers', *Colloid Polym. Sci.*, vol. 280, no. 10, pp. 922–928, Oct. 2002, doi: 10.1007/s00396-002-0709-9.
- [347] A. L. Boskey and A. S. Posner, 'Conversion of amorphous calcium phosphate to microcrystalline hydroxyapatite. A pH-dependent, solution-mediated, solid-solid conversion', *J. Phys. Chem.*, vol. 77, no. 19, pp. 2313–2317, Sept. 1973, doi: 10.1021/j100638a011.
- [348] I. S. Harding, N. Rashid, and K. A. Hing, 'Surface charge and the effect of excess calcium ions on the hydroxyapatite surface', *Biomaterials*, vol. 26, no. 34, pp. 6818–6826, Dec. 2005, doi: 10.1016/j.biomaterials.2005.04.060.
- [349] A. Young, G. Smistad, J. Karlsen, G. Rølla, and M. Rykke, 'Zeta Potentials of Human Enamel and Hydroxyapatite as Measured by the Coulter® DELSA 440', *Adv. Dent. Res.*, vol. 11, no. 4, pp. 560–565, Nov. 1997, doi: 10.1177/08959374970110042501.

- [350] A. Dos Santos *et al.*, 'A study of the physical, chemical and biological properties of TiO<sub>2</sub> coatings produced by micro-arc oxidation in a Ca–P-based electrolyte', *J. Mater. Sci. Mater. Med.*, vol. 25, no. 7, pp. 1769–1780, July 2014, doi: 10.1007/s10856-014-5207-3.
- [351] M.-H. Hong, D.-H. Lee, K.-M. Kim, and Y.-K. Lee, 'Study on bioactivity and bonding strength between Ti alloy substrate and TiO<sub>2</sub> film by micro-arc oxidation', *Thin Solid Films*, vol. 519, no. 20, pp. 7065–7070, Aug. 2011, doi: 10.1016/j.tsf.2011.01.223.
- [352] W. Ma *et al.*, 'Histological evaluation and surface componential analysis of modified micro-arc oxidation-treated titanium implants', *J. Biomed. Mater. Res. B Appl. Biomater.*, vol. 86B, no. 1, pp. 162–169, July 2008, doi: 10.1002/jbm.b.31002.
- [353] X. Ma, S. Zhu, L. Wang, C. Ji, C. Ren, and S. Guan, 'Synthesis and properties of a bio-composite coating formed on magnesium alloy by one-step method of micro-arc oxidation', *J. Alloys Compd.*, vol. 590, pp. 247–253, Mar. 2014, doi: 10.1016/j.jallcom.2013.12.145.
- [354] K.-Y. Law, 'Definitions for Hydrophilicity, Hydrophobicity, and Superhydrophobicity: Getting the Basics Right', *J. Phys. Chem. Lett.*, vol. 5, no. 4, pp. 686–688, Feb. 2014, doi: 10.1021/jz402762h.
- [355] M. R. Bayati, R. Molaei, A. Kajbafvala, S. Zanganeh, H. R. Zargar, and K. Janghorban, 'Investigation on hydrophilicity of micro-arc oxidized TiO<sub>2</sub> nano/micro-porous layers', *Electrochimica Acta*, vol. 55, no. 20, pp. 5786–5792, Aug. 2010, doi: 10.1016/j.electacta.2010.05.021.
- [356] T. G. Tihan, M. D. Ionita, R. G. Popescu, and D. Iordachescu, 'Effect of hydrophilic–hydrophobic balance on biocompatibility of poly(methyl methacrylate) (PMMA)–hydroxyapatite (HA) composites', *Mater. Chem. Phys.*, vol. 118, no. 2–3, pp. 265–269, Dec. 2009, doi: 10.1016/j.matchemphys.2009.03.019.
- [357] R. N. Wenzel, 'RESISTANCE OF SOLID SURFACES TO WETTING BY WATER', *Ind. Eng. Chem.*, vol. 28, no. 8, pp. 988–994, Aug. 1936, doi: 10.1021/ie50320a024.
- [358] J. Q. Chen, X. Z. Liu, L. Ridolfi, B. Du, H. M. Wang, and F. Zhang, 'Analysis of Relationship between Porosity and Roughness of Surface Based on Fractal Model', *Adv. Mater. Res.*, vol. 683, pp. 413–418, Apr. 2013, doi: 10.4028/www.scientific.net/AMR.683.413.
- [359] J. Bico, U. Thiele, and D. Quéré, 'Wetting of textured surfaces', *Colloids Surf. Physicochem. Eng. Asp.*, vol. 206, no. 1–3, pp. 41–46, July 2002, doi: 10.1016/S0927-7757(02)00061-4.
- [360] K. Leśniak-Ziółkowska *et al.*, 'Plasma electrolytic oxidation as an effective tool for production of copper incorporated bacteriostatic coatings on Ti-15Mo alloy', *Appl. Surf. Sci.*, vol. 563, p. 150284, Oct. 2021, doi: 10.1016/j.apsusc.2021.150284.
- [361] S. S. Farhadi, M. Aliofkhaezai, Gh. Barati Darband, A. Abolhasani, and A. Sabour Rouhaghdam, 'Corrosion and wettability of PEO coatings on magnesium by addition of potassium stearate', *J. Magnes. Alloys*, vol. 5, no. 2, pp. 210–216, June 2017, doi: 10.1016/j.jma.2017.06.002.
- [362] D. Quéré, 'Wetting and Roughness', *Annu. Rev. Mater. Res.*, vol. 38, no. 1, pp. 71–99, Aug. 2008, doi: 10.1146/annurev.matsci.38.060407.132434.
- [363] T. T. Chau, W. J. Bruckard, P. T. L. Koh, and A. V. Nguyen, 'A review of factors that affect contact angle and implications for flotation practice', *Adv. Colloid Interface Sci.*, vol. 150, no. 2, pp. 106–115, Sept. 2009, doi: 10.1016/j.cis.2009.07.003.
- [364] R. Arrabal, M. Mohedano, E. Matykina, A. Pardo, B. Mingo, and M. C. Merino, 'Characterization and wear behaviour of PEO coatings on 6082-T6 aluminium alloy with incorporated  $\alpha$ -Al<sub>2</sub>O<sub>3</sub> particles', *Surf. Coat. Technol.*, vol. 269, pp. 64–73, May 2015, doi: 10.1016/j.surfcoat.2014.10.048.
- [365] M. L. R. Schwarz, M. Kowarsch, S. Rose, K. Becker, T. Lenz, and L. Jani, 'Effect of surface roughness, porosity, and a resorbable calcium phosphate coating on osseointegration of titanium in a minipig model', *J. Biomed. Mater. Res. A*, vol. 89A, no. 3, pp. 667–678, June 2009, doi: 10.1002/jbm.a.32000.
- [366] M. B. Rahmany and M. Van Dyke, 'Biomimetic approaches to modulate cellular adhesion in biomaterials: A review', *Acta Biomater.*, vol. 9, no. 3, pp. 5431–5437, Mar. 2013, doi: 10.1016/j.actbio.2012.11.019.
- [367] J.-W. Park, J.-H. Jang, C. S. Lee, and T. Hanawa, 'Osteoconductivity of hydrophilic microstructured titanium implants with phosphate ion chemistry', *Acta Biomater.*, vol. 5, no. 6, pp. 2311–2321, July 2009, doi: 10.1016/j.actbio.2009.02.026.
- [368] X. Nie, A. Leyland, and A. Matthews, 'Deposition of layered bioceramic hydroxyapatite/TiO<sub>2</sub> coatings on titanium alloys using a hybrid technique of micro-arc oxidation and electrophoresis',

- Surf. Coat. Technol.*, vol. 125, no. 1–3, pp. 407–414, Mar. 2000, doi: 10.1016/S0257-8972(99)00612-X.
- [369] Y. Yürektürk, F. Muhaffel, and M. Baydoğan, ‘Characterization of micro arc oxidized 6082 aluminum alloy in an electrolyte containing carbon nanotubes’, *Surf. Coat. Technol.*, vol. 269, pp. 83–90, May 2015, doi: 10.1016/j.surfcoat.2014.12.058.
- [370] F. Tian, Y. Zhang, J. Zhang, and C. Pan, ‘Raman Spectroscopy: A New Approach to Measure the Percentage of Anatase TiO<sub>2</sub> Exposed (001) Facets’, *J. Phys. Chem. C*, vol. 116, no. 13, pp. 7515–7519, Apr. 2012, doi: 10.1021/jp301256h.
- [371] T. Sekiya, S. Ohta, S. Kamei, M. Hanakawa, and S. Kurita, ‘Raman spectroscopy and phase transition of anatase TiO<sub>2</sub> under high pressure’, *J. Phys. Chem. Solids*, vol. 62, no. 4, pp. 717–721, Apr. 2001, doi: 10.1016/S0022-3697(00)00229-8.
- [372] S. Lee, C. Lee, D. Kim, J.-P. Locquet, and J. Seo, ‘Preparation and Photocatalytic Activity of Potassium- Incorporated Titanium Oxide Nanostructures Produced by the Wet Corrosion Process Using Various Titanium Alloys’, *Nanomaterials*, vol. 5, no. 3, pp. 1397–1417, Aug. 2015, doi: 10.3390/nano5031397.
- [373] K. Kutschej, P. H. Mayrhofer, M. Kathrein, P. Polcik, and C. Mitterer, ‘Influence of oxide phase formation on the tribological behaviour of Ti–Al–V–N coatings’, *Surf. Coat. Technol.*, vol. 200, no. 5–6, pp. 1731–1737, Nov. 2005, doi: 10.1016/j.surfcoat.2005.08.044.
- [374] T. Kokubo and H. Takadama, ‘Simulated Body Fluid (SBF) as a Standard Tool to Test the Bioactivity of Implants’, in *Handbook of Biomineralization*, 1st edn, E. Bäuerlein, Ed., Wiley, 2007, pp. 97–109. doi: 10.1002/9783527619443.ch51.
- [375] C. A. Bertran, S. Bertazzo, and L. P. Faria, ‘Surface Charge of Hydroxyapatite and Bone Mineral’, *Key Eng. Mater.*, vol. 330–332, pp. 713–716, Feb. 2007, doi: 10.4028/www.scientific.net/KEM.330-332.713.
- [376] S. Samavedi, A. R. Whittington, and A. S. Goldstein, ‘Calcium phosphate ceramics in bone tissue engineering: A review of properties and their influence on cell behavior’, *Acta Biomater.*, vol. 9, no. 9, pp. 8037–8045, Sept. 2013, doi: 10.1016/j.actbio.2013.06.014.
- [377] P. Huang, K.-W. Xu, and Y. Han, ‘Preparation and apatite layer formation of plasma electrolytic oxidation film on titanium for biomedical application’, *Mater. Lett.*, vol. 59, no. 2–3, pp. 185–189, Feb. 2005, doi: 10.1016/j.matlet.2004.09.045.
- [378] Y. Huang, Y. Qu, B. Yang, W. Li, B. Zhang, and X. Zhang, ‘In vivo biological responses of plasma sprayed hydroxyapatite coatings with an electric polarized treatment in alkaline solution’, *Mater. Sci. Eng. C*, vol. 29, no. 8, pp. 2411–2416, Oct. 2009, doi: 10.1016/j.msec.2009.07.002.
- [379] I. D. S. V. Marques *et al.*, ‘Electrochemical behavior of bioactive coatings on cp-Ti surface for dental application’, *Corros. Sci.*, vol. 100, pp. 133–146, Nov. 2015, doi: 10.1016/j.corsci.2015.07.019.
- [380] Q. Hu *et al.*, ‘Effect of crystallinity of calcium phosphate nanoparticles on adhesion, proliferation, and differentiation of bone marrow mesenchymal stem cells’, *J. Mater. Chem.*, vol. 17, no. 44, p. 4690, 2007, doi: 10.1039/b710936a.
- [381] M. Roy, A. Bandyopadhyay, and S. Bose, ‘Induction plasma sprayed nano hydroxyapatite coatings on titanium for orthopaedic and dental implants’, *Surf. Coat. Technol.*, vol. 205, no. 8–9, pp. 2785–2792, Jan. 2011, doi: 10.1016/j.surfcoat.2010.10.042.
- [382] E. V. Legostaeva, K. S. Kulyashova, E. G. Komarova, M. Epple, Y. P. Sharkeev, and I. A. Khlusov, ‘Physical, chemical and biological properties of micro-arc deposited calcium phosphate coatings on titanium and zirconium-niobium alloy’, *Mater. Werkst.*, vol. 44, no. 2–3, pp. 188–197, Mar. 2013, doi: 10.1002/mawe.201300107.
- [383] A. Krzakała, A. Kazek-Kęsik, and W. Simka, ‘Application of plasma electrolytic oxidation to bioactive surface formation on titanium and its alloys’, *RSC Adv.*, vol. 3, no. 43, p. 19725, 2013, doi: 10.1039/c3ra43465f.
- [384] D. C. L. Vasconcelos, J. A. N. Carvalho, M. Mantel, and W. L. Vasconcelos, ‘Corrosion resistance of stainless steel coated with sol–gel silica’, *J. Non-Cryst. Solids*, vol. 273, no. 1–3, pp. 135–139, Aug. 2000, doi: 10.1016/S0022-3093(00)00155-1.
- [385] R. O. Hussein, X. Nie, and D. O. Northwood, ‘An investigation of ceramic coating growth mechanisms in plasma electrolytic oxidation (PEO) processing’, *Electrochimica Acta*, vol. 112, pp. 111–119, Dec. 2013, doi: 10.1016/j.electacta.2013.08.137.
- [386] M. Molaei, A. Fattah-alhosseini, M. Nouri, and A. Nourian, ‘Systematic optimization of corrosion, bioactivity, and biocompatibility behaviors of calcium-phosphate plasma electrolytic

- oxidation (PEO) coatings on titanium substrates', *Ceram. Int.*, vol. 48, no. 5, pp. 6322–6337, Mar. 2022, doi: 10.1016/j.ceramint.2021.11.175.
- [387] Y. Kim, D. Kim, H. Park, U. Chung, and W. Chung, 'Effect of current step-down on the growth and hardness of PEO coatings on Al6061 alloy', *Procedia Eng.*, vol. 10, pp. 2809–2814, 2011, doi: 10.1016/j.proeng.2011.04.467.
- [388] Ramakrishna, Chilakala, Thenepalli, Thriveni, and Ahn, Ji-Whan, 'Evaluation of Various Synthesis Methods for Calcite-Precipitated Calcium Carbonate (PCC) Formation', *Korean Chem. Eng. Res.*, vol. 55, no. 3, pp. 279–286, June 2017, doi: 10.9713/KCER.2017.55.3.279.
- [389] O. A. Jimoh, N. Mahmed, P. U. Okoye, and K. S. Ariffin, 'Utilization of milk of lime (MOL) originated from carbide lime waste and operating parameters optimization study for potential precipitated calcium carbonate (PCC) production', *Environ. Earth Sci.*, vol. 75, no. 18, p. 1251, Sept. 2016, doi: 10.1007/s12665-016-6053-z.
- [390] C. Huang and P. Cao, 'Tuning Ca:P ratio by NaOH from monocalcium phosphate monohydrate (MCPM)', *Mater. Chem. Phys.*, vol. 181, pp. 159–166, Sept. 2016, doi: 10.1016/j.matchemphys.2016.06.045.
- [391] K. Karthik, S. Dhanuskodi, C. Gobinath, S. Prabukumar, and S. Sivaramakrishnan, 'Dielectric and antibacterial studies of microwave assisted calcium hydroxide nanoparticles', *J. Mater. Sci. Mater. Electron.*, vol. 28, no. 21, pp. 16509–16518, Nov. 2017, doi: 10.1007/s10854-017-7563-5.
- [392] N. Bouropoulos, A. Stampoulakis, and D. E. Mouzakis, 'Dynamic Mechanical Properties of Calcium Alginate-Hydroxyapatite Nanocomposite Hydrogels', *Sci. Adv. Mater.*, vol. 2, no. 2, pp. 239–242, June 2010, doi: 10.1166/sam.2010.1092.
- [393] C. Matei, D. Berger, A. Dumbrava, M. D. Radu, and E. Gheorghe, 'Calcium carbonate as silver carrier in composite materials obtained in green seaweed extract with topical applications', *J. Sol-Gel Sci. Technol.*, vol. 93, no. 2, pp. 315–323, Feb. 2020, doi: 10.1007/s10971-019-05145-6.
- [394] M. Jamil *et al.*, 'Silicon substituted hydroxyapatite: Preparation with Solid-State Reaction, Characterization and Dissolution Properties', *J. Mater. Environ. Sci.*, vol. 9, no. 8, pp. 2322–2327, 2018.
- [395] R. A. Youness, M. A. Taha, H. Elhaes, and M. Ibrahim, 'Molecular modeling, FTIR spectral characterization and mechanical properties of carbonated-hydroxyapatite prepared by mechanochemical synthesis', *Mater. Chem. Phys.*, vol. 190, pp. 209–218, Apr. 2017, doi: 10.1016/j.matchemphys.2017.01.004.
- [396] V. Uskoković, S. Ghosh, and V. M. Wu, 'Antimicrobial hydroxyapatite–gelatin–silica composite pastes with tunable setting properties', *J. Mater. Chem. B*, vol. 5, no. 30, pp. 6065–6080, 2017, doi: 10.1039/C7TB01794D.
- [397] Y. Ahmed, E. Ewais, and S. El-Sheikh, 'Effect of dispersion parameters on the consolidation of starch-loaded hydroxyapatite slurry', *Process. Appl. Ceram.*, vol. 8, no. 3, pp. 127–135, 2014, doi: 10.2298/PAC1403127A.
- [398] L. C. Bell, A. M. Posner, and J. P. Quirk, 'The point of zero charge of hydroxyapatite and fluorapatite in aqueous solutions', *J. Colloid Interface Sci.*, vol. 42, no. 2, pp. 250–261, Feb. 1973, doi: 10.1016/0021-9797(73)90288-9.
- [399] J. Plank and G. Bassioni, 'Adsorption of Carboxylate Anions on a CaCO<sub>3</sub> Surface', *Z. Für Naturforschung B*, vol. 62, no. 10, pp. 1277–1284, Oct. 2007, doi: 10.1515/znB-2007-1008.
- [400] T. K. Mitchell, A. V. Nguyen, and G. M. Evans, 'Heterocoagulation of chalcopyrite and pyrite minerals in flotation separation', *Adv. Colloid Interface Sci.*, vol. 114–115, pp. 227–237, June 2005, doi: 10.1016/j.cis.2004.08.009.
- [401] D. Luo, C. Yan, and T. Wang, 'Interparticle Forces Underlying Nanoparticle Self-Assemblies', *Small*, vol. 11, no. 45, pp. 5984–6008, Dec. 2015, doi: 10.1002/smll.201501783.
- [402] J.-F. Vanhumbeeck, and J. Proost, 'Current Understanding of Ti Anodisation: Functional, Morphological, Chemical and Mechanical Aspects', *Corros. Rev.*, vol. 27, no. 3, pp. 117–204, June 2009, doi: 10.1515/CORRREV.2009.27.3.117.
- [403] L. Pezzato, P. Cerchier, K. Brunelli, A. Bartolozzi, R. Bertani, and M. Dabalà, 'Plasma electrolytic oxidation coatings with fungicidal properties', *Surf. Eng.*, vol. 35, no. 4, pp. 325–333, Apr. 2019, doi: 10.1080/02670844.2018.1441659.
- [404] Z. Huan, L. E. Fratila-Apachitei, I. Apachitei, and J. Duszczyk, 'Characterization of Porous TiO<sub>2</sub> Surfaces Formed on 316L Stainless Steel by Plasma Electrolytic Oxidation for Stent



- Applications', *J. Funct. Biomater.*, vol. 3, no. 2, pp. 349–360, May 2012, doi: 10.3390/jfb3020349.
- [405] D. J. Blackwood, L. M. Peter, and D. E. Williams, 'Stability and open circuit breakdown of the passive oxide film on titanium', *Electrochimica Acta*, vol. 33, no. 8, pp. 1143–1149, Aug. 1988, doi: 10.1016/0013-4686(88)80206-8.
- [406] D. V. Mashtalyar *et al.*, 'Bioactive Coatings Formed on Titanium by Plasma Electrolytic Oxidation: Composition and Properties', *Materials*, vol. 13, no. 18, p. 4121, Sept. 2020, doi: 10.3390/ma13184121.
- [407] S. Abbasi, M. R. Bilesan, and F. Golestani-Fard, 'In vitro evaluation of the biocompatibility and bioactivity of plasma electrolyte oxidized titania/calcium phosphate nanocoatings on Ti', *J. Mater. Sci.*, vol. 54, no. 5, pp. 4277–4286, Mar. 2019, doi: 10.1007/s10853-018-3147-x.
- [408] S. Aliasghari, P. Skeldon, and G. E. Thompson, 'Plasma electrolytic oxidation of titanium in a phosphate/silicate electrolyte and tribological performance of the coatings', *Appl. Surf. Sci.*, vol. 316, pp. 463–476, Oct. 2014, doi: 10.1016/j.apsusc.2014.08.037.
- [409] S. Ignjatović *et al.*, 'The Influence of In Situ Anatase Particle Addition on the Formation and Properties of Multifunctional Plasma Electrolytic Oxidation Coatings on AA2024 Aluminum Alloy', *Adv. Eng. Mater.*, vol. 23, no. 6, p. 2001527, June 2021, doi: 10.1002/adem.202001527.
- [410] B. Myszka, K. Hurlle, K. Zheng, S. E. Wolf, and A. R. Boccaccini, 'Mechanical improvement of calcium carbonate cements by *in situ* HEMA polymerization during hardening', *J. Mater. Chem. B*, vol. 7, no. 21, pp. 3403–3411, 2019, doi: 10.1039/C9TB00237E.
- [411] A. Zamiri and S. De, 'Mechanical properties of hydroxyapatite single crystals from nanoindentation data', *J. Mech. Behav. Biomed. Mater.*, vol. 4, no. 2, pp. 146–152, Feb. 2011, doi: 10.1016/j.jmbbm.2010.11.001.
- [412] Y. Hao *et al.*, 'Fabrication of ultra-low porosity plasma electrolytic oxidation coating on Ta-12W alloys and its formation mechanism', *Surf. Coat. Technol.*, vol. 476, p. 130251, Jan. 2024, doi: 10.1016/j.surfcoat.2023.130251.
- [413] B. Wójciak-Stothard, A. Curtis, W. Monaghan, K. Macdonald, and C. Wilkinson, 'Guidance and Activation of Murine Macrophages by Nanometric Scale Topography', *Exp. Cell Res.*, vol. 223, no. 2, pp. 426–435, Mar. 1996, doi: 10.1006/excr.1996.0098.
- [414] V. C. Mendes, R. Moineddin, and J. E. Davies, 'The effect of discrete calcium phosphate nanocrystals on bone-bonding to titanium surfaces', *Biomaterials*, vol. 28, no. 32, pp. 4748–4755, Nov. 2007, doi: 10.1016/j.biomaterials.2007.07.020.
- [415] Y. Song, Y. Ju, Y. Morita, and G. Song, 'Effect of the nanostructure of porous alumina on growth behavior of MG63 osteoblast-like cells', *J. Biosci. Bioeng.*, vol. 116, no. 4, pp. 509–515, Oct. 2013, doi: 10.1016/j.jbiosc.2013.04.007.
- [416] X. Li, L. Wang, Y. Fan, Q. Feng, F. Cui, and F. Watari, 'Nanostructured scaffolds for bone tissue engineering', *J. Biomed. Mater. Res. A*, vol. 101A, no. 8, pp. 2424–2435, Aug. 2013, doi: 10.1002/jbm.a.34539.
- [417] Đ. Dedić *et al.*, 'Formation of multi-functional coatings composed of Al<sub>2</sub>O<sub>3</sub> and ZrSiO<sub>4</sub> on AA2024 alloy using plasma electrolytic oxidation', *Ceram. Int.*, May 2025, doi: 10.1016/j.ceramint.2025.05.240.
- [418] K. Karageorgiou, M. Paschalis, and G. N. Anastassakis, 'Removal of phosphate species from solution by adsorption onto calcite used as natural adsorbent', *J. Hazard. Mater.*, vol. 139, no. 3, pp. 447–452, Jan. 2007, doi: 10.1016/j.jhazmat.2006.02.038.
- [419] A. Adelinia, A. Yerokhin, D. T. A. Matthews, M. B. De Rooij, and J. Seyyed Monfared Zanjani, 'Pore formation and pore inter-connectivity in plasma electrolytic oxidation coatings on aluminium alloy', *Surf. Coat. Technol.*, vol. 496, p. 131597, Jan. 2025, doi: 10.1016/j.surfcoat.2024.131597.
- [420] A. Keyvani, N. Kamkar, R. Chaharmahali, M. Bahamirian, M. Kaseem, and A. Fattah-alhosseini, 'Improving anti-corrosion properties AZ31 Mg alloy corrosion behavior in a simulated body fluid using plasma electrolytic oxidation coating containing hydroxyapatite nanoparticles', *Inorg. Chem. Commun.*, vol. 158, p. 111470, Dec. 2023, doi: 10.1016/j.inoche.2023.111470.
- [421] W. Boonrawd, K. Awad, V. Varanasi, and E. I. Meletis, 'Surface characteristics and in-vitro studies of TiO<sub>2</sub> coatings by plasma electrolytic oxidation in potassium-phosphate electrolyte', *Ceram. Int.*, vol. 48, no. 5, pp. 7071–7081, Mar. 2022, doi: 10.1016/j.ceramint.2021.11.266.
- [422] K. Leśniak, J. Płonka, M. Śmiga-Matuszowicz, M. Brzychczy-Włoch, and A. Kazek-Kęsik, 'Functionalization of PEO layer formed on Ti-15Mo for biomedical application', *J. Biomed.*

*Mater. Res. B Appl. Biomater.*, vol. 108, no. 4, pp. 1568–1579, May 2020, doi: 10.1002/jbm.b.34504.

- [423] J. Wang *et al.*, ‘Strengthening effect of nano-rutile on Ti–3Zr–2Sn–3Mo–25Nb titanium alloy and mechanism of TiO<sub>2</sub> phase transformation’, *Mater. Chem. Phys.*, vol. 314, p. 128815, Feb. 2024, doi: 10.1016/j.matchemphys.2023.128815.
- [424] A. Santos-Coquillat, M. Mohedano, E. Martinez-Campos, R. Arrabal, A. Pardo, and E. Matykina, ‘Bioactive multi-elemental PEO-coatings on titanium for dental implant applications’, *Mater. Sci. Eng. C*, vol. 97, pp. 738–752, Apr. 2019, doi: 10.1016/j.msec.2018.12.097.
- [425] S. Kyrylenko *et al.*, ‘Effects of the sources of calcium and phosphorus on the structural and functional properties of ceramic coatings on titanium dental implants produced by plasma electrolytic oxidation’, *Mater. Sci. Eng. C*, vol. 119, p. 111607, Feb. 2021, doi: 10.1016/j.msec.2020.111607.
- [426] D. Wei, Y. Zhou, Y. Wang, and D. Jia, ‘Characteristic of microarc oxidized coatings on titanium alloy formed in electrolytes containing chelate complex and nano-HA’, *Appl. Surf. Sci.*, vol. 253, no. 11, pp. 5045–5050, Mar. 2007, doi: 10.1016/j.apsusc.2006.11.012.
- [427] V. Knap, M. Štrbák, B. Hadzima, Z. Florková, D. Kajánek, and M. Jacková, ‘Characterization and corrosion behaviour of a phosphate-based plasma electrolytic oxidation coating on extruded EV31 magnesium alloy’, *Int. J. Mater. Res.*, vol. 114, no. 9, pp. 783–792, Sept. 2023, doi: 10.1515/ijmr-2021-8688.
- [428] E. K. Baldin *et al.*, ‘Plasma Electrolytic Oxidation (PEO) Coated CP-Ti: Wear Performance on Reciprocating Mode and Chondrogenic–Osteogenic Differentiation’, *J. Bio- Tribo-Corros.*, vol. 8, no. 1, p. 29, Mar. 2022, doi: 10.1007/s40735-021-00627-z.
- [429] N. Ao, D. Liu, X. Zhang, and G. He, ‘Microstructural characteristics of PEO coating: Effect of surface nanocrystallization’, *J. Alloys Compd.*, vol. 823, p. 153823, May 2020, doi: 10.1016/j.jallcom.2020.153823.
- [430] H. Li and Z. Wang, ‘Corrosion behavior and incorporation mechanism of Y<sub>2</sub>O<sub>3</sub>-TiO<sub>2</sub> composite coatings fabricated on TC4 titanium alloy by plasma electrolytic oxidation’, *Chem. Phys. Lett.*, vol. 841, p. 141170, Apr. 2024, doi: 10.1016/j.cplett.2024.141170.
- [431] S. Wang, T. Yu, Z. Pang, X. Liu, C. Shi, and N. Du, ‘Improving the fatigue resistance of plasma electrolytic oxidation coated titanium alloy by ultrasonic surface rolling pretreatment’, *Int. J. Fatigue*, vol. 181, p. 108157, Apr. 2024, doi: 10.1016/j.ijfatigue.2024.108157.
- [432] K.-T. Kim, S. S. Nisar, and H.-C. Choe, ‘Mechanical octacalcium phosphate coatings on the plasma electrolytic oxidized pure titanium for bio-implant use’, *Surf. Coat. Technol.*, vol. 480, p. 130602, Mar. 2024, doi: 10.1016/j.surfcoat.2024.130602.
- [433] X. Zhang *et al.*, ‘X-ray Computed Tomographic Investigation of the Porosity and Morphology of Plasma Electrolytic Oxidation Coatings’, *ACS Appl. Mater. Interfaces*, vol. 8, no. 13, pp. 8801–8810, Apr. 2016, doi: 10.1021/acsami.6b00274.
- [434] C. R. Tubío, F. Guitián, J. R. Salgueiro, and A. Gil, ‘Anatase and rutile TiO<sub>2</sub> monodisperse microspheres by rapid thermal annealing: A method to avoid sintering at high temperatures’, *Mater. Lett.*, vol. 141, pp. 203–206, Feb. 2015, doi: 10.1016/j.matlet.2014.11.063.
- [435] D. Tuschel, ‘Why Are the Raman Spectra of Crystalline and Amorphous Solids Different?’, *Spectroscopy*, vol. 32, no. 3, pp. 26–33, 2017.
- [436] C. S. Ciobanu, S. L. Iconaru, F. Massuyeau, L. V. Constantin, A. Costescu, and D. Predoi, ‘Synthesis, Structure, and Luminescent Properties of Europium-Doped Hydroxyapatite Nanocrystalline Powders’, *J. Nanomater.*, vol. 2012, no. 1, p. 942801, Jan. 2012, doi: 10.1155/2012/942801.
- [437] A. Awonusi, M. D. Morris, and M. M. J. Tecklenburg, ‘Carbonate Assignment and Calibration in the Raman Spectrum of Apatite’, *Calcif. Tissue Int.*, vol. 81, no. 1, pp. 46–52, July 2007, doi: 10.1007/s00223-007-9034-0.
- [438] K. Dudek, M. Dulski, T. Goryczka, and A. Gerle, ‘Structural changes of hydroxyapatite coating electrophoretically deposited on NiTi shape memory alloy’, *Ceram. Int.*, vol. 44, no. 10, pp. 11292–11300, July 2018, doi: 10.1016/j.ceramint.2018.03.175.
- [439] G. Penel, G. Leroy, C. Rey, and E. Bres, ‘MicroRaman Spectral Study of the PO<sub>4</sub> and CO<sub>3</sub> Vibrational Modes in Synthetic and Biological Apatites’, *Calcif. Tissue Int.*, vol. 63, no. 6, pp. 475–481, Dec. 1998, doi: 10.1007/s002239900561.

- [440] Y. Ishimaru *et al.*, ‘Raman Spectroscopic Analysis to Detect Reduced Bone Quality after Sciatic Neurectomy in Mice’, *Molecules*, vol. 23, no. 12, p. 3081, Nov. 2018, doi: 10.3390/molecules23123081.
- [441] W. Yue, W. Song, C. Fan, and S. Li, ‘Kinetics of CaCO<sub>3</sub> decomposition at low CO<sub>2</sub> partial pressure in a vacuum fixed bed’, *Chem. Eng. Sci.*, vol. 273, p. 118646, June 2023, doi: 10.1016/j.ces.2023.118646.
- [442] E. Boanini, M. Gazzano, and A. Bigi, ‘Ionic substitutions in calcium phosphates synthesized at low temperature’, *Acta Biomater.*, vol. 6, no. 6, pp. 1882–1894, June 2010, doi: 10.1016/j.actbio.2009.12.041.
- [443] N. Buzgar and A. Ionuț Apopei, ‘The Raman study of certain carbonates’, *Geologie*, vol. 55, no. 2, pp. 97–112, 2009.
- [444] M. M. Krishtal, A. V. Katsman, A. V. Polunin, and A. O. Cheretaeva, ‘Ceramic metal oxide coatings formation by hybrid plasma electrolytic treatment: Interaction scenarios of ceramic NPs with oxide layers’, *Ceram. Int.*, vol. 50, no. 11, pp. 20777–20789, June 2024, doi: 10.1016/j.ceramint.2024.03.206.
- [445] S. Ono, S. Moronuki, Y. Mori, A. Koshi, J. Liao, and H. Asoh, ‘Effect of Electrolyte Concentration on the Structure and Corrosion Resistance of Anodic Films Formed on Magnesium through Plasma Electrolytic Oxidation’, *Electrochimica Acta*, vol. 240, pp. 415–423, June 2017, doi: 10.1016/j.electacta.2017.04.110.
- [446] E. Lokeshkumar *et al.*, ‘Effect of electrolyte composition on the surface characteristics of plasma electrolytic oxidation coatings over Ti 40Nb alloy’, *Surf. Coat. Technol.*, vol. 465, p. 129591, July 2023, doi: 10.1016/j.surfcoat.2023.129591.
- [447] S. C. Troughton, A. Nominé, A. V. Nominé, G. Henrion, and T. W. Clyne, ‘Synchronised electrical monitoring and high speed video of bubble growth associated with individual discharges during plasma electrolytic oxidation’, *Appl. Surf. Sci.*, vol. 359, pp. 405–411, Dec. 2015, doi: 10.1016/j.apsusc.2015.10.124.
- [448] A. Fattah-alhosseini, R. Chaharmahali, B. Dikici, and M. Kaseem, ‘A comprehensive review of plasma electrolytic oxidation (PEO) of tantalum (Ta): Mechanisms, properties, and applications’, *Int. J. Refract. Met. Hard Mater.*, vol. 128, p. 107059, Apr. 2025, doi: 10.1016/j.ijrmhm.2025.107059.
- [449] A. B. Rogov, A. Nemcova, T. Hashimoto, A. Matthews, and A. Yerokhin, ‘Analysis of electrical response, gas evolution and coating morphology during transition to soft sparking PEO of Al’, *Surf. Coat. Technol.*, vol. 442, p. 128142, July 2022, doi: 10.1016/j.surfcoat.2022.128142.
- [450] L. O. Snizhko, A. L. Yerokhin, N. L. Gurevina, V. A. Patalakha, and A. Matthews, ‘Excessive oxygen evolution during plasma electrolytic oxidation of aluminium’, *Thin Solid Films*, vol. 516, no. 2–4, pp. 460–464, Dec. 2007, doi: 10.1016/j.tsf.2007.06.158.
- [451] P. Hu, B. Wei, Y. Cheng, and Y. Cheng, ‘Discharge channel structure revealed by plasma electrolytic oxidation of AZ31Mg alloy with magnetron sputtering Al layer and corrosion behaviors of treated alloy’, *Trans. Nonferrous Met. Soc. China*, vol. 34, no. 1, pp. 139–156, Jan. 2024, doi: 10.1016/s1003-6326(23)66387-3.
- [452] B. Kasalica *et al.*, ‘Mechanisms of plasma electrolytic oxidation of aluminum at the multi-hour timescales’, *Surf. Coat. Technol.*, vol. 390, p. 125681, May 2020, doi: 10.1016/j.surfcoat.2020.125681.
- [453] M. D. M. Tavares *et al.*, ‘Effect of duty cycle and treatment time on electrolytic plasma oxidation of commercially pure Al samples’, *J. Mater. Res. Technol.*, vol. 8, no. 2, pp. 2141–2147, Apr. 2019, doi: 10.1016/j.jmrt.2019.01.020.
- [454] M. Rahmati, K. Raeissi, M. R. Toroghinejad, A. Hakimizad, and M. Santamaria, ‘Effect of Pulse Current Mode on Microstructure, Composition and Corrosion Performance of the Coatings Produced by Plasma Electrolytic Oxidation on AZ31 Mg Alloy’, *Coatings*, vol. 9, no. 10, p. 688, Oct. 2019, doi: 10.3390/coatings9100688.
- [455] T. Yasui, K. Hayashi, and M. Fukumoto, ‘Behaviors of Micro-Arcs, Bubbles, and Coating Growth during Plasma Electrolytic Oxidation of  $\beta$ -Titanium Alloy’, *Materials*, vol. 16, no. 1, p. 360, Dec. 2022, doi: 10.3390/ma16010360.
- [456] S. Wang, X. Liu, X. Yin, and N. Du, ‘Influence of electrolyte components on the microstructure and growth mechanism of plasma electrolytic oxidation coatings on 1060 aluminum alloy’, *Surf. Coat. Technol.*, vol. 381, p. 125214, Jan. 2020, doi: 10.1016/j.surfcoat.2019.125214.

- [457] K. Rokosz *et al.*, 'Metal Ions Supported Porous Coatings by Using AC Plasma Electrolytic Oxidation Processing', *Materials*, vol. 13, no. 17, p. 3838, Aug. 2020, doi: 10.3390/ma13173838.
- [458] Ł. Maj *et al.*, 'Unveiling the mechanisms of coating formation during micro-arc oxidation of titanium in Na<sub>2</sub>HPO<sub>4</sub> electrolyte', *Surf. Coat. Technol.*, vol. 476, p. 130224, Jan. 2024, doi: 10.1016/j.surfcoat.2023.130224.
- [459] A. Anawati, E. Hidayati, and S. Purwanto, 'Effect of Cation Incorporation in the Plasma Electrolytic Oxide Layer Formed on AZ31 Magnesium Alloy', *Appl. Surf. Sci. Adv.*, vol. 17, p. 100444, Oct. 2023, doi: 10.1016/j.apsadv.2023.100444.
- [460] G. Mortazavi, J. Jiang, and E. I. Meletis, 'Investigation of the plasma electrolytic oxidation mechanism of titanium', *Appl. Surf. Sci.*, vol. 488, pp. 370–382, Sept. 2019, doi: 10.1016/j.apsusc.2019.05.250.
- [461] D. Veys-Renaux, Z. Ait El Haj, and E. Rocca, 'Corrosion resistance in artificial saliva of titanium anodized by plasma electrolytic oxidation in Na<sub>3</sub>PO<sub>4</sub>', *Surf. Coat. Technol.*, vol. 285, pp. 214–219, Jan. 2016, doi: 10.1016/j.surfcoat.2015.11.028.
- [462] L. Cheng *et al.*, 'An effective magnetic amorphous titanium phosphate material to remove U(VI) from water: synthesis, characterization, and adsorption properties', *J. Radioanal. Nucl. Chem.*, vol. 331, no. 11, pp. 4705–4719, Nov. 2022, doi: 10.1007/s10967-022-08572-y.
- [463] M. Khorasani, A. Dehghan, M. H. Shariat, M. E. Bahrololoom, and S. Javadpour, 'Microstructure and wear resistance of oxide coatings on Ti–6Al–4V produced by plasma electrolytic oxidation in an inexpensive electrolyte', *Surf. Coat. Technol.*, vol. 206, no. 6, pp. 1495–1502, Dec. 2011, doi: 10.1016/j.surfcoat.2011.09.038.
- [464] Y. Wang *et al.*, 'Effect of frequency on the structure and cell response of Ca- and P-containing MAO films', *Appl. Surf. Sci.*, vol. 256, no. 7, pp. 2018–2024, Jan. 2010, doi: 10.1016/j.apsusc.2009.09.041.
- [465] K. Xi *et al.*, 'Improved corrosion and wear resistance of micro-arc oxidation coatings on the 2024 aluminum alloy by incorporation of quasi-two-dimensional sericite microplates', *Appl. Surf. Sci.*, vol. 585, p. 152693, May 2022, doi: 10.1016/j.apsusc.2022.152693.
- [466] S. A. Ulasevich, A. I. Kulak, S. K. Poznyak, S. A. Karpushenkov, A. D. Lisenkov, and E. V. Skorb, 'Deposition of hydroxyapatite-incorporated TiO<sub>2</sub> coating on titanium using plasma electrolytic oxidation coupled with electrophoretic deposition', *RSC Adv.*, vol. 6, no. 67, pp. 62540–62544, 2016, doi: 10.1039/C6RA10560B.
- [467] X. Li, C. Dong, Q. Zhao, Y. Pang, F. Cheng, and S. Wang, 'Characterization of Microstructure and Wear Resistance of PEO Coatings Containing Various Microparticles on Ti6Al4V Alloy', *J. Mater. Eng. Perform.*, vol. 27, no. 4, pp. 1642–1653, Apr. 2018, doi: 10.1007/s11665-018-3249-2.
- [468] J. Zhou *et al.*, 'Enhancing tribological performance of micro-arc oxidation coatings on Mg-Li alloy with h-BN incorporation', *Ceram. Int.*, vol. 51, no. 11, pp. 13760–13771, May 2025, doi: 10.1016/j.ceramint.2025.01.211.
- [469] A. Bordbar-Khiabani, B. Yarmand, and M. Mozafari, 'Enhanced corrosion resistance and in-vitro biodegradation of plasma electrolytic oxidation coatings prepared on AZ91 Mg alloy using ZnO nanoparticles-incorporated electrolyte', *Surf. Coat. Technol.*, vol. 360, pp. 153–171, Feb. 2019, doi: 10.1016/j.surfcoat.2019.01.002.
- [470] M. Zhang, X. Ma, S. Zhang, L. Hou, and K. H. Kim, 'One-step fabrication of wear resistant and friction-reducing Al<sub>2</sub>O<sub>3</sub>/MoS<sub>2</sub> nanocomposite coatings on 2A50 aluminum alloy by plasma electrolytic oxidation with MoS<sub>2</sub> nanoparticle additive', *Surf. Coat. Technol.*, vol. 497, p. 131796, Feb. 2025, doi: 10.1016/j.surfcoat.2025.131796.
- [471] H. Zheng *et al.*, 'Raman spectroscopy of B-site order–disorder in CaTiO<sub>3</sub>-based microwave ceramics', *J. Eur. Ceram. Soc.*, vol. 23, no. 14, pp. 2653–2659, Jan. 2003, doi: 10.1016/s0955-2219(03)00149-3.
- [472] Y. Wang *et al.*, 'Effect of HA and CO<sub>2</sub> Gas on the Microstructure and Corrosion of Coatings Prepared by Plasma Electrolytic Oxidation of Mg-Nd-Zn-Ca Alloy', *Surf. Interface Anal.*, vol. 57, no. 3, pp. 226–234, Mar. 2025, doi: 10.1002/sia.7380.
- [473] H.-G. Gim, Y.-T. Kim, and J. Choi, 'Polydimethylsiloxane-assisted plasma electrolytic oxidation of Ti for synthesizing SiO<sub>2</sub>-TiO<sub>2</sub> composites for application as Li-ion battery anodes', *Electrochem. Commun.*, vol. 148, p. 107455, Mar. 2023, doi: 10.1016/j.elecom.2023.107455.

- [474] C. Wang, R. Ma, A. Du, Y. Fan, X. Zhao, and X. Cao, 'Growth methods of PEO coatings on 7075 aluminum alloy at two cathodic current densities', *Surf. Coat. Technol.*, vol. 432, p. 128099, Feb. 2022, doi: 10.1016/j.surfcoat.2022.128099.
- [475] K. Xie, A. Ozden, R. K. Miao, Y. Li, D. Sinton, and E. H. Sargent, 'Eliminating the need for anodic gas separation in CO<sub>2</sub> electroreduction systems via liquid-to-liquid anodic upgrading', *Nat. Commun.*, vol. 13, no. 1, June 2022, doi: 10.1038/s41467-022-30677-x.
- [476] J. R. Nelson, R. J. Needs, and C. J. Pickard, 'Navigating the Ti-C-O and Al-C-O ternary systems through theory-driven discovery', *Phys. Rev. Mater.*, vol. 5, no. 12, Dec. 2021, doi: 10.1103/physrevmaterials.5.123801.
- [477] A. Sobolev, A. Valkov, A. Kossenko, I. Wolicki, M. Zinigrad, and K. Borodianskiy, 'Bioactive Coating on Ti Alloy with High Osseointegration and Antibacterial Ag Nanoparticles', *ACS Appl. Mater. Interfaces*, vol. 11, no. 43, pp. 39534–39544, Oct. 2019, doi: 10.1021/acsami.9b13849.
- [478] A. L. Yerokhin, X. Nie, A. Leyland, A. Matthews, and S. J. Dowey, 'Plasma electrolysis for surface engineering', *Surf. Coat. Technol.*, vol. 122, no. 2–3, pp. 73–93, Dec. 1999, doi: 10.1016/s0257-8972(99)00441-7.
- [479] G.-L. Wu, C.-E. Yen, W.-C. Hsu, and M.-L. Yeh, 'Incorporation of cerium oxide nanoparticles into the micro-arc oxidation layer promotes bone formation and achieves structural integrity in magnesium orthopedic implants', *Acta Biomater.*, vol. 191, pp. 80–97, Jan. 2025, doi: 10.1016/j.actbio.2024.11.008.
- [480] P. Whiteside, E. Matykina, J. E. Gough, P. Skeldon, and G. E. Thompson, 'In vitro evaluation of cell proliferation and collagen synthesis on titanium following plasma electrolytic oxidation', *J. Biomed. Mater. Res. A*, vol. 94A, no. 1, pp. 38–46, July 2010, doi: 10.1002/jbm.a.32664.
- [481] F. Xi, X. Zhang, X. Jiang, Y. Kang, X. Wen, and Y. Liu, 'Growth mechanism of oxide layer on Ti-6Al-4 V substrate with different surface topographies during the early stage of micro-arc oxidation', *Surf. Coat. Technol.*, vol. 467, p. 129685, Aug. 2023, doi: 10.1016/j.surfcoat.2023.129685.
- [482] Z. Lujun, L. Hongzhan, M. Qingmei, L. Jiangbo, and L. Zhengxian, 'The mechanism for tuning the corrosion resistance and pore density of plasma electrolytic oxidation (PEO) coatings on Mg alloy with fluoride addition', *J. Magnes. Alloys*, vol. 11, no. 8, pp. 2823–2832, Aug. 2023, doi: 10.1016/j.jma.2021.10.007.
- [483] L. Liu *et al.*, 'Growth mechanism of plasma electrolytic oxidation coating of Zr alloys revealed by layer-specific phase analyses', *Appl. Surf. Sci.*, vol. 702, p. 163336, Sept. 2025, doi: 10.1016/j.apsusc.2025.163336.
- [484] J. Mun, S. W. Kim, R. Kato, I. Hatta, S. H. Lee, and K. H. Kang, 'Measurement of the thermal conductivity of TiO<sub>2</sub> thin films by using the thermo-reflectance method', *Thermochim. Acta*, vol. 455, no. 1–2, pp. 55–59, Apr. 2007, doi: 10.1016/j.tca.2006.11.018.
- [485] X. Liu, S. Wang, N. Du, X. Li, and Q. Zhao, 'Evolution of the Three-Dimensional Structure and Growth Model of Plasma Electrolytic Oxidation Coatings on 1060 Aluminum Alloy', *Coatings*, vol. 8, no. 3, p. 105, Mar. 2018, doi: 10.3390/coatings8030105.
- [486] A. V. Polunin *et al.*, 'Improvement of oxide layers formed by plasma electrolytic oxidation on cast Al Si alloy by incorporating TiC nanoparticles', *Surf. Coat. Technol.*, vol. 423, p. 127603, Oct. 2021, doi: 10.1016/j.surfcoat.2021.127603.
- [487] G. A. Lavrushin, S. V. Gnedenkov, P. S. Gordienko, and S. L. Sinebryukhov, 'Cyclic Strength of Titanium Alloys, Anodized under Micro-Arc Conditions, in Sea Water', *Prot. Met.*, vol. 38, no. 4, pp. 363–365, 2002, doi: 10.1023/A:1019665402579.
- [488] H. Zheng *et al.*, 'A cytocompatible microporous Sr-doped titanium dioxide coating fabricated by plasma electrolytic oxidation', *Front. Mater.*, vol. 10, p. 1210728, June 2023, doi: 10.3389/fmats.2023.1210728.
- [489] Y. Bai, I. S. Park, H. H. Park, T. S. Bae, and M. H. Lee, 'Formation of bioceramic coatings containing hydroxyapatite on the titanium substrate by micro-arc oxidation coupled with electrophoretic deposition', *J. Biomed. Mater. Res. B Appl. Biomater.*, vol. 95B, no. 2, pp. 365–373, Nov. 2010, doi: 10.1002/jbm.b.31724.
- [490] S. Dorozhkin, 'Calcium Orthophosphate-Based Bioceramics', *Materials*, vol. 6, no. 9, pp. 3840–3942, Sept. 2013, doi: 10.3390/ma6093840.
- [491] N. V. Bulina, M. V. Khvostov, I. A. Borodulina, S. V. Makarova, N. A. Zhukova, and T. G. Tolstikova, 'Substituted hydroxyapatite and  $\beta$ -tricalcium phosphate as osteogenesis enhancers', *Ceram. Int.*, vol. 50, no. 18, pp. 33258–33269, Sept. 2024, doi: 10.1016/j.ceramint.2024.06.136.

- [492] C. Morilla Espino, G. F. Estévez, L. Van Der Weerd, L.-F. De Geus-Oei, and J. Jip. Van Den Beucken, 'Innovations for brushite cements toward applications in bone regeneration and drug delivery', *Ceram. Int.*, vol. 51, no. 7, pp. 8219–8230, Mar. 2025, doi: 10.1016/j.ceramint.2024.12.356.
- [493] H. Cheng *et al.*, 'Calcium titanate micro-sheets scaffold for improved cell viability and osteogenesis', *Chem. Eng. J.*, vol. 389, p. 124400, June 2020, doi: 10.1016/j.cej.2020.124400.
- [494] H. Cimenoglu, M. Gunyuz, G. T. Kose, M. Baydogan, F. Ugurlu, and C. Sener, 'Micro-arc oxidation of Ti6Al4V and Ti6Al7Nb alloys for biomedical applications', *Mater. Charact.*, vol. 62, no. 3, pp. 304–311, Mar. 2011, doi: 10.1016/j.matchar.2011.01.002.
- [495] X. Shi, Q. Wang, F. Wang, and S. Ge, 'Effects of electrolytic concentration on properties of micro-arc film on Ti6Al4V alloy', *Min. Sci. Technol. China*, vol. 19, no. 2, pp. 220–224, Mar. 2009, doi: 10.1016/S1674-5264(09)60042-9.
- [496] X. Wang *et al.*, 'Influence of surface structures on biocompatibility of TiO<sub>2</sub>/HA coatings prepared by MAO', *Mater. Chem. Phys.*, vol. 215, pp. 339–345, Aug. 2018, doi: 10.1016/j.matchemphys.2018.05.037.
- [497] K. R. Shin, S. I. Il Yoon, H. W. Yang, Y. G. Ko, and D. H. Shin, 'Formation of  $\beta$ -tricalcium phosphate coating layer on titanium via micro-arc oxidation', *Mater. Res. Innov.*, vol. 18, no. sup2, pp. S2-997-S2-1000, May 2014, doi: 10.1179/1432891714Z.000000000539.
- [498] S.-F. Ou, S.-Y. Chiou, and K.-L. Ou, 'Phase transformation on hydroxyapatite decomposition', *Ceram. Int.*, vol. 39, no. 4, pp. 3809–3816, May 2013, doi: 10.1016/j.ceramint.2012.10.221.
- [499] Z. Zyman, J. Weng, X. Liu, X. Zhang, and Z. Ma, 'Amorphous phase and morphological structure of hydroxyapatite plasma coatings', *Biomaterials*, vol. 14, no. 3, pp. 225–228, Jan. 1993, doi: 10.1016/0142-9612(93)90027-Y.
- [500] B. Jin *et al.*, 'Phase Transformation Mechanism of Amorphous Calcium Phosphate to Hydroxyapatite Investigated by Liquid-Cell Transmission Electron Microscopy', *Cryst. Growth Des.*, vol. 21, no. 9, pp. 5126–5134, Sept. 2021, doi: 10.1021/acs.cgd.1c00503.
- [501] R. A. Surmenev, M. A. Surmeneva, and A. A. Ivanova, 'Significance of calcium phosphate coatings for the enhancement of new bone osteogenesis – A review', *Acta Biomater.*, vol. 10, no. 2, pp. 557–579, Feb. 2014, doi: 10.1016/j.actbio.2013.10.036.
- [502] A. J. Ortiz-Ruiz, J. D. D. Teruel-Fernández, L. A. Alcolea-Rubio, A. Hernández-Fernández, Y. Martínez-Beneyto, and F. Gispert-Guirado, 'Structural differences in enamel and dentin in human, bovine, porcine, and ovine teeth', *Ann. Anat. - Anat. Anz.*, vol. 218, pp. 7–17, July 2018, doi: 10.1016/j.aanat.2017.12.012.
- [503] V. Dehnavi, B. L. Luan, D. W. Shoesmith, X. Y. Liu, and S. Rohani, 'Effect of duty cycle and applied current frequency on plasma electrolytic oxidation (PEO) coating growth behavior', *Surf. Coat. Technol.*, vol. 226, pp. 100–107, July 2013, doi: 10.1016/j.surfcoat.2013.03.041.
- [504] X. Jin *et al.*, ' $\beta$ -TCP particles additive synergistically improves corrosion resistance and biocompatibility of micro-arc oxide coated magnesium alloy', *Mater. Today Commun.*, vol. 36, p. 106694, Aug. 2023, doi: 10.1016/j.mtcomm.2023.106694.
- [505] L. H. Grey, H.-Y. Nie, and M. C. Biesinger, 'Defining the nature of adventitious carbon and improving its merit as a charge correction reference for XPS', *Appl. Surf. Sci.*, vol. 653, p. 159319, Apr. 2024, doi: 10.1016/j.apsusc.2024.159319.
- [506] J. Kawai, H. Adachi, Y. Kitajima, K. Maeda, S. Hayakawa, and Y. Gohshi, 'Inelastic Mean Free Path of Photoelectrons in Ag Determined by Total Reflection X-Ray Photoelectron Spectroscopy', *Anal. Sci.*, vol. 13, no. 5, pp. 797–801, Oct. 1997, doi: 10.2116/analsci.13.797.
- [507] A. Mocanu *et al.*, 'Ion release from hydroxyapatite and substituted hydroxyapatites in different immersion liquids: *in vitro* experiments and theoretical modelling study', *R. Soc. Open Sci.*, vol. 8, no. 1, p. 201785, Jan. 2021, doi: 10.1098/rsos.201785.
- [508] N. A. Kononovich *et al.*, 'Kinetics of Calcium and Phosphate Release from the Surface of Implants Coated Using Different Techniques', *Biomed. Eng.*, vol. 53, no. 3, pp. 190–193, Sept. 2019, doi: 10.1007/s10527-019-09906-z.
- [509] E. Anitua, L. Piñas, A. Murias, R. Prado, and R. Tejero, 'Effects of calcium ions on titanium surfaces for bone regeneration', *Colloids Surf. B Biointerfaces*, vol. 130, pp. 173–181, June 2015, doi: 10.1016/j.colsurfb.2015.04.006.
- [510] E. Anitua *et al.*, 'Influence of calcium ion-modified implant surfaces in protein adsorption and implant integration', *Int. J. Implant Dent.*, vol. 7, no. 1, p. 32, Dec. 2021, doi: 10.1186/s40729-021-00314-1.

- [511] T. B. Kardos, 'Cellular Responses to Metal Ions Released From Implants', *J. Oral Implantol.*, vol. 40, no. 3, pp. 294–298, June 2014, doi: 10.1563/AAID-JOI-D-11-00249.
- [512] C. S. Adams, K. Mansfield, R. L. Perlot, and I. M. Shapiro, 'Matrix Regulation of Skeletal Cell Apoptosis', *J. Biol. Chem.*, vol. 276, no. 23, pp. 20316–20322, Jan. 2001, doi: 10.1074/jbc.M006492200.
- [513] M. Mosharraf, K. M. G. Taylor, and D. Q. M. Craig, 'Effect of Calcium Ions on the Surface Charge and Aggregation of Phosphatidylcholine Liposomes', *J. Drug Target.*, vol. 2, no. 6, pp. 541–545, Jan. 1995, doi: 10.3109/10611869509015925.
- [514] M. M. Dvorak *et al.*, 'Physiological changes in extracellular calcium concentration directly control osteoblast function in the absence of calciotropic hormones', *Proc. Natl. Acad. Sci.*, vol. 101, no. 14, pp. 5140–5145, Apr. 2004, doi: 10.1073/pnas.0306141101.
- [515] Z. S. Abdullah *et al.*, 'Effect of commercially pure titanium implant coated with calcium carbonate and nanohydroxyapatite mixture on osseointegration', *J. Med. Life*, vol. 16, no. 1, pp. 52–61, Jan. 2023, doi: 10.25122/jml-2022-0049.
- [516] S. Li, W. Yu, W. Zhang, G. Zhang, L. Yu, and E. Lu, 'Evaluation of highly carbonated hydroxyapatite bioceramic implant coatings with hierarchical micro-/nanorod topography optimized for osseointegration', *Int. J. Nanomedicine*, vol. Volume 13, pp. 3643–3659, June 2018, doi: 10.2147/IJN.S159989.
- [517] C. Minkin and V. C. Marinho, 'Role of the Osteoclast at the Bone-Implant Interface', *Adv. Dent. Res.*, vol. 13, no. 1, pp. 49–56, June 1999, doi: 10.1177/08959374990130011401.
- [518] N. Sarkar, D. Banerjee, A. Bandyopadhyay, and S. Bose, 'Osteoclast-mediated resorption on additively manufactured porous metal and plasma-sprayed HA-coated Ti implants', *J. Mater. Res.*, vol. 36, no. 19, pp. 3894–3904, Oct. 2021, doi: 10.1557/s43578-021-00278-3.
- [519] H. C. Blair, 'How the osteoclast degrades bone', *BioEssays*, vol. 20, no. 10, pp. 837–846, Dec. 1998, doi: 10.1002/(SICI)1521-1878(199810)20:10%3C837::AID-BIES9%3E3.0.CO;2-D.
- [520] F. Rupp *et al.*, 'A review on the wettability of dental implant surfaces I: Theoretical and experimental aspects', *Acta Biomater.*, vol. 10, no. 7, pp. 2894–2906, July 2014, doi: 10.1016/j.actbio.2014.02.040.
- [521] U.-W. Jung *et al.*, 'Surface characteristics of a novel hydroxyapatite-coated dental implant', *J. Periodontal Implant Sci.*, vol. 42, no. 2, p. 59, 2012, doi: 10.5051/jpis.2012.42.2.59.
- [522] S.-B. Jeong, Y.-C. Yang, Y.-B. Chae, and B.-G. Kim, 'Characteristics of the Treated Ground Calcium Carbonate Powder with Stearic Acid Using the Dry Process Coating System', *Mater. Trans.*, vol. 50, no. 2, pp. 409–414, 2009, doi: 10.2320/matertrans.MRP2008351.
- [523] P. Zhu *et al.*, 'Surface wettability of various phases of titania thin films: Atomic-scale simulation studies', *J. Mol. Graph. Model.*, vol. 118, p. 108335, Jan. 2023, doi: 10.1016/j.jmgm.2022.108335.
- [524] X. Wang and Q. Zhang, 'Role of surface roughness in the wettability, surface energy and flotation kinetics of calcite', *Powder Technol.*, vol. 371, pp. 55–63, June 2020, doi: 10.1016/j.powtec.2020.05.081.
- [525] A. Pabst *et al.*, 'Osseointegration of a New, Ultrahydrophilic and Nanostructured Dental Implant Surface: A Comparative In Vivo Study', *Biomedicines*, vol. 10, no. 5, p. 943, Apr. 2022, doi: 10.3390/biomedicines10050943.
- [526] M. E. Orazem and B. Tribollet, *Electrochemical Impedance Spectroscopy*, 1st edn. Wiley, 2017. doi: 10.1002/9781119363682.
- [527] B. Yeum, *Technical Note 24-Pseudocapacitance Associated with CPE. In ZSimpWin Programme; EChem Software: Ann Arbor, MI, USA, 2002.*
- [528] B. Yeum, *Technical Note 3-Electrical Components associated with Mass Transport. In ZSimpWin Programme; EChem Software: Ann Arbor, MI, USA, 2004.*
- [529] A. Ebrahimi, H. Esfahani, O. Imantalab, and A. Fattah-Alhosseini, 'Biological, antibacterial activities and electrochemical behavior of borided commercially pure titanium in BSA-containing PBS', *Trans. Nonferrous Met. Soc. China*, vol. 30, no. 4, pp. 944–957, Apr. 2020, doi: 10.1016/S1003-6326(20)65267-0.
- [530] S. R. Sousa and M. A. Barbosa, 'Corrosion resistance of titanium CP in saline physiological solutions with calcium phosphate and proteins', *Clin. Mater.*, vol. 14, no. 4, pp. 287–294, Jan. 1993, doi: 10.1016/0267-6605(93)90015-Y.
- [531] M. McCracken, 'Dental Implant Materials: Commercially Pure Titanium and Titanium Alloys', *J. Prosthodont.*, vol. 8, no. 1, pp. 40–43, Mar. 1999, doi: 10.1111/j.1532-849X.1999.tb00006.x.

- [532] Y. Bai, K.-A. Kim, I. S. Park, S. J. Lee, T. S. Bae, and M. H. Lee, 'In situ composite coating of titania–hydroxyapatite on titanium substrate by micro-arc oxidation coupled with electrophoretic deposition processing', *Mater. Sci. Eng. B*, vol. 176, no. 15, pp. 1213–1221, Sept. 2011, doi: 10.1016/j.mseb.2011.06.019.
- [533] X. Lin *et al.*, 'Effect of preparation parameters on the properties of hydroxyapatite containing micro-arc oxidation coating on biodegradable ZK60 magnesium alloy', *Ceram. Int.*, vol. 40, no. 7, pp. 10043–10051, Aug. 2014, doi: 10.1016/j.ceramint.2014.02.104.
- [534] A. K. Kenzhegulov, A. A. Mamaeva, A. V. Panichkin, K. A. Prosolov, A. Brończyk, and D. Capanidis, 'Investigation of the adhesion properties of calcium-phosphate coating to titanium substrate with regards to the parameters of high-frequency magnetron sputtering', *Acta Bioeng. Biomech.*, vol. 22, no. 2, 2020, doi: 10.37190/ABB-01544-2020-02.
- [535] Y. Duan *et al.*, 'The effect of adhesive strength of hydroxyapatite coating on the stability of hydroxyapatite-coated prostheses in vivo at the early stage of implantation', *Arch. Med. Sci.*, vol. 2, pp. 199–208, 2012, doi: 10.5114/aoms.2012.28545.
- [536] S. Cheng, D. Wei, and Y. Zhou, 'Mechanical and corrosion resistance of hydrophilic sphene/titania composite coatings on titanium and deposition and release of cefazolin sodium/chitosan films', *Appl. Surf. Sci.*, vol. 257, no. 7, pp. 2657–2664, Jan. 2011, doi: 10.1016/j.apsusc.2010.10.038.
- [537] C. Chen, Q. Dong, H. Yu, X. Wang, and D. Wang, 'Microstructure of Porous TiO<sub>2</sub> Coating on Pure Ti by Micro-arc Oxidation', *Adv. Eng. Mater.*, vol. 8, no. 8, pp. 754–759, Aug. 2006, doi: 10.1002/adem.200500274.
- [538] V. H. Ingole, S. S. Ghule, T. Vuherer, V. Kokol, and A. V. Ghule, 'Mechanical Properties of Differently Nanostructured and High-Pressure Compressed Hydroxyapatite-Based Materials for Bone Tissue Regeneration', *Minerals*, vol. 11, no. 12, p. 1390, Dec. 2021, doi: 10.3390/min11121390.
- [539] L. Pezzato *et al.*, 'Effect of Different Types of Glass Powders on the Corrosion and Wear Resistance of Peo Coatings Produced on 6061 Aluminum Alloy', *Met. Mater. Int.*, vol. 31, no. 3, pp. 636–653, Mar. 2025, doi: 10.1007/s12540-024-01786-7.
- [540] J. Zhao *et al.*, 'Coating-thickness-dependent physical properties and cutting temperature for cutting Inconel 718 with TiAlN coated tools', *J. Adv. Res.*, vol. 38, pp. 191–199, May 2022, doi: 10.1016/j.jare.2021.07.009.
- [541] S. Durdu and M. Usta, 'The tribological properties of bioceramic coatings produced on Ti6Al4V alloy by plasma electrolytic oxidation', *Ceram. Int.*, vol. 40, no. 2, pp. 3627–3635, Mar. 2014, doi: 10.1016/j.ceramint.2013.09.062.
- [542] A. Mandelli, M. Bestetti, A. Da Forno, N. Lecis, S. P. Trasatti, and M. Trueba, 'A composite coating for corrosion protection of AM60B magnesium alloy', *Surf. Coat. Technol.*, vol. 205, no. 19, pp. 4459–4465, June 2011, doi: 10.1016/j.surfcoat.2011.03.066.
- [543] A. Kazek-Kęsik, M. Krok-Borkowicz, G. Dercz, A. Donesz-Sikorska, E. Pamuła, and W. Simka, 'Multilayer coatings formed on titanium alloy surfaces by plasma electrolytic oxidation-electrophoretic deposition methods', *Electrochimica Acta*, vol. 204, pp. 294–306, June 2016, doi: 10.1016/j.electacta.2016.02.193.
- [544] P. A. Steinmann, Y. Tardy, and H. E. Hintermann, 'Adhesion testing by the scratch test method: The influence of intrinsic and extrinsic parameters on the critical load', *Thin Solid Films*, vol. 154, no. 1–2, pp. 333–349, Nov. 1987, doi: 10.1016/0040-6090(87)90377-4.
- [545] S. J. Bull, 'Failure mode maps in the thin film scratch adhesion test', *Tribol. Int.*, vol. 30, no. 7, pp. 491–498, July 1997, doi: 10.1016/S0301-679X(97)00012-1.
- [546] A. Kazek-Kęsik *et al.*, 'Biocompatibility analysis of titanium bone wedges coated by antibacterial ceramic-polymer layer', *Sci. Rep.*, vol. 14, no. 1, p. 23085, Oct. 2024, doi: 10.1038/s41598-024-72931-w.
- [547] J. He, W. Feng, B.-H. Zhao, W. Zhang, and Z. Lin, 'In Vivo Effect of Titanium Implants with Porous Zinc-Containing Coatings Prepared by Plasma Electrolytic Oxidation Method on Osseointegration in Rabbits', *Int. J. Oral Maxillofac. Implants*, vol. 33, no. 2, pp. 298–310, Mar. 2018, doi: 10.11607/jomi.5764.
- [548] S. V. Gnedenkov, S. L. Sinebryukhov, A. V. Puz', and R. E. Kostiv, 'In vivo Osteogenerating Properties of Calcium Phosphate Coatings on Ti-6Al-4V Titanium Alloy', *Biomed. Eng.*, vol. 51, no. 2, pp. 116–119, July 2017, doi: 10.1007/s10527-017-9696-5.



- [549] A. L. Yerokhin, X. Nie, A. Leyland, and A. Matthews, 'Characterisation of oxide films produced by plasma electrolytic oxidation of a Ti–6Al–4V alloy', *Surf. Coat. Technol.*, vol. 130, no. 2–3, pp. 195–206, Aug. 2000, doi: 10.1016/S0257-8972(00)00719-2.
- [550] Q. B. Li, C. C. Liu, W. B. Yang, and J. Liang, 'Growth mechanism and adhesion of PEO coatings on 2024Al alloy', *Surf. Eng.*, vol. 33, no. 10, pp. 760–766, Oct. 2017, doi: 10.1080/02670844.2016.1200860.
- [551] O. Mishchenko *et al.*, 'From Synthesis to Clinical Trial: Novel Bioinductive Calcium Deficient HA/ $\beta$ -TCP Bone Grafting Nanomaterial', *Nanomaterials*, vol. 13, no. 12, p. 1876, June 2023, doi: 10.3390/nano13121876.
- [552] A. Myakinin *et al.*, 'In vitro evaluation of electrochemically bioactivated Ti6Al4V 3D porous scaffolds', *Mater. Sci. Eng. C*, vol. 121, p. 111870, Feb. 2021, doi: 10.1016/j.msec.2021.111870.
- [553] V. R. M. Gonçalves *et al.*, 'Micro-arc oxidation treatment applied on the surface of  $\beta$  Ti Nb matrix composites as a strategy to modulate cellular behavior', *Surf. Coat. Technol.*, p. 132113, Apr. 2025, doi: 10.1016/j.surfcoat.2025.132113.
- [554] H. J. Robinson, A. E. Markaki, C. A. Collier, and T. W. Clyne, 'Cell adhesion to plasma electrolytic oxidation (PEO) titania coatings, assessed using a centrifuging technique', *J. Mech. Behav. Biomed. Mater.*, vol. 4, no. 8, pp. 2103–2112, Nov. 2011, doi: 10.1016/j.jmbbm.2011.07.009.
- [555] M. H. Muhammad *et al.*, 'Beyond Risk: Bacterial Biofilms and Their Regulating Approaches', *Front. Microbiol.*, vol. 11, p. 928, May 2020, doi: 10.3389/fmicb.2020.00928.
- [556] A. Hajjaji, M. Elabidi, K. Trabelsi, A. A. Assadi, B. Bessais, and S. Rtimi, 'Bacterial adhesion and inactivation on Ag decorated TiO<sub>2</sub>-nanotubes under visible light: Effect of the nanotubes geometry on the photocatalytic activity', *Colloids Surf. B Biointerfaces*, vol. 170, pp. 92–98, Oct. 2018, doi: 10.1016/j.colsurfb.2018.06.005.
- [557] H. J. Busscher and H. C. Van Der Mei, 'How Do Bacteria Know They Are on a Surface and Regulate Their Response to an Adhering State?', *PLoS Pathog.*, vol. 8, no. 1, p. e1002440, Jan. 2012, doi: 10.1371/journal.ppat.1002440.
- [558] H. H. Tuson and D. B. Weibel, 'Bacteria–surface interactions', *Soft Matter*, vol. 9, no. 17, p. 4368, 2013, doi: 10.1039/c3sm27705d.
- [559] M. Rabe, D. Verdes, and S. Seeger, 'Understanding protein adsorption phenomena at solid surfaces', *Adv. Colloid Interface Sci.*, vol. 162, no. 1–2, pp. 87–106, Feb. 2011, doi: 10.1016/j.cis.2010.12.007.
- [560] M. Kastantin, B. B. Langdon, and D. K. Schwartz, 'A bottom-up approach to understanding protein layer formation at solid–liquid interfaces', *Adv. Colloid Interface Sci.*, vol. 207, pp. 240–252, May 2014, doi: 10.1016/j.cis.2013.12.006.
- [561] H. Wu *et al.*, 'Engineered porous bio-ceramic coating with antibacterial and excellent biocompatibility on the surface of low modulus multi-component titanium alloy', *Surf. Coat. Technol.*, vol. 506, p. 132121, June 2025, doi: 10.1016/j.surfcoat.2025.132121.
- [562] Y. Husak *et al.*, 'Influence of silver nanoparticles addition on antibacterial properties of PEO coatings formed on magnesium', *Appl. Surf. Sci.*, vol. 654, p. 159387, May 2024, doi: 10.1016/j.apsusc.2024.159387.
- [563] E. Nikoomezari *et al.*, 'Impressive strides in antibacterial performance amelioration of Ti-based implants via plasma electrolytic oxidation (PEO): A review of the recent advancements', *Chem. Eng. J.*, vol. 441, p. 136003, Aug. 2022, doi: 10.1016/j.cej.2022.136003.
- [564] C. Y. Guo, J. P. Matinlinna, and A. T. H. Tang, 'Effects of Surface Charges on Dental Implants: Past, Present, and Future', *Int. J. Biomater.*, vol. 2012, pp. 1–5, 2012, doi: 10.1155/2012/381535.
- [565] P. K. Szweczyk *et al.*, 'Mimicking natural electrical environment with cellulose acetate scaffolds enhances collagen formation of osteoblasts', *Nanoscale*, vol. 15, no. 15, pp. 6890–6900, 2023, doi: 10.1039/D3NR00014A.
- [566] M. Kosmulski, 'The significance of the difference in the point of zero charge between rutile and anatase', *Adv. Colloid Interface Sci.*, vol. 99, no. 3, pp. 255–264, Dec. 2002, doi: 10.1016/S0001-8686(02)00080-5.
- [567] Q. Zhou, A. Wang, and H. Yin, 'Hydrothermal synthesis of CaTiO<sub>3</sub> cuboid-like nanoparticles starting from metatitanic acid and calcium hydroxide and their adsorption performance for Cd(II), Pb(II), Ni(II), and Co(II) cations', *Desalination Water Treat.*, vol. 185, pp. 247–261, May 2020, doi: 10.5004/dwt.2020.25426.

- [568] A. Pierre, J. M. Lamarche, R. Mercier, A. Foissy, and J. Persello, 'CALCIUM AS POTENTIAL DETERMINING ION IN AQUEOUS CALCITE SUSPENSIONS', *J. Dispers. Sci. Technol.*, vol. 11, no. 6, pp. 611–635, Dec. 1990, doi: 10.1080/01932699008943286.
- [569] A. Drechsler, A. Caspari, and A. Synytska, 'Influence of roughness and capillary size on the zeta potential values obtained by streaming potential measurements', *Surf. Interface Anal.*, vol. 52, no. 12, pp. 991–995, Dec. 2020, doi: 10.1002/sia.6792.
- [570] A. Chakra, C. Puijk, G. T. Vladislavljević, C. Cottin-Bizonne, C. Pirat, and G. Bolognesi, 'Surface Chemistry-based Continuous Separation of Colloidal Particles via Diffusiophoresis and Diffusioosmosis', 2024, *arXiv*. doi: 10.48550/ARXIV.2412.00246.
- [571] C. Schnitzer and S. Ripperger, 'Influence of Surface Roughness on Streaming Potential Method', *Chem. Eng. Technol.*, vol. 31, no. 11, pp. 1696–1700, Nov. 2008, doi: 10.1002/ceat.200800180.
- [572] I. O. Smith, M. J. Baumann, and L. R. McCabe, 'Electrostatic interactions as a predictor for osteoblast attachment to biomaterials', *J. Biomed. Mater. Res. A*, vol. 70A, no. 3, pp. 436–441, Sept. 2004, doi: 10.1002/jbm.a.30098.
- [573] J. Dias Corpa Tardelli and A. Cândido Dos Reis, 'Influence of surface electric charge of Ti implants on osteoblastic interaction: A systematic review', *Saudi Dent. J.*, vol. 34, no. 5, pp. 335–345, July 2022, doi: 10.1016/j.sdentj.2022.04.003.
- [574] C. B. Tovani, A. N. Faria, P. Ciancaglini, and A. P. Ramos, 'Collagen-supported CaCO<sub>3</sub> cylindrical particles enhance Ti bioactivity', *Surf. Coat. Technol.*, vol. 358, pp. 858–864, Jan. 2019, doi: 10.1016/j.surfcoat.2018.11.071.
- [575] D. Wei *et al.*, 'Rapid Fabrication, Microstructure, and *in Vitro* and *in Vivo* Investigations of a High-Performance Multilayer Coating with External, Flexible, and Silicon-Doped Hydroxyapatite Nanorods on Titanium', *ACS Biomater. Sci. Eng.*, vol. 5, no. 9, pp. 4244–4262, Sept. 2019, doi: 10.1021/acsbiomaterials.9b00414.
- [576] M. Lorenzetti, T. Luxbacher, S. Kobe, and S. Novak, 'Electrokinetic behaviour of porous TiO<sub>2</sub>-coated implants', *J. Mater. Sci. Mater. Med.*, vol. 26, no. 6, p. 191, June 2015, doi: 10.1007/s10856-015-5521-4.
- [577] M. Gruening *et al.*, 'Enhancement of Intracellular Calcium Ion Mobilization by Moderately but Not Highly Positive Material Surface Charges', *Front. Bioeng. Biotechnol.*, vol. 8, p. 1016, Sept. 2020, doi: 10.3389/fbioe.2020.01016.
- [578] M. Marcolongo *et al.*, 'Osteoblast Attachment on Biomaterials as a Function of Surface Charge', *MRS Proc.*, vol. 550, p. 121, 1998, doi: 10.1557/PROC-550-121.
- [579] H. Kawasaki *et al.*, 'Human induced pluripotent stem cells are resistant to human cytomegalovirus infection primarily at the attachment level due to the reduced expression of cell-surface heparan sulfate', *J. Virol.*, vol. 98, no. 3, pp. e01278-23, Mar. 2024, doi: 10.1128/jvi.01278-23.
- [580] D. Kabaso *et al.*, 'Mechanics and electrostatics of the interactions between osteoblasts and titanium surface', *Comput. Methods Biomech. Biomed. Engin.*, vol. 14, no. 5, pp. 469–482, May 2011, doi: 10.1080/10255842.2010.534986.
- [581] J. L. Brash, T. A. Horbett, R. A. Latour, and P. Tengvall, 'The blood compatibility challenge. Part 2: Protein adsorption phenomena governing blood reactivity', *Acta Biomater.*, vol. 94, pp. 11–24, Aug. 2019, doi: 10.1016/j.actbio.2019.06.022.
- [582] M. J. Wilhelm *et al.*, 'Determination of bacterial surface charge density via saturation of adsorbed ions', *Biophys. J.*, vol. 120, no. 12, pp. 2461–2470, June 2021, doi: 10.1016/j.bpj.2021.04.018.
- [583] D. E. Smith, A. Dhinojwala, and F. B.-G. Moore, 'Effect of Substrate and Bacterial Zeta Potential on Adhesion of *Mycobacterium smegmatis*', *Langmuir*, vol. 35, no. 21, pp. 7035–7042, May 2019, doi: 10.1021/acs.langmuir.8b03920.
- [584] A. J. Wyness, D. M. Paterson, E. C. Defew, M. I. Stutter, and L. M. Avery, 'The role of zeta potential in the adhesion of *E. coli* to suspended intertidal sediments', *Water Res.*, vol. 142, pp. 159–166, Oct. 2018, doi: 10.1016/j.watres.2018.05.054.
- [585] C. Burel, R. Dreyfus, and L. Purevdorj-Gage, 'Physical mechanisms driving the reversible aggregation of *Staphylococcus aureus* and response to antimicrobials', *Sci. Rep.*, vol. 11, no. 1, p. 15048, July 2021, doi: 10.1038/s41598-021-94457-1.
- [586] W. K. Kao, P. M. Gagnon, J. P. Vogel, and R. A. Chole, 'Surface charge modification decreases *Pseudomonas aeruginosa* adherence in vitro and bacterial persistence in an in vivo implant model', *The Laryngoscope*, vol. 127, no. 7, pp. 1655–1661, July 2017, doi: 10.1002/lary.26499.

- [587] P. Zhu, Y. Masuda, and K. Koumoto, 'The effect of surface charge on hydroxyapatite nucleation', *Biomaterials*, vol. 25, no. 17, pp. 3915–3921, Aug. 2004, doi: 10.1016/j.biomaterials.2003.10.022.
- [588] K. Yamashita, N. Oikawa, and T. Umegaki, 'Acceleration and Deceleration of Bone-Like Crystal Growth on Ceramic Hydroxyapatite by Electric Poling', *Chem. Mater.*, vol. 8, no. 12, pp. 2697–2700, Jan. 1996, doi: 10.1021/cm9602858.
- [589] L. F. Cooper and S. Shirazi, 'Osseointegration—the biological reality of successful dental implant therapy: a narrative review', *Front. Oral Maxillofac. Med.*, vol. 4, pp. 39–39, Dec. 2022, doi: 10.21037/fomm-21-77.

## 7. DISSEMINATION OF RESULTS

### Review article

1. V. Grebnevs, et.al. Toward bioactive calcium carbonate and hydroxyapatite-based coatings via plasma electrolytic oxidation – A review of challenges and current state-of-the-art. *Surface and Coatings Technology*, 2025, 506, 132135.  
<https://doi.org/10.1016/j.surfcoat.2025.132135>

### Research articles

1. V. Grebnevs, et. al. Modification of physicochemical properties and bioactivity of oxide coatings formed on Ti substrates via plasma electrolytic oxidation in crystalline and amorphous calcium phosphate particle suspensions. *Applied Surface Science*, 2022, 598, 153793.  
<https://doi.org/10.1016/j.apsusc.2022.153793>
2. V. Grebnevs, et.al. Advancements in plasma electrolytic oxidation with particle suspensions: a novel approach for the direct incorporation of calcium carbonate. *Applied Surface Science*, 2025, 713, 164360.  
<https://doi.org/10.1016/j.apsusc.2025.164360>
3. V. Grebnevs, et.al. Functional carbonate-hydroxyapatite coatings prepared via plasma electrolytic oxidation process in particles suspension. *Surface and Coatings Technology*, submission date: 03.07.2025, current status: preparation of revised manuscript.

### Conferences

1. 83rd International Scientific Conference of the University of Latvia, February 14, 2025, Riga, Latvia // V. Grebnevs, et al. PEO Method As An Alternative Towards Carbonate And Apatite Coatings – A Review Of Current State Of Art (oral presentation).
2. IEEE 12th International Conference “Nanomaterials: Applications & Properties”, September 11-16, 2022, Krakow, Poland // V. Grebnevs, et. al. Plasma Electrolytic Oxidation in Amorphous Particle Suspensions as a Way to Improve Surface Texture and Bioactivity of the Oxide Coatings (poster presentation).
3. Joint International Conference 'Functional Materials and Nanotechnologies' and 'Nanotechnology and Innovation in the Baltic Sea region' - FM&NT – NIBS 2022, July 3-6, 2022, Riga, Latvia // V. Grebnevs, et al. Amorphous calcium phosphate suspensions as a way to attain bioactivity of PEO coatings (poster presentation).
4. 22nd International Scientific Conference “EcoBalt 2021”, October 21-23, 2021, Riga, Latvia // V. Grebnevs, et al. Solutions On The Way To Preparation Of Carbonated Titanium Implant Coatings Via Plasma Electrolytic Oxidation In Suspensions (poster presentation).
5. The 20th International Conference on Total Reflection X-ray Fluorescence Analysis and Related Methods (TXRF2025), September 9-12, 2025, Kielce, Poland // V. Grebnevs, et al. Unlocking precision in hydroxyapatite analysis with TXRF: addressing challenges in Ca/P quantification (poster presentation, not directly related to the dissertation topic).